UNIVERSIDAD AUTÓNOMA DE MADRID

DOCTORAL THESIS

A new perpective on the evolution of galaxies: from global to local scales

Author:
Javier Casado

Supervisor:
Dr. Yago Ascasibar
Co-Supervisor:
Dr. Ángeles Díaz

A thesis submitted in fulfillment of the requirements for the degree of Doctor of Astrophysics

in the

Department of Theoretical Physics

October 21, 2016

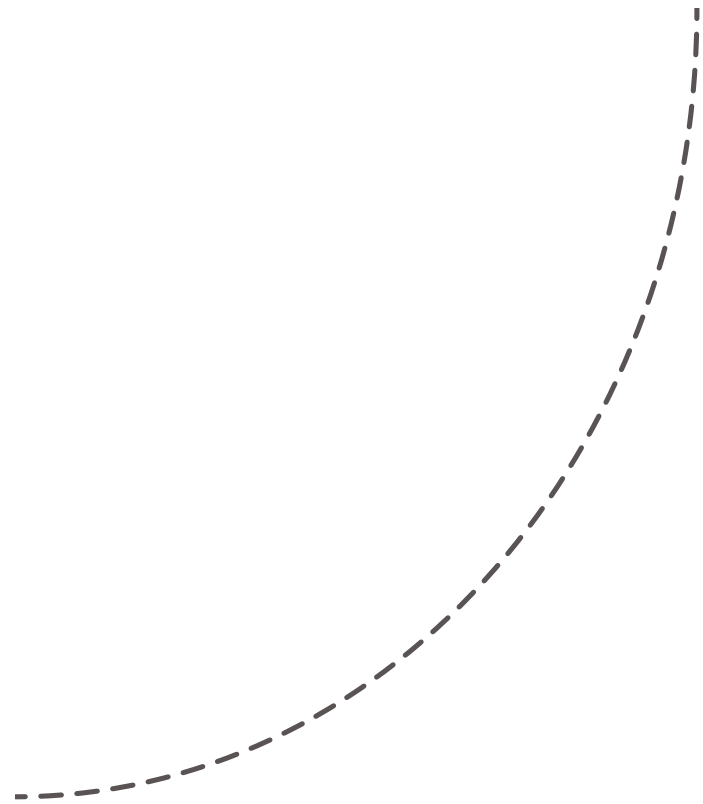

Para mis dos familias:
la que siempre ha estado ahí
y la que me ha escogido a lo largo de los años
y me ha dado cobijo

UNIVERSIDAD AUTÓNOMA DE MADRID

Abstract

Department of Theoretical Physics

Doctor of Astrophysics

A new perpective on the evolution of galaxies: from global to local scales

by Javier Casado

This thesis dissertation addresses the topic of galaxy formation and evolution with the main purpose of shedding some light on the main mechanism(s) responsible for the self-regulation of the star formation activity in the nearby Universe.

As a first step, we revisit the classic "nature or nurture" debate in this context by using a sample of ∼82000 objects extracted from the Sloan Digital Sky Survey. Our analysis cross-correlates two proxies of the specific star formation rate, the equivalent width (EW) of the Hα line and the (u-r) colour, with other physical properties (mass, metallicity, environment, morphology, and the presence of close companions) leading to the discovery of a relatively tight "ageing sequence" in the colour–EW plane. This trend favours a scenario where the secular conversion of gas into stars (i.e. nature) is the main physical driver of star formation and the gradual transition from a "chemically primitive" (metal-poor and intensely star-forming) state to a "chemically evolved" (metal-rich and passively-evolving) system.

To address the dependence on local and global properties, we investigate in further detail the resolved colour-EW diagram of ∼40 matching objects from the CALIFA survey. The IFS data reveal that the smooth "ageing" process always takes place, inside-out (i.e. the central parts are more evolved than the outskirts), across the entire extent of all galaxies. The current state of the different regions seems to be mostly driven by local processes, albeit global properties (in particular, galaxy morphology) may play an important role.

The analysis of low signal-to-noise (S/N) measurements was critical in order to reach these conclusions. To make an optimal use of this valuable information, we developed the Bayesian Technique for Multi-image Analysis (BaTMAn) algorithm for the segmentation of multidimensional data, with emphasis on the statistically-meaningful binning of IFS observations. When applied to our dataset, the method significantly reduces the scatter in the colour-EW diagram, convincingly demonstrating that there may be different ageing paths depending on the details of the local star formation history.

In our view, the new generation of IFS surveys calls for new analysis tools and methodologies, and a rigorous assessment of their accuracy (and that of the associated errors!) requires a battery of realistic test cases where the correct solution is known. The final part of this thesis describes the production of synthetic IFS observations, with similar characteristics to the CALIFA products, based on hydrodynamical simulations. This ongoing project will allow us to explore the optimal strategy to study galaxy ageing from current and forthcoming IFS data, and it will provide the scientific community with a powerful tool to test their analysis pipelines.

Acknowledgements

Los últimos años conforman la gran experiencia que define quién soy ahora mismo, y han supuesto un aprendizaje mucho mayor a nivel personal que a nivel científico. A todos aquellos que han participado del mismo les dedico estas líneas.

Don't forget to include your project advisor..., decía el template de esta tesis. No podría en ningún caso. Yago, eres, con mucho, un científico brillante y has resultado ser un director de tesis cojonudo. Pero más allá de eso eres la persona que me rescató del lugar en que me encontraba hace 3 años. Eres la persona que ha luchado por mí y por este proyecto aún sabiendo a lo que se enfrentaba. Gracias por aquel primer café. Gracias por los que nos quedan.
Habla con Ángeles, me dijo. Y eso hice. Desembocó en un segundo café que nos lleva hasta hoy. Gracias de corazón Ángeles. Por tu humanidad, por tu saber hacer, por tu ciencia, por hacerme parte de tu "familia", en definifiva, "por tus plantitas" (como dijo Carlos Hoyos). Esas plantas son un ejemplo de lo que representas, para mí y para todos los que te rodeamos: una oportunidad diferente, en muchos casos, una segunda oportunidad.
Gracias
Queda la supervisora en la sombra. Aquella que no existe, que no está en los papeles, de la que nadie sabe nada pero que siempre se presenta a las 10:30, perfectamente conjuntada (pendientes incluidos) y enciende y apaga tu luz del despacho para que, voluntariamente, te tomes un café. Eres, sin duda alguna, el pegamento. Gracias Marta, por tu Juanqui, Carlos, Teresa, Javi y Pluto. Por Concha. Por todo aquello que no es ciencia (y por la ciencia también, claro).
A mi familia de la autónoma. La lista es interminable (y alguno se me olvidará, ya lo siento de primeras).
A mi gente de todos los días (pero sobre todo los viernes "de raciones"). Ana, Jon, Hugo, Willy, Pak. No puedo sino reirme...
Alba, quién me lo iba a decir. $\sim$132 mesarios dan muchas cosas, como confianza. Gracias camarada.
A Pili, Miguel y Nico. Habéis sido la parte real de un mundo, a menudo, hermético. Gracias familia.
A Miguel (Alonso), sencillamente por la compañia. Por estar ahí.
A la música, que me concedió otras dos familias más.
A los Black Daniel's Popcorn Makers les debo muchísimo. Habéis sido durante mucho tiempo mi válvula de escape. Con muchos escenarios y muchas batallas compositivas a las espaldas sois mi orgullo. Coleti, Peri, Victor, Guille, Dani, Carlos, esto también es vuestro.
Entreversos vino más tarde, con más experiencia, con otros ideales. El aprendizaje ha sido brutal. Pablo, Bart, Areta, Víctor, todavía nos queda música pendiente. Falta gente, lo se...
Rafa, gracias por otra visión de la música, por otra visión de la vida. Por otro tipo de belleza.
Mery, cantar contigo "la magia de tu mirada" no me lo quitará nadie.
Pablo (mi rubia). Toda mi música ha pasado por tus manos y tu pitufa: Borrella's, Jueves Band, Mesiflua, Malpaís y Black. Soy muy afortunado al poder contar contigo dentro y fuera del escenario. Gracias man!
Gracias a mi familia balonmanera, gracias Jorge por el rojo.
Gracias a mi familia nevata. En especial, Omar, Ángela, gracias por acogerme con tanto cariño. No me siento de la casa rural.
Gracias Rubén (RGB), por tu amistad y por todo el trabajo. Esta tesis SI que es tuya.
Thank you Giovanni, for all our work and for sharing all the coffee. We co-own a coffee machine and a chapter of our thesis, that's a good start!
And thank to my AIP family, for a refreshing way to science.

Gracias Felipe, gracias Adina. Dos bodas y muchas horas de baile (y mucha comida) ayudaron a gestar esta tesis.
Itso. Nuestra historia está ligada a las estrellas. Rozhen nos hizo inseparables. Es precioso poder contar con alguien que discrepa contigo, que no siempre te entiende, pero que se esfuerza en quererte entender. Porque cada vez que nos encontramos me da la sensación de que no nos hemos ido. Gracias, "imash khubava usmivka".

Gracias Mamá, gracias Papá. Discrepar es de las mejores cosas que nos podían pasar. Apoyarnos pese a todo es nuestro regalo.
Gracias Tito, gracias Malu. La distancia nos ha llevado a encontrarnos, y a no estar tan lejos.

Y ya lo último. Mi hogar.
Aura, mi compañera en el camino hacia Mordor. Por aquellas sesiones interminables de George Michael en el 504, mil gracias.
Elena, gracias por Berlín. Gracias por las ganas renovadas y las aventuras por venir.
Willón. Vivir contigo ha sido un placer y una pesadilla. Contar contigo es un privilegio. Eres culpable de muchas risas y co-propietario de una Champions con el Groningen F.C. Tu y yo encontramos 7Balcones. Tu y yo cortamos y lijamos aquellos pallets que casi nos cuestan un divorcio. Eso no tiene precio.
Gracias Mario, gracias Jess. Cuando hablo de cobijo hay un lugar especial en mí para vosotros. Hay un lugar especial para ese sofá. Hay un lugar para nuestra familia, que está bien para más de un rato.
Marina, eres el mayor descubrimiento de esta tesis. Has sido el apoyo fundamental de los últimos años y la razón de que sea quien soy y de mis batallas ganadas. Mi activismo, mi feminismo. No podría explicarme sin tí. Gracias por ello. La más grande de todas.
A Andrea, Sharon, Caroline, y Jim por su disco "unplugged", sin el cuál esta tesis NO existiría y este mundo sería un poco más oscuro.
H, te he dejado para el final. En realidad hay poco que contar. Te lo sabes todo porque llevas ahí desde siempre. Hemos vivido prácticamente cada aventura juntos. Eres el compañero incondicional, eres el primer y último recurso. Darte las gracias por algo en concreto significaría dejarme algo en el tintero. Por toda una vida juntos. Gracias

Contents

Chapter 1

Introduction

"I would rather have questions that can't be answered than answers that can't be questioned" - R. Feynman

Galaxies are the building blocks of the universe.

This sentence can be read in many books, in many more articles and, surely, in every PhD thesis covering this topic. This one will be no exception to the rule.

What everyone of us interprets out of this sentence is, however (and fortunately), different. I like to think that the reason to phrase it this way is because our Universe obeys rules we do not fully understand. Part of the Nature enclosed in this Universe, the part we know a little of, behaves according to a set of physical laws we barely begin to understand and whose extent we start to have a glimpse of. This striking puzzle we are left with covers a wide range of spatial and temporal scales that are terribly intertwined[1]. When we think about galaxies, about how they form and evolve, we must take into account the larger-scale processes that make the Universe grow and expand and that are believed to set the conditions prior to galaxy formation. Neither can we forget about the physics acting at nearly atomic scales that are responsible for radiative cooling and star formation, without which none of us would be wondering about all these questions.

It is beyond the scope of this thesis (and consequently its introduction) to cover or even mention all processes involved in galaxy formation and evolution. However I will try to briefly present the current paradigm as it is understood `\today`[2] (October 21, 2016) with the intention of providing context to the work I have carried out over the last three years. This is what I think I know at the time of writing these lines, but please, ask me tomorrow, in a few weeks, or in a few years time, and I hope I can tell you something different. It would mean that I had a lot of fun in the meantime.

1.1 Galaxies

Astronomy is a very special branch of science, among other things because it is impossible to get our hands dirty by carrying out any experiment in a laboratory. Observational astronomers squeeze all the information they can out of the only thing they have in hand: the light from distant objects. In this Section, we review our current knowledge of how galaxies form their stars, based on photometric and spectroscopic observations of the local Universe. This is the kind of data that this thesis is based upon, and one important caveat is that they represent "static" images of the objects we are interested in. Therefore, one must be very careful when interpreting them in terms of causal and/or temporal relations.

On the other hand, observations of galaxies in our relatively close vicinity provide us with an exquisite level of detail, which makes possible to peek into the processes that take

[1] The Universe is just like that... THANK YOU UNIVERSE, THE PICTURES ARE AWESOME!

[2] Date at which this manuscript was compiled for the last time.

place at scales significantly smaller than the characteristic size of the galaxies. In particular, the widespread use of integral-field spectroscopy (IFS) over the past decade has revolutionised our understanding of these fascinating objects, and a large fraction of the present work is devoted to improve our analysis and interpretation of such data.

1.1.1 From global...

Galaxies as a whole come in a large variety of sizes, shapes, colours, dynamical properties, chemical composition, etc. In this thesis we will consider that the global properties of a galaxy that are potentially most relevant for regulating star formation are its total mass, its morphology, and the environment it inhabits. These properties are strongly correlated, and it seems natural to think that there must exist a (set of) physical mechanism(s) responsible for setting all of them. However, until the underlying causal relations are not properly identified, it will not be possible to single out any of these quantities as more "fundamental" than the others.

Morphology

The first thing astronomers realized when they were able to differentiate stars from some blurred objects in photographic plates, later identified as external galaxies, was that they featured very different shapes.

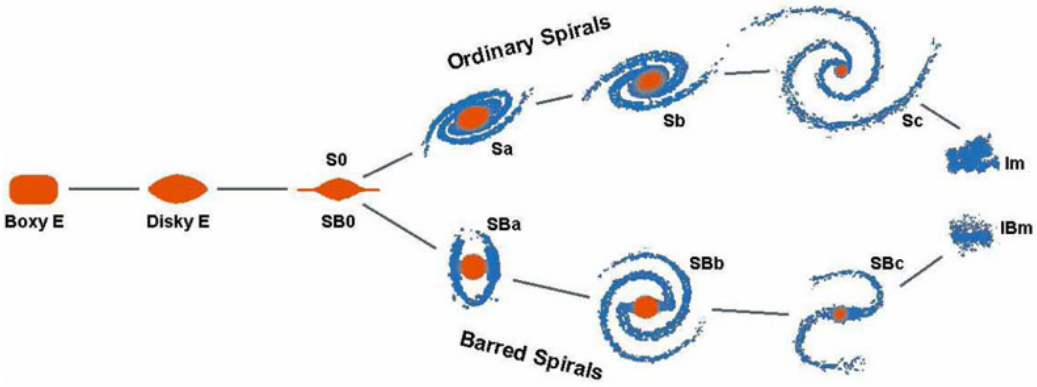

FIGURE 1.1: The Hubble sequence of galaxies as seen by Kormendy and Bender (1996). Rounded, featureless elliptical galaxies (also known as early-type) are displayed on the left of the diagram while a more complex classification dependent on the presence of bars segregates spiral galaxies (also known as late-type) into two different sequences on the right. Further subdivision among the spiral subsamples is based on or the relative importance of the bulge with respect to the disk. Beware the connecting lines!

Historically, galaxies were first classified by eye by Edwin Hubble in 1936 (Hubble, 1936). Such classification, known as the "Hubble sequence" or "Hubble tuning-fork" diagram, is shown in Figure 1.1 in the more recent version by Kormendy and Bender (1996). Alternatively, a more quantitative approach to morphological classification is based on the surface brightness (hereafter SB) profile, which is often fit by the expression

$$I(r) \propto \exp\left[-\left(\frac{\mathrm{r}}{\mathrm{r}_{50}}\right)^{\frac{1}{\mathrm{n}}}\right] \tag{1.1}$$

proposed by Sersic (1968) in terms of the half-light radius r_{50} and the Sérsic index n, characterising the spatial extent of the object and the concentration of light in the central regions,

respectively (see e.g. Graham et al., 2005). Galaxies that are visually classified as spirals tend to show low Sérsic index, $n \sim 1$, whereas ellipticals are usually best fit with $n \sim 4$ (Shen et al., 2003), consistent with the pioneering results obtained by de Vaucouleurs (1948).

Nevertheless, a single Sérsic index is not always sufficient to model the entire SB profile of many galaxies. The central regions of ellipticals are often not well described by equation (1.1), and one gets a better fit for spirals and lenticulars with a model that combines a declining exponential disk and a Sérsic profile that describes the central bulge. In general terms, spiral galaxies essentially consist of:

- a flat, rotationally-supported disk that features more or less prominent spiral arms.
- a central stellar bulge component, typically supported by velocity dispersion (resembling the structure of elliptical galaxies). It can be a massive classical bulge or a much lighter, rotationally-supported pseudo-bulge. It can also include a bar-like structure which shows up in 50-70 % of the luminous spiral objects (see e.g. Marinova et al., 2008, and references therein).
- a large spherical stellar halo that includes many globular clusters.
- a nearly spherical dark matter halo. Although it is not directly observable, its presence is necessary in order to explain the observed rotation curves (Freeman, 1970; Rubin, Ford, and . Thonnard, 1980).

The relative importance of the bulge light with respect to the disk component in spirals has lead astronomers to historically sub-classify these galaxies from bulge-dominated (Sa) to disk-dominated (Sc) systems. More recently, bulge-disk decomposition of late-type objects (Koopmann and Kenney, 1998; Hameed and Devereux, 2005) has led to several quantitative criteria to classify spirals in terms of the bulge-to-total (B/T) or bulge-to-disk (B/D) ratio. The inclusion of bars (indicated with a middle B in the name) in such classification gives rise to a secondary sequence in the "fork" diagram of Figure 1.1, although there is no clear reason to consider that these two branches are associated to different evolutionary tracks. Ellipticals, on the other hand, display a smoother and more symmetric appearance. Their light is much more concentrated, and they certainly do not show spiral arms or bars (although they are not completely featureless objects). Finally, S0 galaxies (historically called "lenticulars" because of their lens appearance) have intermediate properties between ellipticals and spirals. They are concentrated, rotationally-supported systems, and they have a disk component without spiral arms.

An important difference between morphological types is their gas content. The disks of spiral galaxies contain a significant fraction of cold gas, where hydrogen is mostly in atomic (HI) or molecular (H_2) form, as well as a sizeable amount of dust. S0s typically contain very little cold gas (particularly in the molecular phase), and most of the gas in elliptical galaxies forms a diffuse, ionized, spherical halo, at very high temperature. Nevertheless, ellipticals are not completely devoid of cold gas (see e.g. Gomes et al., 2016a; Gomes et al., 2016b), and many of them (of the order of $\sim$75%) show evidence for dust extinction in the optical (Colbert, Mulchaey, and Zabludoff, 2001).

Since cold (molecular) gas is the fuel for star formation, it is not surprising that galaxies of different morphology are forming stars at very different rates: in general terms, ellipticals, lenticulars, and spirals tend to display increasingly lower specific star formation rate (SSFR). There are plenty techniques to infer, directly or indirectly, the star formation rate (see e.g. Kennicutt, 1998; Moustakas, Kennicutt, and Tremonti, 2006; Calzetti, 2008; Gallazzi et al., 2006; Cid Fernandes et al., 2007; Panter, 2009), usually relying on the measurement of spectral features such as the intensity of the Hα emission line or D_n(4000Å) break, and/or the estimation of optical or UV colors. Most of these proxies trace the ratio of young stars

with respect to the total stellar population (i.e. the SSFR) on different timescales. Usually, spectral features are more sensitive to very young stars, able to ionize the surrounding medium (with lifetimes of the order of 10 Myr), whereas colours, specially in the optical range, trace star formation on scales of several hundred Myr.

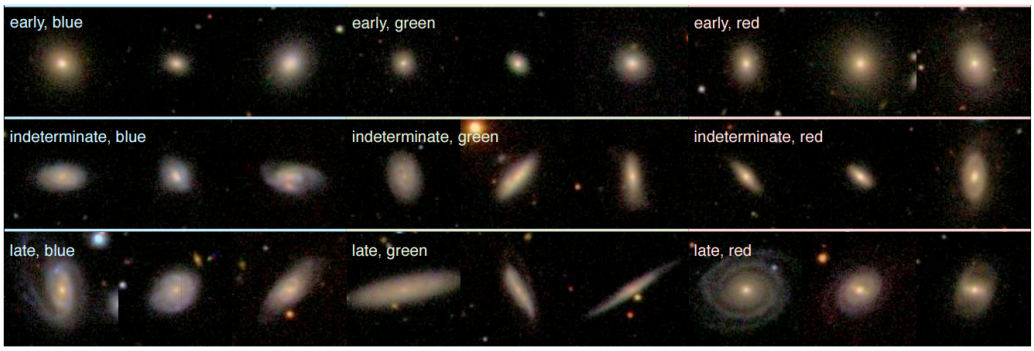

FIGURE 1.2: Composite g-r-i SDSS images of galaxies classified by morphology and colour, Figure taken from Schawinski et al. (2014). Morphological classification corresponds to the Galaxy Zoo project (Lintott et al., 2008). From top to bottom, galaxies are labelled as early-types, intermediate and late-types. From left to right the systems are sorted according to their colour following the classical blue-cloud, green valley, and red-sequence glassification.

Although one may find every possible combination of galaxy morphology and colour in the nearby universe (see Figure 1.2), it is long known that both properties are strongly correlated. In general, spiral galaxies typically display ongoing star formation in their disks, albeit one can also find a wide population of redder objects, preferentially among those displaying larger bulge-to-disk ratios (i.e. Sa). As shown in Figure 1.3, the stellar populations of classical bulges tend to be older, and hence redder. Correcting for dust content and projection effects would only reinforce this result.

On the contrary, the vast majority of Es are consistent with being passively evolving systems (see e.g. Bregman, Temi, and Bregman, 2006; Bressan et al., 2006). Some elliptical galaxies show recent star formation, predominantly among low-mass systems (Trager et al., 2000; Thomas et al., 2005), at the level of $\sim 1-3\%$ of their stellar mass, and recent results from GALEX (Yi et al., 2005; Kaviraj et al., 2007; Schawinski et al., 2007) reveal that between 15% and 30% of early types host stellar populations younger than 1 Gyr. Nevertheless, their spectra are still dominated by the light of old K giants, which imprints the population of elliptical galaxies with nearly the same (red) optical broad-band colour.

If we pay attention to their loci in Figure 1.4, where S0 are coloured in light green, and compare it with Figure 1.3, we will see that lenticulars are almost indistinguishable from the population of Es (red dots in Figure 1.4) and also overlap with the population of Sa galaxies (green points in Figure 1.3). Then, it is not only that S0's may show 'intermediate' morphologies, but also their structural parameters, Sérsic index (n) and *half-light* radius (r_{50}), their colours ($(g-r)$) and luminosities (M_r) are consistent with those of a transient/intermediate population. All these evidences, supplemented by measurements of their rotation velocity, have led many astronomers (e.g. Bedregal, Aragón-Salamanca, and Merrifield, 2006) to interpret S0 galaxies as a population of spirals that ran out of gas and ended their star formation, but the issue is far from settled (cf. Burstein et al., 2005; Sandage, 2005).

As can be seen in Figure 1.5 (from Schawinski et al., 2014, using stellar mass instead of magnitude), galaxy morphology is closely related to the segregation between the so-called

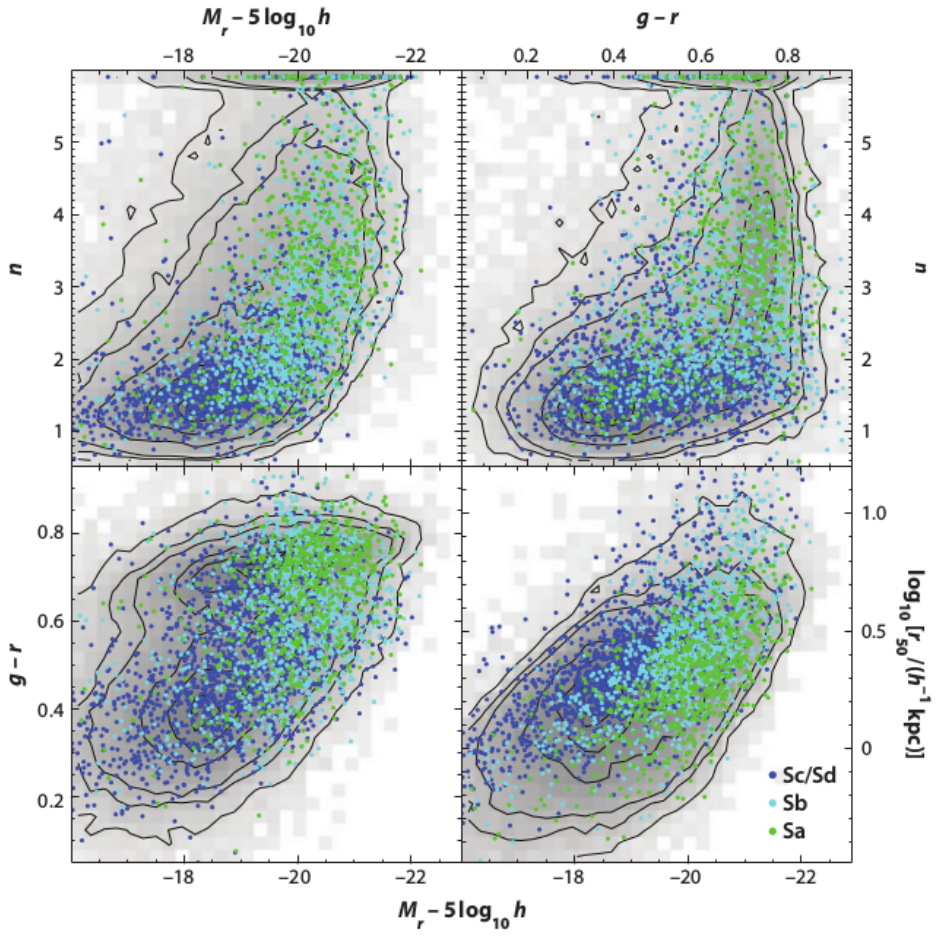

FIGURE 1.3: Distribution of spiral galaxies in the space of absolute magnitude (M_r), color ($g-r$), *half-ligh* radius (r_{50}), and Sérsic index (n). Objects are color-coded as Sa (green), Sb (cyan), Sc or Sd(blue) in terms of their morphological type as stored in the NED catalogue. Barred objects are included here too. Figure taken from Blanton and Moustakas (2009).

'red sequence' and the 'blue cloud' identified in the colour-colour or colour-magnitude diagrams (Strateva et al., 2001; Baldry et al., 2004; Baldry et al., 2006). Although we will argue in the present thesis that the distinction between "blue-cloud", "star-forming" galaxies and the "red-sequence", "passive" population is rather artificial, our results will provide additional support to the connection between morphology and SSFR, suggesting that this global property of the galaxies may indeed be one of the key aspects of the problem.

Mass

In principle, one could have two galaxies with different masses and identical intensive properties (morphology, stellar-to-gas fraction, SSFR, colours, metallicity, etc.). One would simply be a scaled version of the other. However, most of these properties have been observed to correlate strongly with stellar mass. Since the mass of a galaxy traces the depth of its gravitational potential, it would not be surprising that it played a role on the processes of gas accretion, cooling, star formation, and feedback, but the physical details are far from being well understood.

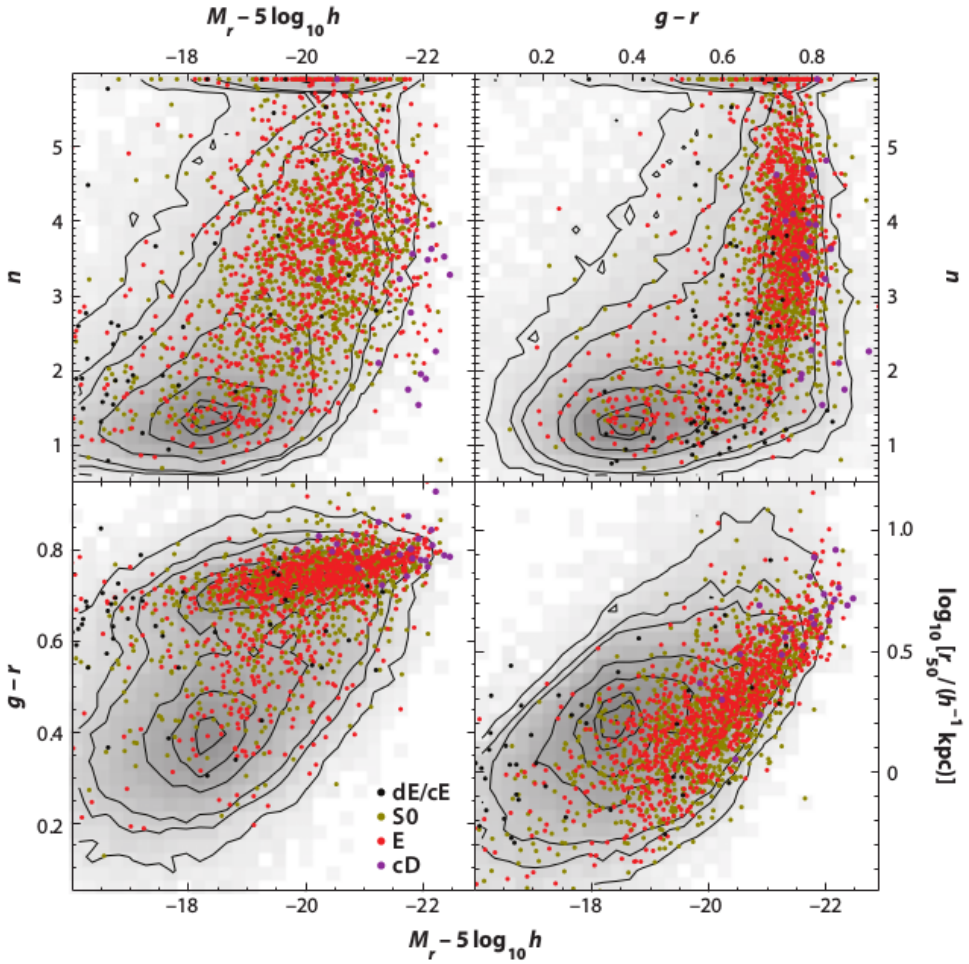

FIGURE 1.4: Distribution of elliptical galaxies, S0 in the space of absolute magnitude (M_r), color ($g - r$), *half-ligh* radius (r_{50}), and Sérsic index (n). Objects are color-coded as S0 (light green), Es (red), dE(black), and cD(purple). Figure taken from Blanton and Moustakas (2009). Equivalent to Figure 1.3.

As shown in Figures 1.3, 1.4, and 1.5, less massive (or fainter) galaxies tend to display lower bulge-to-disk ratios (late-type morphologies) and bluer colours (even at fixed morphology). The vast majority of low-mass objects are blue, star-forming spirals, whereas the most massive ones tend to be red, passive, and concentrated ellipticals. In addition, recent surveys of the 21-cm hyperfine transition of the hydrogen atom and several transitions of the CO molecule (see e.g. the review by Blanton and Moustakas, 2009, and references therein) have been able to create a census of the HI and H2 content in nearby galaxies, showing that, on average, low-mass systems are much more gas-rich (higher gas fraction) than their massive counterparts. Nevertheless, the relation is not entirely one-to-one. Most blue galaxies are in general low-mass systems featuring star-forming disks, but red galaxies include a significant fraction of dust-reddened spirals and S0 galaxies. At $M_r \sim -20$, at least one third of the red sequence display Sa or even later morphologies.

Observationally, much of our knowledge is biased towards such "intermediate"-mass systems, and a large fraction of the discussion above about the properties of spiral, elliptical, and lenticular galaxies implicitly refers to objects that are roughly as massive as our very own Milk Way. On the one hand, every instrument has a finite sensitivity, and all objects fainter than a certain flux limit will remain utterly invisible. On the other hand, the most massive objects are so rare that a vast extension of the Universe has to be probed in order

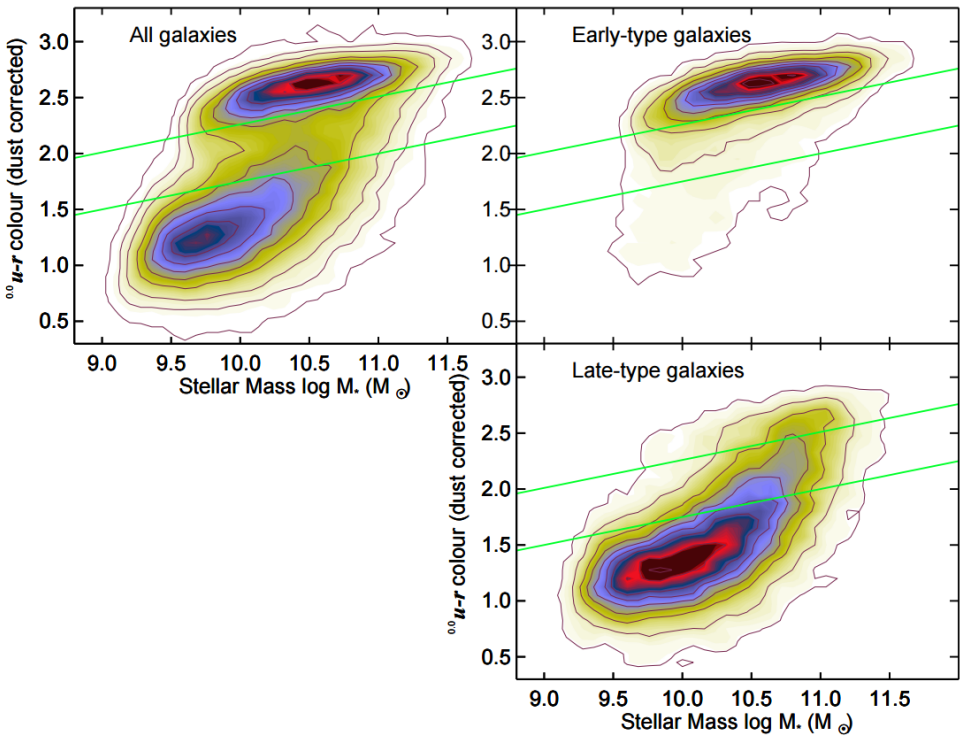

FIGURE 1.5: Colour-mass (equivalent to the colour-magnitude) diagram taken from Schawinski et al. (2014). The figure illustrates (top left panel) the so called bimodality of the galaxy population, with galaxies either populating the red-sequence or blue-cloud. Green lines illustrate the less densely populated area, commonly referred to as the 'green valley', that accounts for intermediate colours. Right panels show that the colour separation correlates with morphology.

to have a minimal chance to detect one of them.

Due to historical reasons, objects with absolute magnitude in the B band $M_B \gtrsim -18$ are commonly referred to as dwarf galaxies. Although they contain a relatively small fraction of the total number of stars, these objects are believed to be the most abundant galaxies in the Universe. They cover a broad luminosity range (up to 6 orders of magnitude) with very faint objects being detected down to $M_V \simeq -2.6$ (Martin et al., 2007). Such low fluxes are only reachable in our immediate vicinity, and therefore studies of dwarf galaxies are restricted to the local volume. Given their low gravitational potential, these systems are very interesting objects to study galaxy evolution, as they are expected to be strongly affected by stellar feedback, environmental changes, or interactions. According to their gas content and star formation properties, dwarf galaxies can be divided into two main groups:

- **gas-rich systems with ongoing star formation**
  Roughly as a continuation of the population of spiral galaxies, dwarf irregulars (dIrr) with sizes < 5 kpc, containing one or a few HII regions, display a higher gas fraction as their stellar mass decreases, and they seem to be randomly distributed in the universe. While the kinematics of the smaller systems depict chaotic patterns, the larger dIrr show evidence for rotational support. The most extreme objects among dIrr are blue compact dwarfs (BCD) and HII galaxies, typically showing sizes of the order of ~ 2 kpc. Their gas content is even higher than that of dIrr, and the estimates of their dark matter content are higher than that of typical galaxies. BCD's show stellar

masses of the order of $M_* \sim 10^9$, while their dark matter component is of the order of $M_{DM} \sim 10^{11}$ (Skillman, 1996; Tajiri and Kamaya, 2002; van Zee, 2001).

- **gas-poor systems dominated by an old population**
  On the other hand, dwarf ellipticals (dE) and dwarf spheroidals (dSph) are fainter extensions of the early-type systems. Contrary to dIrr, these objects are relatively regular, and they are found primarily within groups and clusters of galaxies. They show very little (if any) gas content, and they are dominated by a very old population with maybe a few young stars. They also span a broad range in luminosity and have a large dark matter content (Gilmore et al., 2007).

On the other extreme, brightest cluster galaxies (BCG) are defined as the most optically luminous object in massive ($\gtrsim 10^{14}$ $M_\odot$) clusters. There is, of course, only one BCG per cluster, and there is often a large gap with respect to the size and magnitude of the next most luminous object in the system. They deviate from the scaling relations of less massive galaxies, and they typically show signatures of a complex kinematic structure. All these facts hint that BCGs are probably the most extreme example of dry mergers as the origin of elliptical galaxies, albeit the wide variety among Es casts doubts about its generalisation to all such systems.

Environment and interactions

The dichotomy between gas-rich and gas-poor dwarf galaxies and the systematic differences between BCGs and field ellipticals evidence that the influence of the environment on the evolution of any given galaxy cannot be neglected. Although different methods exist in the literature (see e.g. Kaiser, 1987; Balogh et al., 2004b; Kauffmann et al., 2004; Cooper et al., 2005; Yang et al., 2007; Muldrew et al., 2012), galactic environment is often characterized by the local (over)density defined on a certain scale, which is know to correlate with the mass of the dark matter halo that hosts the system. This density is usually estimated from the projected distance to neighbouring galaxies, imposing an appropriate magnitude threshold to avoid Malmquist bias and a maximum relative velocity to minimize projection effects.

In principle, galaxies living in a denser environment are subject to more interactions, both with other galaxies as well as with the hot gas of the intracluster medium (ICM) in galaxy groups and clusters:

- *Galaxy harassment* (Moore, Katz, and Lake, 1996), specially frequent in the densest environments, encompasses all tidal interactions between a satellite galaxy with the host halo as well as with the other satellite galaxies (via high-speed encounters). This process would be able to disrupt and even radically change the morphology of the systems involved, and it is believed to play an important role in galaxy clusters.

- *Galaxy mergers* are are easily visible in 1-2% of all luminous galaxies, including both systems in 'clear interaction' (i.e. two objects in a single image tearing each other apart) as well as disrupted objects (displaying tidal tails, putatively as a result of a recent merger/interaction) and 'close pairs' (typically < 50 kpc projected separation on the sky). Unfortunately, morphological disruptions are a dubious merger indicator, as galaxies may undergo a variety of internal processes (e.g. supernova explosions, AGN feedback) that could disrupt their morphology. On the other hand, counting galaxy pairs is a process that can suffer from severe contamination and selection biases, even in the case of redshift-selected samples. Besides, there are many types of galaxy mergers (depending on the galaxy masses, morphologies, relative speed, and

orientation), and each of the three 'indicators' mentioned above trace different stages whose time scale is still unclear. Mergers come in a wide variety of forms (minor versus major, dry versus wet, etc.) and do take place in all kind of environments. They are frequently pointed out as the main culprit of driving morphological changes (Kormendy and Kennicutt, 2004), triggering star formation bursts and AGN activity, dynamically heating stellar disks (Tapia, Balcells, and Eliche-Moral, 2010), or generating counter-rotating cores in ellipticals (Balcells and Quinn, 1990).

- *Ram-pressure stripping* is a process, first proposed by Gunn and Gott (1972), by which a galaxy entering a dense environment (namely, a cluster) will experience a strong pressure from the hot ICM, opposite to its motion and capable of sweeping out its gas reservoir. Observations (see e.g. Ebeling, Stephenson, and Edge, 2014) show that this process has the power to truncate star formation in relatively short time scales, of the order of $\sim 10^7$ yr.

- *Strangulation* is a slightly different mechanism by which the gas reservoir of a galaxy would be exhausted. As the system enters a denser environment, the temperature of the surrounding gas increases and the accretion of cold gas decreases to negligible levels. As a consequence, the galaxy will starve, and star formation will eventually cease, albeit on a longer time scale as there is no gas removal.

Observations show that, although some galaxies live in isolation, most of them have companions or reside in dense groups or clusters. According to Tully (1987), over 70% of the galaxies in the local Universe are located in galaxy groups with typical sizes of ~ 1 Mpc^3, and it is well known that galaxy morphology (Dressler, 1980), broad-band color and Sérsic index (e.g. Hashimoto and Oemler, 1999; Blanton et al., 2005; Yang et al., 2007), and luminosity (e.g. Hoyle et al., 2005) do depend on environment. In low-density environments, blue disk galaxies completely dominate the low-mass population, whereas early-type galaxies are common at the high-mass end of the distribution. Only in the field do ellipticals show evidence for the presence of a small amount (less than 1%) of cold atomic and molecular gas (Morganti et al., 2006). As we move to denser environments, the fraction of objects displaying red colour and early-type morphology increases, with lenticular galaxies replacing spirals near the centre of massive clusters (Dressler et al., 1997), while the population of star-forming galaxies decreases, becoming almost negligible even among the faintest objects. Interestingly, the environmental dependence of the structural parameters (morphology or Sérsic index) is considerably reduced if galaxies are selected in terms of any property (e.g. a fixed value of colour, D_n4000, etc.) that traces their star-formation history (Park et al., 2007; Ball, Loveday, and Brunner, 2008; Bamford et al., 2009).

1.1.2 ... to local scales

At the present day, it is clear that galactic evolution is deeply intertwined with global properties such as morphology, mass, and environment. However, the detailed physical processes that are responsible for the observed correlations and their relative importance are far from being completely understood. Moreover, if we consider the mechanisms responsible for driving star formation in galaxies we cannot ignore that star formation itself is a very local process (mainly restricted to HII regions located in the arms of spiral galaxies). Hence, it is reasonable to assume that local properties may play an important role in regulating the formation of new stars (and, why not, dominate and/or drive global ones).

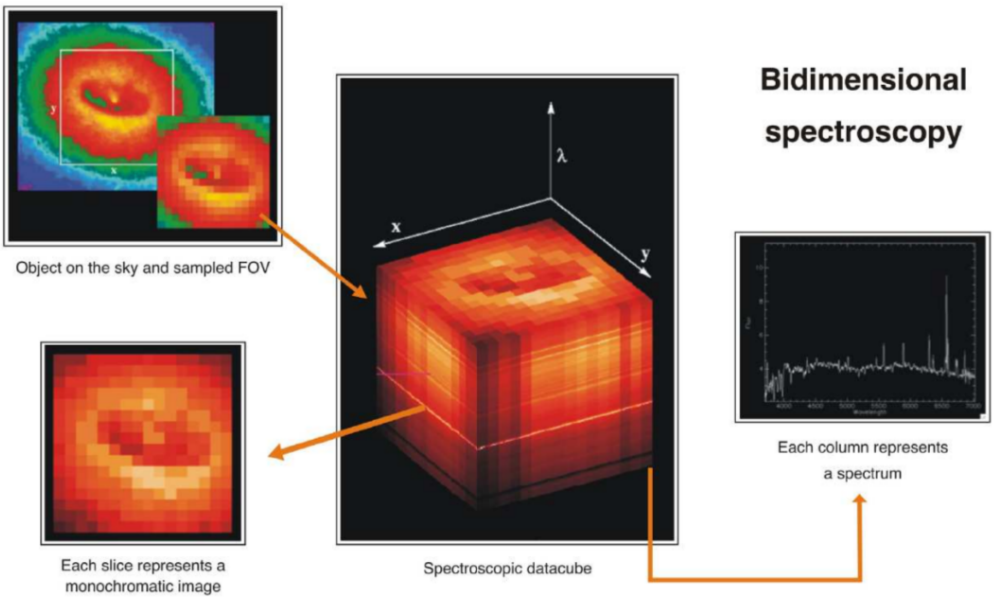

FIGURE 1.6: Explanatory scheme of the essential aspects of 3D spectroscopy. IFS datacubes (central image) can be interpreted as a set of monochromatic images (layers) stacked in a 3-dimensional matrix. The two "spatial dimensions" locate the position of every spaxel, which contains a full spectrum corresponding allocated along the third "spectral" dimension. This figure has been taken from Rosales-Ortega (2009)

The advent of Integral-Field Spectroscopy

Over the last years, a much deeper insight on the mechanisms that regulate star formation in galaxies has been provided by the advent of systematic integral-field spectroscopic surveys (IFS, see the book by Allington-Smith, 2007). Figure 1.6 (taken from Rosales-Ortega, 2009, ,who adapted it from that of M. Roth, `http://tinyurl.com/IFS-principle`) illustrates the basic idea behind IFS observations: the field-of-view (FoV) covered by the instrument is sampled into discrete regions (called spaxels), every one of which contains a spectrum. The advantages of this observational technique are obvious. In the particular case of galaxy observations, IFS provides spatially-resolved spectra over a significant extent of the system. With this kind of data one can study the local physical properties of the gas, dust, and stars with an unprecedented level of detail and simultaneously reduce (and understand) the aperture effects common in broadly used spectroscopic sky surveys (such as SDSS, Abazajian et al., 2009, , this thesis work is a good example of it). To put some numbers, the Calar Alto Legacy Integral Field Area (CALIFA, Sánchez et al., 2012a), IFS survey that will be used in this work, offers a wide spatial coverage, up to 2.5 R_e, in combination with a good spatial resolution ($\sim$1kpc). This kind of data has enabled to recover and study in detail some of the important structures in galaxies, such as spiral arms, bars, bulges, giant HII regions, etc.

Despite its short history, IFS has achieved a notable success bringing extremely relevant changes to the established paradigm. Among the most striking results obtained using Integral-Field Spectroscopy we must highligh the work conducted by Emsellem et al. (2007) and Cappellari et al. (2007), which clearly illustrates the power of this observational technique. The work of these authors studied the kinematics of elliptical galaxies and revealed that Es (believed for a long time to be "simple" systems) depict a variety of velocity patterns. IFS analysis was then responsible of changing the classical picture of galaxy morphology by separating elliptical galaxies into two different families, slow and fast rotators

(seggregation based on their stellar kinematics).

- *Slow rotators* are weakly triaxial and more massive (they dominate the Es population above $M \approx 10^{11}\mathrm{M}_{\odot}$). Their isophotes have elliptical shapes from any observed direction, present "cores" in their central part (i.e. their SB profiles flatten in the center), and have no disk features. These objects are generally found near the halo centre of groups and clusters which has been linked to a plausible dry merger origin. Supporting this theory, slow rotators show peculiar kinematic features such as twists or kinematic decoupled cores (Krajnović et al., 2011). Their stellar populations tend to be older and show enhancement of α-elements. They also contain strong radio sources and Xray emitting gas.

- *Fast rotators* are axisymmetric and dominate the low- and intermediate-mass population (Cappellari et al., 2011). These oblate systems show clear disky isophotes which has been the origin of their missclassifications as disky-E or S0 when seen edge-on. They are generally satellite galaxies showing younger (younger than slow rotators, still older than spirals) populations which convert them in clear candidates for environmental quenching. Speculated to be the evolution of spirals entering higher density environments (Cappellari et al., 2013) they are less concentrated than slow rotators and they lack both radio and X-ray emission.

A consequence of all these findings is a new morphological classification scheme and a new scenario of galaxy evolution, as illustrated in Figure 1.7.

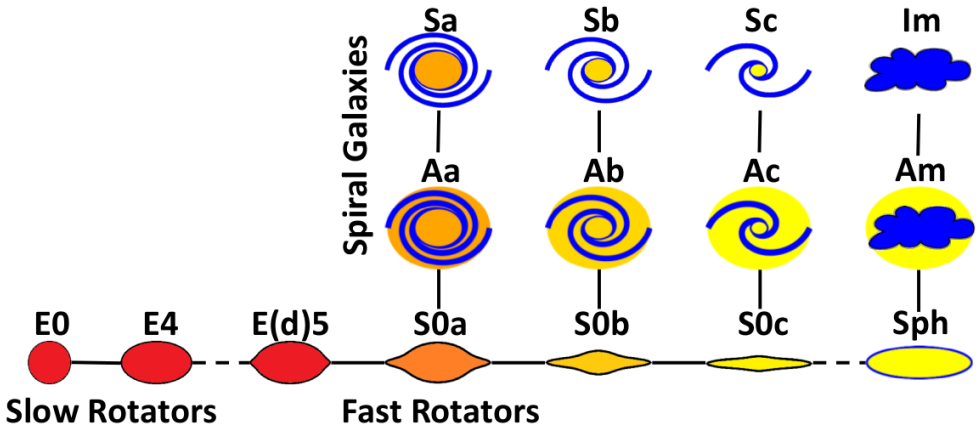

FIGURE 1.7: The "comb" morphology diagram, adapted from Cappellari et al. (2011) and Kormendy and Bender (2012). In this version of the "morphologycal" diagram of galaxies the fast rotators, flat early-type galaxies with disky isophotes and high values of rotational velocity would be direct evolutionary states of the spiral galaxies with similar bulge-to-disk/total ratios. Again, very much is hidden in the morphology of galaxies and one must be very careful with "connecting lines"!

Another important result of several IFS studies is that some of the global scaling relations, such as the mass-metallicity relation (Sánchez et al., 2013), the metallicity-gas fraction relation (Ascasibar et al., 2015), or the star formation main sequence (Cano-Díaz et al., 2016), hold on local scales. This findings not only emphasize the fundamental nature of these scaling relations but support the hypothesis of local processes playing a major role in driving galaxy evolution. The number of science cases studied so far with IFS data is large and diverse, and it will continue growing in the advent of the new data to come (see Sánchez et al., 2016a, for a complete list of scientific results of the CALIFA collaboration).

Notwithstanding the above mentioned success, IFS has several major difficulties to overcome.

On the one hand, the scientific community still lacks from statistically robust samples of galaxies observed with this technique (these observations are much more time consuming and require a longer and more complex analysis time). This situation is going to change in the coming years, as there are many observational programmes that are producing (or will produce) systematic IFS surveys targeted at different galaxy populations, e.g. SAMI (Croom et al., 2012), MaNGA (Bundy et al., 2015), MUSE (Bacon et al., 2004), WEAVE (Dalton et al., 2014) and HARMONI (Thatte et al., 2014).

On the other hand, IFS obtains multiple spectra in a single observation. To provide some examples, CALIFA observations use $\sim$ 300 spectroscopic fibres per pointing ($\sim$900 per object) to obtain of the order of $\sim$3000 spectra, while the MUSE instrument provides 90.000 spectra per pointing[3], using 24 spectrograph units simultaneously. This necessarily implies that the amount of light per element of spatial and spectral resolution is typically lower than in traditional observations, which, in turn, leads to a lower signal-to-noise (even more so considering the fact that the large fields of view of these instruments often target the fainter outer regions of the galaxies in addition to the bright central part).

In conclusion, Integral-Field Spectroscopy comes at the price of a higher level of complexity in the analysis of the data. Many studies carried out in the recent years present algorithms that have been specifically designed to handle the low S/N problem. Some examples relevant for the present thesis project are the work conducted by Cappellari and Copin (2003) that investigates the properties of the stellar population in early-type galaxies or the study of HII regions in galaxies described in (Sánchez et al., 2012c). What these two cases (and many other IFS tools) have in common is that they perform a spatial binning of the data as first step of their analysis in order to increase the signal-to-noise (S/N) to carry out meaningful measurements. However, IFS observations show that galaxies have plenty substructure and these binning techniques, if used naively, can lead to a loss of information (in addition to the obvious loss in spatial resolution). Present (and future) IFS instruments, such as MUSE, (will) provide observations with an exquisite spatial resolution, which emphasizes the need for dedicated analysis tools. Besides, the design of these algorithms requires a thorough calibration, which is particularly true in the case of IFS observations. We devote part of the work presented here to address these technical issues.

1.2 This thesis

This thesis approaches the topic of galaxy evolution from an observational point of view, with the main purpose of deciphering which is (are) the main mechanism(s) responsible for the evolution of galaxies. We aim to disentangle the relative importance of *"nature"* and *"nurture"* processes, as well as *"local"* and *"global"* ones, from two complementary strands of work:

On one hand, we consider photometric and spectroscopic (single-fibre) data from the Sloan Digital Sky Survey (SDSS) as well as IFS data from the Calar Alto Legacy Integral Field Area (CALIFA) survey. With the former we conduct a statistically-robust study of some of the properties of galaxies that we expect have a major role in driving their evolution. We use the second dataset (CALIFA), much smaller in number, to extend our study across the galaxy, avoiding aperture effects and focusing on the systematics of comparing the two datasets.

On the other hand, the inclusion of IFS observations and the importance of low signal-to-noise regions compels us to devote a substantial part of the work in this thesis to the

[3] YEAH!

design of dedicated analysis tools. The need for coherent calibration of the these (and other) analysis pipelines motivates the final part of this dissertation, which covers the generation of reliable synthetic IFS datacubes from hydrodynamical simulations of galaxy formation and evolution in a cosmological context.

1.2.1 Structure

This manuscript is structured as follows:

Chapter 2 depicts the exhaustive analysis of ∼82500 galaxies extracted from the Sloan Digital Sky Survey. We present a cross-correlation of two proxies of the SSFR, the equivalent width of the Hα line and the (u-r) colour, with other physical properties (mass, metallicity, environment, morphology, and the presence of close companions) in order to investigate their relative importance in driving galaxy evolution, distinguishing between *"ageing"* (gradual conversion of gas into stars, with only moderate fluctuations in the star formation rate), *"quenching"* (a sudden interruption of the star formation activity) and *"rejuvenation"* (a starburst episode that actually decreases the mass-weighted age of the stellar population).

In Chapter 3, we extend the analysis to consider those objects that have been observed within the CALIFA collaboration. In this part of the dissertation we present a careful characterization of the considered sample and a comparative analysis. The goal is to verify the results of Chapter 2 and explore the role of local and global properties of galaxies in driving the *ageing* process.

Chapter 4 introduces BaTMAn (Bayesian Technique for Multi-image Analysis), a novel image segmentation technique based on Bayesian statistics. This part of the dissertation is then devoted to the description and testing of the binning algorithm, and emphasizes the need for carefully characterizing IFS data prior to their analysis.

Chapter 5 describes the "SELGIFS data challenge" project in which we introduce a robust method to convert hydrodynamical simulations of realistic galaxies into synthetic IFS observations using radiative transfer tools. We cover in this work the formatting of the simulated data into CALIFA observations and the production of maps of the resolved properties (as measured prior to "virtually observing" them) in order to test observational analysis tools (such as the one presented in Chapter 4).

Chapter 6 summarizes our results and describes future projects derived from this thesis work. Brief closing remarks are presented in Chapter 7.

1.2.2 Scientific Acknowledgements

All the work that will be presented in this dissertation is part of collaborative projects that are already published, in the process of publication of in draft version. A brief introductory note at the beginning of every chapter contains information about the authorship and publication status. Nonetheless, we would like to explicitly acknowledge here some individuals and collaborations without which these lines would not have been possible.

Chapter 2 makes use of the freely available data of the Sloan Digital Sky Survey (SDSS), a major multi-filter imaging and spectroscopic redshift survey using a dedicated 2.5m wide-angle optical telescope at Apache Point Observatory. Without such an enormous and fruitful observational project, not only this thesis but much of the amazing science conducted in the past 15 years would not have been possible.

Chapter 3 could not have been accomplished without the exhaustive work of the Calar Alto Legacy Integral Field Area (CALIFA) collaboration, which has provided the scientific community with a complete and fully characterized sample of IFS observations of nearby galaxies. Neither should we forget the essential work of Dr. Rubén García Benito, who

performed the direct analysis of the datacubes with his SHIFU pipeline to obtain some of the observables needed for this work.

The work presented in Chapter 4 also counted with the collaboration of Dr. Rubén García Benito, who performed a similar analysis to the one presented in Chapter 3. This part of the thesis presents a new analysis tool that has required an exhaustive testing, and many volunteers provided their time, ideas, and data. Here we would like to thank Dr. E. Bellocchi, Dr. L. Galbany, Dr. P. Weilbacher, and MsC. O. S. Choudhury for their particularly useful feedback.

Finally, Chapter 5 is part of a collaboration project led by MsC. G. Guidi, who was responsible for running the radiative transfer code SUNRISE and computing the physical properties of the simulated dataset. The simulations used in this work have been run by Dr. C. Scannapieco and Dr. M. Aumer, making use of the dark matter-only simulation of the Aquarius project. The author of this thesis is responsible for the characterization (field of view, spatial and spectral resolution, noise, format) of the CALIFA data and its implementation in the synthetic datacubes, as well as the measurement of observational properties and the testing of observational analysis pipelines (work in progress).

Chapter 2

SSFR in SDSS galaxies: nature or nurture?

This chapter is based on the article:
"Nature or nurture? Clues from the distribution of specific star formation rates in SDSS galaxies"
by J. Casado, Y. Ascasibar, M. Gavilán, R. Terlevich, E. Terlevich, C. Hoyos, & A. I. Díaz
published in MNRAS 451, 888, 2015

2.1 Introduction

Galaxies are known to evolve through a mixture of intrinsic ('nature') processes, such as gas accretion, conversion into stars, and chemical enrichment, as well as through interactions ('nurture') with other galaxies. The observed distribution of their physical properties (e.g. stellar and gas mass, metallicity, SSFR, luminosities and colours) is set by a more or less complex combination of internal and external processes, but their relative importance is still a matter of debate. This first chapter of the thesis presents a complete study of the mechanisms that regulate the (specific) star formation rate in nearby galaxies based on the study of a spectroscopic sample of galaxies extracted from the Sloan Digital Sky Survey (hereafter SDSS). More specifically, this work focuses on the role of dense environments and close interactions on quenching and/or triggering star formation.

Over the last decades, many studies have found that star-forming galaxies (the so-called 'blue cloud') are neatly segregated from passively-evolving systems (the 'red sequence') in a colour-magnitude diagram (e.g. Tully, Mould, and Aaronson, 1982; Strateva et al., 2001; Baldry et al., 2004; Baldry et al., 2006). Objects in the intermediate region, known as the 'green valley', are typically considered a transition population (e.g. Bell et al., 2004; Faber et al., 2007; Martin et al., 2007; Schiminovich et al., 2007; Wyder et al., 2007; Mendez et al., 2011; Gonçalves et al., 2012). Many of them display signatures of active galactic nuclei (AGN) in the optical spectrum (e.g. Salim et al., 2007; Schawinski et al., 2007; Schawinski et al., 2010), and their colours are often interpreted as evidence for a putative 'quenching' process that would quickly interrupt any star formation activity.

A mandatory early step considered in this thesis work was to define, and in some cases revisit/clarify, certain evolutionary concepts. Along this chapter (an the entire manuscript), we will use the word 'quenching' in the sense of a discrete event that instantaneously (or in a very short time scale) truncates the star formation activity in a given galaxy. In contrast, we will use the term 'ageing' to denote a gradual increase in the mass-weighted average age of the stellar population

$$\tau_*(t) = t - \frac{\int_0^t t' \, \psi(t') \, \mathrm{d}t'}{\int_0^t \psi(t') \, \mathrm{d}t'} \tag{2.1}$$

without any sudden change in its star formation rate (SFR) $\psi(t)$. With this definition, it can be easily shown that galaxies become 'older' as they evolve unless their stellar mass

increases faster than exponentially (e.g. during a strong starburst). Therefore, all galaxies are subject to 'ageing', whereas they may or may not undergo 'quenching' or 'rejuvenation burst' episodes.

It has long been known that galaxy colours are strongly correlated with environment, suggesting that 'quenching' might be a 'nurture' process. The location of the red sequence is fairly independent on galaxy density (Sandage and Visvanathan, 1978), and the position of the blue cloud in the colour-magnitude diagram varies only weakly (e.g. Balogh et al., 2004b). Most galaxies in the blue cloud display similar SSFRs, varying relatively slowly with mass (Noeske et al., 2007; Speagle et al., 2014), and it has been shown (e.g. Balogh et al., 2004a; Tanaka et al., 2004; Park et al., 2007; Wijesinghe et al., 2012) that the distribution of Hα equivalent widths for the star-forming population, selected on line intensity and/or colour, is not a strong function of local density. However, the fraction of red and blue galaxies is a strong function of the environment.

One possible interpretation would be that all galaxies evolve along a 'star-forming sequence' until a quenching event would rapidly drive them through the green valley towards the red sequence (see e.g. Peng et al., 2010). According to these authors, there are two different quenching mechanisms, one related to mass (i.e. 'nature') and one related to environment ('nurture'). As galaxies grow in mass, some unidentified process would shut down star formation with a probability that scales linearly with the instantaneous star formation rate (as opposed to e.g. a fixed mass threshold). 'Environment quenching' would be driven by galactic overdensity, and it is found to be roughly independent of stellar mass or cosmic epoch up to $z \sim 1$, consistent with the infall of the galaxy into a larger dark matter halo. Both mechanisms are independent, and their total effect on the fraction of red galaxies is fully separable.

This kind of scenarios implicitly assume that star-forming and passive galaxies form two distinct groups. However, some studies question the very existence of such a bimodality in the galaxy population. Applying data mining techniques, Ascasibar and Sánchez Almeida (2011) found that almost all SDSS galaxies are distributed along a well-defined curve in the multidimensional space defined by their spectra. Only optically-bright active galaxies appear as an independent, roughly orthogonal branch that intersects the 'main sequence' exactly at the point of the transition between star-forming and passive systems. The location of such transition is thus well defined, but there is no apparent gap, as far as the optical spectra are concerned.

As recently pointed out by Schawinski et al. (2014), galaxy morphology may be an important piece of the puzzle. While early-type galaxies display signatures of rapid quenching, leading to a fast transition through the green valley, late-type galaxies are consistent with slowly-declining star formation rates, with typical time scales of the order of several Gyr. They do not separate into a blue cloud and a red sequence, but rather span almost the entire $(u - r)$ colour range without any gap or valley in between. The apparent bimodality in the colour-magnitude diagram arises from the superposition of both morphological populations.

Schawinski et al. (2014) identify early-type galaxies with merger-induced (i.e. nurture) quenching, whereas they advocate for a discrete quenching event in the distant past of late-type galaxies, perhaps associated with reaching a certain halo mass (i.e. nature), that would have shut off the infall of new cold gas. However, the instantaneous SFR would not drop immediately, but gradually decrease until the cold gas reservoir is exhausted. Therefore, this process would qualify as 'ageing' rather than 'quenching' according to our terminology.

Here we would like to statistically quantify the secular evolution of the SSFR as well as the relevance of environment and interactions. Galaxies in dense environments are subject to a plethora of processes, such as tidal forces, strangulation of the gas supply, ram-pressure stripping, or galaxy harassment (see e.g. Boselli and Gavazzi, 2006) that would suppress the

star formation rate, although the exact time scale is still debated (see e.g. Wijesinghe et al., 2012, and references therein).

On the other hand, close interactions with neighbouring galaxies can lead to gas compression and trigger star formation (see e.g. Li et al., 2008; Ellison et al., 2008; Ideue et al., 2012). Extreme objects such as ultraluminous infrared galaxies are always found to be strongly interacting systems (Sanders and Mirabel, 1996; Surace et al., 1998). However, the mechanisms that set the star formation rate at the low-mass end are yet unclear. Some of these systems show very high SSFRs, often interpreted as massive 'rejuvenation' bursts of star formation (e.g. Heckman et al., 1998), but there is little evidence that these episodes are triggered by interactions with nearby neighbours (see e.g. Fujita, 1998; Martig and Bournaud, 2008; Lamastra et al., 2013; Lanz et al., 2013, and references therein). HII galaxies represent the most extreme objects in this mass range. They are, in general, blue compact dwarf (BCD) galaxies showing very strong and narrow Balmer emission lines with large equivalent widths (Sargent and Searle, 1970), and they have the lowest metal content of any star-forming galaxy (Searle and Sargent, 1972; Rosa-González et al., 2007). Observations show that the most luminous HII galaxies tend to live in very low density environments without obvious companions (see e.g. Telles and Terlevich, 1995; Vilchez, 1995), although they show irregular morphologies and large velocity dispersions, consistent with a 'nurture' origin (Telles, Melnick, and Terlevich, 1997).

In this chapter we will present the results of a statistically robust study of the physical properties of star-forming galaxies in the local universe. We aimed to disentangle the contribution of nature and nurture to galaxy ageing, quenching, and rejuvenation focusing on the role of stellar mass, local environment, close interactions, and metallicity in setting the SSFR. Although there is a vast amount of literature on this topic, this work presents one of the most comprehensive studies of all the relevant galaxy properties to date. It has also sufficient statistics to provide a fair representation of very faint objects, extreme values of the SSFR, and evolutionary phases that last for relatively short times. We have chosen to use purely observable quantities rather than model-dependent inferences, and we propose new tracers of galactic overdensity and close interactions. Most importantly, we propose a physical interpretation of our results that is somewhat different from the currently most widely accepted scenarios.

In the following pages we will describe the selection and characterization of the galaxy sample, and we will present the distribution of the different observables considered, their correlations, and the implications regarding the mechanisms regulating star formation. We will also discuss the theoretical interpretations of our results and derive our conclusions.

2.2 Observational data

2.2.1 Sample definition

In order to proceed with the analysis we require a large sample of galaxies (hereafter *main*) that will be used to define neighbours and environment, as well as to select the set of subsamples whose physical properties will be discussed throughout this chapter.

All data used in the present analysis are obtained from the SDSS Data Release 7 (Abazajian et al., 2009) database. Only objects within the completeness threshold of $m_r < 17.77$ and catalogued as galaxies by the spectroscopic pipeline (entries listed in table SpecObj[1]) were chosen to become part of the *main* sample. Line measurements are obtained from table SpecLine, and absolute magnitudes in the r band, M_r, have been computed from the

[1] http://cas.sdss.org/dr7/en/help/browser/browser.asp

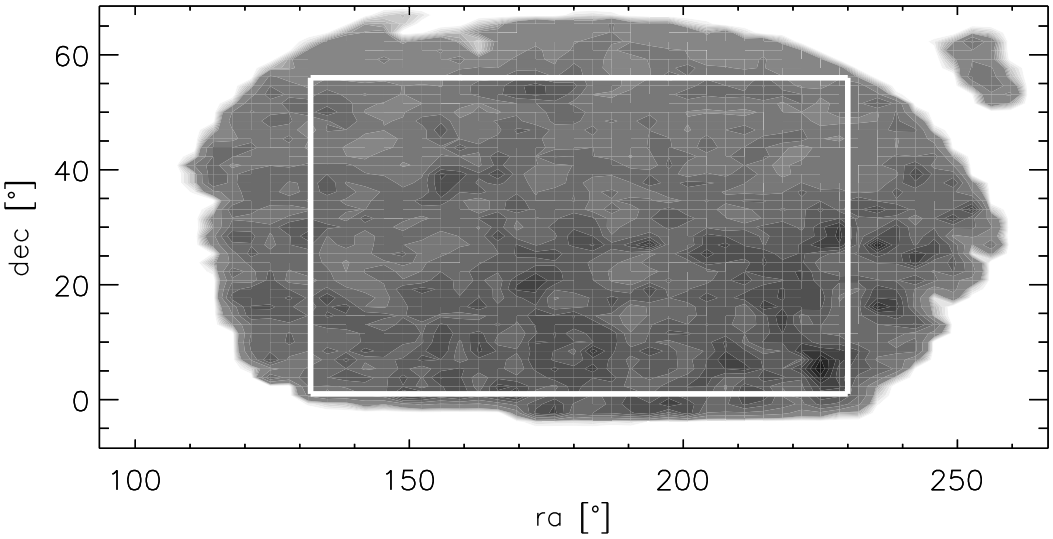

FIGURE 2.1: Spatial distribution of the *main* sample of galaxies, and region of the sky from which the *star-forming* subsample is selected.

apparent model magnitude[2] listed in the photometric catalogue (PhotoObjAll table) using the spectroscopic redshift distance.

In addition, we impose the following criteria to select our target galaxies from the *main* sample:

1. $132.0 < \mathrm{RA} < 230.0$ and $1.0 < \mathrm{DEC} < 56.0$
2. $m_\mathrm{r} < 17.5$
3. $0.02 < z < 0.07$

As can be readily seen in Figure 2.1, the region of the sky from which the *star-forming* subsample is selected (white square) leaves at least 2° (~ 3 and 10.5 Mpc for $z = 0.02$ and 0.07, respectively) with respect to the main sample footprint, in order to minimize boundary effects when studying interactions and environment. The restriction in apparent magnitude ($m_\mathrm{r} < 17.5$) ensures that every object with a similar-mass companion would be properly identified. The upper redshift considered roughly corresponds to an absolute magnitude $M_r < -20.0$, which is approximately the threshold below which most galaxies are actively forming stars, and the lower redshift cut prevents selection effects due to local structure.

We then classify our target galaxies into four different subsamples:

1. Galaxies with signal-to-noise ratio $S/N > 2$ in the Hα, Hβ, [OIII], and [NII] emission lines, classified as AGN according to the Kewley et al. (2006) criterion based on their position on the BPT diagnostic diagram (Baldwin, Phillips, and Terlevich, 1981, see Figure 2.2) are labelled as *agn* and will not be considered further.
2. Galaxies with $S/N > 2$ in all the above lines, classified as *star-forming* according to Kewley et al. (2006), will be referred as such hereafter. For these systems, the imposed S/N ensures that the quality of the spectra is sufficient to estimate the gas-phase metallicity from the O3N2 ratio.
3. Galaxies where Hα is observed in absorption with $S/N > 2$ will be referred to as *passive*.
4. All other objects are classified as *intermediate*.

[2] http://www.sdss.org/dr7/algorithms/photometry.html#mag_model

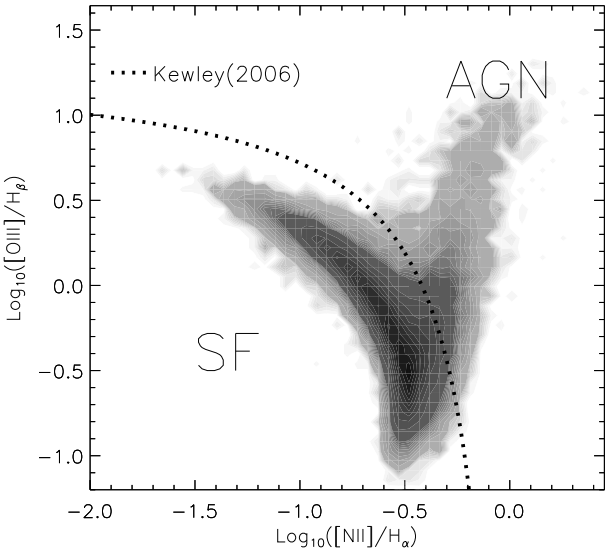

FIGURE 2.2: Distribution of galaxies with $S/N > 2$ measurements of the emission lines in the BPT diagram. A dotted line shows the Kewley et al. (2006) criterion used to separate star-forming galaxies from AGN.

2.2.2 Physical characterization

In order to characterize our galaxy samples in a model-independent fashion we will use direct observables as proxies for their physical properties.

First and foremost, we will use two different indicators of the SSFR, which is the main focus of the present study. On the one hand, we will consider the equivalent width of the Hα emission line, EW(Hα), where the line intensity traces the presence of young stars while the underlying continuum is set by the whole star formation history of the galaxy (see e.g. Terlevich et al., 2004). On the other hand, we will also use the $(u-r)$ colour obtained from the *model* magnitudes, sensitive to the presence of massive, short-lived stars that dominate the bluer spectral bands. The main differences between both observables are that EW(Hα) is subject to aperture effects (see below) and that it traces a younger stellar population than $(u-r)$. Therefore, these two indicators probe the SSFR on different spatial and temporal scales.

In order to describe the intrinsic properties (i.e. 'nature') of our objects, throughout the present work we will use the absolute magnitude in the r band, M_r, as a proxy for stellar mass, and we will use both terms interchangeably. To account for their evolutionary state, from the point of view of chemical enrichment, we will use the observational indicator

$$\mathrm{O3N2} = \log \frac{[\mathrm{OIII}]}{\mathrm{H}\beta} - \log \frac{[\mathrm{NII}]}{\mathrm{H}\alpha} \tag{2.2}$$

that is well known to decrease monotonically with the gas-phase metallicity (Alloin et al., 1979) and thus with stellar-to-gas fraction (Searle and Sargent, 1972; Edmunds, 1990; Ascasibar et al., 2015).

Concerning the effects of 'nurture' on the SSFR, we will quantify the environment in terms of the local galaxy overdensity, estimated from the projected distance to the fifth nearest neighbour in the *main* sample. We propose the relative distance between the first and second neighbours as a simple indicator for the presence of close companions, and we will interpret galaxy morphology as a possible tracer of galaxy-galaxy interactions.

The definition of distance is a key aspect in the characterization of close interactions and environment. Spectroscopic redshifts are available for every object in our sample which

permits distance calculations in 3D space. However, redshift measurements are strongly affected by the peculiar velocities of galaxies (especially important in denser environments such as galaxy clusters). As our galaxy sample covers all kind of environments, this effect will act irregularly and introduce a bias. In order to avoid such problems, we base our clustering calculations on projected distance measurements, as it is widely done in the literature (see e.g. Kaiser, 1987; Cooper et al., 2005; Muldrew et al., 2012, and references therein).

For every target galaxy with redshift $z_{\rm gal}$, we select potential neighbours from the *main* sample within a range $z_{\rm gal} \pm 0.005$ (which corresponds to ~ 15 Mpc or ~ 1500 km/s velocity difference). Then, the distance to each object in this redshift shell is calculated as the great-circle distance, i.e. projected onto the surface of a sphere with radius $d_A(z)$, where

$$d_A(z) = \frac{d_L(z)}{(1+z)^2} \tag{2.3}$$

is the angular diameter distance, and $d_L(z)$ corresponds to the luminosity distance at redshift z.

Since our *main* sample is magnitude-limited, the number density of galaxies decreases with redshift as the faintest objects drop out from the sample. Hence, the average distances to the neighbours increase with z. We circumvent this problem by normalizing such distances to a characteristic radius

$$\overline{r}(z) = \frac{d_A(z)}{\sqrt{N_{\rm gal}(z \pm 0.005)}} \tag{2.4}$$

that is proportional to the average distance between galaxies, assuming they were uniformly distributed over the solid angle $\Delta\Omega$ within the redshift shell $z \pm 0.005$ (i.e. $\pi\,\overline{r}^2 \propto \Delta\Omega\, d_A^2/N_{\rm gal}$). $N_{\rm gal}$ refers to the number of galaxies within the redshift shell under consideration. Then, we will use the normalized distance to the fifth neighbour, $R_5/\overline{r}$, as a redshift-independent estimator of the local galaxy density (i.e. an indicator of the environment where the galaxy lives in). Galaxies in voids display values of the order of a few, whereas cluster galaxies feature values well below unity.

In order to test for the presence of close companions, we chose to use the ratio between the squared projected distances to the first and second neighbours. For a uniform random distribution in two dimensions, R_1^2/R_2^2 should be uniformly distributed between 0 and 1, irrespective of the local galaxy density. A low value of R_1 is not in itself indicative of interactions, and it is trivially obtained e.g. for all cluster galaxies. In contrast, very low values of R_1^2/R_2^2 may mean (in a probabilistic sense) that the first neighbour is much closer than expected for a purely random distribution, and thus they trace the fraction of close galaxy pairs in a statistical sample.

Finally, the morphology of a galaxy is also a powerful indicator of its dynamical and merger history. Thanks to the Galaxy Zoo 1 citizen science project (Lintott et al., 2008), almost every galaxy in the SDSS spectroscopic catalogue has a visual morphology classification. From the votes of the 'citizen scientists', debiased from redshift-dependent resolution effects that may blur galactic features (such as spiral arms) in SDSS images, galaxies are classified as *ellipticals* or *spirals* (clockwise, anti-clockwise and edge on) if either category receives at least 80% of the votes. Objects that do not reach the 80% threshold are designed as *uncertain*, including a fraction of merging systems. According to Darg et al. (2010), a visual merger identification can be considered reliable when it receives more than 40% of the votes. Based on these criteria, we label every object in our sample as *early-type*, *late-type*, *uncertain* (excluding mergers) or *merger*.

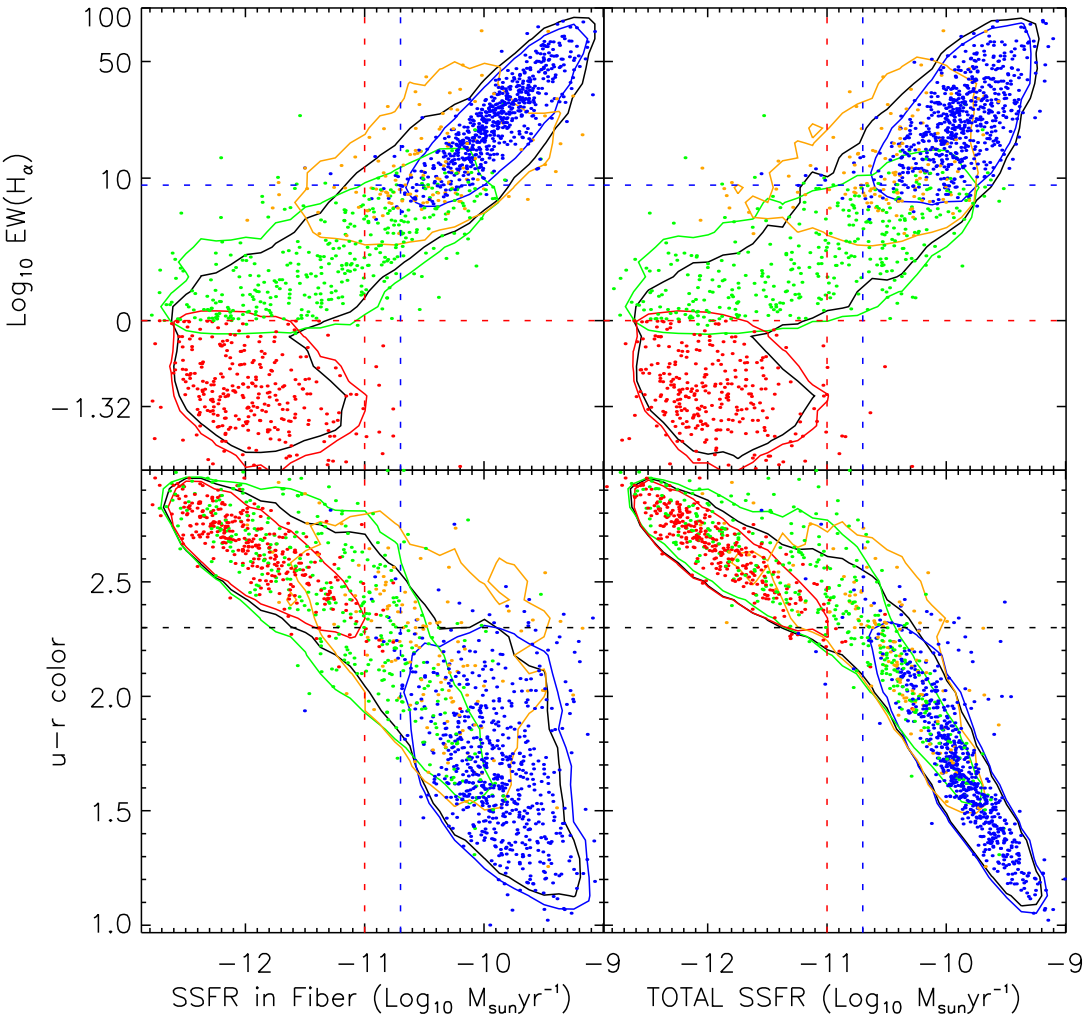

FIGURE 2.3: Comparison between model SSFR (Brinchmann et al., 2004) and our observational proxies. Left panels correspond to the SSFR within the fibre, and right panels show the total SSFR. Top and bottom panels show Hα equivalent width and $(u-r)$ colour, respectively. Contours in blue, red, green, and orange correspond to the area that encloses 90% of the *star-forming*, *passive*, *intermediate*, and *agn* subsamples. Points correspond to a random selection of 1500 target galaxies, and they are similarly coloured according to the subsample they belong to.

2.2.3 Observational biases

Although our physical characterization is intended to be as objective as possible, it is not completely free from observational biases, some of them inherent to the selection function of the spectroscopic SDSS.

For instance, the minimum fibre separation in the detector implies that galaxies in the spectroscopic catalogue can only be as close ~ 55 arcsec in the sky (physical distances of ~ 22.5 and ~ 74 kpc at our redshift limits of $z = 0.02$ and 0.07, respectively). This might introduce some bias in the distance to the fifth neighbour, and it poses a serious problem for the identification of close pairs (see e.g. Behroozi et al., 2015, and references therein).

In addition, most of the quantities we consider are based on astrometric and/or photometric measurements, but aperture effects may be an issue for spectroscopic observables such as the equivalent width of the Hα line or the O3N2 ratio. The aperture of the SDSS fibre (3 arcsec in diameter) corresponds to $\sim 1-4$ kpc at $z = 0.02-0.07$, and therefore these measurements may not always be representative of the whole galaxy.

Aperture bias has been thoroughly discussed in the literature (e.g. Brinchmann et al., 2004; Iglesias-Páramo, Vílchez, and Galbany, 2013), and models that take into account the photometry outside the fibre have been proposed in order to correct the spectroscopic SSFR from aperture effects. In Figure 2.3 we compare the direct measurements of EW(Hα) and $(u-r)$ with the aperture-corrected SSFR inferred from the Brinchmann et al. (2004) prescription, as implemented in the MPA-JHU pipeline[3].

Equivalent width is tightly correlated with the model SSFR in the area covered by the fibre (top left panel), at least as far as *star-forming* and *intermediate* galaxies are concerned. For *passive* galaxies, the Hα absorption line is actually more prominent in systems with higher SSFR due to a larger contribution of A stars to their optical spectrum. The aperture correction proposed by Brinchmann et al. (2004) does not change these general trends, but it broadens the correlation with the extrapolated SSFR, as shown on the top right panel. $(u-r)$ colour, on the other hand, is an excellent proxy for the model SSFR over the whole galaxy (bottom right panel), and it is well correlated with the theoretical estimate inside the fibre, even for *passive* galaxies (bottom left panel).

The distribution of *star-forming*, *intermediate*, and *passive* galaxies in Figure 2.3 clearly shows that our sample selection criteria are roughly equivalent to fixed thresholds in SSFR, colour, or equivalent width. The latter arises from the minimum signal-to-noise imposed, which is dominated by the contrast (i.e. the equivalent width rather than the absolute luminosity) of the Hβ line with respect to the underlying continuum. Our $S/N > 2$ criterion, and thus our definition of the *star-forming* subsample, is in practical terms very similar to EW(Hα)>10 Å, $(u-r) < 2.3$, or SSFR$> 3 \times 10^{-11}$ yr^{-1}, which may not be statistically representative of the overall galaxy population and introduce a significant source of bias.

Passive galaxies typically populate the range $(u-r) > 2.3$ and SSFR $< 10^{-11}$ yr^{-1}. The *intermediate* subsample is presumably dominated by emission-line objects with EW(Hα) $<$ 10 Å, most likely weakly star forming galaxies, but, given the low signal-to-noise ratio, it also includes an uncertain fraction of absorption-line systems and AGN. We have made no attempt to correct for such effects.

Finally, we have also assumed that the value of O3N2 within the spectroscopic fibre is representative of the whole galaxy. This measurement does not account for radial abundance gradients, and (assuming the fibre is placed at the centre of the galaxy) it would be biased high for large spirals. The precise impact of aperture bias on our results concerning gas-phase metallicity is hard to predict, but the observed values of the radial abundance gradients in CALIFA disk galaxies suggest a variation of the order of ~ -0.2 dex between 0.3 and 2 effective radii (Sánchez et al., 2014).

[3] http://www.mpa-garching.mpg.de/SDSS/DR7/

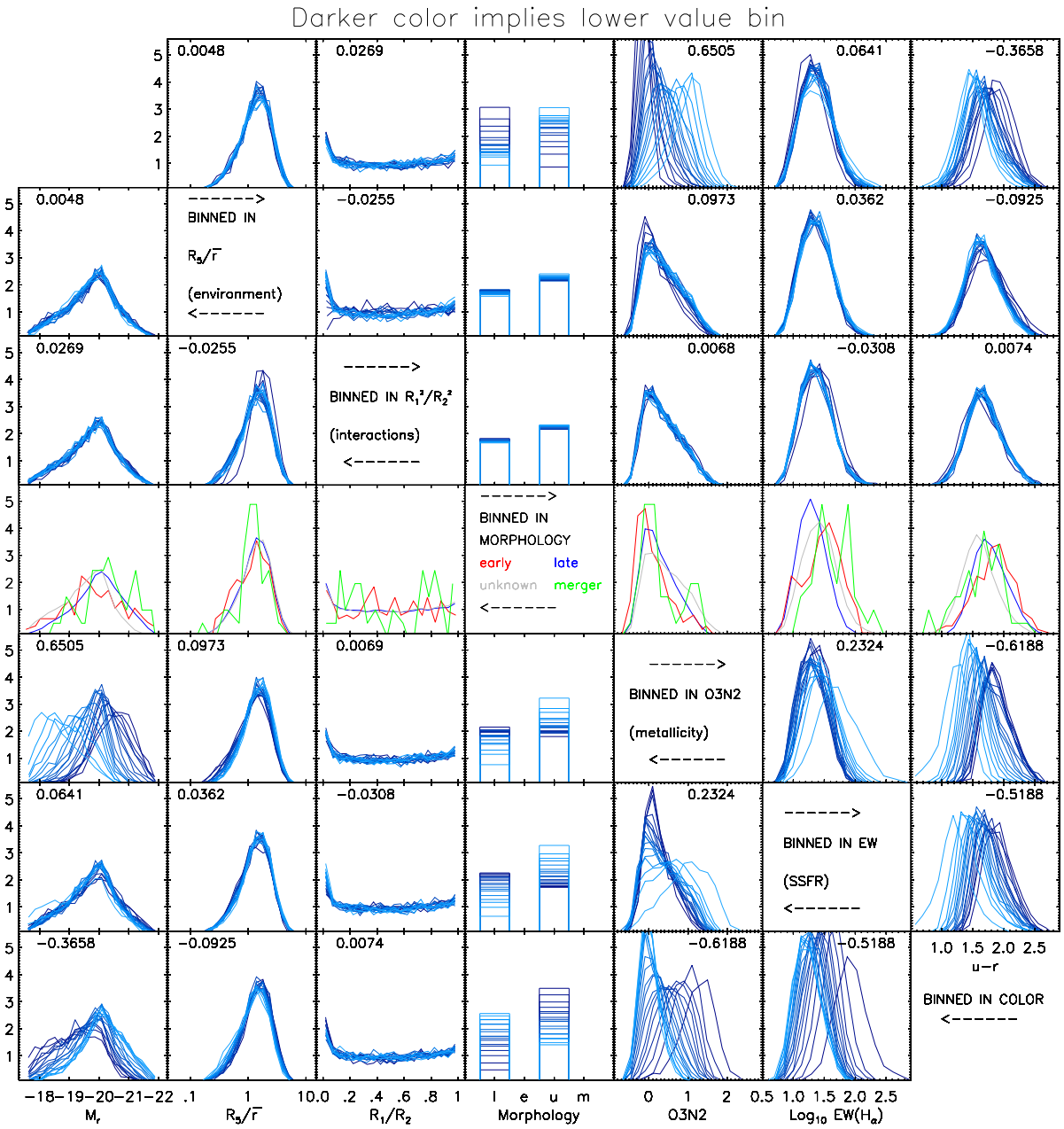

FIGURE 2.4: From left to right, different columns show the distribution of mass (M_r), environment ($R_5/\bar{r}$), interactions (R_1^2/R_2^2), morphology (based on the Galaxy Zoo visual classification), metallicity (O3N2), and specific star formation rate, traced by EW(Hα) and $(u-r)$ colour, for our subsample of *star-forming* galaxies. Different lines correspond to adaptive bins in another of these properties (one per row) containing 2000 galaxies each. Darker colours correspond to lower value bins, i.e. imply higher mass, denser environments, low values of R_1^2/R_2^2, higher metallicity, lower EW, and bluer colour, respectively.

2.3 Results

In order to study the physical mechanisms that regulate star formation, discriminating between 'nature' and 'nurture' processes, we present in this section a thorough characterization of the distribution and cross-correlations between stellar mass, environment, close companions, morphology, gas-phase metallicity, and specific star formation rate, using the observational proxies discussed in Section 2.2.2.

2.3.1 Star-forming galaxies

Our main results for the subsample of *star-forming* galaxies are summarized in Figure 2.4, where each column shows histograms of M_r, $R_5/\bar{r}$, R_1^2/R_2^2, galaxy Zoo morphological classification, O3N2, equivalent width of the Hα line, and $(u-r)$ colour. In each row, different lines represent adaptive bins in the corresponding physical property, containing 2000 galaxies each. Numbers within each panel indicate the Spearman's rank correlation coefficient between both variables.

When galaxies are binned by mass (top row), there are no apparent trends in the distributions of $R_5/\bar{r}$ and R_1^2/R_2^2. We find (as others before, e.g. Gómez et al., 2003) that *star-forming* galaxies tend to live in the field, and very few such objects are found in the densest environments. Furthermore, we show here that this statement is not only valid in a qualitative sense; the distribution of $R_5/\bar{r}$ is independent on galaxy mass as long as the galaxy is classified as star-forming according to our criteria (see figure 2.5 for a comparison to the *intermediate* and *passive* populations).

In contrast, the well-known relation between metallicity and luminosity (Lequeux et al., 1979) is clearly visible in the distribution of O3N2, with more luminous galaxies (darkest lines) displaying systematically lower values of O3N2 (higher metallicities). There is a very weak trend in the distribution of equivalent widths (top row, sixth panel), in the sense of a more extended tail (i.e. a larger fraction of galaxies with higher SSFR, such as blue compact dwarfs and HII galaxies) in low-mass systems. The trend is clearer when considering $(u-r)$ colour (rightmost panel), although the values of the rank correlation coefficients indicate that there is a weaker correlation between luminosity and colour or equivalent width than between luminosity and metallicity.

When galaxies are classified in terms of the environmental density (second row), we do not find any difference in the luminosity function of *star-forming* galaxies nor the distribution of their Hα equivalent widths. Nevertheless, we can observe that galaxies in the densest environments tend to be slightly more metal-rich (darkest lines in the second row, fifth column), in agreement with recent results (e.g. Hughes et al., 2013), and display marginally redder colours.

Concerning the role of close companions, the distribution of R_1^2/R_2^2 (plotted on the panels in the third column) is roughly uniform, as expected for a random Poisson distribution in two dimensions. However, there is a clear excess at $R_1^2/R_2^2 < 0.1$ that we interpret as an indicator of interactions with the nearest neighbour. The only difference between these galaxies (represented by the darkest lines in the third row) and the rest of the star-forming population is the lack of such close pairs in dense environments. Since galaxies move at larger relative speeds in clusters than in the field, the typical type of two-body interaction is an impulsive encounter ('harassment') rather than the formation of a close pair and subsequent merger (see e.g. Boselli and Gavazzi, 2006). There seems to be a very mild enhancement of the SSFR for the darkest bin ($R_1^2/R_2^2 < 0.077$), observed in both Hα and $(u-r)$ colour, but its statistical significance is rather weak.

The fifth row is binned in gas-phase metallicity, traced by the O3N2 line ratio. One can see, as in the reciprocal panels in first and second rows, both the luminosity-metallicity

relation and (to a much lesser extent) the slight deviation of the most metallic systems towards denser environments. A clear correlation exists between O3N2 and SSFR, with lower-metallicity objects showing bluer $(u-r)$ colour and higher EW(Hα). In particular, about fifty per cent of the objects in the lowest metallicity bin (with O3N2 > 1.25, i.e. less than half solar according to Pérez-Montero and Contini, 2009) feature values of the equivalent width higher than 50 Å.

In the sixth row, where galaxies are binned according to their equivalent width, no evident correlation is found with galaxy density or the presence of close companions. There is a marginal trend with luminosity, with the highest equivalent widths (larger than 65 Å) appearing in systematically low-mass systems, as well as a significant correlation with O3N2 (albeit with a smaller correlation coefficient than the luminosity-metallicity relation). Similar results are obtained using $(u-r)$ colour (seventh row) as an alternative proxy for the SSFR. No correlation is found with our nurture indicators ($R_5/\bar{r}$, R_1^2/R_2^2), but there is a clear trend with galaxy luminosity. The correlation with metallicity is even stronger than that observed for EW(Hα).

Concerning morphological types, the fourth column of Figure 2.4 presents the fraction of galaxies classified as *late-type*, *early-type*, *uncertain* (excluding mergers) or *mergers*, binned in terms of each of the other proxies. Conversely, the fourth row shows the distribution of each galactic property, segregated by our four morphological types (one can no longer build adaptive bins of 2000 galaxies).

Our *star-forming* subsample consists mainly on objects with late (43.15%) and uncertain (56.28%) morphologies, while early-type (0.45%) and mergers (0.12%) are barely present. None of our 'nurture' proxies ($R_5/\bar{r}$ and R_1^2/R_2^2) seems to correlate with morphology, but we must recall that this refers to the *star-forming* subsample only. The trends observed for the late-type and uncertain objects show that the former are, on average, more massive, more metallic, redder, and display lower values of EW(Hα). Early-type *star-forming* galaxies (160 objects) tend to display slightly higher metallicities, redder colours, and higher equivalent widths. There are only 43 merging systems in the *star-forming* subsample, and therefore it is difficult to conclude whether there is a statistically significant increase in their average equivalent width.

2.3.2 Separating 'ageing' and 'quenching'

As shown in Section 2.2.3, the signal-to-noise threshold imposed for our *star-forming* subsample is roughly equivalent to a selection criterion EW(Hα)> 9 Å. From Figure 2.4, we have just concluded that there is only a slight dependence of the SSFR on galaxy luminosity, and almost no dependence on environmental density, when such a threshold is imposed.

We will now address the relation between galaxy mass, environment, and star formation, including also the *intermediate* and *passive* subsamples, thus covering all possible values of the Hα equivalent width (with our adopted sign convention, negative values indicate a stellar absorption feature). Once again, we first arrange all galaxies in bins (either in M_r or $R_5/\bar{r}$) containing 10000 objects. Galaxies within each bin are then classified as *star-forming*, *intermediate*, or *passive*, as described in Section 2.2.2, and the respective fractions, as well as the conditional probability distribution of the physical property not used for the binning ($R_5/\bar{r}$ or M_r), are plotted in Figure 2.5. *Star-forming* galaxies are shown on the top panels, whereas the central and bottom panels display *intermediate* and *passive* systems, respectively.

Let us start by focusing on the distribution of $R_5/\bar{r}$, plotted on the leftmost column of the figure. While *star-forming* and *intermediate* galaxies tend to live in the field, *passive* galaxies can be found in all kinds of environments. In contrast with the other two populations, they also display a remarkably different behaviour at high and low luminosities. At

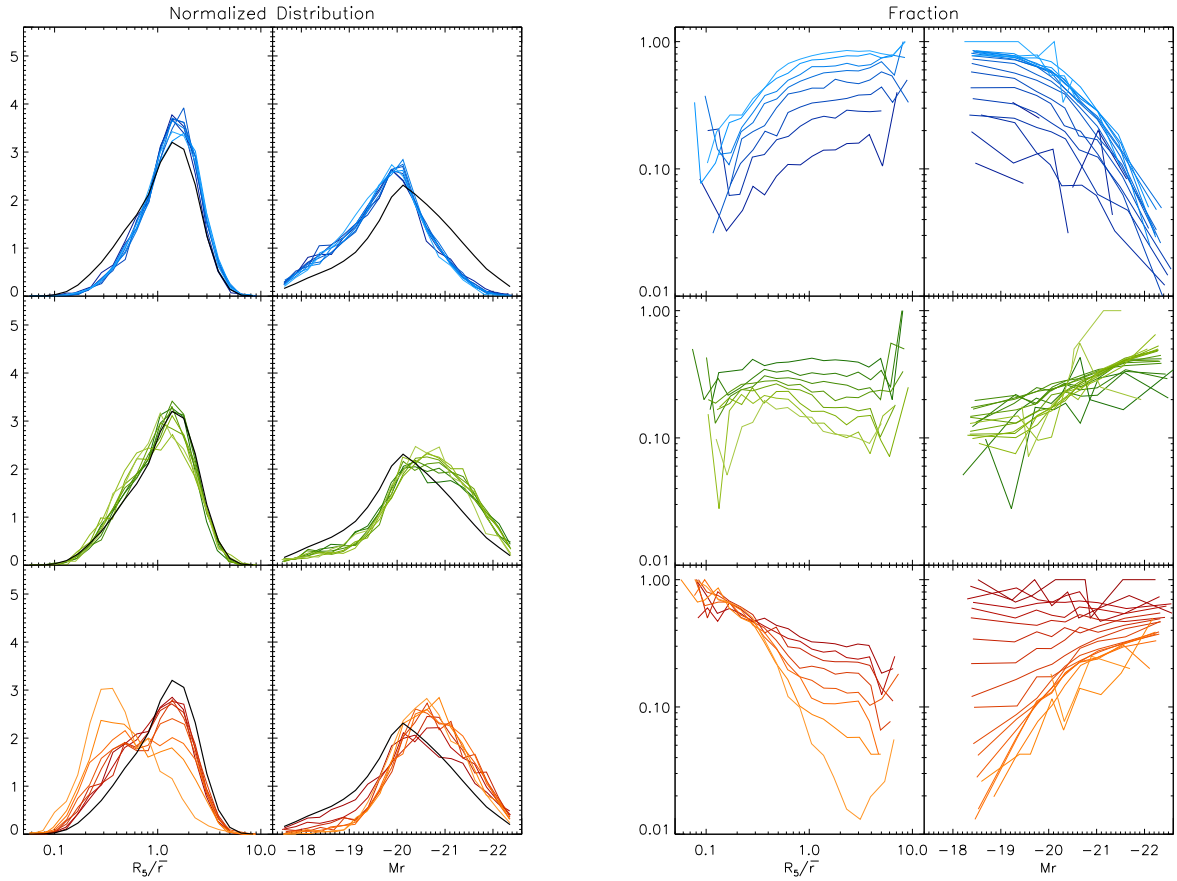

FIGURE 2.5: Distribution (left panels) of $R_5/\bar{r}$ (environment, left) and M_r (mass, right) for the *star-forming* (blue), the *intermediate*(green) and the *passive*(red) subsamples. The fraction of the three subsamples (right panels) is also represented against $R_5/\bar{r}$ and M_r. Line shading correspond to bins in the other variable and are fixed to contain 10000 galaxies. Darker colours correspond to lower value bins, i.e., more massive objects and denser environments. Black solid line in left panels correspond to the distribution of the whole sample.

the low-mass end (light-shaded lines) they are mostly located in dense environments, but the distribution of $R_5/\bar{r}$ quickly becomes bimodal as we consider higher luminosity bins. High-mass *passive* galaxies (showing Hα in absorption with $S/N > 2$) can be found both in clusters and in the field, confirming the idea that there are indeed two mechanisms that may reduce (not necessarily 'quench' on a short time scale) the star formation activity of a given galaxy to a negligible level. One of these mechanisms would be related to galaxy mass (and, most probably, its 'nature'), whereas the other, clearly related to the environmental density (i.e. 'nurture'), would act upon galaxies of all masses (see e.g. Peng et al., 2010).

As it has been previously reported in the literature, the fraction of star-forming galaxies (selected by either colour or Hα) at fixed stellar mass is a strong function of local density, and there is also a clear dependence on galaxy luminosity at fixed $R_5/\bar{r}$. The fraction of galaxies classified as *star-forming* according to our criteria (top panels on the right column of Figure 2.5) is indeed a monotonically decreasing function of both luminosity and galactic overdensity, although, contrary to some previous studies (cf. Tanaka et al., 2004), we do not find evidence for a sharp transition at any particular value of either quantity.

Moreover, we would like to argue that the distinction between *passive* and *intermediate* galaxies is also a critical factor in order to discriminate between 'ageing' and 'quenching' mechanisms. In low-density environments, most of the galaxies that are not *star-forming* fall in the *intermediate* category, i.e. the fraction of truly *passive* systems (Hα unambiguously detected in absorption) is systematically lower than that of *intermediate* objects for all luminosities. As we will discuss later in more detail, the average SSFR of the field population is a decreasing function of stellar mass, but it seldom becomes negligible, especially for late-type galaxies; it merely tends to drop more and more often below the selection threshold defining the *star-forming* class.

As noticed by several authors (e.g. Baldry et al., 2006; Peng et al., 2010), the effects of mass and environment on the fraction of *star-forming* galaxies are fully separable, and the curves with different shading on both of the top panels of the right column are parallel to each other. However, these objects may gradually move towards the *intermediate* population due to 'ageing', staying there for a long time, or quickly migrate through the *intermediate* class towards the *passive* group due to a sharp quenching of their star formation activity.

If only a mass-independent quenching mechanism were at work, the fraction of *passive* galaxies would increase at the expense of both *star-forming* and *intermediate* objects in equal proportion, and therefore the ratio between their fractions would stay constant. In contrast, one can readily observe that the effect of the environment on the fraction of *intermediate* galaxies is not independent on mass. The curves on the middle panels of the right column in Figure 2.5 are not parallel to each other, and they bear relatively little relation to the fraction of *star-forming* galaxies on the top panels.

Our results show that, as the local density increases, a certain fraction of the *star-forming* population becomes *intermediate* and another undetermined fraction becomes *passive*. At the same time, a fraction of the *intermediate* galaxies turns *passive*, but they are approximately balanced by a similar number of *star-forming* galaxies moving into the *intermediate* realm. Incidentally, the final fraction of *intermediate* galaxies turns out to be rather insensitive to the environmental density (middle right panel).

This process is further examined in Figure 2.6, where we show the distribution of SSFR, traced by both colour and equivalent width, in different bins of mass *and* environment. We confirm the finding of Balogh et al. (2004b) that the mean $(u - r)$ colour of the 'blue' population (a mixture of *intermediate* and *star-forming* galaxies) becomes progressively redder with increasing galactic overdensity. A similar trend can be seen in EW(Hα), whose distribution is plotted on the left panels. As the density increases, the distribution becomes more asymmetric, with a tail extending into the *intermediate* region, and its peak moves slightly

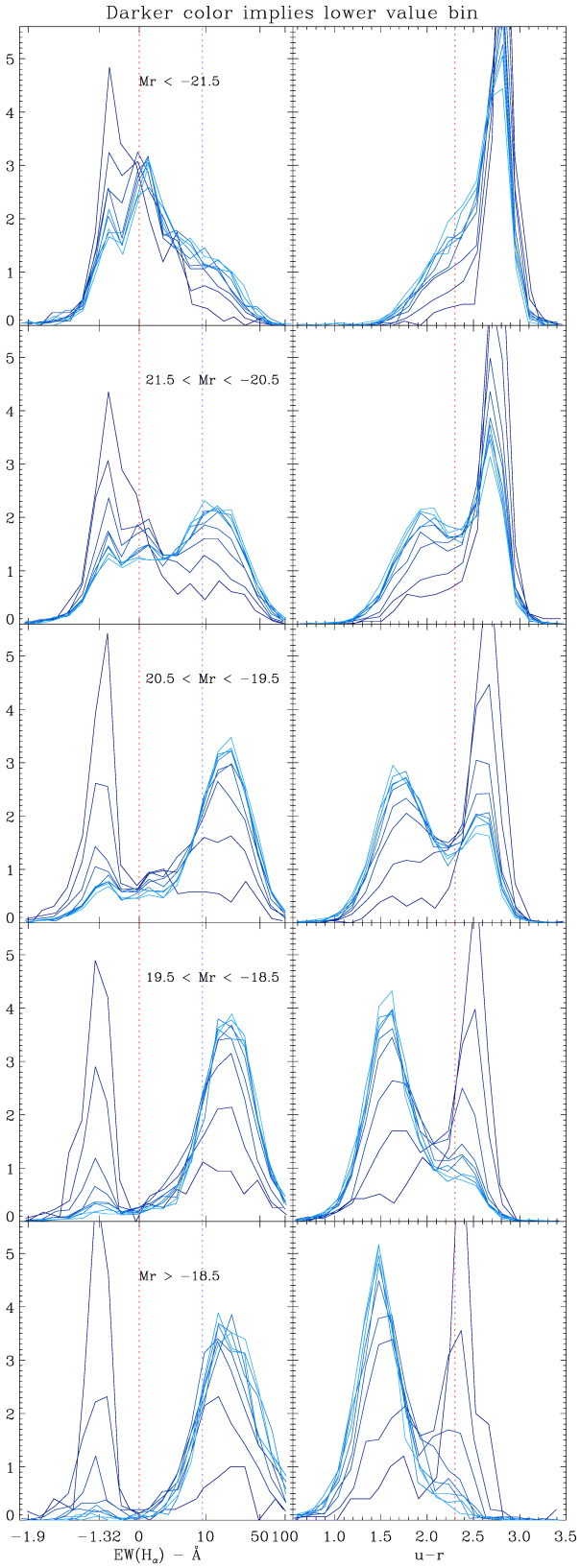

FIGURE 2.6: Normalized distributions of EW(Hα) (left) and $(u - r)$ (right) for different luminosity bins (brightest galaxies are plotted on the top panels). Line shading indicates environmental density, with darker colours corresponding to the lowest values of $R_5/\bar{r}$ (densest environments). The binning in $R_5/\bar{r}$ has been computed from the whole target sample (10000 galaxies per bin), and it is the same in all panels.

towards lower values of the equivalent width. While these effects are consistent with a mild 'ageing' associated to denser environments, the dominant mechanism at play is a fast quenching of the star formation rate, responsible for quickly driving the objects towards the peak associated to the *passive* population.

However, the role of *intermediate* galaxies is not entirely clear in this context. Are they transition objects, caught during the short interval of the transformation from *star-forming* into *passive* after their SFR has suddenly dropped to zero, or will they live there for a long time, because their SFR has just decreased slightly (e.g. due to a shortage of external gas supply)?

In order to discern 'ageing' from 'quenching' (i.e. the time derivative of the star formation rate), it is interesting to compare two tracers of the SSFR that are sensitive to different time scales. As recently shown by Schawinski et al. (2014), early- and late-type galaxies occupy very different regions of the NUV$-u$ $-$ r colour-colour diagram, with the former displaying systematically redder (NUV$-u$) colours, even for similar values of $(u-r)$. Since UV emission probes star formation on shorter time scales (of the order of $10^7 - 10^8$ yr) than optical colours ($10^8 - 10^9$ yr), they concluded that early-type galaxies in the 'green valley' have undergone a rapid end to star formation, whereas late-type galaxies with similar $(u-r)$ colours have experienced at most a slow decline in their star formation activity.

Rather than UV colours, we will use here the equivalent width of the Hα line to probe the SSFR on scales of the order of $\sim 10^7$ yr. Roughly speaking, the intensity of the Hα line is proportional to the mass of O and B stars, whereas the continuum traces the total stellar mass. Thus, EW(Hα)$\sim M_7/M$, where M_7 denotes the stellar mass created during the last 10 Myr. On the other hand, $(u-r)$ is sensitive to the presence of A stars, and it varies on scales of the order of 300 Myr. To first order, one may consider that $(u-r) \sim M_{8.5}/M$, although this is only a coarse approximation (e.g. in the absence of dust extinction, no galaxy can be redder than a single stellar population with the current age of the universe).

If the star formation rate of a given galaxy evolved slowly ($\psi/\dot{\psi} > 300$ Myr), there should be a one-to-one relation between its Hα equivalent width and its $(u-r)$ colour, since both would be tracing exactly the same quantity; SSFR$= \psi/M$. We will refer to this relation (the location of all galaxies with smooth star formation histories on the EW-colour diagram) as the 'ageing' sequence.

If star formation were suddenly shut off, nebular Hα emission would drop to negligible values on $\sim$ 10-Myr scales, but the galaxy would still retain some memory of its original blue colour. In fact, there would be a large amount of A stars and, therefore, recently quenched galaxies are expected to feature *stronger* absorption lines (and bluer colours) than a genuinely old stellar population (Dressler and Gunn, 1983). The higher the SSFR before the quenching event, the stronger the Hα absorption and the bluer $(u-r)$ after 10 Myr. During the subsequent Gyr, A stars would gradually die; Hα absorption will become weaker, and colours will become redder, until the galaxy eventually joins the red extreme of the 'ageing' sequence. Galaxies in this phase would occupy a completely different region of the EW-colour diagram, forming a well-defined line where EW(Hα) is a monotonically *increasing* function of $(u-r)$ that we will term the 'quenched' sequence.

The $(u-r)$ colour – EW(Hα) diagram of our sample of SDSS galaxies is plotted in Figure 2.7, segregated by morphological type and environment, and coloured according to the object luminosity. Although the ticks and labels in the y-axis indicate the actual value of EW(Hα), the plotted quantity is in fact log(EW/Å+2) in order to show both emission and absorption lines on a common logarithmic scale.

At the lowest overdensities, late-type galaxies seem to be well described by a single 'ageing' sequence (i.e. $\psi/\dot{\psi} > 300$ Myr). The vast majority of them are forming stars at *some* level, but they span a broad range of SSFRs, going from very active to very quiescent

main_sequence_EW_u_r_MERGERS_final.jpg

systems, and we do not detect any sharp transition whatsoever between the *star-forming*, *intermediate*, and *passive* populations.

Field early-type galaxies appear at the end of this sequence. Some of them display weak Hα emission, but almost none of them shows clear signatures (blue colours and strong Hα absorption) of a recent quenching event. Most of these systems are consistent with very low values of the SSFR (not necessarily of the instantaneous SFR) and a very old stellar population, in the sense of the mass-weighted average defined in equation (2.1).

Galaxies with uncertain morphology are distributed along the whole sequence, but it is interesting to note that they reach the most extreme values at both ends (in fact, this category accounts for more than 80% of the galaxies with EW(Hα) > 65 Å). From Figure 2.7, it becomes evident that galaxies showing the strongest quenching signatures also tend to display a disturbed appearance. Interestingly, field galaxies unambiguously classified as ongoing mergers can only be found at the blue extreme.

In the densest environments, the 'ageing' sequence defined by late-type galaxies moves toward redder colours and lower equivalent widths. There is a general displacement of the sequence, consistent with the results plotted in Figure 2.6, in the sense that galaxies of a given luminosity tend to be slightly older in dense environments. However, the overall sequence stays roughly invariant (if anything, perhaps even narrower than in the field), with very few objects showing obvious post-quenching signatures. Therefore, we conclude that late-type galaxies in dense environments have systematically lower SSFR and older stellar populations given their mass, but their star formation rate has not undergone any sudden change.

In contrast, many early-type galaxies in dense environments are arranged in a tight disposition with stronger Hα absorption in bluer systems, consistent with the quenching scenario. Furthermore, if we focus on galaxies in different luminosity bins, one can see them all over the 'quenched' sequence, tracing the time elapsed since star formation stopped, but fainter objects, which typically started with higher SSFR, reach bluer colours and deeper absorption features than more massive systems.

The 'ageing' and 'quenched' sequences are also evident in galaxies with uncertain morphology, which constitute (as in the field) more than fifty per cent of the population. They seem to reach bluer colours in the quenched sequence, but they do not particularly stand out among the ageing population. A small number of mergers seem to be associated to objects with enhanced star formation, but most of them are located at the red extreme of the quenching sequence.

2.3.3 The SSFR-luminosity relation

There is ample observational evidence that there exits a tight relation between the stellar mass and instantaneous/specific SFR of star-forming galaxies, often referred to as the 'galactic main sequence' (see e.g. Noeske et al., 2007; Speagle et al., 2014, and references therein). At low masses, the star formation rate is roughly proportional to the stellar mass, and therefore all star-forming galaxies display similar SSFRs, almost independent on luminosity. The situation at high masses is still debated, but there is growing consensus that massive star-forming galaxies have consistently lower SSFR (albeit similar or higher SFR) than their smaller counterparts, especially in the local universe (e.g. Whitaker et al., 2014; Ilbert et al., 2014; Tasca et al., 2014).

The SSFR of our galaxy sample, traced by either $(u-r)$ colour or EW(Hα), is plotted in Figure 2.8 as a function of galactic luminosity M_r, segregated by morphology and environment as in Figure 2.7. In the EW(Hα)$-M_r$ plane (top panels), galaxies are colour-coded by $(u-r)$, whereas in the colour-magnitude diagram (bottom panels), red, green, and blue correspond to different bins in equivalent width.

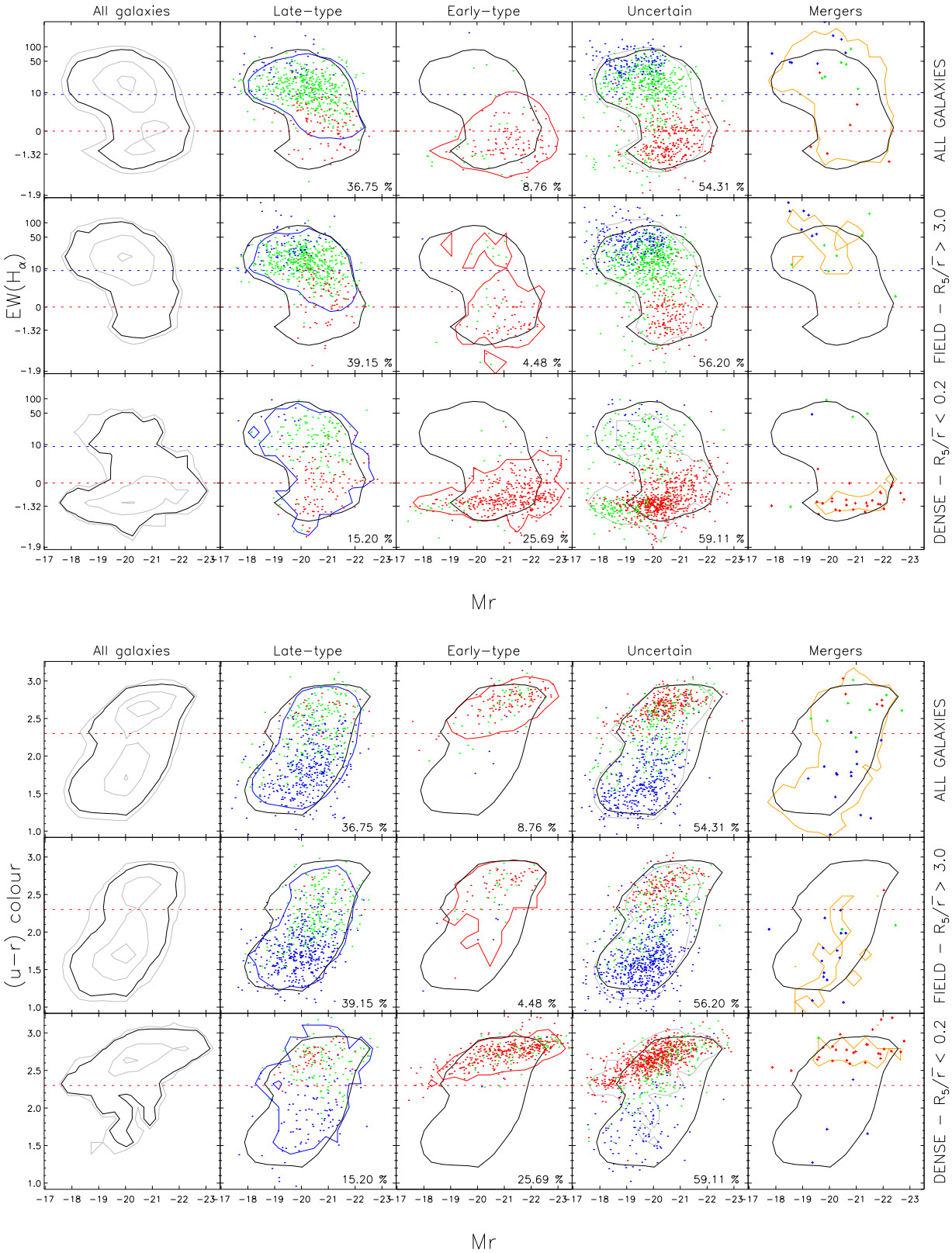

FIGURE 2.8: Galactic SSFR-luminosity relation, using Hα equivalent width (top) and $(u-r)$ colour (bottom) as proxies for the SSFR. Figure schema is the same as in Figure 2.7. The colours of the points correspond to: Top – three different bins in $(u-r)$ colour: red, objects with $(u-r) > 2.5$; green objects with $1.5 < (u-r) < -2.5$; and blue, objects with $(u-r) < 1.5$. Bottom – three different bins in EW(Hα): red, objects with EW(Hα)< 0.0; green objects with $0.0 <$EW(Hα)< 10.0 ; and blue, objects with EW(Hα)> 10.0.

Since galaxies of early-type morphologies are known to display consistently redder colours than late-type spirals (see the colour-magnitude diagrams on the bottom panels; cf. Schawinski et al., 2014), it is not surprising that they also feature lower equivalent widths, often (yet not always) showing the Hα line in absorption (top panel). Nevertheless, some early-type galaxies, especially in the field, display obvious signs of star formation, both in EW(Hα) and in $(u-r)$. As noted above, they seem to represent the low-SSFR end of the 'ageing sequence' in Figure 2.7. Figure 2.8 suggests that, in the absence of environmental effects (i.e. in the filed) there is a single relation between SSFR and M_r.

We would strongly advocate for including *intermediate* and *passive* galaxies, of any morphological type, in the 'galactic main sequence'. As noted by Whitaker et al. (2014), the shape of the sequence does not change by more than 0.1 dex when the whole galaxy population is considered. Combining our Figures 2.7 and 2.8, we do not find observational support for any quenching mechanism acting on field galaxies. The most massive systems tend to have formed most of their stars a long time ago and have arranged them into an early morphological type, but there seems to be a continuous variation over the full range of SSFR.

In particular, our results strongly disagree with the two-population scenario, where some galaxies form stars with a given, mass-independent SSFR, until they are suddenly quenched (e.g. Peng et al., 2010). The apparent trend of a constant SSFR (as in e.g. Figure 2.4) is entirely due to the selection of *star-forming* systems. As shown in Figure 2.3, our subsamples of *star-forming*, *intermediate*, and *passive* galaxies roughly correspond to fairly well defined cuts in colour or equivalent width. In fact, they are statistically representative of the traditional 'blue cloud', 'green valley', and 'red sequence' regions selected from the colour-magnitude diagram. We argue that any such classification of the galaxy population introduces a serious bias on the average (S)SFR as a function of galaxy mass.

The situation in dense environments is completely different. The stellar population of late-type galaxies becomes, on average, slightly older, and some of these objects do indeed belong to the *passive* class. At a given luminosity, the distribution of equivalent widths seems to broaden, reaching significantly lower values of EW(Hα), whereas the $(u-r)$ colours tend to become somewhat redder, consistent with the 'ageing' effect discussed in the context of Figures 2.6 and 2.7. The fraction of elliptical galaxies increases dramatically with respect to the field, and many of them display signatures that are consistent with recent quenching. Both statements are particularly evident in the case of low-mass galaxies, which typically display the highest SSFRs at low overdensities, and therefore the effect of the environment can be more clearly noticed as a sharp discontinuity between the galaxy properties of the 'ageing' and 'quenched' populations.

Galaxies with merging signatures display a clearly bimodal distribution. In the field, they feature the highest SSFR, especially as far as the EW(Hα) is concerned, whereas in dense environments they are systematically located at the red extreme, although it is not obvious whether they are more likely to belong to the 'ageing' or the 'quenched' sequence (cf. Figure 2.7).

2.3.4 The SSFR-metallicity relation of star-forming galaxies

Our results so far are consistent with a single 'galactic ageing sequence' where most galaxies spend the largest part of their lives, including both passive and star-forming systems, with early- or late-type morphologies. In addition to the correlations discussed in the present work, many other relations between the relative properties (colours, equivalent width, spectral shape, metallicity, gas fraction, mass-weighted mean age of the stellar population...) of a given galaxy have previously been reported (see e.g. Ascasibar and Sánchez Almeida,

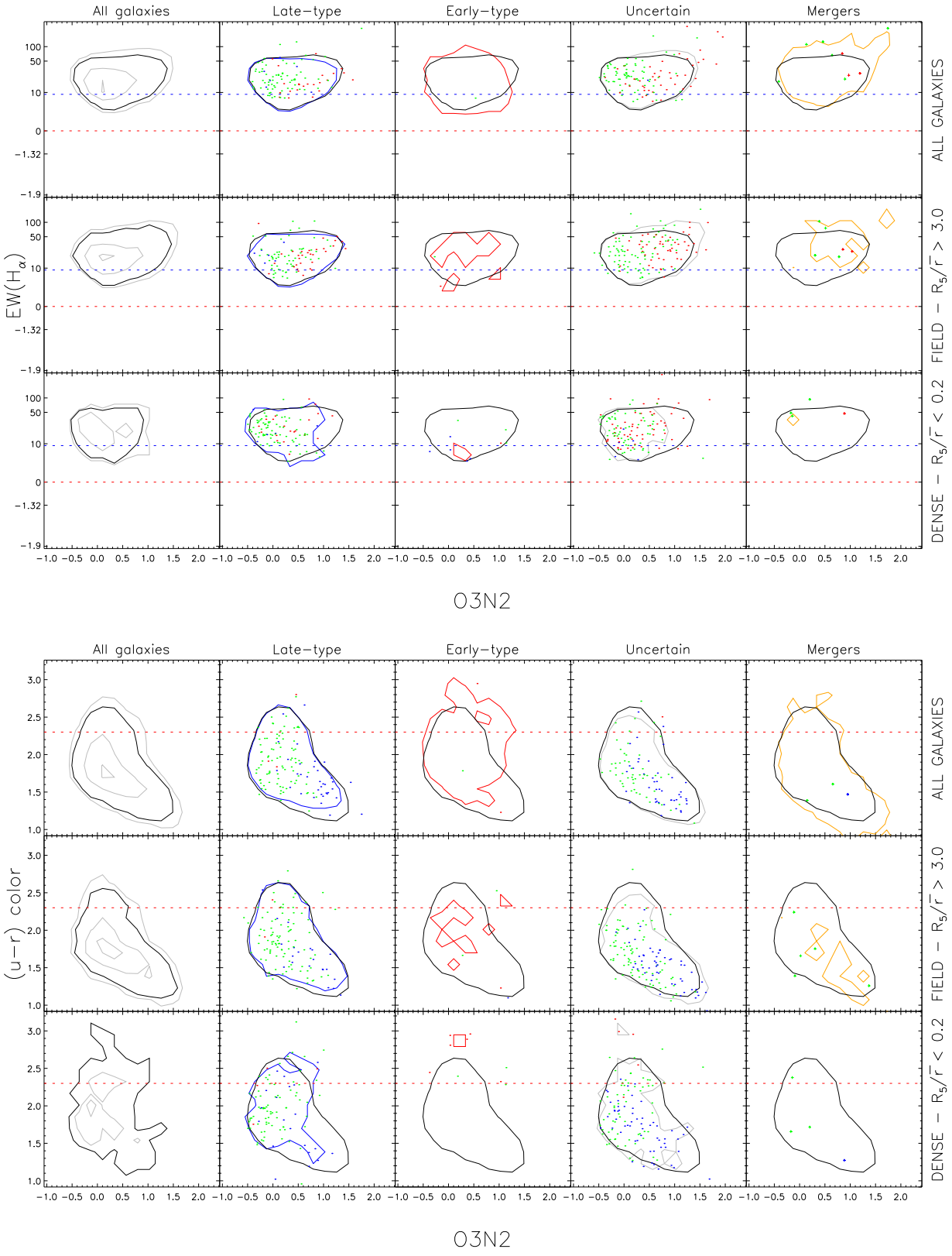

FIGURE 2.9: Galactic SSFR-metallicity relation, using Hα equivalent width (top) and $(u-r)$ colour (bottom) as proxies for the SSFR, and O3N2 for the gas-phase oxygen abundance. Figure schema is the same as in Figure 2.7. The colours of the points correspond to: both, top and bottom – three different bins in *mass* (M_r) : red, objects with $M_r < -21.5$; green objects with $-21.5 < M_r < -19.5$; and blue, objects with $M_r > -19.5$.

2011; Ascasibar et al., 2015), and therefore any of these parameters can be used to describe the current state of the galaxy in terms of its location along the sequence.

Here we will attempt to use the gas-phase oxygen abundance, traced by the O3N2 line ratio. As shown in Figure 2.4, the SSFR (measured in terms of colour or equivalent width) presents a higher correlation coefficient with O3N2 than it does with the absolute magnitude M_r. On theoretical grounds, the gas-phase metallicity is expected to be closely related to the integrated star formation history of the galaxy, not only for the closed-box model (Searle and Sargent, 1972), but for more elaborate scenarios including inflow and outflow of gas (e.g. Edmunds, 1990), even on resolved scales (Ascasibar et al., 2015). The main disadvantage, of course, is that enough signal-to-noise ratio is necessary in order to estimate the O3N2 line ratio, and therefore we have restrained the discussion to the *star-forming* subsample.

The observed relation between the SSFR and O3N2 of *star-forming* galaxies, illustrated in Figure 2.9, is indeed tighter than the relation between SSFR and luminosity discussed in the previous section. As it was previously reported when discussing Figure 2.4, the trend is clearer when using $(u-r)$ colour as a proxy for SSFR. The SSFR-metallicity relation is fully compatible with 'ageing' dominating the evolution of most *star-forming* galaxies, displaying almost exclusively late-type and uncertain morphologies. Interestingly, we do see that the few mergers present in the sample do not only show, on average, higher SSFR, but also lower chemical abundance, than late-type or uncertain systems, hinting that they may be associated to the accretion of low-metallicity gas towards the main galaxy. In all cases, galaxies with high SSFR (i.e. younger stellar populations) are metal-poor, and vice versa. Additional work would be required in order to investigate whether the observed correlation between SSFR and metallicity is not only stronger, but indeed more fundamental than the correlation with stellar mass.

Regarding denser environments (recall here that we are missing *passive* and *intermediate* galaxies) we find that there is an evident lack of low-metallicity objects that could be explained either by an accelerated ageing (induced by e.g a reduction of the gas accretion rate with respect to the field) or by unidentified quenching mechanisms (e.g. stripping and/or rapid consumption) completely removing the gas from our systems and sending them to the quenched sequence. In the latter case, it might be possible to find a quenching signature in the relation between SSFR and the mass-weighted stellar metallicity.

2.4 Discussion

In this section, we would like to propose a scenario where a combination of both nature and nurture processes is responsible for regulating the SSFR of a given galaxy. As we emphasized in the introduction of this chapter, we distinguish between smooth variations of the instantaneous/specific SFR (ageing), a sudden interruption of the star formation activity (quenching), and a transient episode of star formation that is sufficiently intense as to decrease the mass-weighted age of the underlying stellar population (rejuvenation burst). Let us now briefly explore some possible physical mechanisms that may be responsible for these qualitatively different behaviours.

2.4.1 Ageing

In low-density environments, we argue that most galaxies should be expected to start their lives in a 'chemically-primitive' (gas-rich, metal-poor, young stellar population, and high SSFR) state. As they turn their gas into stars and enrich it with metals, they would gradually move towards a 'chemically-evolved' (gas-poor, metal-rich, old stellar population, and low

SSFR) state. Let us stress once again that this 'ageing' process is *unavoidable* unless the star formation rate increases exponentially in time. While possible, such sudden changes in the SSFR (see the subsection on 'rejuvenation bursts' below) do not seem to dominate the overall evolution of typical field galaxies, although they may significantly perturb it for a limited amount of time and/or for a limited fraction of objects.

Considering the average properties of the galaxy population, unaffected by environmental factors, this work firmly establishes the existence of an 'ageing sequence'; i.e. a fairly tight relation between the average EW(Hα) and $(u-r)$ colour of unperturbed galaxies (extensive to O3N2, at least for the *star-forming* subsample). This sequence is *not* meant to represent chronological evolution, but a particular region of the parameter space where most galaxies are found *at the present time* (and there is, in fact, no reason to expect that it should be invariant with cosmic epoch). It merely reflects the relation that must exist between the physical properties of 'young' and 'old' galaxies if their star formation rate has varied slowly with time according to some smooth function $\psi(t)$, whose analytical description lies well beyond the scope of the present discussion.

Quite remarkably, dwarf galaxies (and, in particular, HII galaxies) tend to be located closer to the primitive extreme of the sequence, whereas more luminous systems tend to be, on average, more chemically evolved. The physical origin of the relation between the total mass and the mass-weighted age of the stellar population (or the gas-phase metallicity) is an open question. Ageing is related to the speed at which the gas is accreted and turned into stars, which may be affected by several 'nature' and 'nurture' processes. The observed dependence on the environmental conditions may thus help us constrain the dominant physical mechanisms at work.

Galaxies in the field are consistent with a single trend, without any obvious discontinuity associated to the stellar mass or SSFR. For 'ageing' galaxies at fixed luminosity, there is a mild shift towards more chemically-evolved systems (higher metallicities and lower SSFR) in dense environments. Since both the stellar mass and the galaxy overdensity are related to the mass of the host dark matter halo, this shift might be associated with 'nature' processes driven by the relative efficiencies of gas infall, cooling, and consumption as a function of halo mass. In addition, 'nurture' processes, such as the strangulation of cold gas supply, may play a role in the accelerated 'ageing' in dense environments.

As a final remark, let us note that galaxies with a smooth star formation history may be subject to morphological evolution, triggered by both internal and external mechanisms, and they may also be temporarily offset from the 'ageing sequence' due to discrete quenching or rejuvenation events. As long as they remain in the field, they will continue accreting gas and forming stars. After some time, they will return to the 'ageing sequence' and recover their original morphology, which may be most likely late-type or uncertain.

The time scales of such recovery will depend on the mass of the object, the availability of gas, and intensity of the event under consideration. We argue that field elliptical galaxies, located at the end of the 'ageing sequence', are representative of the last stages of secular galactic evolution. We do not observe any convincing evidence that they have recently interrupted their star formation activity due to a merger event. Rather, we propose that these galaxies, being more massive, already had a lower SSFR previous to such event, and therefore they kept their post-merger elliptical morphology up to the present day. In this scenario, early-type morphologies would be a consequence, rather than the cause, of a reduced SSFR.

2.4.2 Quenching

One of the main results of the present work is that we only find unambiguous evidence for quenching in dense environments. In these cases, star formation does not evolve gradually

until the gas reservoir is exhausted. On a very short time scale, these galaxies are removed from the 'ageing sequence' by shutting down star formation to a level that Hα is clearly detected in absorption. Then, they evolve over the lifetime of A stars along a 'quenched sequence' in the colour-equivalent width diagram, until both branches merge at the 'red-and-dead' extreme.

The critical role played by the galactic overdensity hints that quenching is directly related to the mass of the dark matter halo. It seems reasonable to expect that, for star formation to stop, it is necessary to prevent further accretion of cold gas. This would be the reason why most galaxies in the field (in particular, low-mass galaxies) are almost invariably found among the 'ageing' population. Even if a discrete event might momentarily quench their star formation activity, it would be quickly resumed as a consequence of efficient gas accretion and cooling.

Nevertheless, the very existence of a 'quenched sequence' implies that the physical process(es) responsible for environmental quenching must be very fast. Preventing the accretion of new cold gas is a necessary but not sufficient condition; the galaxies' reservoir must be almost entirely consumed on a time scale much shorter than the lifetime of A stars. Other 'nurture' processes, such as ram-pressure compression and stripping, or tidal interactions and mergers with other galaxies, could contribute to quench star formation in dense environments, probably leaving a morphological signature. From the top panel of Figure 2.8, we do indeed find that most of the low-mass galaxies featuring Hα absorption lines have early-type or uncertain morphologies. Some of them are classified as spirals, though, and it is difficult to assess whether the events (most likely nurture-related) responsible for the morphological transformation have also played a dominant role in the quenching of star formation, or, by the contrary, the observed morphology is a consequence of quenching, analogously to the scenario we proposed for field elliptical galaxies.

2.4.3 Rejuvenation bursts

Both 'ageing' and 'quenching' drive our systems towards a more 'chemically evolved' state. In particular cases (arguably much more common in the early universe), it is possible that some galaxies evolve towards more 'chemically primitive' states for a limited period of time. For instance, accretion of pristine gas well above the star formation rate would reduce the stellar-to-gas fraction and dilute the chemical composition. It is also likely that such event drives a burst of star formation that would increase the metal abundance and stellar fraction, as well as the SSFR, yielding a higher equivalent width for the duration of the burst as well as higher luminosities and bluer colours for a longer time. In extreme cases (regardless of gas accretion), a star-formation burst would decrease the mass-weighted average age of the stellar population. This is our definition of 'rejuvenation'.

Assuming that these processes leave an imprint on galaxy morphology, one can assess their statistical relevance on galaxy evolution by studying the correlations between colour, equivalent width, luminosity, and metallicity for galaxies displaying disturbed morphologies. Our results clearly show that visually-identified mergers display systematically higher EW(Hα) and lower $(u-r)$ for a given M_r than galaxies with late-type morphology (or even those with uncertain morphology) for low-mass galaxies in low-density environments, i.e. those where a significant gas reservoir is expected. We interpret this as evidence for merger-induced rejuvenation.

However, most galaxies with high SSFR have uncertain morphologies, which could well be associated to a recent merger, but they could also be due to intrinsic 'nature' processes (e.g. stochastic star formation), especially in low-mass galaxies. We can only ascertain that galaxies with irregular morphology have, on average, slightly higher SSFR than late-types, although the effect seems to be milder than the enhancement observed in ongoing

mergers (which represent a very small fraction of the galactic population). We argue that 'rejuvenation' episodes contribute to the scatter observed in both, the 'ageing sequence' and the relations between SSFR, metallicity, and luminosity. Nevertheless, these processes are not the dominant mechanism regulating neither the star formation nor the chemical evolution in galaxies.

It is possible, though, that they are important in particular types of objects, such as e.g. HII galaxies. The presence of an underlying host with an older stellar population (see e.g. Papaderos et al., 1996; Amorín et al., 2009; Janowiecki and Salzer, 2014) hints that these objects are good candidates for a 'rejuvenation' episode. However, it is not entirely clear whether the mass-weighted age of the stellar population, defined in equation (2.1), has decreased as a consequence of a recent star formation burst or the SSFR has been a smooth function of time throughout most of their history. Recent observations do indeed suggest that low-mass star-forming galaxies, including blue compact dwarfs, have formed 90 per cent of their stellar mass between 0.5 and 1.8 Gyr ago, consistent with the expectation from the SSFR-luminosity (or SSFS-metallicity) relation of 'ageing' galaxies (Rodríguez-Muñoz et al., 2015).

Since EW(Hα) is sensitive to star formation ~ 10-Myr scales, we argue that close pairs or merger signatures should be clearly visible in the majority systems in the interaction-induced burst scenario. Therefore, our results support the idea that HII galaxies are simply the 'chemically primitive' extreme of the 'ageing sequence', but we do not find evidence that their SSFR has increased drastically on very short time scales.

2.5 Conclusions

We have carried out an analysis of the mechanisms driving and regulating star formation in the local universe. To do so we have selected a sample of galaxies from the SDSS DR7 spectroscopic catalogue, applying restrictions in apparent magnitude, redshift, and position in the sky, and then classified them as *star-forming* (35425 objects), *agn* (8099 objects), *passive* (19266 objects), or *intermediate* (19826 objects) according to the observed intensity and signal-to-noise ratio of some of their optical spectral lines.

For the *star-forming* subsample, we have studied the distribution of absolute magnitudes in the r-band (M_r), the normalized distance to the fifth nearest neighbour ($R_5/\bar{r}$), the ratio of squared projected distances of the first two neighbours (R_1^2/R_2^2), the morphologies derived from the galaxy Zoo visual classification project, the O3N2 metallicity indicator, the equivalent width of the Hα line, and the $(u-r)$ colour. Although we find evidence that mergers may temporarily increase the SSFR, we conclude that most (non-merging) *star-forming* systems evolve through internal processes, i.e. 'nature', as we do not find, on average, any statistically-significant signature of the interaction-induced scenario. We do find, however, that *star-forming* galaxies tend to be found in the field, and we show that the distribution of environmental density is in fact independent on other galaxy properties, including luminosity. As far as we are aware, this is the first time such result has been reported in the literature.

Our analysis also shows that the restriction in signal-to-noise used to define our *star-forming* subsample, roughly equivalent to a fixed threshold in EW(Hα) or $(u-r)$, creates an artificial bimodality when comparing *star-forming* and *passive* galaxies. Including the *intermediate* population, we arrive at the following conclusions:

1. In low-density environments, most present-day galaxies are distributed along a relatively narrow 'ageing sequence' in the EW(Hα)-$(u-r)$ plane. At the 'chemically young' extreme, galaxies have high SSFR (blue colours and high equivalent widths), low metallicity (high O3N2), and late-type or uncertain morphology. We argue that,

at the 'chemically old' extreme, galaxies tend to display elliptical morphologies because the SSFR is insufficient to rebuild a significant disk. Brighter galaxies tend to be more chemically evolved, resulting in clear correlations between SSFR and luminosity or metallicity, but all of them are consistent with a smoothly-varying SSFR driven by secular ('nature') processes, with little evidence for recent 'quenching' or 'rejuvenation' episodes.

2. In dense environments, we detect a 'quenched sequence' in the EW(Hα)-($u-r$) plane, consistent with a very rapid truncation of the star formation activity. Most of these objects display early-type or uncertain morphologies, but it is difficult to establish a causal connection between galaxy interactions and the drop in SSFR.

We thus propose a scenario where 'nature' is more important than 'nurture' in regulating star formation in galaxies. Starting their lives as 'chemically primitive' objects, they gradually turn their gas into stars with a slowly-evolving SSFR and evolve towards 'chemically old' systems, leading to the observed relation between EW(Hα) and ($u-r$) colour. Apart from this *unavoidable* 'ageing' process, galaxies are also susceptible to 'quenching' (in dense environments) and/or 'rejuvenation' episodes (associated to extreme bursts of star formation). The ability to return to the 'ageing sequence' after such events is linked to the external gas supply. Galaxies will become *red and dead* either when they totally exhaust their gas reservoir and stop forming stars (end of the 'ageing sequence') or when they suffer a quenching event in a dense environment and they are no longer capable of accreting gas ('quenched sequence'). Mergers and galaxy-galaxy interactions may temporarily affect the instantaneous SSFR, but they merely seem to add statistical fluctuations to the main relation.

The work presented in this chapter was conducted analysing a carefully selected sample of aproximately 82500 galaxies. This allows us to derive statistically robust conclusions based on the *average* properties of local galaxies. However, some of the proxies considered suffer from a strong *aperture bias* that, in theory, should restrict our results to those areas of galaxies covered by the 3 arcsec fibre. Besides, SDSS fibres point to the brightest parts of the systems (as observations were designed in such way) introducing a selection bias. Therefore, this work presents the "ageing" of galaxies for the first time in this thesis but also leaves a series of open questions:

- *How important are these aperture effects and how will they affect the results of this study?*
- *Do galaxies age on their entire extent or do we expect any radial behaviour?*

In order to answer these questions we extended this work to a selected sample of IFS observations that we will introduce in the following chapter.

Chapter 3

Ageing and quenching in CALIFA galaxies.

This chapter is a based on the article:
"Galaxy evolution on resolved scales. Ageing and quenching in CALIFA galaxies."
by J. Casado, Y. Ascasibar, R. García-Benito and A.I. Díaz
∼ draft version ∼

3.1 Introduction

As proposed in the previous chapter, the effects of ageing and quenching in galaxies can be investigated by means of the colour-equivalent width diagram, whose physical interpretation is qualitatively illustrated in Figure 3.1. Both quantities are proxies for the SSFR, but they are sensitive to different stellar populations and therefore to different time scales. On the one hand, the intensity of the Hα line is proportional to the number of O and B stars, responsible for the ionizing ultraviolet radiation. When considered in terms of equivalent width (EW), it roughly traces the fraction of stellar mass that has formed over the last $10 - 30$ Myr. On the other hand, broad-band colours are more sensitive to the overall shape of the spectral energy distribution, and they trace older stellar populations, varying on time scales of the order of $\sim 0.1 - 1$ Gyr.

If the star formation rate varies smoothly over the whole life of a galaxy, the system slowly moves from the 'primitive' extreme on the upper left – blue colours and high EW, which also imply low metallicity and high gas fraction (see e.g. Ascasibar et al., 2015) – towards the 'evolved' extreme on the bottom right (red colours and EW of the order of $1 - 2$ Å in *absorption*, which we denote as negative values). The main result presented in Chapter 2 (and probably also the main result of this thesis) is indeed that most galaxies in the field describe a relatively tight 'ageing sequence' in the colour-equivalent width plane (green line in Figure 3.1), that we interpret in terms of gradual evolution driven by the secular conversion of gas into stars.

However, as we also discussed in the final part of the previous chapter, this result is based on SDSS measurements of very nearby galaxies and may be severely affected by aperture bias. The $3''$ fibre translates into a physical diameter of $1.2 - 4$ kpc for the redshift range considered in the above mentioned work ($0.02 < z < 0.07$), and it only covers the brightest part (typically the centre, or a giant HII region in some extreme cases) of the objects under study. To tackle this issue, in this chapter we extend the study of the colour-equivalent width diagram to a sample of 40 objects considered in the SDSS analysis that have also been observed by the Calar Alto Legacy Integral-Field Area (CALIFA) survey (Sánchez et al., 2012a). The field-of-view (FoV) of the PPAK/PMAS instrument consists of an hexagon of $65'' \times 74''$, and the CALIFA sample has been diameter-selected so that it typically reaches up to about ~ 2 effective radii, ensuring a representative coverage of the observed galaxies

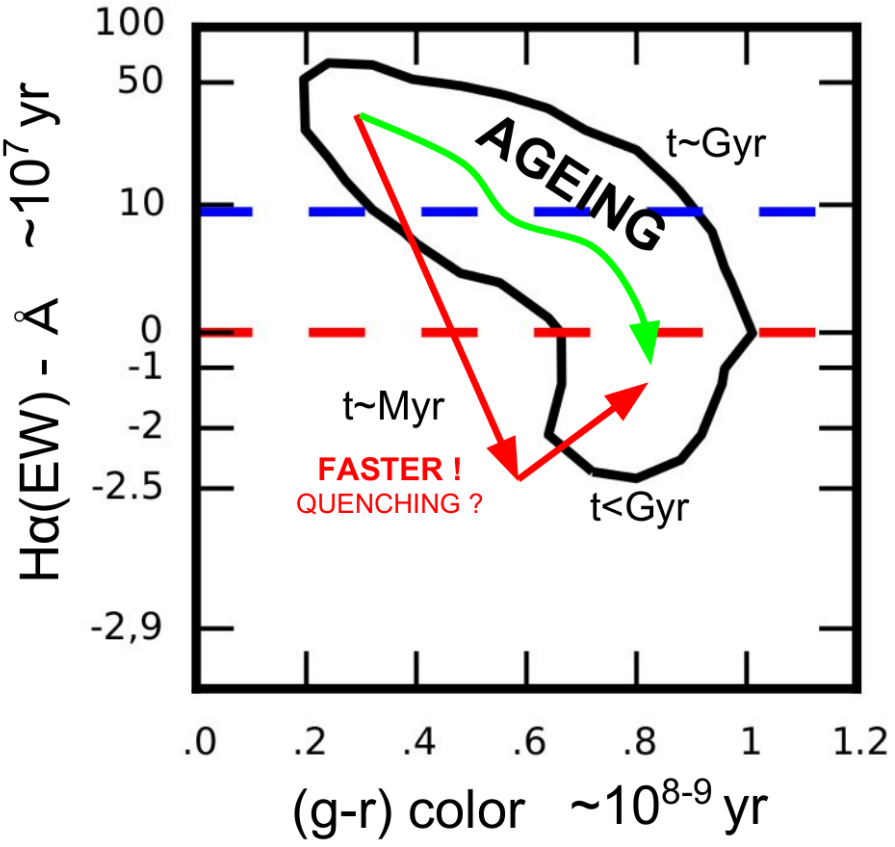

FIGURE 3.1: Illustration of the "ageing" process in galaxies as interpreted from the colour-equivalent width diagram. The y-axis depicts the equivalent width of the Hα line, whose strength is driven by the light of O and B stars, tracing SF in timescales of the order of 10^7yr. The x-axis corresponds to the (g-r) colour, mainly driven by the emission of the continuum, less sensitive to sudden changes in the SF and tracing timescales of the order of 10^{8-9}yr. The black contour corresponds to the location of 90% of the sample considered in Chapter 2 (SDSS). The red dashed line corresponds to the zero value in EW, separating absorption and emission in the diagram. Blue dashed line corresponds to EW(Hα)=9Å, minimum threshold equivalent to imposing a S/N $>$ 3 in the four emission lines used in the BPT diagram, illustrating a dangerous source of bias. Green solid line corresponds to the location of our proposed "ageing sequence", consequence of the secular evolution (nature) of "galaxies", i.e. conversion of gas into stars. The steeper red arrow represents a much rapid and abrupt transition through the diagram corresponding to complete quenching of the star formation activity.

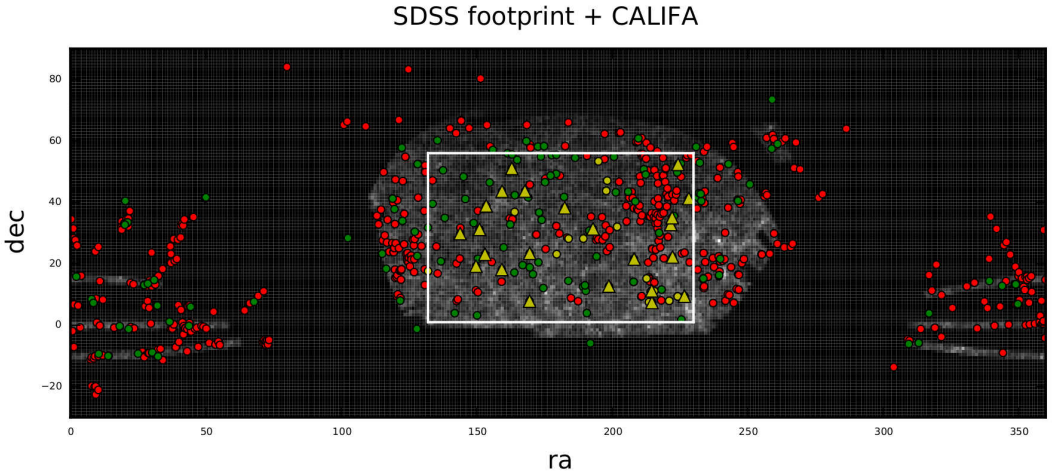

FIGURE 3.2: Spatial distribution of the SDSS spectroscopic galaxy sample (defined as *main* sample in Casado et al., 2015). The white square limits the region used in the analysis of Chapter 2. Red and green circles correspond to the *main* and *extension* samples of the CALIFA survey, respectively. Yellow symbols represent the location of the *overlapping* sample (triangles correspond to the 24 objects whose results we present in this chapter).

(Walcher et al., 2014). In this continuation work we consider integral-field spectroscopic (IFS) data in order to:

- Study the impact of the well-known aperture effect affecting SDSS spectroscopic data and verify the results of Chapter 2.
- Investigate the ageing and quenching processes on resolved scales over the whole galactic extent.
- Consider the effect of local properties (CALIFA spaxel size roughly corresponds to ∼1kpc physical size) in driving the "ageing" of galaxies.

In the coming sections we describe the galaxy sample considered for this work and its physical characterization. In order to mimic the procedure conducted in Chapter 2 we present a comparison of the proxies used in our analysis of SDSS galaxies with ancillary data available for our IFS data (CALIFA). Finally we explore the colour-EW diagrams for every given object, discuss the theoretical interpretations of our results and derive our conclusions.

3.2 Observational data

The main purpose of the present work is to study in more detail the colour-EW diagram using IFS observations. To do so we will select all the galaxies considered in Chapter 2 that have been observed within the CALIFA collaboration[1]. This sample, we will refer to as *overlapping*, fulfils all the selection criteria imposed in the previous work and that we now briefly summarize.

All data used in Chapter 2 correspond to objects catalogued as galaxies by the spectroscopic pipeline (entries listed in table SpecObj) of the SDSS Data Release 7 (Abazajian et al.,

[1] http://califa.caha.es/

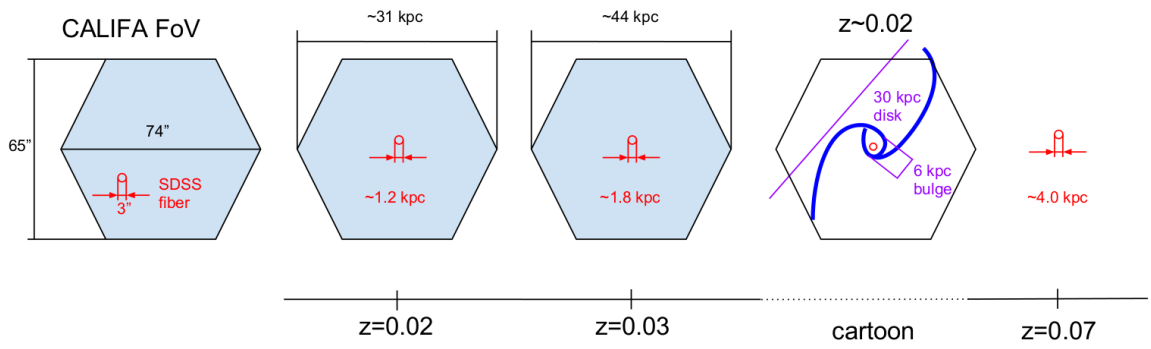

FIGURE 3.3: Cartoon that illustrates the differences between the CALIFA FoV (hexagon of $65'' \times 74''$) and the SDSS spectroscopic fibre ($3''$), which is usually centred on the brightest region. The CALIFA subsample used in the present work covers a redshift range $z \sim [0.02-0.03]$ while the SDSS sample analysed in Casado et al. (2015) was restricted to the redshift range $z = [0.02 - 0.07]$.

2009) database[2]. The sample is restricted in apparent magnitude $m_{\rm r} < 17.5$ to ensure that every object with a similar-mass companion is properly identified, and limited to a region of the sky (white square in Figure 3.2) to minimize boundary effects in the neighbour search. We also imposed a redshift range $0.02 < z < 0.07$, where the upper limit implies completeness for absolute magnitude $M_r < -20.0$, and the lower redshift cut avoids local structure. The final sample consisted of $\sim$ 82000 objects, for which several galactic properties were derived (see Casado et al., 2015, for a detailed description).

The *overlapping* sample (galaxies common to both samples, yellow symbols in Figure 3.2) consists of only 40 objects[3]. More than half of the $\sim$ 600 objects observed by the CALIFA survey (red and green circles) lay outside the region of the sky considered in the work of Chapter 2, and the size of the overlapping sample is further reduced when we impose the same redshift range, since many of the CALIFA galaxies are located at $z < 0.02$. However, it must be noted that the total number of *spectra* analysed is approximately the same as in the previous work, since each datacube contains of the order of $2000 - 2500$ useful spaxels. More precisely, we will consider COMBO CALIFA datacubes from the DR2 (see García-Benito et al., 2015a).

The main advantage of using IFS data is that we can now investigate the spatial distribution of the star formation activity over a significant fraction of the total extent of our galaxies (see Figure 3.3). For the narrow redshift range of our resolved sample, $z \sim 0.02 - 0.03$, the field-of-view covers up to $\sim 30 - 40$ kpc, corresponding to up to ~ 2.0 effective radii (R_e) in most cases.

3.2.1 Physical characterization

As we aim to reproduce, validate and extend the analysis conducted in Chapter 2 we will again briefly outline how the sample was characterized in the previous work. We used the absolute magnitude in the r band, M_r as a proxy for the stellar mass. To quantify the environment in terms of the local galaxy overdensity we derived the projected distance to the fifth nearest neighbour normalized to the average intergalactic distance $\overline{r}$(z) . We also made use of the visual morphology classification conducted by the Galaxy Zoo 1 citizen science project (Lintott et al., 2008). Finally, the (u-r) colour (SDSS filters) and the equivalent width of the Hα line were used as proxies of the specific star formation rate.

[2] http://cas.sdss.org/dr7/en/help/browser/browser.asp

[3] This is work in progress, and only 24 galaxies have been completely analysed so far

In the present work we will use some of these values to characterize the global properties of the *overlapping* sample. Besides, the environmental characterization, $R_5/\bar{r}$, was derived making use of the entire SDSS spectroscopic sample and was proven to be a robust indicator of the local galaxy overdensity. Part of the present work will be devoted to the comparison of the above mentioned proxies with available ancillary data derived within the CALIFA collaboration (measurements for the environment, the mass and the morphology, Walcher et al., 2014). The availability of integral-field spectroscopy data will allow us to measure galaxy colours and the EW(Hα) with a better spatial sampling and size coverage. However, SDSS single-fibre measurements obtained in the work of Chapter 2 will also be considered to illustrate aperture effects.

Figure 3.4 shows the location of the *overlapping* sample (SDSS values) in the EW(Hα)-magnitude and colour-magnitude diagrams with respect to the SDSS sample considered in Chapter 2. We can see that most of our objects show Hα in emission but with EW values below 10 Å, i.e. our galaxies neither qualify as star-forming or passive according to the information extracted from the SDSS fibre. We can also observe that most of them reside in the "red sequence" (colour-magnitude diagram, bottom) and show M_r <-20, i.e. our sample lacks low-mass objects (consistent with the CALIFA observational strategy) belonging to the blue-cloud. Some of these properties are listed in Table 3.1.

Global properties

In Casado et al. (2015) we used the absolute magnitude in the r band, M_r, as a proxy for stellar mass. However, the CALIFA collaboration has a stellar mass catalogue for its entire dataset computed from the SDSS optical ugriz, GALEX UV, and 2MASS NIR growth curve magnitudes using the prescription presented in Walcher et al. (2008). We consider this value in our analysis (labelled as $M_{*,\mathrm{JW}}$ in Table 3.1), which is shown in Figure 3.5 to be in good agreement with the proxy used in Chapter 2. The dashed lines in this plot delimit the mass bins that we use in the following sections and highlight the limited mass range of our sample.

As will be shown below, morphology is one of the global properties of a galaxy that is most strongly correlated with its star formation history. In Chapter 2 we used Galaxy Zoo morphological classification, according to which a large number the galaxies were assigned to the 'unknown' category. Given the correlation between SF and morphology, these 'unknown' objects are believed to represent a transition population, the most interesting objects for exploring ageing and quenching processes.

We also make use of the morphological classification described in Walcher et al. (2014), based on visual inspection of SDSS images in the r and i bands. This classification is available in the ancillary dataset and is in good agreement with the Galaxy Zoo I classification (Lintott et al., 2008), as it can be seen in Figure 3.6. The number of objects considered in the comparison plot is larger (137 objects) than that of the *overlapping* sample, as we are just testing both classifications and no restrictions regarding environmental measurements are needed. Figure 3.6 presents two colour maps comparing the two classifications. A clear conclusion is that early-types and late-types are consistently classified in both schemes while S0's, S0a's and Sa's are more difficult to identify, giving rise to the 'unknown' population. We further bin our sample into five different groups based on Walcher et al. (2014) morphogies: early types (E0-E7), lenticulars (S0-S0a) , early-spirals (Sa-Sab), Sb's and late-spirals (Sbc-Sd). Our goal is to arrange our sample in order to study (in the following sections) the relation between morphology and the global location of our objects in the colour-equivalent width diagram.

Finally, we have used $R_5/\bar{r}$, the normalized distance to the fifth 'spectroscopic' neighbour, as a proxy to characterize the environment (see Chapter 2 for a detailed description).

CALIFAID	NAME	Morpho(Zoo)	$R_5/\bar{r}$	$M_{\rm GVM}$	$M_{*,\rm JW}$	M_r
500	UGC07145	Sbc (L)	0.6181	11.72	10.24	-20.93
581	UGC08004	Scd (L)	1.5178	11.42	9.84	-20.45
665	UGC08781	Sb (L)	0.1990	12.79	10.87	-22.00
789	NGC5888	Sb (L)	0.5634	13.11	11.16	-22.47
278	UGC05108	Sb (L)	1.5972	12.41	10.77	-21.79
774	UGC09537	Sb (L)	1.9823	12.76	11.10	-22.27
307	UGC05359	Sb (L)	2.1304	11.96	10.50	-21.36
319	NGC3160	Sab (L)	0.2764	13.81	10.81	-21.20
311	NGC3106	Sab (L)	0.4976	12.65	10.99	-22.08
785	UGC09711	Sab (L)	0.5518	12.34	10.75	-21.09
381	IC0674	Sab (L)	1.8640	12.35	10.75	-21.87
386	UGC06312	Sab (L)	2.1968	12.34	10.93	-21.45
776	UGC09539	Sab (U)	2.4797	12.03	10.67	-21.21
314	UGC05498NED01	Sa (L)	1.4075	12.12	10.66	-20.95
340	NGC3303	S0a (U)	0.2778	12.26	10.87	-19.92
613	UGC08322	S0a (U)	0.7570	12.68	11.02	-21.83
728	IC0994	S0a (U)	0.6237	13.69	10.99	-21.80
360	NGC3406NED01	S0 (U)	0.1955	12.53	11.20	-21.90
730	NGC5549	S0 (E)	0.3503	13.82	11.31	-22.72
782	UGC09629	E7 (U)	2.2966	12.52	10.98	-21.85
773	UGC09518	E6 (E)	0.4260	13.10	11.20	-22.49
341	UGC05771	E6 (E)	1.5025	12.76	10.92	-21.94
387	NGC3615	E5 (E)	0.2877	13.14	11.34	-22.42
318	NGC3158	E3 (U)	0.1308	13.81	11.62	-22.79
225	IC2407	Sbc (L)	2.3039	11.74	10.32	-20.50
714	UGC09067	Sbc (L)	1.0695	13.12	10.40	-21.60
719	NGC5519	Sb (L)	1.4250	11.86	10.61	-21.68
735	UGC09199	Sb (L)	1.6813	12.08	10.62	-20.98
610	UGC08267	Sb (L)	0.7792	12.08	10.64	-21.03
624	NGC5157	Sab (L)	1.0917	12.54	11.00	-22.24
772	UGC09492	Sab (L)	1.9160	12.65	11.08	-22.09
593	UGC08107	Sa (U)	1.1332	12.76	10.94	-21.91
364	UGC06036	Sa (L)	1.0031	12.50	10.99	-21.55
520	NGC4211NED02	S0a (U)	0.8635	12.27	10.10	-20.10
479	NGC4003	S0a (L)	1.3522	12.46	10.95	-21.69
562	IC3598	S0 (U)	0.9469	12.32	10.85	-21.63
612	NGC5029	E6 (E)	0.3656	13.44	11.29	-22.69
726	NGC5532	E4 (E)	0.1615	13.69	11.44	-23.11
781	IC1079	E4 (E)	0.2906	13.49	11.31	-22.37
727	NGC5546	E3 (E)	0.2458	13.82	11.36	-22.73

TABLE 3.1: *Overlapping* sample: galaxies analysed in Chapter 2 included in the CALIFA survey. "CALIFAID" corresponds to the label assigned by the CALIFA collaboration, and "NAME" corresponds to the NGC, UGC, or NED catalogue. "Morpho" refers to the visual morphological classification conducted by Walcher et al. (2014); the letter in parenthesis corresponds to the classification (Early-type, Late-type, Unknown) of the Galaxy Zoo I project (Lintott et al., 2008). "$R_5/\bar{r}$" is the environmental characterization performed in Chapter 2, and "$M_{\rm GVM}$" correspond to the group virial mass in Yang et al. (2007) ($\log_{10}(M_\odot/h)$). $M_{*,\rm JW}$ corresponds to the stellar mass derived by Walcher et al. (2008) ($\log_{10}(M_\odot)$, and M_r is the *modelmag* magnitude in the r band obtained from the SDSS DR7 database. The table is divided in 2 parts by a solid horizontal line indicating the sample presented in this work (top) and the galaxies whose analysis is still in progress (bottom).

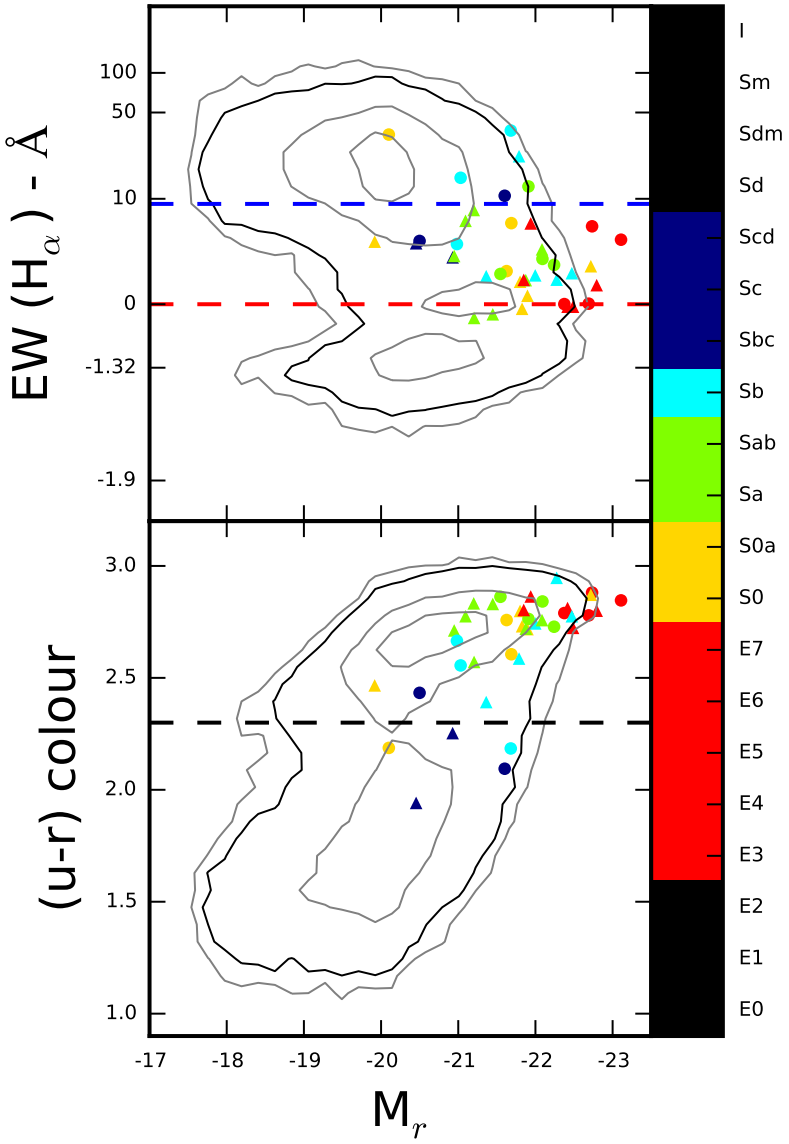

FIGURE 3.4: Location of the *overlapping* sample (40 objects) in the EW(Hα)-magnitude and colour-magnitude diagrams. The contours are the same as in Casado et al. (2015), corresponding to the location of the SDSS-based sample. The colour code corresponds to the morphological bins we define in Section 3.2.1 following the Walcher et al. (2014) classification.

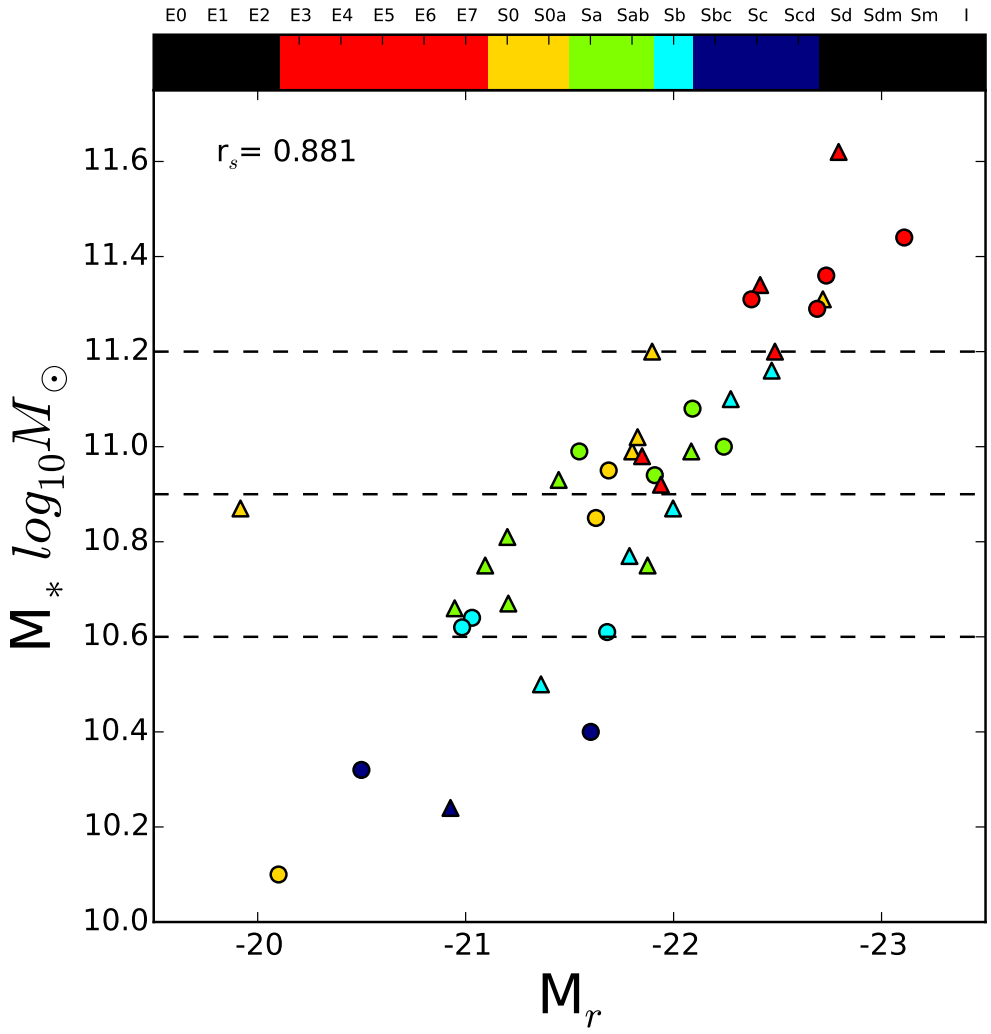

FIGURE 3.5: Plot comparing the total stellar masses estimated using growth curve magnitudes from SDSS, GALEX and 2MASS ($M_{*,\mathrm{JW}}$, Walcher et al., 2008) with the *model* absolute magnitude in the r band (M_r, proxy used in Chapter 2) for the entire *overlapping* sample. The colour code is the same as in Figure 3.4. Spearman's rank correlation coefficient, $r_s = 0.881$, is quoted in the top left corner. Different symbols differentiate between already (triangles) and not yet (circles) analysed. Dashed lines delimit the mass bins used in Figures 3.11 and 3.12.

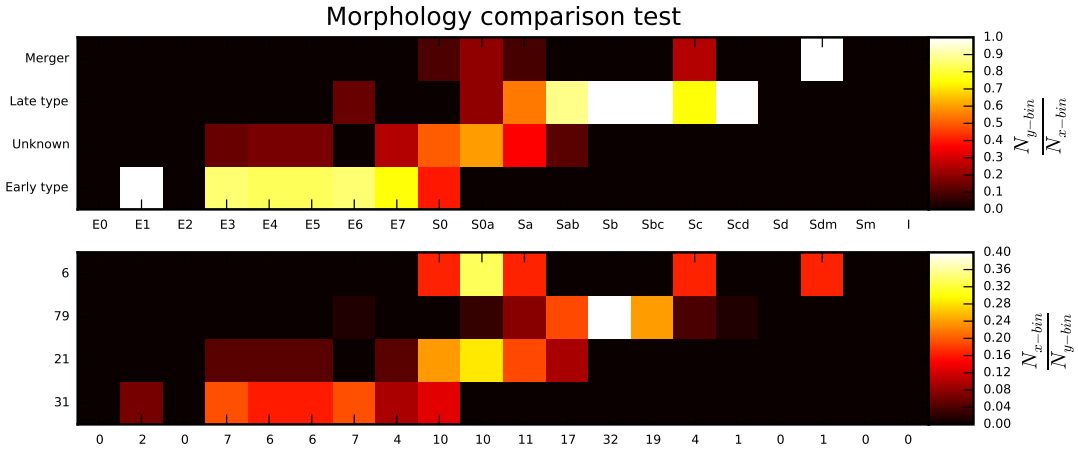

FIGURE 3.6: Morphological classification of the 137 objects in both the CALIFA mother sample (not all of them were observed) and Casado et al. (2015), comparing the results of the Galaxy Zoo 1 citizen science project (Lintott et al., 2008) used in Chapter 2 and the visual classification performed for the CALIFA survey (Walcher et al., 2014).

The work conducted by Walcher et al. (2014) characterizes the environment of the CALIFA galaxies using several indicators. In the present work we will compare our proxy, $R_5/\bar{r}$, with the estimation for the group virial mass computed from the SDSS group catalogue created by Yang et al. (2007). These authors used a group finder to determine group membership and halo masses within the SDSS DR7 sample of galaxies. Their algorithm iteratively identifies potential group members, determines a characteristic luminosity for the defined group, and estimates the mass, size and velocity dispersions of the dark matter halo. To do so, it assumes a group mass-to-light ratio adjusted at every iteration, and the group membership is updated until convergence. This value is listed as 'group virial mass' in Table 3.1 together with $R_5/\bar{r}$, and Figure 3.7 shows their good agreement. This figure also illustrates how we will make use of both proxies to characterize the environment. Galaxies in "dense" environments (bottom-right dashed box) show $R_5/\bar{r}< 0.75$ and $M_{\rm GVM} > 12 - 75$, while "field" ones depict $R_5/\bar{r}> 1.75$ and $M_{\rm GVM} < 12.5$. The rest are classified as "intermediate".

Our galaxy classification according to global properties is illustrated in Figure 3.8, where SDSS postage-stamp images are grouped in terms of morphology and environment. Our sample covers all possible combinations except very isolated (field) early-type galaxies and late spirals in any extreme environment. The latter is mostly due to our lower redshift cut, which excludes the vast majority of the (already few) low-mass objects observed by CALIFA (in fact, we barely have a handful objects below $10^{10.6}$ $M_\odot$). Due to the well-known correlation between mass and morphology (see Chapter 1), this implies that the latest morphological types are severely underrepresented in our *overlapping* sample.

Local properties

To measure the intensity of the nebular emission lines in a given spectrum and simultaneously account for stellar absorption, we use STARLIGHT (Cid Fernandes et al., 2005), which models the spectral energy distribution of the underlying stellar population by fitting the observed spectrum with a linear combination of single stellar populations spanning different ages and metallicities. We use the the spectra provided by Vazdekis et al. (2010) for

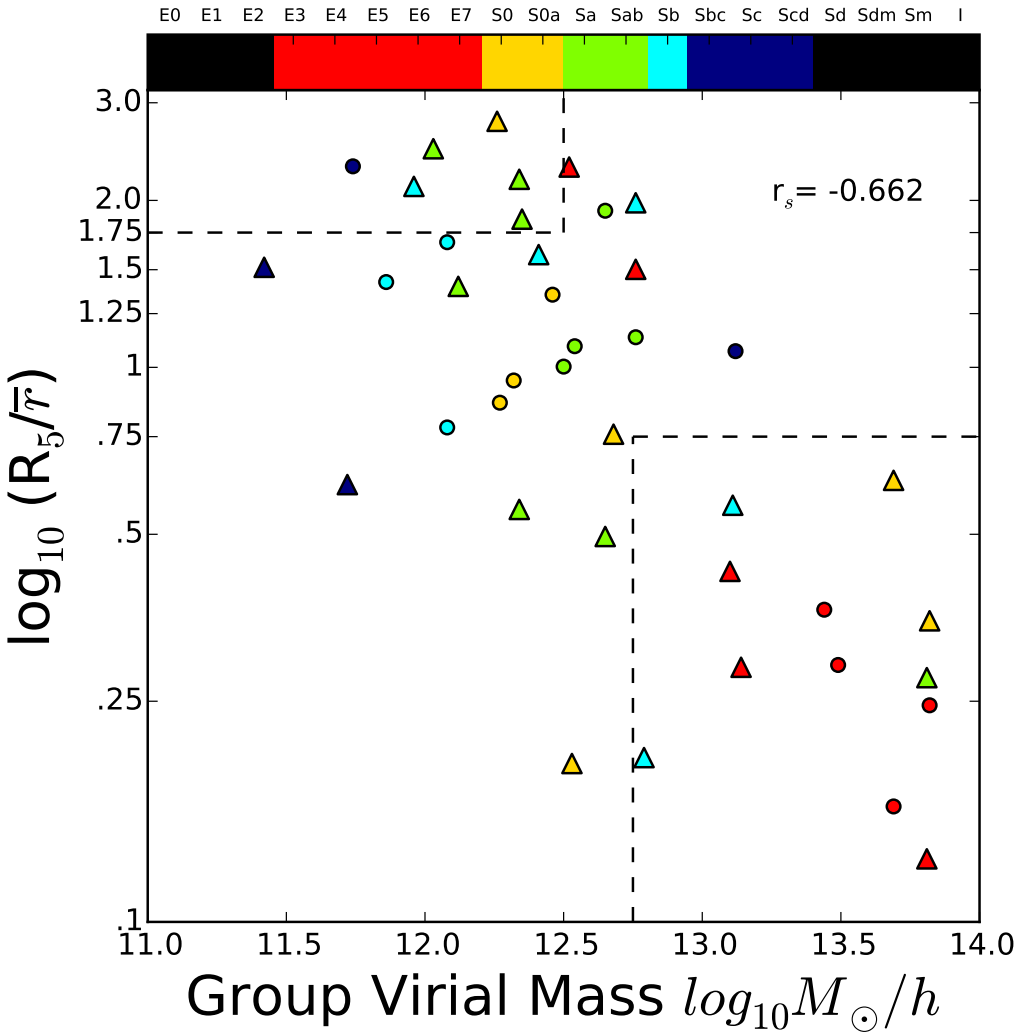

FIGURE 3.7: Comparison between the group virial mass $M_{\rm GVM}$ derived by Yang et al. (2007) and the overdensity $R_5/\bar{r}$ measured by Casado et al. (2015) for our *overlapping* sample. Colours and symbols are the same as in Figure 3.4. Dashed-line boxes correspond to our definitions of "dense" (bottom-right, $R_5/\bar{r}< 0.75$ and $M_{\rm GVM} > 12-75$) and "field" (top-left, $R_5/\bar{r}> 1.75$ and $M_{\rm GVM} < 12.5$) environments used in Figures 3.8, 3.9, 3.10, and 3.11.

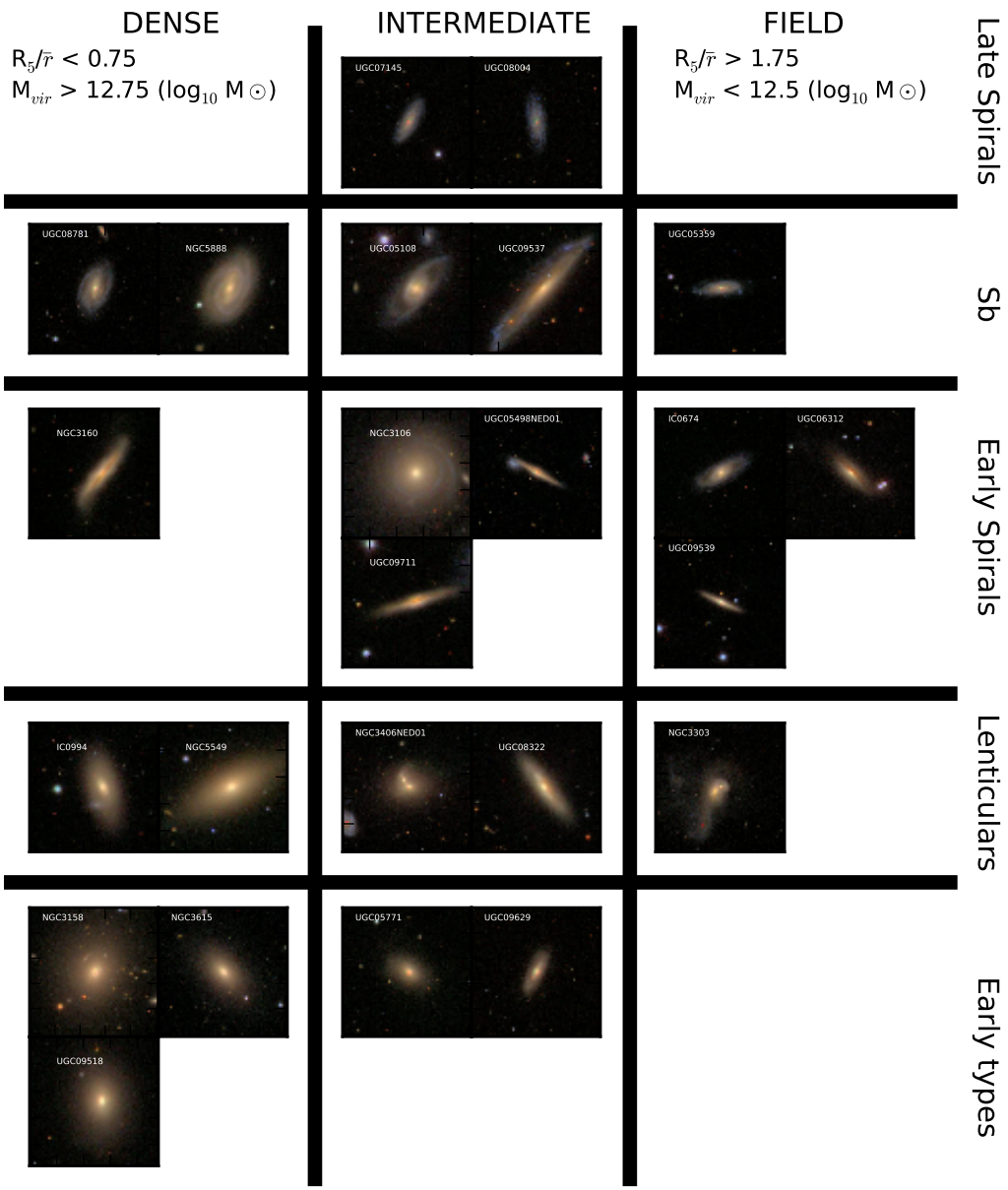

FIGURE 3.8: SDSS postage-stamp images of the analysed sample. Thick solid lines correspond to the bins in morphology (rows) and environment (columns) discussed in Section 3.2.1. The arrangement of the galaxies within each box is arbitrary.

populations older that 64 Myr and González Delgado et al. (2005) models for younger ages. Dust effects are modelled as a foreground screen, assuming a Cardelli, Clayton, and Mathis (1989) reddening law with $R_V = 3.1$. Then, we subtract the estimated stellar continuum from the observed spectrum and obtain the line flux with the SHerpa IFU line fitting software (SHIFU; García-Benito, in preparation), based on CIAO's SHERPA package (Freeman, Doe, and Siemiginowska, 2001; Doe et al., 2007). Small deviations with respect to the stellar continuum are taken into account by a first order polynomial, and independent Gaussians have been fitted for the emission lines.

To obtain the surface brightness and the different galaxy colours we convolve the spectra in every spaxel with broad band filters from the SDSS. Maps of the surface brightness in the r band are plotted in Figure 3.9 for each of our galaxies, and we will use this quantity as a proxy for the local environment. In general, high values of the surface brightness can only be reached in the innermost part, close to the galactic centre, whereas low values are representative of the outskirts. As a rule of thumb, an SDSS r-band surface brightness of the order of 22 mag/arcsec^2 roughly corresponds to one effective radius, R_e. Physically, surface brightness traces the local density, and it seems reasonable to expect that higher values are associated to shorter timescales and a more efficient conversion of gas into stars. According to this argument, the central parts should be more "chemically evolved" than the outer regions, consistent with the inside-out galaxy formation scenario.

Besides the flux and equivalent width of the Hα line, we also estimate the fluxes corresponding to the other three emission lines involved in the BPT diagram (Baldwin, Phillips, and Terlevich, 1981), Hβ, [OIII] and [NII], in order to briefly discuss in Section 3.4.1 the possible connections with the trends observed in the resolved colour-equivalent width diagram.

3.3 Results

The resolved colour-equivalent width diagrams of all our galaxies are shown in Figures 3.10, 3.11, and 3.12, arranged by groups of morphology and environment, environment and mass, and mass and morphology. Each panel depicts one galaxy. A black solid line indicates the contour containing 90% of the spaxels, compared to the contour (grey line) obtained for the $\sim$ 82500 SDSS galaxies (3″ fibres) in Chapter 2. The overall contour, considering all CALIFA objects together, is shown by the solid black line in the example panel at the bottom-right of Figures 3.10 and 3.11 (bottom-left in Figure 3.12).

A first remarkable result is that these contours mostly overlap, i.e. the vast majority of CALIFA measurements are enclosed within the same boundaries defined by the SDSS 90% contour. This is important, as it suggests that the physical processes driving the ageing of galaxies within the 3″ aperture of SDSS observations extend to the regions covered by the FoV of CALIFA observations (up to $\sim$ 30 kpc in our sample), and it is consistent with a common physical mechanism driving the "ageing" of galaxies both in the brightest central parts typically targeted by the SDSS fibres as well as in the much fainter outskirts considered in this follow-up work.

As we have seen in Chapter 2, different objects may present different stages of the "ageing" process. However, at variance with the SDSS data, IFS observations reveal that the location in the colour-equivalent width diagram of all the regions within a single object is typically not concentrated, but broadly extended along the "ageing sequence". This result strengths the hypothesis of "ageing" being a *very local process*, and it emphasizes the relevance of considering aperture effects when dealing with SDSS data.

In order to evaluate the effect of the aperture bias associated to the SDSS data, four extra measurements are included in every panel of Figure 3.10: the values derived from the SDSS

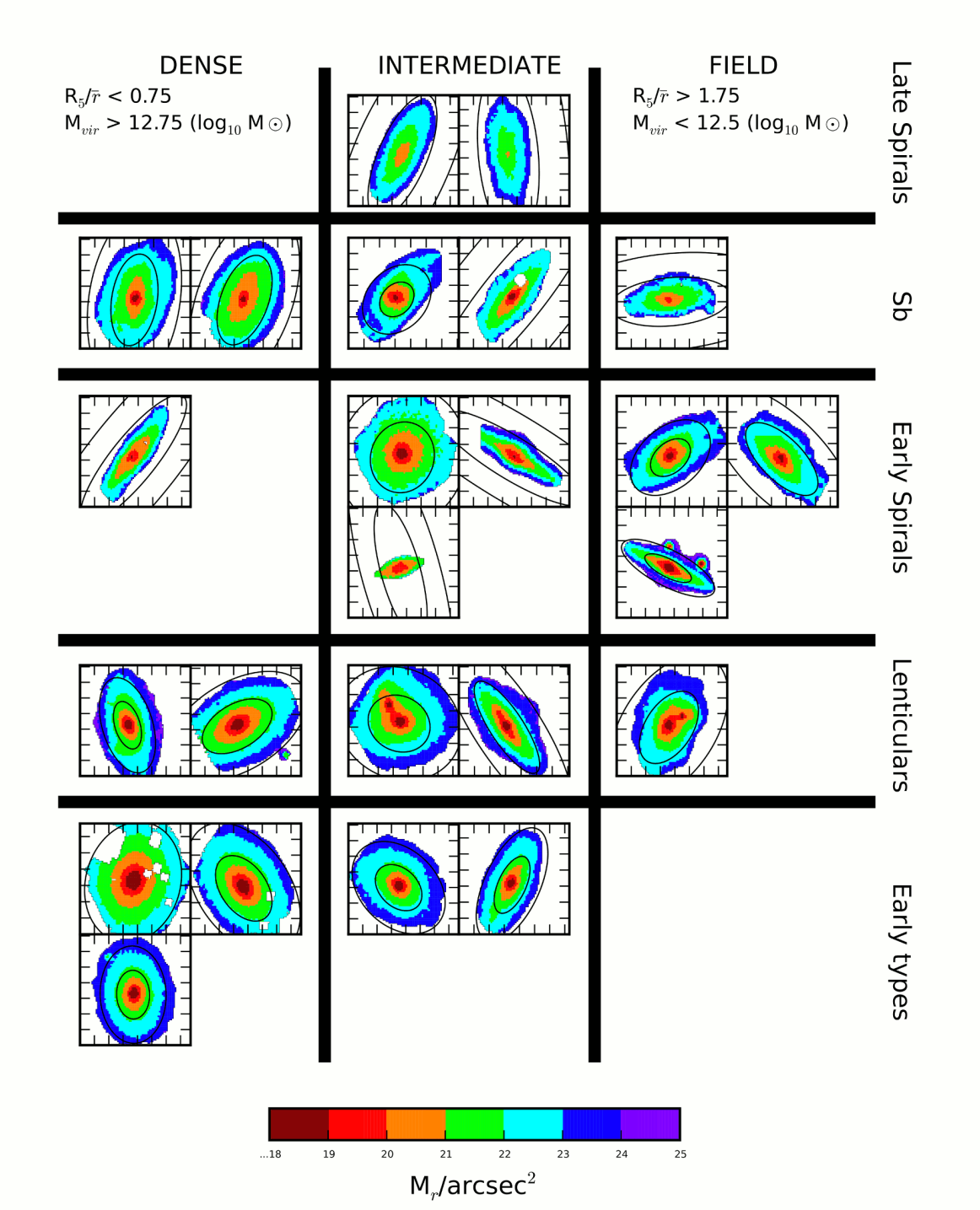

FIGURE 3.9: Surface brightness maps (SDSS r-band, synthesised from the CALIFA data) for all the analysed sample. Colour bins correspond to the colour-code of the contours in Figures 3.10, 3.11, and 3.12. Black ellipses indicate 1 and 2 effective radii, R_e.

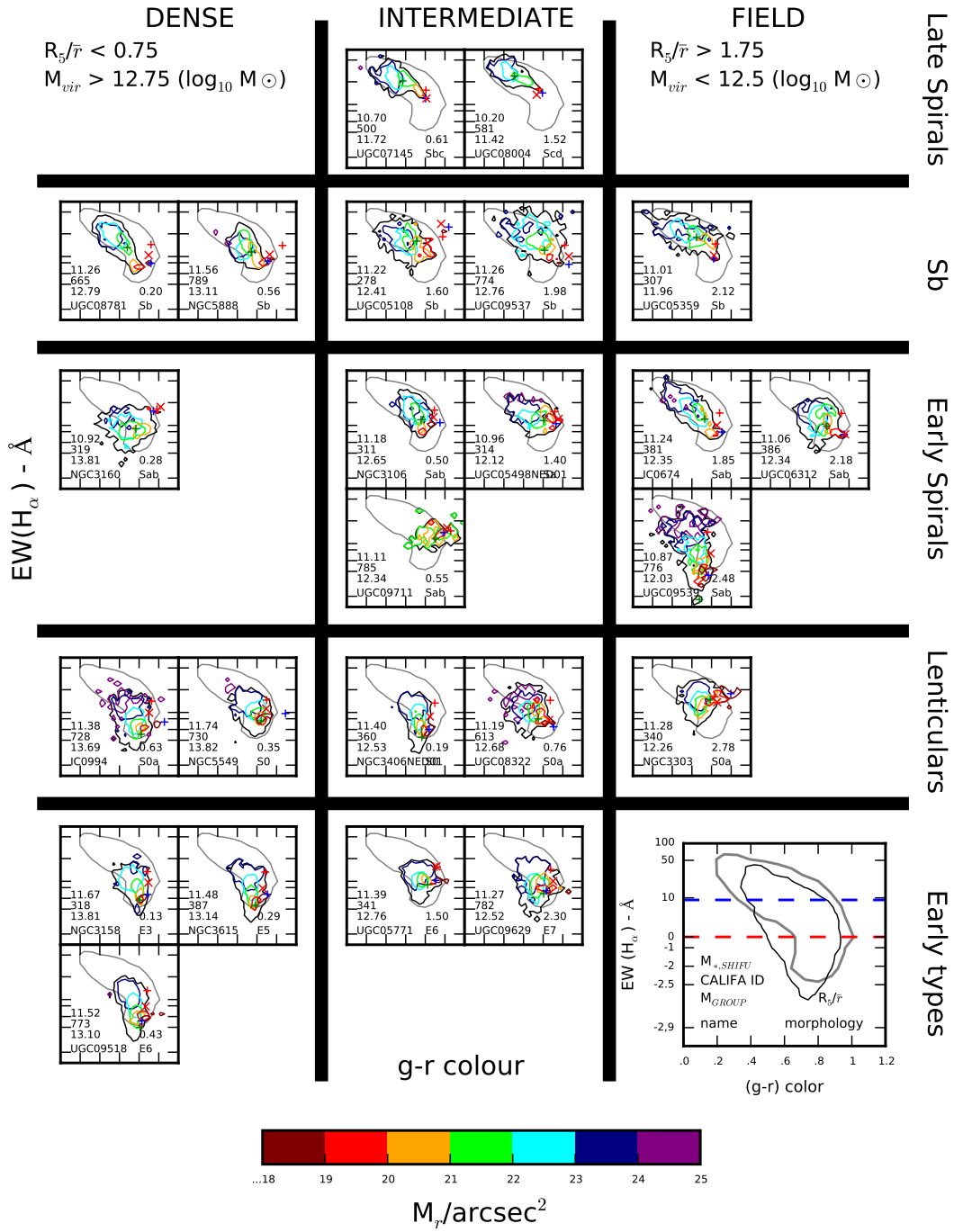

FIGURE 3.10: Colour-equivalent width diagram (Casado et al., 2015) on resolved scales, with individual galaxies arranged by morphology (rows) and environment (columns). Black contours enclose 90% of the spaxels in each galaxy, while coloured ones correspond to 60% of the spaxels within the surface brightness bins defined in Figure 3.9. The grey contour in every panel corresponds to 90% of the SDSS sample considered in (Casado et al., 2015), also plotted in the larger example panel at the bottom-right (the black contour in that panel showing the result for all the CALIFA galaxies together). In each individual panel, the red 'x', red plus sign, blue plus sign, and green plus sign represent the MPA-JHU SDSS measurement, our derived value for the SDSS spectrum, the nuclear spectrum, and the integrated spectrum, respectively (see text for details).

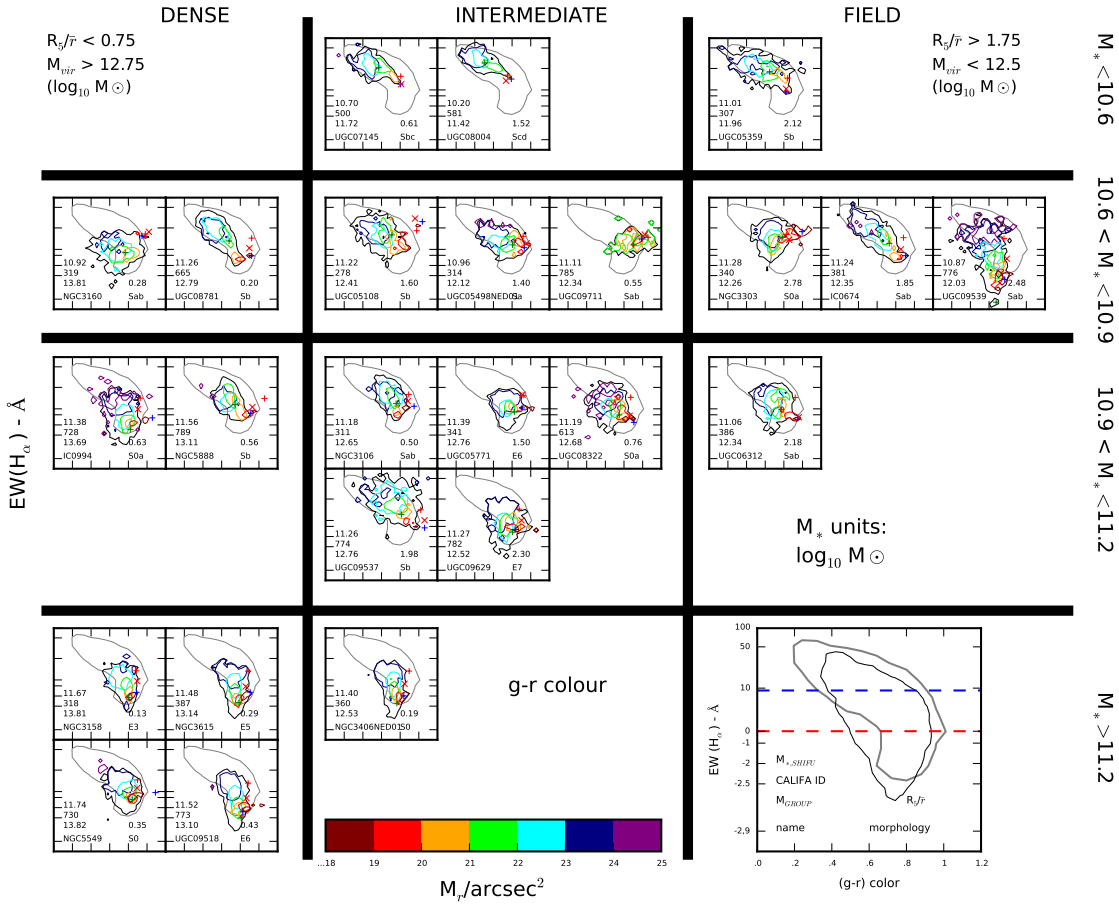

FIGURE 3.11: Plot identical to Figure 3.10, but arranged based on morphology and stellar mass.

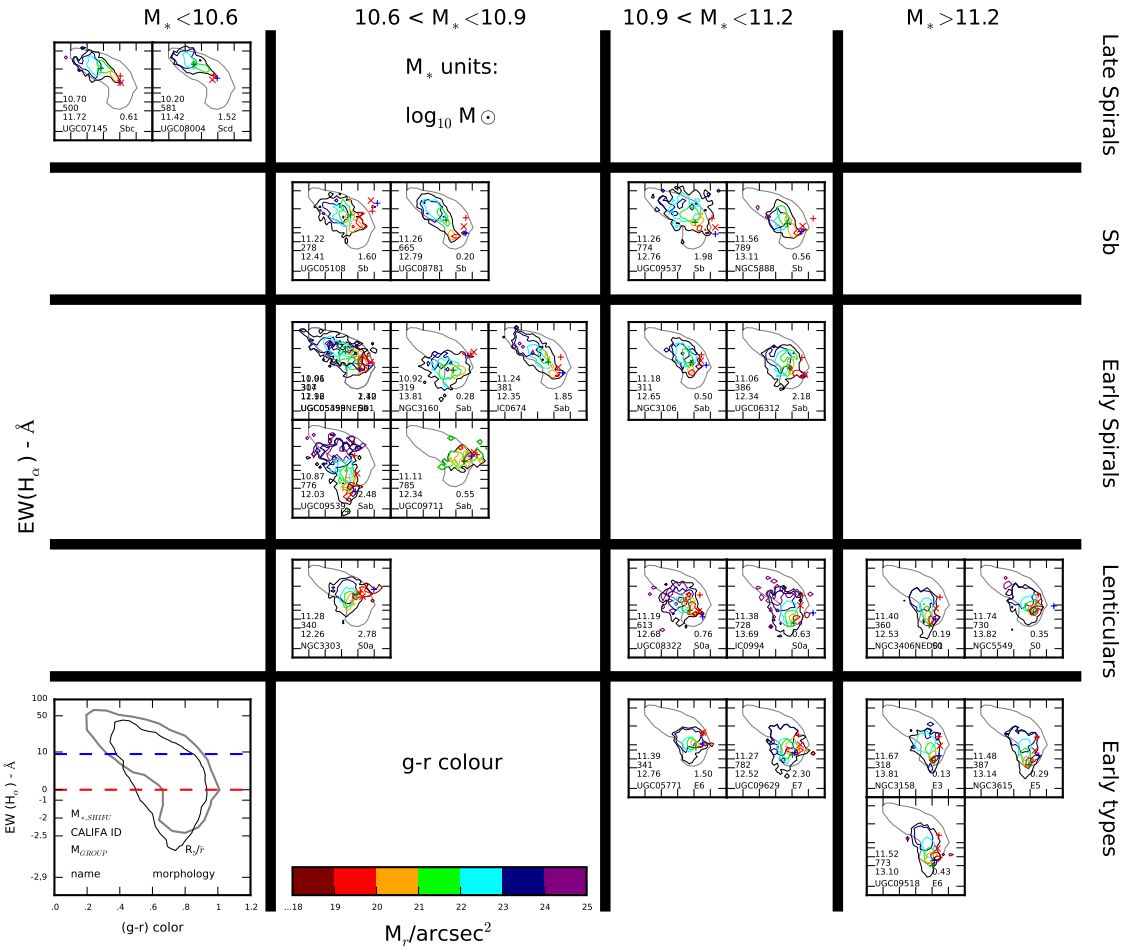

FIGURE 3.12: Plot identical to Figure 3.10, but arranged based on environment and stellar mass.

spectra by the MPA-JHU (red 'x') and STARLIGHT plus SHIFU (red plus sign) pipelines, the 'nuclear' values corresponding to brightest central spaxel at $\lambda = 5635$Å(blue plus sign) and the integrated value for the whole galaxy (green plus sign). The results show that SDSS measurements typically correspond to CALIFA nuclear values, usually located in the reddest extreme of the area covered by the object in the colour-EW diagram. Thus, they poorly represent the overall evolutionary state of the galaxy along the "ageing sequence". As an example, spiral objects from Scd to Sa morphologies display SDSS measurements that would qualify them as intermediate or passive galaxies, i.e. showing very little or no star formation. On the contrary, the present analysis of CALIFA IFS data shows that the vast majority of the regions in these objects are actually forming stars, showing much higher Hα equivalent widths and bluer colours, and therefore they should be classified as star-forming galaxies. As a matter of fact, *none* of the galaxies in the overlapping sample is completely quiescent, and all of them do display Hα emission in the outer parts.

Aperture effects are certainly a major concern. The black ellipses in Figure 3.9 show that almost every object in our sample is observed up to $\sim 2R_e$, which is one of the main advantages of the CALIFA survey. Forthcoming surveys such as MaNGA (Bundy et al., 2015) will offer a much larger sample (∼10.000 nearby galaxies) carefully selected to consistently cover stellar masses from $M_* \geq 10^9$ M$_\odot$ with roughly flat stellar mass distribution. However, their spatial coverage will still be limited, reaching only up to $\sim 1.5R_e$ for 67% of the targets (primary sample). Our study highlights the fact that the outskirts of galaxies can be very different from their inner counterparts, reinforcing the need of a wide spatial coverage in this kind of studies.

When we consider Figure 3.10 in combination with Figure 3.9, we can identify the trends observed in surface brightness as "radial" trends. The central parts of the objects (higher surface brightness) show redder colours and lower Hα equivalent widths (most of them in absorption). Whichever physical mechanism is driving the "ageing" of galaxies, it behaves in an inside-out fashion. This result is not new. However, CALIFA data show that the transition between the centre and the outer parts of galaxies is continuous in the colour-equivalent width diagram. Such radial trend is present for every galaxy in our sample (although it is most obvious among Sb, Sab, and Sa galaxies), and it supports the idea that "ageing" is a universal mechanism affecting all galaxies of all types over their entire extent. In particular, this process is not restricted to galaxies undergoing a transitional process from a "star-forming" to a "passive" state, but it is the normal mode of evolution throughout cosmic history. We do not find evidence for any sort of bimodality on resolved scales.

Although "ageing" seems to proceed faster in high stellar density regions, which arguably favour the accretion and consumption of gas, we do not find a universal relation between evolutionary state and local surface brightness. Quite the contrary, our results demonstrate that the resolved colour-equivalent width diagrams show a wide variety of distributions, even at fixed surface brightness. While the regions of the two late spirals (top row) are narrowly located along the "chemically-primitive" part of the sequence, objects classified as lenticulars (S0a and S0) and ellipticals predominantly gather near the "evolved" end, showing most of their Hα in absorption. The rest of the objects (Sb's, Sab's and Sa's) show a "mixed" distribution in the diagram (elongated across the colour-EW plane), compatible with some parts of them actively forming stars, some other with negligible star formation, and the vast majority showing mild activity (with $0 <$EW(Hα)< 10 Å) and intermediate colours. If the secular conversion of gas into stars (ageing) is the main driving mechanism of the evolution of a galaxy,it should not be surprising to find these continuous distributions in the colour-EW diagram, i.e. the existence of this population of "mixed" galaxies (which, in fact, dominate our sample, and are not unlike our very own Milky Way) must be fairly common in the universe.

3.4 Discussion

3.4.1 Local versus global properties

One question we try to assess by comparing Figure 3.10 with Figures 3.11 and 3.12 (they show exactly the same results, arranged in a different fashion) is the relative importance of local properties (surface brightness) with respect to global ones (morphology, environment and mass) in driving the observed distribution in the colour-equivalent width diagram.

We argued before that local processes, traced by the surface brightness, may play an important role in controlling the process of "ageing" in galaxies. The distributions in the colour-EW diagram are elongated, and they present radial trends consistent with the inside-out galaxy formation scenario. Nevertheless, when we consider the shape of the contours of these objects in the "ageing diagram", it seems that they correlate more strongly with morphology or environment (global properties) than they do with surface brightness. Figures 3.10, 3.11, and 3.12 suggest that galaxy morphology is probably the global property that is most strongly correlated with the location of the contours in the diagrams. Once the morphological type is set, it is not clear whether it is mass or environment that plays a major role. Objects with higher masses and/or living in denser environments show redder colours and lower EW(Hα). At the end, our three global properties are known to correlate with each other, and it is thus complicated to determine which one of them is driving the other. In any case, our results seem to support a scenario where global properties determine the evolution of the galaxy as a whole, whereas it is the local properties (in particular, mass density) that determine how such evolution takes place within the system.

Another possible "local" process that has been proposed to play a major role in driving galaxy evolution is the presence of an Active Galactic Nuclei (AGN). The vast amounts of energy that these physical processes generate, despite their small size and location, have been suggested as relevant feedback mechanisms and serious candidates for plausible quenching in galaxies. For this reason we have created resolved BPT diagnostic diagrams (Baldwin, Phillips, and Terlevich, 1981) for every one of our objects (see Figure 3.13) in order to study the possible AGN origin of the observed "ageing" trends. While there is no clear correlation, this figure suggest that there might be a trend concerning the location of the contours and the morphology of the object, supporting the results of the previous sections. We can see that the late spirals of the first row are the only objects whose regions are neatly located in the star-forming part of the BPT diagram (dashed line corresponds to Kewley et al., 2006, criteria). As we consider the other spirals in our sample (Sb's, Sab's and Sa's), we move to the LINER-like/AGN part of the diagram. Finally, lenticulars and ellipticals are almost entirely located in this part of the diagram, even considering that their measurements display a lot of scatter.

3.4.2 The variety in the "ageing" diagram

In the previous chapter we interpreted the existence of a narrow distribution in the colour-EW diagram (grey contours in Figures 3.10, 3.11, and 3.12) as a signature of a dominant, secular evolutionary mode in galaxies acting on timescales of the order of $\sim$Gyr. We also proposed that any change in the star formation taking place on shorter timescales ($\lesssim 300$ Myr), i.e. a rejuvenation or quenching episode, would lead to a steeper trend in the diagram, as it would modify the EW(Hα) much faster than it would alter the colour (see Figure 3.1).

We found little evidence of quenching in the SDSS sample, always associated to objects that display early and unknown morphologies located in dense environments. However, the results of the present work show that only the two objects classified as late spirals (Sbc and Scd, plotted in the first row) show trends fully compatible with long "ageing"

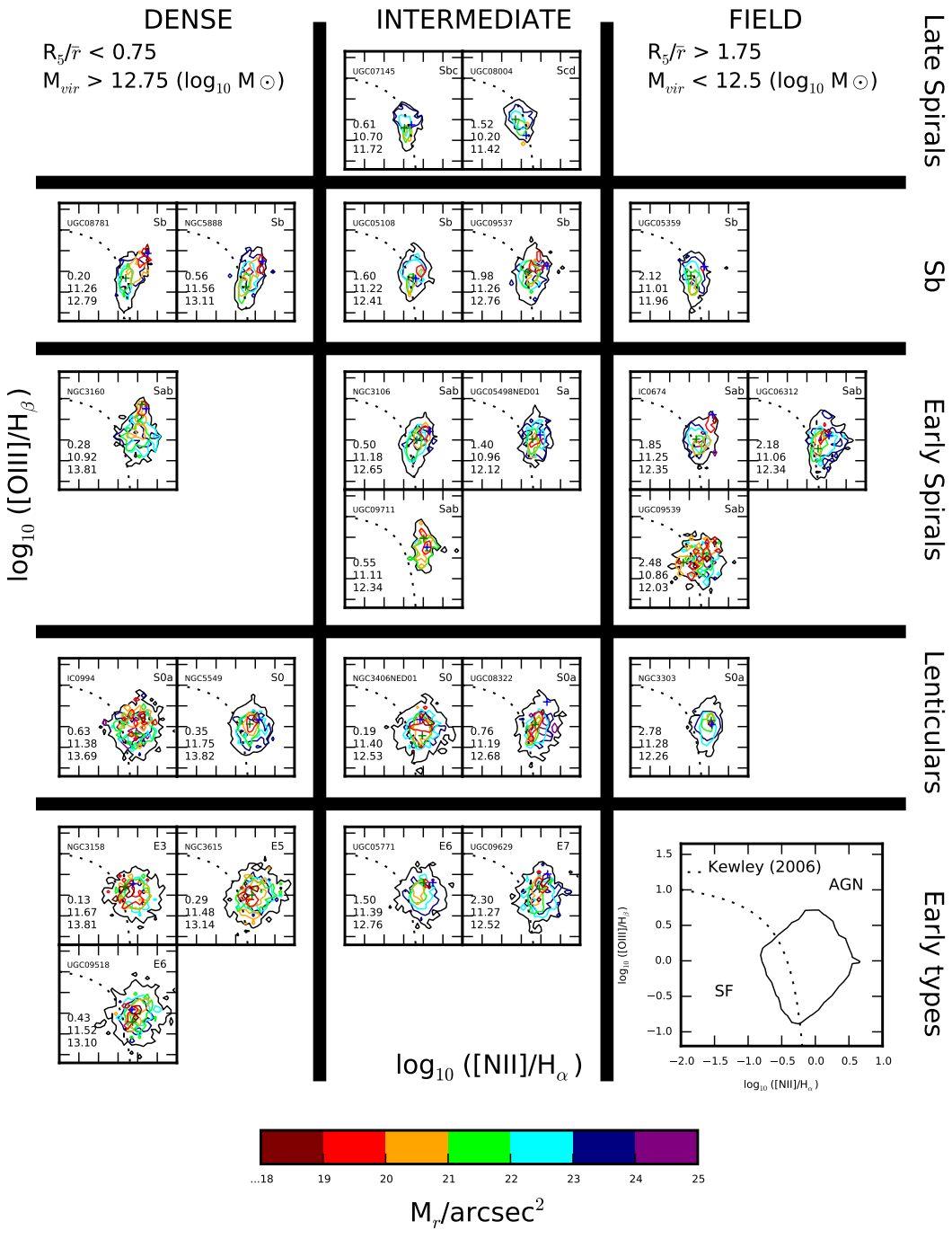

FIGURE 3.13: BPT diagram (Baldwin, Phillips, and Terlevich, 1981) of the analysed sample colour-coded following the bins in surface brightness of Figure 3.9. Contours follow the same colour criteria described in Figure 3.10.

timescales. The rest of the spiral population (Sb's, Sab's and Sa's) often depict steeper trends that would be compatible with faster evolution (not necessarily quenching, which would occur on an even shorter timescale), hinting that there may be different "ageing" tracks. The objects susceptible of undergoing a "rapid" ageing tend to show steeper trends in the green and orange contours (i.e. surface brightness between 20 and 22 mag/arcsec^2), and these show up in galaxies with late-type morphologies (Sb's), for which most of their regions are still forming stars. Objects with "earlier morphologies" (in particular, lenticulars: S0a's and S0's) seem to have finished such evolutionary phase, as the vast majority of their spaxels are located in the evolved end of the "ageing sequence".

Unfortunately, the sample considered is too small (and the scatter is too large) to derive any strong conclusion on the universality of the "ageing sequence". Nevertheless, it is clear that, once again, the physical process(es) that we are observing seem to be driven by (or at least depend on) local properties, while simultaneously there is an evident correlation with morphological type. All our results combined are compatible with the idea of strangulation and/or rapid gas exhaustion in some galaxies. If gas accretion is interrupted, or is less efficient, one would expect that galaxies "age" more rapidly as they consume their remaining gas. This would explain the observed steeper trends and the inside-out effect. Other mechanisms, such as ram-pressure stripping, would lead to a more significant decrement of the star formation activity in the outer part, which is completely inconsistent with our results, and can therefore be confidently ruled out. Whether galaxy morphology is driving the process or a consequence of it is also an important (but yet unsolved) question.

3.5 Summary and Conclusions

We now summarize the results of this work:

- The characterization of the SDSS sample conducted in Chapter 2 relative to the morphology, mass and environment, is consistent with other estimators in the literature used within the CALIFA collaboration (measurements of group properties, derivation of stellar masses, and visual morphological classifications obtained from Yang et al., 2007; Walcher et al., 2008; Walcher et al., 2014).

- Aperture effects are large and terrible misleading when considering the position of an object in the colour-equivalent width diagram. The original sample used Chapter 2, based on SDSS fibre measurements, is not only poorly representing galaxies in terms of coverage (this we knew) but is seriously biased. One can find examples in which more than 90% of the area covered by CALIFA observations ($\sim 2R_e$) populates the star forming region of the 'ageing' diagram, while the SDSS fibre points at the passive bulge located at the red end of the sequence.

- Galaxies 'age' on resolved scales and over their entire extent. Although surely affected by scatter, most of the spaxels considered for all objects fall within the 90% contour obtained for the SDSS sample. The low number statistics and the lack of completeness of our *overlapping* sample do not allow us to derive a new locus for a "resolved ageing sequence". Actually, we find marginal evidence that there may be different paths through the colour-equivalent width diagram, although it is difficult to demonstrate due to the large amount of scatter.

- The distribution of the entire population (spaxels) of each object in the colour-EW diagram depends mainly on its morphology, as well as (secondarily) on mass and environment. Spaxels/regions of isolated late-type objects populate the star-forming

part of the sequence, while early-types dominate the its evolved, red end. The "intermediate" objects (Sb's, Sab's and Sa's) show in some cases a steeper trend compatible with a faster evolutionary stage.

- Most trends observed in the resolved "ageing" diagram present a radial dependence (as interpreted from the surface brightness dependence). This result suggests that, whichever the physical mechanism responsible for driving the process of ageing, behaves in an inside-out fashion. In order to investigate the plausible AGN origin of such behaviour, we have explored the distributions of the different regions of our objects in the BPT diagram. Their location depends strongly on morphology, reinforcing the previous result. However, there is no clear evidence that favours the AGN origin of the radial trends.

This follow-up work reinforces the proposed "ageing" scenario proposed in Chapter 2, suggesting that it is a universal process (unavoidable) affecting objects of all morphological types and to their entire extent, from the bright bulges and star forming regions (typically targeted with the SDSS fibre) to the faint outskirts of galaxies.

Chapter 4

BaTMAn: Bayesian Technique for Multi-image Analiysis

This chapter is a based on the article:
"BaTMAn: Bayesian Technique for Multi-image Analiysis"
by J. Casado, Y. Ascasibar, R. García-Benito, G. Guidi, O. S. Choudhury,
E. Bellocchi, S.F. Sánchez and A.I. Díaz
sent for publication to MNRAS

4.1 Introduction

One of the basic problems in astronomical data analysis is the characterization of spatially-resolved information and the measurement of physical properties (and their variation) across extended sources. As illustrated in the previous chapters, a coherent and consistent treatment of our datasets is of paramount importance for this thesis work, as we make use of spatially-resolved data and specially focus on low signal-to-noise one.

A key result of the work presented in Chapter 2 is that we must avoid (or at least be very careful with) the imposition of any kind of signal-to-noise (hereafter S/N) threshold, as it may erase valuable information. Specially important is the case of the colour-equivalent width diagram depicted in Figure 2.7, where the imposition of a minimum S/N criteria will lead to the disappearance of the "ageing sequence". In the follow-up work covered in Chapter 3 we extend the analysis of the "ageing" process using Integral Field Spectroscopy data in order to circumvent the "aperture bias" affecting SDSS one (see Section 2.2.3). However, although we solve the aperture problem by considering a wider field-of-view, we include a new one that has to do with the characterization of low S/N data. SDSS fibres are known to point to the brightest areas in galaxies. These are usually located in the bulges or SF regions of these objects and generally depict high S/N values (the higher the intensity, the lower the relative S/N). As we extend our analysis to the outer and, in general, fainter regions of some of these systems (see Section CALIFA survey) we include low S/N data and potentially add severe noise to our study. A standard way to tackle this issue (to reduce the noise) is to bin our spatially resolved dataset into larger regions. This coaddition will increase the signal-to-noise. Unfortunately, it will simultaneously lead to an obvious loss in spatial resolution and, if done carelessly, a more than likely loss of the information available in the unbinned data. In conclusion, our work requires a specific tool that allows to properly study low S/N IFS data, characterize it and reduce, if possible, the noise of any derived analysis. However, in this chapter we aim to assess a much bigger question, which is:

How can we perform a careful tessellation of our dataset that does not lead to the loss of information?

The problem of source identification and characterization is certainly not new among astronomers. In fact, it was very early in the history of astronomy that this kind of tasks became increasingly demanding as new observations started to provide larger and larger amounts of data, prompting the need for a certain level of automation. Many current and forthcoming datasets are so vast that a significant part of the analysis is left entirely to computer programs.

One of the first instances of such application is the identification of (potentially extended and/or blended) sources in photometric images. Since the advent of large extragalactic surveys in the late 70's, a wide variety of techniques have been developed in order to automatically create source catalogues from astronomical images (e.g. Stetson, 1987; Bertin and Arnouts, 1996; Makovoz and Marleau, 2005; Savage and Oliver, 2007; Molinari et al., 2011; Hancock et al., 2012; Men'shchikov et al., 2012, among many others).

The emergence of Integral-Field Spectroscopy (IFS) has literally added a new dimension to the problem. Spatial and spectral information are now combined in order to locate the sources (see e.g. Koribalski, 2012, and references therein, in the context of radio observations of the 21-cm line), or even tackle specific scientific problems beyond source detection. In the past years, many algorithms have been designed to compute and characterize maps that trace the spatial distribution of a given physical quantity such as e.g. the temperature and composition of the hot intracluster medium (Sanders and Fabian, 2001; Diehl and Statler, 2006), the properties of the stellar population in early-type galaxies (Cappellari and Copin, 2003), the moments of the velocity distribution along the line of sight (Krajnović et al., 2006), or the emission of warm ionized gas and HII regions in galaxies (; Sánchez et al., 2012c; Sánchez et al., 2016b). Most of these tool perform a spatial segmentation of an image (or an IFS datacube) as first step of their analysis, as they usually require a minimum S/N in order to carry out meaningful measurements. The of binning schemes used to this purpose are mostly either based on a Voronoi tessellation (e.g. Sanders and Fabian, 2001; Cappellari and Copin, 2003; Diehl and Statler, 2006) or rely upon the identification of suitable intensity thresholds (e.g. Stetson, 1987; Bertin and Arnouts, 1996; Sánchez et al., 2012c). Surprisingly, none of them considers the plausible loss of information. Only the recent code developed by Sánchez et al. (2016b), also aiming to obtain a tessellation with a target S/N, imposes a 'continuity' requirement slightly equivalent to a morphological "signal-saving" criterium. We have already argued that carelessly averaging over too large area may (in some cases, strongly) bias the results and their physical interpretation if the signal within the chosen region is not homogeneous. Hence, none of the tools available in the literature (very few of them are actually accessible) suited our purposes.

For this reason, in this chapter we present an alternative binning approach that is not aimed to obtain a specific S/N but to identify spatial regions where the signal is statistically consistent with being constant within the provided errors: if two regions carry the same information, it will always be advantageous to merge them in order to (further) increase the signal-to-noise ratio; if they are 'different' (do not carry the same information), they should be kept separate in order not to introduce artificial biases. Such prescription preserves the information contained in the input dataset, and it imposes no condition on the shape of the tessellation. At the same time, it is extremely general, and it can be applied to any kind of spatially-resolved data.

In the following sections we will describe the mathematical basis of the method and the details of the algorithm and its implementation. We will also present and analyse the results of applying our tool to a set of benchmark problems. Finally, we will summarize our conclusions and present several scientific case applications includying, not only results for the "ageing sequence" analysis covered in Chapters 2 and 3 but some other plausible uses of our algorithm.

4.2 Mathematical formulation of the problem

BATMAN (Bayesian Technique for Multi-image Analysis) is a new binning scheme designed to perform an adaptive segmentation on a three-dimensional dataset that serves as inceptive step for its further analysis. We will refer to these sets as 'datacubes' or 'multi-images' along the chapter, as they consist of an arbitrary number (n_λ 'layers' or 'wavelengths') of spatially-arranged two-dimensional data (individual 'images' or 'maps'). We will focus on IFS data throughout this work, and we will use the term 'spaxel' to denote the individual and minimum spatial element of a dataset. However, the procedure can be applied to any set of images, or to any kind of spatially-distributed data. In particular, the algorithm can also be applied to a single image (i.e. single-'layer', 2D dataset) in what we will refer to as 'monochromatic' binning mode.

More precisely, BATMAN works on an *input dataset* $D = \{X, E\}$ consisting of two $n_{\rm row} \times n_{\rm col}$ multi-images X and E, with $N = n_{\rm row} \times n_{\rm col}$ spaxels each, whose spatial positions we will tag with the indices $\{i, j\}$. Every spaxel has a set of n_λ 'measurements' $x_{ij\lambda}$ and 'errors' $e_{ij\lambda}$

$$\begin{aligned} X &= \{x_{ij\lambda}\} \\ E &= \{e_{ij\lambda}\} \end{aligned} \tag{4.1}$$

associated to its spatial location, where $i = [1, n_{\rm row}]$, $j = [1, n_{\rm col}]$, and $\lambda = [1, n_\lambda]$. Different 'layers' may correspond to broad-band observations of the same object, different wavelengths in an IFS datacube, or even maps with completely different information (e.g. mass surface density, velocity, velocity dispersion, age, metallicity, equivalent width, etc).

The goal of the algorithm is to divide the input dataset into spatially-connected 'regions' that carry the same information, i.e. where all the measurements $x_{ij\lambda}$ are statistically compatible with being random samples of the same underlying signal $S_{ij\lambda}$ given the Gaussian errors $e_{ij\lambda}$. In the current implementation, BATMAN makes use of Bayesian statistics to connect adjacent spaxels into 'regions' (and merge adjacent regions into larger ones) as long as it is more likely that the true values of the measured quantities (the 'signal') are constant within the merged region ($S_{ij\lambda} = \theta_{r\lambda}\ \forall\{i, j\}$ in region r) than a collection of several independent domains with different values. More elaborate (e.g. quadratic) models of the underlying signal may be considered in future versions of the code.

Thus, the *output dataset* is an optimized 'segmentation model' $M = \{R, \Theta\}$ consisting of $n_{\rm reg}$ connected regions (with every spaxel $\{i, j\}$ assigned to the region r_{ij}) where the signal at the different bands is assumed to be well described by the constant values $\theta_{r\lambda}$:

$$\begin{aligned} R &= \{r_{ij}\} \\ \Theta &= \{\theta_{r\lambda}\} \end{aligned} \tag{4.2}$$

with $r = [1, n_{\rm reg}]$. R refers thus to the tessellation of the image, fully specified by a $n_{\rm row} \times n_{\rm col}$ matrix containing the labels r_{ij} assigned to every spaxel, and Θ corresponds to the set of $n_{\rm reg} \times n_\lambda$ parameters $\theta_{r\lambda}$ used to describe the signal.

According to the frequentist approach, the best segmentation model would be given by the values of R and Θ that maximise the *likelihood*, i.e. the probability of obtaining the measurements X, given the errors E and the $n_{\rm reg}$ regions specified by R and Θ. The model proposed for this work assumes that the observed values $x_{ij\lambda}$ are statistically-independent random variables, with Gaussian probability distributions whose dispersions are given by the errors $e_{ij\lambda}$ while their means $\theta_{r_{ij}\lambda}$ are to be determined. With these considerations, one

can express the likelihood as

$$p(X|E,R,\Theta) = \prod_{i=1}^{n_{\rm row}} \prod_{j=1}^{n_{\rm col}} \prod_{\lambda=1}^{n_\lambda} \frac{e^{-\frac{(x_{ij\lambda}-\theta_{r_{ij}\lambda})^2}{2e^2_{ij\lambda}}}}{\sqrt{2\pi e^2_{ij\lambda}}} = \prod_{r=1}^{n_{\rm reg}} \prod_{i,j\in r} \prod_{\lambda=1}^{n_\lambda} \frac{e^{-\frac{(x_{ij\lambda}-\theta_{r\lambda})^2}{2e^2_{ij\lambda}}}}{\sqrt{2\pi e^2_{ij\lambda}}} \tag{4.3}$$

where the second product in the last term simply loops over the spaxels in a given region.

Within the Bayesian framework BATMAN is based upon, the approach is slightly different, and it comprises several additional ingredients. One must declare not only a likelihood for the data given the model, but also a *prior* probability distribution $\pi(R,\Theta)$ of the model parameters. The construction of the prior π is based on our previous knowledge about the problem, and it will certainly affect the inferences we obtain from our data. As an example, it could favour certain tessellations (roundish bin shapes, such as in Cappellari and Copin, 2003; Sánchez et al., 2012c; Sánchez et al., 2016b) or avoid/penalize unphysical values (e.g. negative values of the signal).

The Bayesian approach combines the prior with the likelihood of observing the measurements X (making use of Bayes' theorem) to compute the *posterior* probability distribution of the model parameters

$$p(R,\Theta|D) = \frac{\pi(R,\Theta)\; p(X|E,R,\Theta)}{\mathcal{E}(M)} \tag{4.4}$$

The Bayesian *evidence* for our segmentation model M

$$\mathcal{E}(M) = p(X|E,M) = \sum_R \int \pi(R,\Theta)\; p(X|E,R,\Theta)\; {\rm d}\Theta \tag{4.5}$$

is the sum over all possible tessellations R and signal values Θ, and it can be considered as the overall probability of observing the measurements X, given the errors E, assuming that our model provides an accurate description of the data (in frequentist terms, the likelihood of model M). The expected values of the model parameters and their uncertainties can be computed from the posterior probability distribution (4.4).

In BATMAN, the problem of image segmentation is split in two parts:

1. the estimation of the signal distribution Θ given a fixed segmentation R
2. the further selection of the most probable tessellation

The exact procedures followed to solve the respective Bayesian parameter estimation and model selection problems are discussed in the following sections.

4.2.1 Parameter estimation

Given a fixed tessellation R, BATMAN will evaluate the posterior probability distribution $p(\Theta|R,D)$ describing the signal $\theta_{r\lambda}$ in every region r at every wavelength λ.

Following a Bayesian procedure, we first assume that the measurements X are described by the Gaussian likelihood function (see Eq. 4.3). Then, as we do not expect any specific distribution for the values of $\theta_{r\lambda} \in \Theta$, we have adopted a uniform (sometimes referred to as 'noninformative' or 'objective') prior. The uniform probability distribution

assigns equal probability to all values of the parameter, reflecting our initial ignorance. In order to obtain a *proper* prior, for which the total probability is normalized to unity (in contrast to an *improper* prior, where the integral diverges to infinity), the possible values of the signal $\theta_{r\lambda}$ are restricted to a finite range of values:

$$\begin{aligned} \pi_1(\theta_{r\lambda})\,\mathrm{d}\theta_{r\lambda} &= \frac{1}{H_\lambda - L_\lambda}\,\mathrm{d}\theta_{r\lambda} \\ L_\lambda < \theta_{r\lambda} &< H_\lambda \end{aligned} \tag{4.6}$$

where upper and lower limits H_λ and L_λ correspond to the highest and lowest values measured at that particular wavelength, anywhere within the image (i.e. the maximum and minimum $x_{ij\lambda}$ over i and j for a given λ).

From a practical point of view, this prescription automatically selects a reasonable range for the signal (irrespective of e.g. measurement units in the different layers of the multi-image), but, from a strict Bayesian perspective, one may object that we have actually looked at the data in order to set our prior. In order to generalise expression (4.6), we introduce n_λ additional parameters $0 < k_\lambda \leq 1$ such that

$$\begin{aligned} \pi(\Theta)\,\mathrm{d}\Theta &= \prod_{\lambda=1}^{n_\lambda}\prod_{r=1}^{n_{\mathrm{reg}}} \pi(\theta_{r\lambda})\,\mathrm{d}\theta_{r\lambda} \\ &= \prod_{\lambda=1}^{n_\lambda}\left(\frac{k_\lambda}{H_\lambda - L_\lambda}\right)^{n_{\mathrm{reg}}}\mathrm{d}\theta_{r\lambda} \\ L_\lambda - \Delta_\lambda < \theta_{r\lambda} &< H_\lambda + \Delta_\lambda \end{aligned} \tag{4.7}$$

where $\Delta_\lambda = \frac{1-k_\lambda}{2k_\lambda}(H_\lambda - L_\lambda)$. The choice $k_\lambda = 1$ results in equation (4.6), whereas $k_\lambda = 0$ would yield the improper prior $-\infty < \theta_{r\lambda} < \infty$. Thus, the value of k_λ provides a qualitative indication of the weight given to the information contained in H_λ and L_λ.

Using Bayes' theorem, the posterior probability distribution for the signal is given by

$$p(\Theta|R,D)\,\mathrm{d}\Theta = \frac{\pi(\Theta)\,p(X|E,R,\Theta)}{\mathcal{E}(R)}\,\mathrm{d}\Theta \tag{4.8}$$

where $p(X|E,R,\Theta)$ is the likelihood defined in equation (4.3), and the evidence for the tessellation R can be expressed as

$$\mathcal{E}(R) = p(X|E,R) = \int \pi(\Theta)\,p(X|E,R,\Theta)\,\mathrm{d}\Theta \tag{4.9}$$

Since we have adopted a uniform prior, and our model likelihood is a product of $n_{\mathrm{row}} \times n_{\mathrm{col}} \times n_\lambda$ Gaussians, it is easy to verify[1] that the posterior probabilities

$$P(\theta_{r\lambda}|R,D) \propto e^{-\frac{(\theta_{r\lambda}-\mu_{r\lambda})^2}{2\sigma_{r\lambda}^2}} \tag{4.10}$$

are independent Gaussians with mean

$$\mu_{r\lambda} = \sigma_{r\lambda}^2 \sum_{i,j\in r} \frac{x_{ij\lambda}}{e_{ij\lambda}^2} \tag{4.11}$$

[1] Using that $\sum_i \frac{(x-\mu_i)^2}{2\sigma_i^2} = \frac{(x-\mu)^2}{2\sigma^2} - \frac{\mu^2}{2\sigma^2} + \sum_i \frac{\mu_i^2}{2\sigma_i^2}$ with $\frac{1}{\sigma^2} \equiv \sum_i \frac{1}{\sigma_i^2}$ and $\mu \equiv \sigma^2 \sum_i \frac{\mu_i}{\sigma_i^2}$.

and dispersion

$$\frac{1}{\sigma_{r\lambda}^2} = \sum_{i,j\in r} \frac{1}{e_{ij\lambda}^2} \tag{4.12}$$

for any value of the prior parameters k_λ.

In other words, the expected value $\mu_{r\lambda}$ of the signal within any given region r reported by BATMAN (and the associated 'formal errors' $\sigma_{r\lambda}$) are obtained from an *inverse-variance weighted average* over the region.

Finally, the evidence for the tessellation R is given by

$$\begin{aligned}
\mathcal{E}(R) &= \int \prod_{r=1}^{n_{\rm reg}} \prod_{\lambda=1}^{n_\lambda} \pi(\theta_{r\lambda}) \prod_{i,j\in r} \frac{e^{-\frac{(x_{ij\lambda}-\theta_{r\lambda})^2}{2e_{ij\lambda}^2}}}{\sqrt{2\pi e_{ij\lambda}^2}} \,\mathrm{d}\theta_{r\lambda} \\
&= \prod_{r=1}^{n_{\rm reg}} \prod_{\lambda=1}^{n_\lambda} \frac{k_\lambda}{H_\lambda - L_\lambda} \frac{\int e^{-\sum_{ij\in r} \frac{(x_{ij\lambda}-\theta_{r\lambda})^2}{2e_{ij\lambda}^2}} \,\mathrm{d}\theta_{r\lambda}}{\prod_{ij\in r} \sqrt{2\pi e_{ij\lambda}^2}} \\
&\equiv \prod_{r=1}^{n_{\rm reg}} \mathcal{E}_r
\end{aligned} \tag{4.13}$$

with

$$\begin{aligned}
\mathcal{E}_r &\equiv \prod_{\lambda=1}^{n_\lambda} \frac{k_\lambda \int e^{-\frac{(\theta_{r\lambda}-\mu_{r\lambda})^2}{2\sigma_{r\lambda}^2} + \frac{\mu_{r\lambda}^2}{2\sigma_{r\lambda}^2} - \sum_{ij\in r} \frac{x_{ij\lambda}^2}{2e_{ij\lambda}^2}} \,\mathrm{d}\theta_{r\lambda}}{(H_\lambda - L_\lambda) \prod_{ij\in r} \sqrt{2\pi e_{ij\lambda}^2}} \\
&= \prod_{\lambda=1}^{n_\lambda} \frac{k_\lambda \, e^{\frac{\mu_{r\lambda}^2}{2\sigma_{r\lambda}^2} - \sum_{ij\in r} \frac{x_{ij\lambda}^2}{2e_{ij\lambda}^2}} \sqrt{2\pi\sigma_{r\lambda}^2}}{(H_\lambda - L_\lambda) \prod_{ij\in r} \sqrt{2\pi e_{ij\lambda}^2}}
\end{aligned} \tag{4.14}$$

4.2.2 Model selection

Once we obtain the evidence $\mathcal{E}(R)$ for any tessellation R and the posterior probability distribution of the recovered signal Θ associated to R, we face the question of selecting the 'optimal' segmentation that is most likely to describe our dataset. This is the second time we apply a Bayesian approach to our dataset, but two main differences exist with respect to the parameter estimation problem described in the previous section:

1. the set of all possible tessellations is discrete, whereas the values of the signal are continuous variables

2. we will require BATMAN to select one *and only one* 'optimal' tessellation rather than a probabilistic description (which is, as we will discuss later, not 'strictly Bayesian').

Except for these two differences, the Bayesian approach to model selection is very similar to parameter estimation: first, we must specify our priors $\pi(R)$ and then combine them with the appropriate likelihood $P(X|E,R)$ in order to obtain the posterior probability distribution $P(R|D)$ from Bayes' theorem.

We have no preliminary information relative to the preferred tessellations, and BATMAN will not impose any geometrical constraint (e.g. roundness) other than ensuring that all the regions defined by the matrix r_{ij} are physically connected. It is however foreseen

that some practical applications of the algorithm may have preference for a larger or smaller number of regions $n_{\rm reg}$, and therefore we have chosen a prior of the form

$$\pi(R) = k_{\rm R}^{n_{\rm reg}} \tag{4.15}$$

where $k_{\rm R}$ is to be defined by the user. The value $k_{\rm R} = 1$ corresponds to the improper uniform prior, that assigns equal probability to all valid segmentations regardless of the number of regions they contain; $k_{\rm R} < 1$ would favour that the multi-image is divided into a small number of (large) regions, whereas $k_{\rm R} > 1$ would favour that individual spaxels are kept independent or cluster into a large number of small regions.

The likelihood of a tessellation R (i.e. the probability of measuring X, considering all possible values of Θ) is simply the evidence $\mathcal{E}(R)$ defined in equation (4.9), and thus the posterior probability distribution of R is given by

$$P(R|D) = \frac{\pi(R)\,\mathcal{E}(R)}{\mathcal{E}(M)} \tag{4.16}$$

where $\mathcal{E}(M)$ denotes the overall evidence for our complete segmentation model set M. Due to the discrete nature of R,

$$\mathcal{E}(M) = \sum_R \pi(R)\,\mathcal{E}(R) \tag{4.17}$$

where the R runs over all possible tessellations.

The current version of BATMAN outputs the matrix r_{ij} (labels corresponding to the tessellation) that maximises the posterior probability $P(R|D)$, along with the corresponding values of $\mu_{r\lambda}$ and $\sigma_{r\lambda}$. Let us argue at this point that, to some extent, the very concept of 'model selection' is intrinsically not Bayesian. If, for example, $P(R_+|D) = 0.5 + \delta$ and $P(R_-|D) = 0.5 - \delta$, one can only choose R_+, no matter how small δ may be, if forced to take a decision. We do think that a strictly Bayesian algorithm would never select a unique segmentation, but calculate the posterior probability of all possible tessellations and weight them in order to provide a fully probabilistic description of the underlying signal, spaxel by spaxel. However, such approach would yield a 'smoothing' technique rather than a 'segmentation' tool, and it will not be discussed further in the present work.

4.3 Numerical implementation

BATMAN is based on the philosophy that the purpose of a segmentation algorithm is to group together the 'spaxels' of a 'multi-image' that carry the same information (measurements $x_{ij\lambda}$ compatible with identical signal $S_{ij\lambda}$ within the errors $e_{ij\lambda}$) into larger 'regions'. According to the arguments presented in Section 4.2, this goal can be mathematically formulated as the maximisation of the Bayesian posterior probability of the tessellation R, fully described by the $n_{\rm row} \times n_{\rm col}$ matrix r_{ij} specifying the label of the region that each spaxel (i, j) belongs to. Once R is fixed, we have shown that the posterior probability distribution of the 'signal' $\theta_{r\lambda}$ within each region r at 'wavelength' (or 'layer') λ is Gaussian, with mean $\mu_{r\lambda}$ and standard deviation $\sigma_{r\lambda}$ given by an inverse-variance weighted average over the region, i.e. equations (4.11) and (4.12), respectively.

In practice, the number of possible tessellations is so large that evaluating all their evidences is completely infeasible. Therefore, BATMAN follows a greedy iterative procedure, merging adjacent regions until no further increase in the posterior probability $P(R|D)$ is possible:

1. A unique label $l_{ij} = [1, N]$ is assigned to each spaxel. The initial segmentation R_N considers that every spaxel is an independent region, i.e. $n_{\rm reg} = N$, $r_{ij} = l_{ij}$, $\mu_{r\lambda} = x_{ij\lambda}$, and $\sigma_{r\lambda} = e_{ij\lambda}$. From now on, we will drop the subscript and denote the number of regions simply as n.

2. On every iteration, starting from $n = N$, BATMAN compares the posterior probability of R_n with all possible candidate tessellations $R_{c,n-1}$ that can be obtained by merging any two adjacent[2] regions in R_n. More precisely, it evaluates the ratios $\frac{P(R_{c,n-1}|D)}{P(R_n|D)}$ for all these candidate tessellations with $n-1$ regions each.

3. The algorithm selects the optimal tessellation for the next iteration, R_{n-1}, as the candidate displaying the highest probability (i.e. the largest ratio with respect to R_n). If none of the $R_{c,n-1}$ is found to be more likely than R_n, no further iterations will be performed.

4. On exit, BATMAN outputs the matrices containing the labels r_{ij} of the different regions, the mean posterior signal maps $\mu_{r\lambda}$, and and their standard deviation $\sigma_{r\lambda}$ for the final 'optimized' tessellation R_n.

A critical part of the algorithm is thus the evaluation of the probability ratios

$$\begin{aligned}\frac{P(R_{c,n-1}|D)}{P(R_n|D)} &= \frac{\pi(R_{c,n-1})\,\mathcal{E}(R_{c,n-1})}{\pi(R_n)\,\mathcal{E}(R_n)} \\ &= \frac{\pi(R_{c,n-1})\,\prod_{r'\in R_{c,n-1}}\mathcal{E}_{r'}}{\pi(R_n)\,\prod_{r\in R_n}\mathcal{E}_r}\end{aligned} \tag{4.18}$$

where r and r' refer to the regions defined in R_n and $R_{c,n-1}$, respectively. Due to our iterative procedure, these two models only differ in that two regions of R_n (let us name them A and B) that have been merged into a single region $A \cup B$ in $R_{c,n-1}$. Substituting expression (4.14) for the contribution of each region to the evidence and equation (4.15) for the prior probability of each tessellation, one arrives to

$$\begin{aligned}\frac{P(R_{c,n-1}|D)}{P(R_n|D)} &= \frac{k_{\rm R}^{n-1}}{k_{\rm R}^{n}}\frac{\mathcal{E}_{A\cup B}}{\mathcal{E}_A\,\mathcal{E}_B} \\ &= k_{\rm R}^{-1}\prod_{\lambda=1}^{n_\lambda}\frac{(H_\lambda - L_\lambda)\,\sigma_{A\cup B,\lambda}\,e^{\frac{\mu^2_{A\cup B,\lambda}}{2\sigma^2_{A\cup B,\lambda}}}}{k_\lambda\sqrt{2\pi}\,\sigma_{A\lambda}\,\sigma_{B\lambda}\,e^{\frac{\mu^2_{A\lambda}}{2\sigma^2_{A\lambda}}+\frac{\mu^2_{B\lambda}}{2\sigma^2_{B\lambda}}}} \\ &\equiv K^{-1}\prod_{\lambda=1}^{n_\lambda}(H_\lambda - L_\lambda)\frac{e^{-\frac{(\mu_{A\lambda}-\mu_{B\lambda})^2}{2(\sigma^2_{A\lambda}+\sigma^2_{B\lambda})}}}{\sqrt{2\pi(\sigma^2_{A\lambda}+\sigma^2_{B\lambda})}}\end{aligned} \tag{4.19}$$

where the prior parameters $k_{\rm R}$ and k_λ can be neatly separated from the term comparing the measurements in regions A and B in terms of their dispersions. In fact, it is evident from expression (4.19) that the combined effect of $k_{\rm R}$ and k_λ can be grouped into a single number

$$K \equiv k_{\rm R}\prod_{\lambda=1}^{n_\lambda}k_\lambda \tag{4.20}$$

that encapsulates all our choices about the prior probability distributions for r_{ij} and $\theta_{r\lambda}$. Since all other quantities (including H_λ and L_λ, which denote the maximum and minimum

[2] We consider contiguous spaxels in the horizontal or vertical directions, but not along the diagonals.

values of $x_{ij\lambda}$, respectively) are driven by the data, K is the only free parameter of our algorithm.

4.4 Test cases

In order to illustrate the capabilities of the algorithm, assess its performance, and provide general guidelines to understand its operation, we have considered a set of four different input datasets as benchmark problems. Two of them are based on a synthetic multi-image (Section 4.4.1) that poses several potentially challenging situations (e.g. different shapes, with and without sharp boundaries, different noise statistics and signal-to-noise ratios, overlap between independent structures, etc.), and the other two are based on integral-field spectroscopic observations of the local galaxy NGC 2906 (Section 4.4.2).

These four datasets consist of several 'layers' or 'wavelentghs' (i.e. they are all 'multi-images' according to our terminology). For every one of them we have run BATMAN in two different ways: one considering all the layers simultaneously and obtaining a single common tessellation (we will refer to this approach as 'multi-λ') and another in which we consider every 'layer' individually and obtain an independent segmentation for every one them ('monochromatic' approach). This yields a total of eight test cases, as summarized in Table 4.2.

For all of them, we carry out two independent runs adopting $K = 1$ and $K = 10^{-6}$. The former (obtained e.g. by setting both $k_{\rm R}$ and every k_λ to unity) corresponds to a binning criterion that tends to keep small regions separated; reducing the value of K (e.g. by decreasing either $k_{\rm R}$ and/or the product of the different k_λ) favours the coaddition of spaxels and leads to the definition of larger regions.

4.4.1 Synthetic data

Our synthetic multi-images consist of 3 layers (arbitrarily labelled R, G, and B) that display different objects over a null background where the signal value is set to $S_0 = (0, 0, 0)$. The R layer shows a quarter of a circle in the bottom-left corner with signal $S_{\rm circle} = (1, 0, 0)$, the G layer displays a triangle with $S_{\rm triangle} = (0, 7, 0)$ located the centre of the image, slightly overlapping with the circle, and the B image shows an ellipse centred in the top-right corner (again, slightly overlapping with the triangle) that displays a continuous, radially-decreasing gradient $S_{\rm ellipse} = (0, 0, [17 - 1])$.

This three-layer datacube

$$S = (S_{\rm R}, S_{\rm G}, S_{\rm B}) = S_0 + S_{\rm circle} + S_{\rm triangle} + S_{\rm ellipse} \tag{4.21}$$

represents the *signal* of our synthetic problem. From these data, we generate two different *input* multi-images

$$x_{ij\lambda} = S_{ij\lambda} + n_{ij\lambda} \tag{4.22}$$

by adding random Gaussian noise n with different statistics. The 'uniform-noise' datacube follows a Gaussian probability distribution with zero mean and dispersion $e_{\rm uniform} = (1, 1, 1)$ for all layers of every spaxel. We also generate a 'CCD-like' datacube (mimicking the characteristics of charge-coupled devices) as a result of adding a white-noise component with dispersion $\sigma^2_{\rm W} = (0.5, 0.5, 0.5)$ and a Poisson noise component where the dispersion $\sigma^2_{\rm P}$ grows linearly with the signal $S_{ij\lambda}$ at any given band and location, according to the expression

$$e^2_{{\rm ccd}:ij\lambda} = \sigma^2_{\rm W} + \sigma^2_{{\rm P}:ij\lambda} = \frac{1 + S_{ij\lambda}}{2} \tag{4.23}$$

	S	$e_{\rm ccd}$	$(S/N)_{\rm ccd}$
Background	0	0.5	0
R: Circle	1	1	1
G: Triangle	7	2	3.5
B: Ellipse	$[1-17]$	$[1-3]$	$[1-5.67]$

TABLE 4.1: Values of the signal S of each individual component of the synthetic test multi-image (4.21) in the relevant layer (R,G, or B), followed by the corresponding 'CCD-like' noise $e_{\rm ccd}$ given by expression (4.23) and the signal-to-noise ratio $(S/N)_{\rm ccd} = S/e_{\rm ccd}$. For the 'uniform-noise' datacube, $e_{\rm uniform} = (1,1,1)$ implies $(S/N)_{\rm uniform} = S/e_{\rm uniform} = S$.

The numeric values of the intensities and noise levels in our synthetic test problems have been chosen so that the signal-to-noise ratio

$$(S/N)_{ij\lambda} = S_{ij\lambda}/e_{ij\lambda} \tag{4.24}$$

covers a range from one to 17 in the 'uniform' case and up to approximately 6 for the 'CCD-like' noise. The precise values for the errors and signal-to-noise ratios within each region are summarized in Table 4.1.

4.4.2 Astronomical observations

In order to illustrate the use of the algorithm in a typical science case, we consider two different segmentation problems related to the measurement of the intensity of the Balmer emission lines in the local spiral galaxy NGC 2906. Observations have been retrieved from the public database of the Calar Alto Legacy Intergral-Field spectroscopic Area (CALIFA) survey (Sánchez et al., 2012a). More precisely, they correspond to the COMBO datacubes delivered in Data Release 2 (see García-Benito et al., 2015a, for a detailed description), with a uniform wavelength coverage from 3650 to 7200 Å, sampled in constant steps of 2 Å.

We will consider two completely different approaches to address the problem. In the first one, we measure the intensity of the Hα(6563Å), Hβ(4861Å), Hγ(4340Å), and Hδ(4101Å) emission lines spaxel by spaxel, and then take the resulting intensity maps, with their corresponding errors, as a four-layer input multi-image (i.e. first measure and then bin with BATMAN). As an alternative approach, we run BATMAN directly on the raw IFS data, selecting four wavelength intervals of ± 15 Å around each line (see Table 4.2), and then measure their intensity from the integrated spectrum within each region (i.e. first bin the datacube directly with BATMAN and then measure).

In both cases, we follow exactly the same procedure to measure the intensity of the Balmer lines in a given spectrum. In order to account for stellar absorption lines, we use STARLIGHT (Cid Fernandes et al., 2005) to model the spectral energy distribution of the underlying stellar population, fitting the observed spectrum with a linear combination of simple stellar populations spanning different ages and metallicities. We use the the spectra provided by Vazdekis et al. (2010) for populations older that 64 Myr and González Delgado et al. (2005) models for younger ages. Dust effects are modelled as a foreground screen, assuming a Cardelli, Clayton, and Mathis (1989) reddening law with $R_V = 3.1$. Then, we subtract the estimated stellar continuum from the observed spectrum and obtain the line flux with the SHerpa IFU line fitting software (SHIFU; García-Benito, in preparation), based on CIAO's SHERPA package (Freeman, Doe, and Siemiginowska, 2001; Doe et al., 2007). Small deviations with respect to the stellar continuum are taken into account by a first order polynomial, and independent Gaussians have been fitted for the emission lines.

	TEST CASE	INPUT: ($n_{\rm row} \times n_{\rm col} \times n_{\lambda}$)	$n_{\rm output}$	FIGURES	PANELS
#1	synthetic + uniform noise 'monochromatic'	R: ($73 \times 78 \times 1$) G: ($73 \times 78 \times 1$) B: ($73 \times 78 \times 1$)	3	1, 3, 4	top-right
#2	synthetic + uniform noise 'multi-λ'	($73 \times 78 \times 3$)	1	1, 3, 4	top-middle
#3	synthetic + ccd-like noise 'monochromatic'	R: ($73 \times 78 \times 1$) G: ($73 \times 78 \times 1$) B: ($73 \times 78 \times 1$)	3	1, 3, 4	bottom-right
#4	synthetic + ccd-like noise 'multi-λ'	($73 \times 78 \times 3$)	1	1, 3, 4	bottom-middle
#5	NGC 2906: SHIFU maps 'monochromatic'	Hα: ($71 \times 78 \times 1$) Hβ: ($71 \times 78 \times 1$) Hγ: ($71 \times 78 \times 1$) Hδ: ($71 \times 78 \times 1$)	4	2, 5	top-right
#6	NGC 2906: SHIFU maps 'multi-λ'	($71 \times 78 \times 4$)	1	2, 5	top-middle
#7	NGC 2906: CALIFA data '$\Delta\lambda = \pm 15$Å'	Hα: ($71 \times 78 \times 14$) Hβ: ($71 \times 78 \times 15$) Hγ: ($71 \times 78 \times 15$) Hδ: ($71 \times 78 \times 15$)	4	2, 5	bottom-right
#8	NGC 2906: CALIFA data 'full set'	($71 \times 78 \times 59$)	1	2, 5	bottom-middle

TABLE 4.2: Summary of the test cases presented in Section 4.4 and discussed in Section 4.5. The labelling and nomenclature used to refer each case are quoted on the first two columns, respectively. The dimensionality of the input data is listed on the third column, whereas the fourth column provides the number of output tessellations (i.e. the number of times BATMAN is run), and the last two columns indicate the location of the corresponding results in the chapter figures. Every test case has been run with two different values for the prior parameter, $K = 1$ and $K = 10^{-6}$.

The intensity distribution of the Balmer emission lines in NGC 2906 is fairly clumpy (see Figure 4.2), with a relatively large number of individual compact HII regions arranged in a ring-like structure. This configuration is clearly visible in the Hα maps, where the signal is stronger, but it is much more difficult to identify in the weakest lines, especially Hδ. In addition, there is a weak diffuse component of much lower surface brightness, arising from a combination of intrinsic emission from diffuse ionized gas (Haffner et al., 2009) and light from the compact HII regions that is scattered towards the observer by dust particles in the interstellar medium (see e.g. Ascasibar et al., 2016).

Although the actual solution is obviously not available in this case, all our emission lines arise from the same element, and therefore they should all roughly trace the same spatial distribution (mostly determined by the electron number density, with a secondary dependence on the local electron temperature). However, the intensity of the lines decreases with frequency, and therefore they probe very different signal-to-noise ratios, from values of the order unity, especially in the outer parts, to well above one hundred in the regions of brightest Hα emission.

4.4.3 Analysis procedure

As mentioned above, we have approached our four input datasets (both synthetic and astronomical) in two different ways. On the one hand, we make use of the default binning mode ('multi-λ') where all the information is considered at the same time (all 'layers' binned simultaneously) and one optimal tessellation is computed for the whole dataset. On the other hand, an alternative 'monochromatic' procedure is also considered, where BATMAN is run individually on every layer of the multi-image dataset (hence, several times) and an independent tessellation is derived for every one of them. A summary of all the resulting test cases is provided in Table 4.2. Every test has been repeated twice, adopting the values $K = 1$ and $K = 10^{-6}$ for the combined prior parameter.

In the synthetic multi-images, BATMAN has been applied to the three layers (R, G, and B) separately ('monochromatic', cases #1 and #3) and simultaneously ('multi-λ', cases #2 and #4). The two test cases based on SHIFU measurements of NGC 2906 (cases #5 and #6) follow an approach completely analogous to the synthetic multi-images. The only difference is that now the data consist of four different (but physically not independent) 'layers', one for each Balmer line. In case #5, BATMAN is run in 'monochromatic' mode, producing 4 different segmentations, while in case #6 it is run only once, yielding a single 'multi-λ' tessellation. For the remaining observational test cases, #7 and #8, we have applied BATMAN directly on the IFS data from the CALIFA survey (spectra and error). We have run our algorithm separately on every 30 Å-wide slice around each line, thus obtaining 4 independent tessellations (test case #7), as well as to the full 59-layer multi-image (the four 30 Å-wide slices together, case #8), where a single tessellation is returned. Although these tests are scientifically identical to test cases #5 and #6 (4 balmer lines binned separately and simultaneously), they are technically different: BATMAN is applied in 'multi-image' mode every time, many more 'wavelengths' are being considered, and there is no pre-processing of the data (lines are measured with SHIFU after the binning).

As a final remark, let us note that there is another important difference between test cases #7 and #8 (direct application of the algorithm on the IFS datacube) and the rest. In test cases $\#1 - 6$, the input data are maps of the measured quantities. BATMAN provides not only an optimal tessellation, but also the expected value $\mu_{r\lambda}$ and the dispersion $\sigma_{r\lambda}$ of the signal within every region, based on the posterior probability distribution. On the contrary, test cases #7 and #8 bin directly a cutted portion of the spectral energy distributions. Although BATMAN returns again the three products (r_{ij}, $\mu_{r\lambda}$ and $\sigma_{r\lambda}$) only the tessellation

is further used by SHIFU in order to derive the flux of each line and the corresponding error, taking into account noise covariance in CALIFA data (see e.g. Husemann et al., 2013; García-Benito et al., 2015a) as part of its pipeline. Therefore, the estimated errors may be considerably larger (by about a factor of 3, depending on the number of spaxels within each region) than those implied by equation (4.12).

4.5 Results

Based on the test cases described in the previous section, we now address the quality of the output tessellation in terms of its ability to adapt to the underlying signal, the dependence of the results on the adopted priors, the accuracy of the formal errors estimated by the algorithm, and the improvement with respect to the original input data.

4.5.1 Large-scale morphology

Figures 4.1 and 4.2 show the results of applying BATMAN to our synthetic and astrophysical test cases, respectively, adopting the extreme values $K = 1$ and $K = 10^{-6}$ for the prior parameter, and considering both the full input data set as well as individual layers in order to compute the Bayesian evidence (see Table 4.2). From visual inspection, one can readily verify that, in almost all cases, the tessellations returned by the algorithm adapt extremely well to the structures that were present in the input data.

In the synthetic datacubes (Figure 4.1), BATMAN successfully recovers the different objects regardless of their topology. The output tessellations present a variety of sizes and shapes that are driven by the input signal, and they show no preference for any given direction. Comparing the results obtained for the 'uniform' and 'CCD-like' noise schemes, we conclude that the ability of the algorithm to trace the underlying structure is not very sensitive to the statistical characteristics of the noise. The minor differences that exist in the recovered tessellations can be explained in terms of the dissimilar signal-to-noise ratios.

When applied to the real data (Figure 4.2), our algorithm manages to identify most of the clumps associated with physical HII regions, albeit with significant difficulty in the case of Hδ. In particular, among the Hδ recovered maps, the poorest results are obtained for case #5, where only the Hδ intensity and its error map, as computed by SHIFU, are used as input dataset. Interestingly, the situation improves when BATMAN is run directly on the CALIFA COMBO dataset. Even when only a narrow spectral region, '$\Delta = \pm 15$ Å', around Hδ is provided as input (case #7), the ring-like structure where most of the emission comes from is prominently visible in the recovered signal.

By construction, BATMAN gathers together spaxels that contain the same information (compatible signal within the errors). Hence, it is reassuring, but not surprising, that it successfully recovers the circle and the triangle in the R and G layers of the synthetic multi-images, as these regions do indeed feature exactly the same signal value. However, this is not the case for the gradient in the B-band ellipse or the observations of NGC 2906, where the signal varies more or less smoothly across any layer. Our segmentation model, described in Section 4.2, does not consider the presence of gradients inside the regions. Therefore we expect the optimal tessellation to trace the isocontours perpendicular to the direction of any gradient that may exist in the signal. The size of the regions will be determined by the intensity of the gradient and the signal-to-noise ratio. Roughly speaking, the size of the isocontours should be of the order of the typical uncertainties $e_{ij\lambda}$ within the region, so that the algorithm can tell that the signal is indeed different from the values in the immediate vicinity.

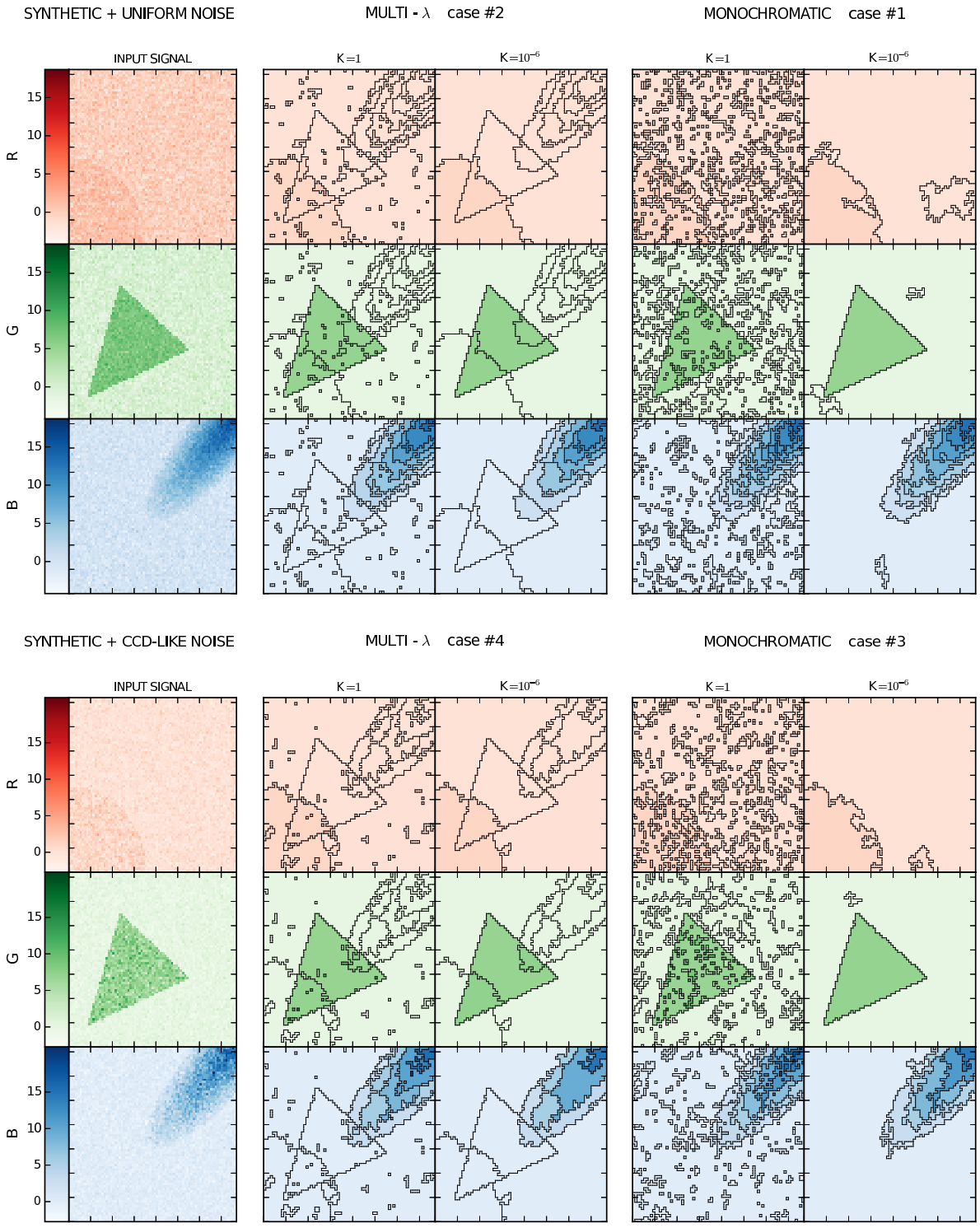

FIGURE 4.1: Results of applying BATMAN to our synthetic test cases in 'multi-λ' mode (i.e. considering all the layers in the input data simultaneously; test cases #2 and #4, central columns) and 'monochromatic' mode (considering each layer separately, cases #1 and #3, right columns). Two runs are performed in every case, with $K = 1$ (left) and $K = 10^{-6}$ (right). The input signal is displayed in the left column. Rows within each panel correspond to the different layers in the multi-image. The segmentation obtained in every case is indicated with solid black lines and is common to the three layers in the 'multi-λ' test cases #2 and #4 and specific to every one in the 'monochromatic' test cases #1 and #3.

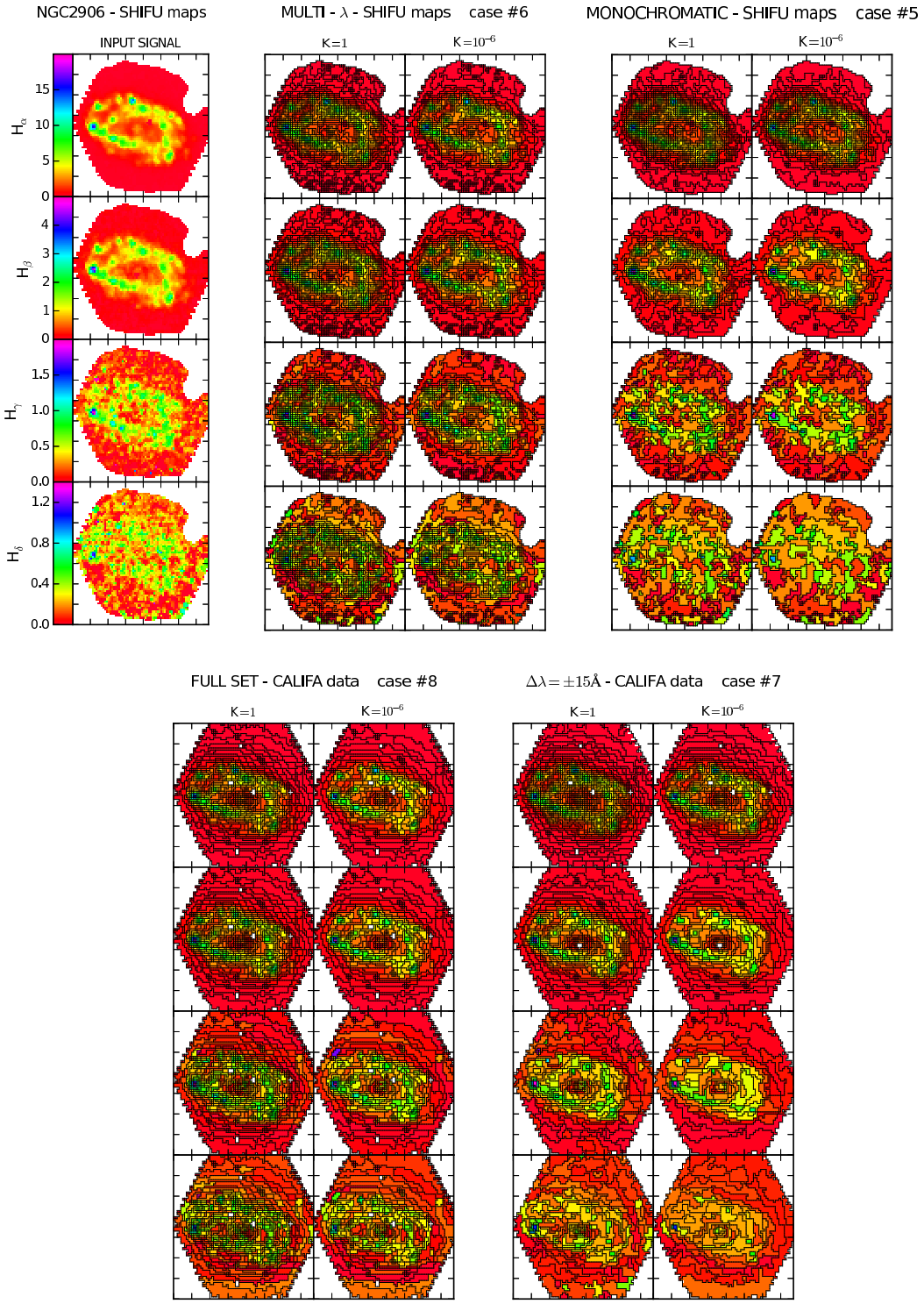

FIGURE 4.2: Results for our observational test cases based on CALIFA observations of NGC 2906. The structure of the plot is identical to that of Figure 4.1 for the upper panels (test cases #5 and #6), which show the output of applying BATMAN to the intensity maps of the Balmer lines measured by SHIFU on a spaxel-by-spaxel basis. The lower panels show the results obtained for test cases #7 and #8, which are conceptually identical to #5 and #6, respectively, but are both multi-λ tessellations of selected slices of the IFS datacube (see the description in Section 4.4.2 and Table 4.2); it is impossible to represent the input signal in 2D for these cases. The colour maps denote flux in standard CALIFA units, i.e. $10^{-16}(erg/s/cm^2)$; they correspond to the BATMAN output in test cases #5 and #6 (upper panels), and to SHIFU measurements posterior to the segmentation in test cases #7 and #8 (bottom panels).

This expectation is consistent with the behaviour that can be observed in Figures 4.1 and 4.2. The area of the synthetic multi-images covered by the ellipse is divided into concentric regions that roughly follow its shape. Most of the tessellations in NGC 2906 tend to feature annuli that trace the isocontours of the considered signal. It is worth noting that, in one of the astrophysical tests (#5 and #6), this refers to the measured intensities of the emission lines, whereas in the other (#7 and #8) it corresponds to the surface brightness at different wavelengths, including not only the emission lines but also the adjacent continuum. In the central part of the galaxy, the signal-to-noise ratio is high. There are many regions consisting of very few spaxels, and all the lines are clearly detected. In the outskirts, where the signal is weaker, the regions are larger, and the overall normalization of the continuum plays a major role in setting their shape.

Since the morphology of the tessellation traces the spatial structure of the input data, the results depend on how these data are fed to the algorithm. The first noticeable difference between the binning modes described in Section 4.4.3 (and summarized in Table 4.2) is that the 'multi-λ' procedure yields a single tessellation for all layers. Conversely, the regions of each layer in the 'monochromatic' mode have been obtained separately, and hence they are different and independent on one another.

In our synthetic problem, the circle, triangle, and ellipse are, by construction, truly independent objects, and they appear as such when BATMAN is run in the monochromatic mode. In contrast, when the (R,G,B) layers are considered as a multi-image, the overlap regions are *different* from the rest, as they would correspond to 'yellow' and 'purple' colours rather than pure 'red', 'green', or 'blue'. Hence, BATMAN separates these regions from the 'main' objects (circle, triangle, and ellipse) according to the monochromatic definition. Both solutions are equally correct, and which one is to be preferred depends on the specific scientific goals to be achieved. It is entirely up to the user's judgement to decide what information should be considered relevant in order to decide whether two regions are 'different'. As an equivalent scientific example, the different layers in a multi-image may correspond to spatially-resolved maps of the *mass* and/or the *fraction* of young stars in a given galaxy, their age, metallicity, radial velocity, velocity dispersion, etc., and one can be interested in analysing all/some of these properties separately ('monochromatic' mode) or considering all of them at the same time ('multi-λ' mode). The choice of the input data is a critical step of any analysis, and it will obviously play an important role in determining the solution found by the algorithm.

We also face such a decision in our specific examples of astrophysical test cases, where one may adopt different prescriptions with the ultimate goal of recovering intensity maps of the Balmer emission lines. Is it more appropriate to make a first estimate on a spaxel-by-spaxel basis, and then bin the maps in order to increase the signal-to-noise ratio, or is it better to find an optimal tessellation based on the raw data and then carry out the measurements? In either case, is it more convenient to consider each line separately, or all of them simultaneously? Although it is certainly not our goal to answer these questions, it is interesting to compare several different approaches in order to illustrate the effect that this kind of choices has on the optimal tessellation that BATMAN returns.

When all the SHIFU measurements are taken as input data (case #6, Figure 4.2), the output tessellation is largely driven by the Hα map, which has the highest signal-to-noise ratio. Based on the information provided by this line alone, it is relatively easy to realize that two given spaxels are different if one of them belongs to an HII region and the other corresponds to diffuse emission, where the intensity is considerably lower. The information contained in the weakest lines (Hγ and Hδ) is also used, but it carries a much lower weight, and it merely represents a minor-order correction. If we run BATMAN separately on each map (case #5, Figure 4.2), the tessellation obtained for Hα is very similar to the multi-wavelength regime. For Hβ and Hγ, the size of the regions increases due to the lower signal-to-noise

ratio, but the overall structure is still the same. For Hδ, the algorithm adapts to the structures that are present in the input data, but these are severely affected by the noise. This is clearly a disadvantage in our test problem, since we know that the signals in the different layers are not independent. However, this may not be true in the general case (e.g. if there was a signal that was present *only* in Hδ), and then it could well be possible that it is more adequate to consider the noisy dimensions separately in order to maximise their weight on the tessellation.

When applied directly to the IFS data (case #7 and #8, Figure 4.2), the algorithm is able to recover the ring-like structure in all cases, even when only a 30-Å interval around Hδ is taken as input. The central regions of the galaxy are always divided into relatively small regions, whereas the outer parts are tessellated in roughly concentric rings. The overall morphology is actually fairly robust, and the main differences between the different prescriptions are related to the region sizes. In fact, the tessellations obtained from each of the individual intervals (case #7), as well as from the full data set (case #8), are qualitatively similar, at variance with the results based on the synthetic test problems or the SHIFU maps.

4.5.2 Features on small scales

In our synthetic tests (see Figure 4.1), it is evident that BATMAN recovers many more aggregations of one (or a few) spaxels when only a single 'layer' is analysed ('monochromatic' mode) than when all layers in the multi-image are considered simultaneously ('multi-λ'). These regions are statistically significant according to BATMAN's criteria, i.e. the posterior probability ratio (4.19) indicates that it is more likely that the enclosed signal is statistically different from that of the adjacent regions. We do know, however, that these regions may be 'real' only in the sense that the input data are indeed different as the result of statistical fluctuations of the noise[3]. As we increase the number layers to be considered, we enlarge the number of dimensions and hence the amount of information associated to every spaxel. Random aggregations of a few adjacent spaxels become much harder to form, since it is very unlikely that all layers happen to deviate in the same direction and thus the spaxels are identified as an independent region. In the same way, a true signal is also more difficult to detect: a clear difference in one layer becomes less and less significant if it is diluted among a plethora of other channels carrying unrelated information (and/or noise).

In reality, it is far from trivial to discriminate weak signals from random fluctuations, and this is again a challenge left for the final user. In our tests based on astronomical data, the situation is further complicated by the large differences in S/N from one line to another as well as the potential presence of observational artefacts. For the Hα maps, based on either SHIFU measurements or CALIFA data, including information from the other Balmer lines tends to reduce the number of regions in the areas where the signal is stronger (i.e. within the ring-like structure), preferentially removing regions with one or two spaxels. In the outer parts, though, a number of single-spaxel regions arise in the multi-wavelength tessellations due to the presence of outliers in *any* of the other layers. Although a careful study would be required in order to assess whether these outliers are physical, it is our preliminary impression that most of the single-spaxel regions in the galaxy outskirts are due to artificial features in the data. For all the Balmer lines other than Hα, the monochromatic tessellations always yield much larger regions than the multi-wavelength result, because of their much smaller signal-to-noise ratio.

In addition to the signal-to-noise of the input data, the number and size of the regions output by BATMAN are also set by the prior parameter K. As explained in Section 4.3, the iterative merging procedure continues as long as there is any candidate tessellation $R_{c,n-1}$

[3]This is the so-called *look-elsewhere* effect: a large fluctuation at a random place is extremely unlikely, but a few large fluctuations *somewhere* in the sample are indeed expected.

where the posterior probability ratio (4.19) is larger than unity, or, equivalently,

$$\prod_{\lambda=1}^{n_\lambda}(H_\lambda - L_\lambda)\frac{e^{-\frac{(\mu_{A\lambda}-\mu_{B\lambda})^2}{2(\sigma^2_{A\lambda}+\sigma^2_{B\lambda})}}}{\sqrt{2\pi(\sigma^2_{A\lambda}+\sigma^2_{B\lambda})}} > K \tag{4.25}$$

Thus, the combined prior parameter K regulates the contrast that is required in order to consider that two regions correspond to different signal values. The effect of considering different values of the combined prior parameter K is illustrated in Figures 4.1 and 4.2 by depicting the results obtained for $K = 1$ and $K = 10^{-6}$ in all our example test cases. A decreasing value of K essentially increases the probability of merging regions, and some of the small fluctuations discussed above are removed as a result of a less strict compatibility criterion.

In terms of the prior probability distributions (4.7) and (4.15), regulated by the parameters k_λ and $k_{\rm R}$, respectively, a low value of K is closer to the 'non-informative' (infinite) improper uniform prior, and therefore it means that we have little previous knowledge about the signal and/or that we prefer a segmentation with as few regions as possible. Both statements are absolutely equivalent, both formally as well as in practice. $K \sim 1$ uses the information contained in H_λ and L_λ to minimise the probability that two regions with physically different signal are merged together. Lower values of this parameter reduce the contamination associated to random fluctuations in the input data and increase the signal-to-noise ratio at the expense of missing the weakest genuine signals. The optimal value of K is problem-dependent, and it can only be decided upon trial and error. Fortunately, our results suggest that there are relatively little differences between adopting values as extreme as $K = 1$ and $K = 10^{-6}$, both in synthetic as well as in real data.

To sum up, we can conclude that BATMAN is able to adapt to the structures present in the data, both at large and small scales. The resulting tessellation depends slightly on the adopted priors and, most importantly, on the precise choice of the input data set. Therefore, it is important to devote some time to investigate these issues as a preliminary step of any scientific analysis. The local signal-to-noise ratio and the precise value of the combined prior parameter K (the only free parameter of the algorithm) affect the number and size of the regions identified by the algorithm, especially when gradients are present, but neither of them has a significant effect on the overall morphology of the tessellation. Other aspects, such as the actual shape of the underlying structure, or the statistical properties of the noise, do not seem to play a major role.

4.5.3 Quality of the reconstruction

One of the reasons to tessellate a multi-image is to obtain a better reconstruction of the underlying signal, especially in the low signal-to-noise regions. In order to calibrate the improvement with respect to the original input data, we study in Figure 4.3 the distribution of the residuals for our two synthetic test cases, where $S_{ij\lambda}$ is known, in terms of the input errors $e_{ij\lambda}$,

$$\Delta_{ij\lambda} = \frac{\mu_{r_{ij}\lambda} - S_{ij\lambda}}{e_{ij\lambda}} \tag{4.26}$$

with $\mu_{r_{ij}\lambda} = \mu_{r\lambda}$ for all spaxels $\{i,j\} \in r$, i.e. $r_{ij} = r$. For the input multi-image, where $\mu_{r_{ij}\lambda} = x_{ij\lambda}$, the residuals $\Delta_{ij\lambda}$ follow by construction independent Gaussian distributions with zero mean and unit dispersion. Therefore, the residual maps on the left column of Figure 4.3 are statistical realizations of white noise for all layers, without any spatial structure, both for the 'uniform' and 'ccd-like' schemes.

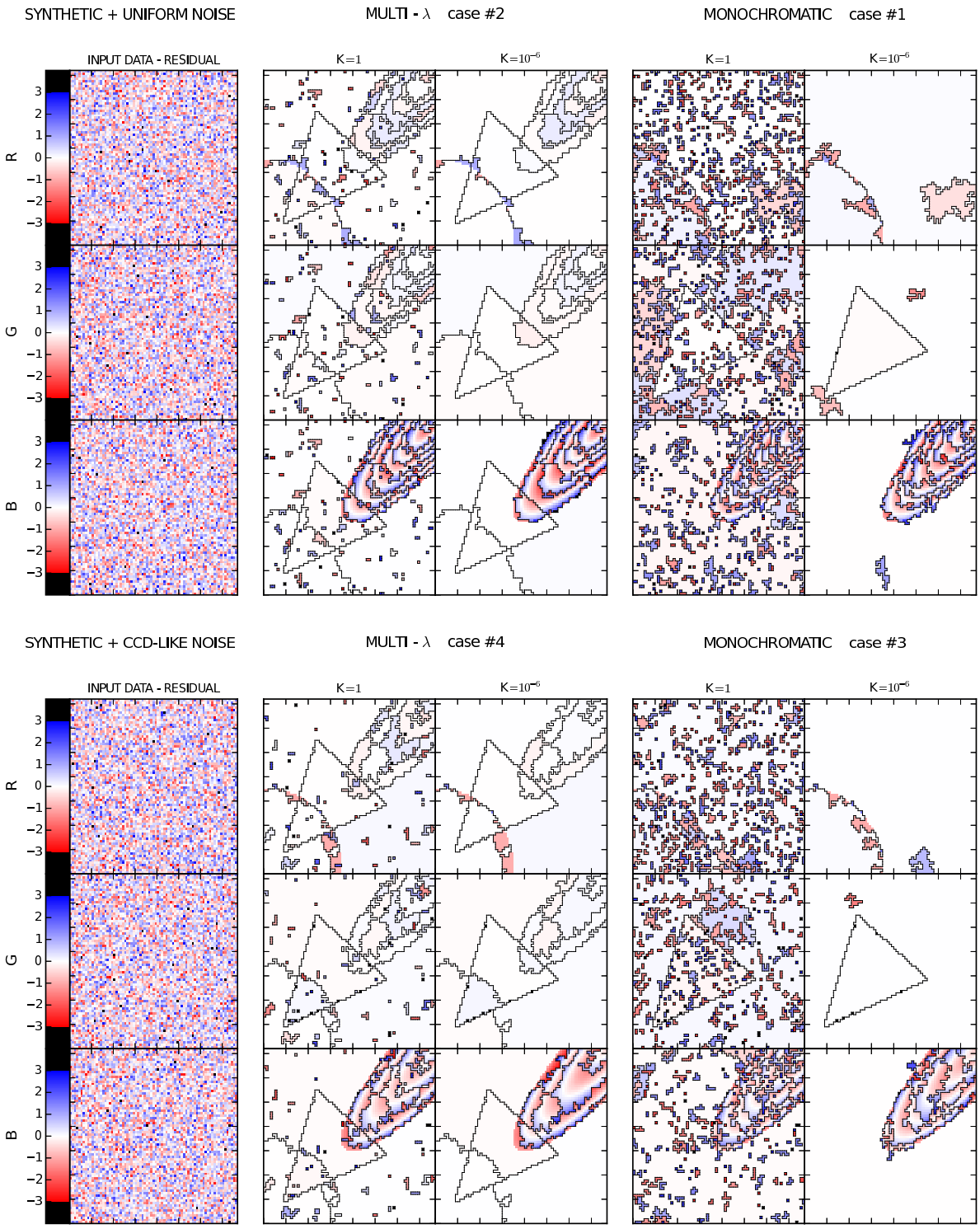

FIGURE 4.3: Maps of the residuals $\Delta_{ij\lambda} = \frac{\mu_{r_{ij}\lambda} - S_{ij\lambda}}{e_{ij\lambda}}$ for our synthetic test cases. The structure of the plot is identical to Figure 4.1.

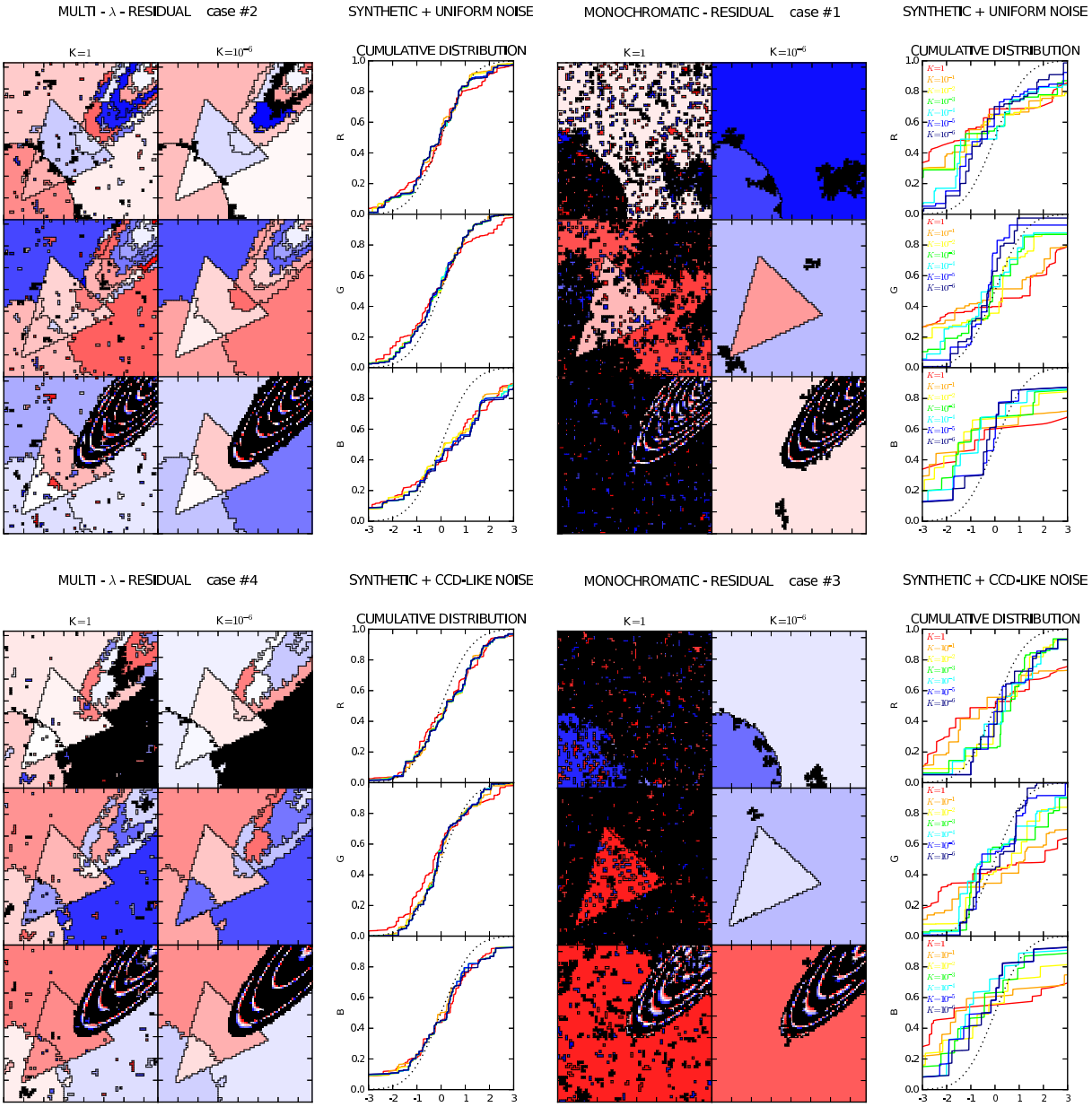

FIGURE 4.4: Maps and cumulative distributions of the estimated residuals $\hat{\Delta}_{ij\lambda} = \frac{\mu_{r_{ij}\lambda} - S_{ij\lambda}}{\sigma_{r_{ij}\lambda}}$ for our synthetic test cases. The structure of the plot is similar to that of Figure 4.1 except for the missing input data. We include cumulative distributions to study the behaviour of the formal errors $\sigma_{r\lambda}$ returned by the algorithm, where different colours correspond to different values of the prior parameter K (see labels in the figure). In order to improve the statistics, the data plotted in these cumulative curves correspond to the results of applying BATMAN to 10 random realizations of the noise.

As can be seen in the other maps, the posterior mean values $\mu_{r\lambda}$ obtained for every BATMAN region are representative of the signal values within the region. In the R and G layers, where the signal within the circle, the triangle, and the background is indeed constant, $\mu_{r\lambda}$ is very close to the true value ($\Delta_{ij\lambda} \simeq 0$, white colour in the residual maps) as long as the region is correctly identified.

In some cases, though, a small number of spaxels may be assigned to a region where the underlying signal is actually different: in our synthetic tests, this only happens near the boundaries of the R circle, which are difficult to trace due to the low signal-to-noise ratio ($S/N = 1$). One may expect that such misclassifications yield $\Delta_{ij\lambda} \sim \mathcal{O}(1)$. If the contrast between any two areas is larger than $e_{ij\lambda}$ (as it occurs e.g. in the triangle in the G band), the difference between adjacent spaxels on each side of the boundary is statistically significant. It is thus very unlikely that they become connected by our iterative procedure before merging with the other surrounding spaxels that belong to the correct region. Although these errors are indeed possible, they are restricted to a few isolated spaxels in the G layer of the 'ccd-like' case, where $S/N = 3.5$ (see Table 4.1).

As discussed above, BATMAN can also identify regions around sufficiently high (a few sigma) random fluctuations on small scales when high values of the combined prior parameter K are adopted, especially in the 'monochromatic' case. Again, random fluctuations larger than $\Delta_{ij\lambda} \sim \mathcal{O}(1)$ are statistically very unlikely, and therefore the residuals in the affected spaxels are of this order (red/blue colours in Figure 4.3).

Errors of similar magnitude also occur in the presence of gradients, where continuous variations of the signal $S_{ij\lambda}$ are physically present in the data, whereas $\mu_{r\lambda}$ is assumed, by definition, to be constant within every region. Even if the isocontours are correctly traced by the tessellation, and the value of $\mu_{r\lambda}$ is representative of the average signal within the region, we expect, following the same argument applied to the misclassifications, that $\Delta_{ij\lambda} \sim \mathcal{O}(1)$. Otherwise, the deviant spaxel would be associated to the adjacent bin of correspondingly higher or lower intensity. The effect of gradients is illustrated by the ellipse in the B band, where a characteristic red-white-blue pattern is clearly visible within every BATMAN region.

We thus conclude from Figure 4.3 that the expected values of the posterior probability $\mu_{r\lambda}$ returned by our algorithm provide a more accurate representation of the underlying signal than the original input data over most of the multi-image. Only for the 'catastrophic' failures discussed above, residuals of the order of $\Delta_{ij\lambda} \sim \mathcal{O}(1)$ may be found.

Another important aspect is the quality of the formal errors $\sigma_{r\lambda}$ derived from equation (4.12) in Section 4.2.1. In the ideal case, where all the underlying assumptions are met, the estimated residual

$$\hat{\Delta}_{ij\lambda} = \frac{\mu_{r_{ij}\lambda} - S_{ij\lambda}}{\sigma_{r_{ij}\lambda}} \tag{4.27}$$

should follow a normal distribution. However, the presence of gradients in the signal and the identification of spurious regions will cause that the formal errors $\sigma_{r\lambda}$ reported by BATMAN should be treated with caution and merely taken as a (realistic) lower limit to the actual uncertainty in the recovered signal.

A more quantitative assessment is provided in Figure 4.4, where we plot colour maps of the estimated residual $\hat{\Delta}_{ij\lambda}$. We also present histograms of its cumulative distribution (based on 10 independent realizations of the random noise) for different values of the combined prior parameter K. Using our synthetic tests we find that, for $K < 10^{-3}$ (lines of green-blue colour), the statistical distribution of the estimated residuals $\hat{\Delta}_{ij\lambda}$ is *similar, but not exactly equal* to the expected normal distribution. For $K = 1$, values of $|\hat{\Delta}_{ij\lambda}| > 3$ (black areas in the colour maps) are common in the 'monochromatic' case and relatively frequent

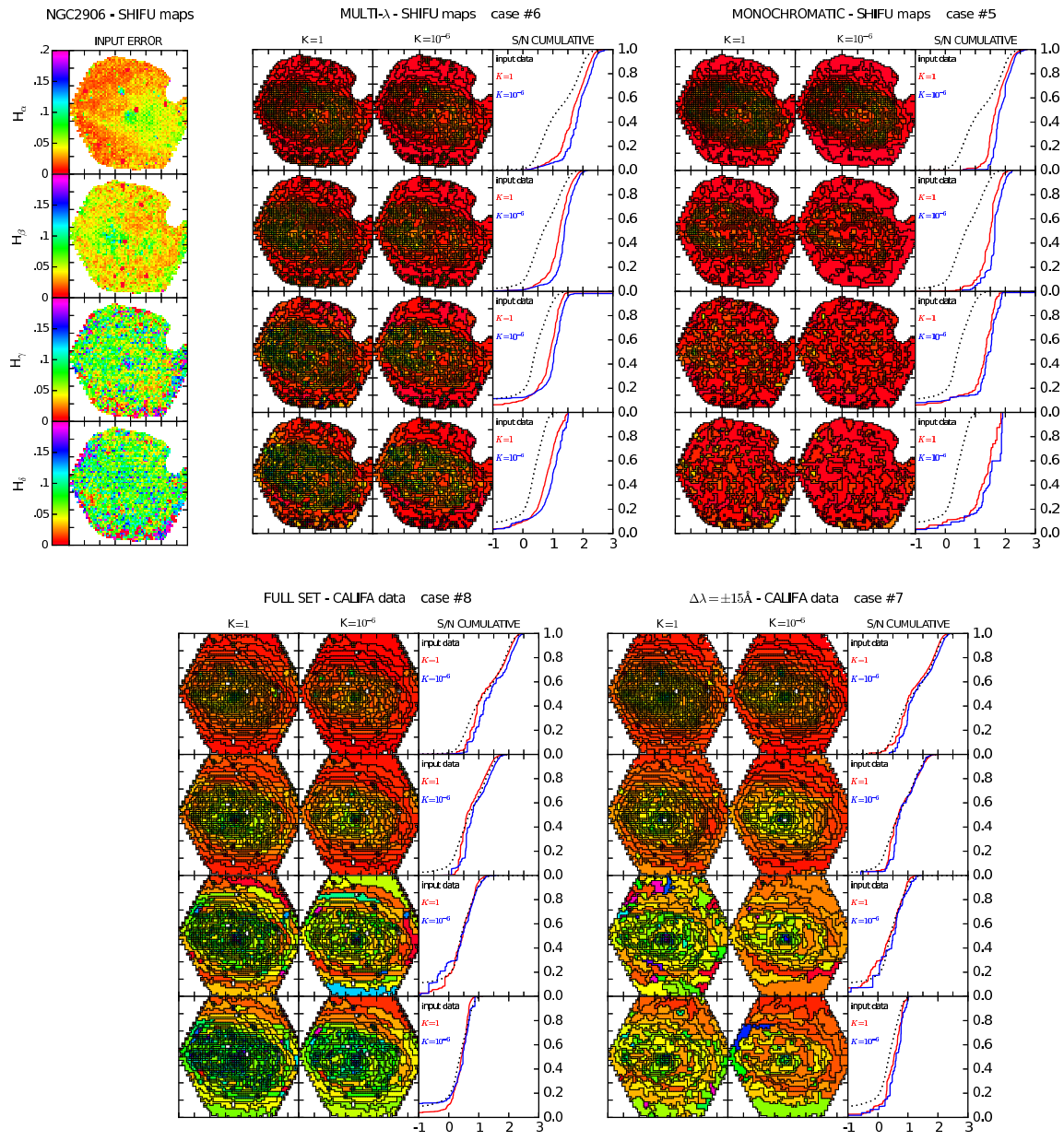

FIGURE 4.5: Results of applying BATMAN to our observational test cases, error maps and cumulative distributions of the 'recovered' signal-to-noise ratios. The structure of the plot is identical to Figure 4.2 except for the inclusion of the cumulative distributions. Red and blue cumulative curves correspond to $K = 1$ and $K = 10^{-6}$ results. The dotted black curve corresponds to the SHIFU maps used as input for test cases #5 and #6 and ploted in the left column. The colour maps correspond to flux errors for every line in standard CALIFA units, i.e. $10^{-16}(erg/s/cm^2)$. The signal-to-noise ratio is represented in logarithmic scale.

in the 'multi-λ' analysis. In the latter (and/or for $K < 10^{-3}$), they represent a small fraction of the multi-image and therefore they have a barely noticeable effect on the cumulative distribution.

The most important departure with respect to the ideal behaviour is due to the presence of gradients in the data. Although the algorithm manages to identify regions where the underlying signal is *approximately* constant, equation (4.12) is based on the assumption of strict equality, and physical variations within the region (of the order of $e_{ij\lambda}$) are not taken into account in the error budget. As can be seen in Figure 4.4, this source of systematic error may result in $\sigma_{r\lambda}$ underestimating the true residuals in any given spaxel by as much as a factor of the order of two, which arguably constitutes a reasonable upper limit, albeit not necessarily a worst-case scenario.

In order to investigate a more realistic example, let us now try to address the quality of the reconstruction in our astrophysical test cases. As in any practical application, the underlying signal is unknown, and the true solution is not available. In the top panels of Figure 4.5 we compare the error maps $e_{ij\lambda}$ of the SHIFU spaxel-by-spaxel measurements with the formal errors $\sigma_{r\lambda}$ recovered by BATMAN, both in the 'monochromatic' (case #5) and the 'multi-λ' (case #6) binning modes. For test cases #7 and #8, we plot on the bottom panels of Figure 4.5 the errors $e_{r\lambda}$ reported by SHIFU when the regions defined by BATMAN from the CALIFA data are given as input.

In all cases, we do observe that the formal errors decrease (i.e. the colour maps become redder) and their distribution becomes more uniform thanks to the segmentation. Although the improvement is certainly not surprising in the top panels ($\sigma_{r\lambda}$ decreases roughly as the square root of the number of spaxels in region r), it is an expected but non-trivial result in the bottom panels. In fact, the errors in the line measurements performed by SHIFU after the BATMAN segmentation ($e_{r\lambda}$) are much more similar to the results of the spaxel-by-spaxel analysis ($e_{ij\lambda}$) than suggested by equation (4.12).

This is due to a combination of different non-linear effects. The most important is arguably the correlation between the noise in adjacent spaxels in CALIFA data, for which BATMAN assumption of statistical independence is a poor approximation. The propagation of the errors through the SHIFU pipeline takes it into account through a correction factor that attains values of the order of $\sim 2-3$ for regions with $\sim 8-66$ spaxels see Appendix A in García-Benito et al., 2015a, for details. Other issues, such as potential misclassifications, gradients, and the heterogeneous quality of the observational data (including the error estimates) across different spaxels also contribute to increase the uncertainty.

Yet, the bottom panels in Figure 4.5 indicate a significant reduction of the errors $e_{r\lambda}$ in the low signal-to-noise areas (e.g. the boundaries) of the multi-image, where large (often annular) regions are identified by BATMAN. This improvement is consistent with the intensity maps displayed in Figure 4.2, where the level of random fluctuations in these regions is substantially reduced compared to the spaxel-by-spaxel results shown in the top left panels. In areas where the S/N of the CALIFA datacubes is high, our algorithm tends to return regions consisting of one or a few spaxels, and the results (both the intensity and its error) are virtually unchanged with respect to the spaxel-by-spaxel measurements.

We also investigate in Figure 4.5 the changes in the cumulative distribution of the *estimated* signal-to-noise, comparing $x_{ij\lambda}/e_{ij\lambda}$ (spaxel-by-spaxel measurements) with $\mu_{r\lambda}/\sigma_{r\lambda}$ in the BATMAN output (cases #5 and #6) and with $x_{r\lambda}/e_{r\lambda}$ (SHIFU measurements on BATMAN regions; cases #7 and #8).

First of all, we would like to argue that the interpretation of these quantities is not straightforward, and some of the first impressions conveyed by the histograms in Figure 4.5 are grossly misleading. In particular, they might seem to suggest at first sight that the best strategy to tackle this particular problem is to run BATMAN on the SHIFU measurements,

as this approach leads to the strongest reduction in the formal errors $\sigma_{r\lambda}$ and the largest increase in the estimated S/N (especially for Hδ in the 'monochromatic' case).

This is certainly at odds with our discussion in Section 4.5.1, based upon visual inspection of the maps in Figure 4.2. The original S/N in this particular case is so poor that BATMAN is barely able to even recover the large-scale morphology of the underlying signal. As a consequence, the regions of the tessellation contain spaxels where the signal may vary considerably, and the formal errors are thus expected to be underestimated by about a factor of two, according to our previous test (Figure 4.4). As mentioned above, the correlation between the noise of adjacent spaxels represents a further source of uncertainty, leading to an additional underestimation of the error that grows logarithmically with the number of spaxels in the region under consideration (García-Benito et al., 2015a).

The improvement of $x_{r\lambda}/e_{r\lambda}$ (cases #7 and #8) with respect to the spaxel-by-spaxel measurements $x_{ij\lambda}/e_{ij\lambda}$ looks much more modest, but we think it is more realistic.

When the signal-to-noise ratio is relatively high (e.g. $S/N > 5 - 10$, inner parts of the galaxy), the CALIFA data are good enough to distinguish fairly minor differences between adjacent spaxels. Since BATMAN's goal is to keep all the information that is present in the multi-image, the resulting regions tend to be small. Due to the reduced number of spaxels and the presence of correlated noise, the measurement errors $e_{r\lambda}$ associated to these regions are only slightly smaller than $e_{ij\lambda}$. Whether further merging would be justifiable in order to obtain larger regions and reach a higher signal-to-noise ratio is not a decision to be taken by the algorithm. If we decided that the differences that are present in the data (e.g. the intensity and shape of the stellar continuum) are not relevant for our purpose of measuring the Balmer lines, we should provide a different input dataset (e.g. a continuum-subtracted spectrum) that is free from such irrelevant information.

When $S/N < 3$ (e.g. in the outskirts), Figure 4.5 shows that BATMAN regions are large enough to decrease the errors, even considering the effect of correlated noise. However, it is precisely in this regime (particularly for the weakest Balmer lines) that SHIFU tends to fail to identify the emission line and/or return spurious values of both fluxes and errors (e.g. many of the blue and purple dots in the Hγ and Hδ error maps). These 'catastrophic' spaxels make a significant contribution to the fraction of spaxels with $S/N < 1$. If they are not merged with the surroundings (as it is often the case when BATMAN considers the 'full set' of spectroscopic data), there is little apparent improvement in the signal-to-noise. If, on the contrary, they are incorporated into the adjacent regions, they may spoil the fit for the whole region, leading to the large blue/purple areas in the '$\pm$15-Å' panels for Hγ and Hδ.

Moreover, the *estimated* signal-to-noise x/e is a random variable expected to follow a normal distribution centred at the true value of S/N, which has a significant impact on the histograms plotted in Figure 4.5 whenever the noise is comparable to the signal. In our example, the colour maps in Figures 4.2 and 4.5 indicate that both the errors and the amplitude of random fluctuations in the outer regions have decreased by a similar amount when SHIFU is run on the binned spectra, compared to the spaxel-by-spaxel measurements. Although this is certainly a valuable improvement, it barely reflects in the distribution of signal-to-noise ratios.

Although it is not the goal of the present work to deal with all these effects, they illustrate the kind of problems that one may face when analysing real scientific data and the way BATMAN handles them by default. Most importantly, they help showing that the formal errors returned by the algorithm provide an estimate of the true uncertainties roughly as good as the underlying assumptions apply to the particular problem at hand. Thus, we strongly advise not to blindly take them (nor the estimated signal-to-noise ratios) at face value.

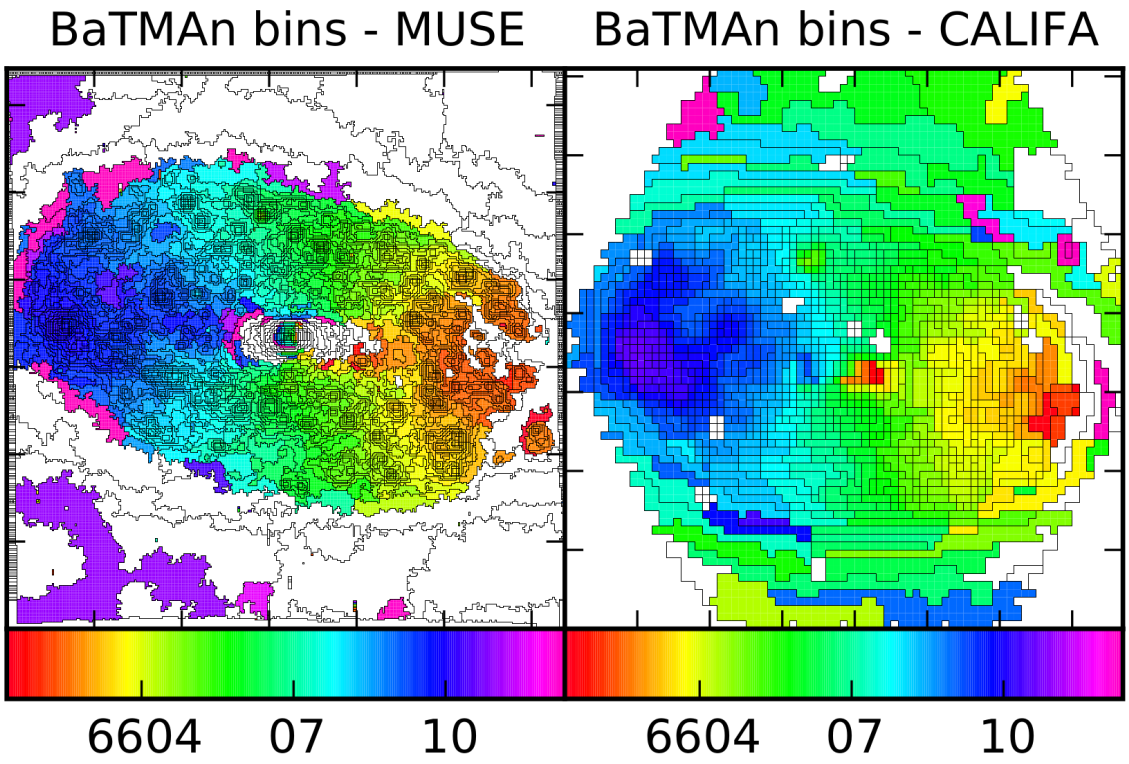

FIGURE 4.6: "Velocity maps" for the galaxy NGC2906 as observed within the MUSE (left) and the CALIFA (right) collaborations. The maps present the binning obtained with BATMAN when a cutted datacube centered in the Hα line is considered. The colour code corresponds to the position (observed wavelength) of the peak of the line.

4.6 Scientific uses of BATMAN

As emphasized in the introduction of this chapter, the BATMAN binning algorithm stems from the need of an analysis tool that characterizes and carefully tessellates a given dataset without losing information in order to take the most advantage of the low S/N data. This new binning philosophy can be used to tackle many scientific problems, some of which we briefly comment in this section.

As a first example to illustrate the potential of BATMAN and the need for this kind of information-adaptive tools, let us consider the recovery of the gas velocity field in MUSE (Bacon et al., 2010) IFS data. Figure 4.6 displays the segmentation performed by BATMAN on a 30 Å-section of the datacube selected around the Hα line ($\lambda_{\mathrm{H}\alpha,\mathrm{obs}} \pm 15$ Å). We perform the same procedure with two IFS datasets corresponding to MUSE (left) and CALIFA (right) observations of the same object, NGC2906. The colour code corresponds to the position of the peak of the recovered Hα line (observed wavelength) after the tessellation. White colours correspond to regions in which either more than one peak (plausible multiple kinematic components) or no peak (low S/N, outskirts) is found. In general, higher spatial resolution tends to imply a lower S/N per spaxel. The increase in spatial resolution from CALIFA to MUSE data is enormous (a factor of the order of 25), and in this particular example it is not fully compensated by the larger telescope aperture, given the adopted exposure times. While the S/N in CALIFA ensures that most spaxels contain sufficient information to derive individual velocities, our results show that BATMAN is capable of recovering a lot of substructure in the MUSE data, most of which does not present a rounded shape, as assumed in many popular tessellation schemes (e.g Cappellari and Copin, 2003; Sánchez

et al., 2012c; Sánchez et al., 2016b).

The advent of highly spatially-resolved IFS data strengthens the case for the widespread adoption of more advanced segmentation tools in the forthcoming years. One of the future projects that we aim to conduct is a comparison test of different binning algorithms. Of particular relevance will be the comparison with the broadly-used Voronoi tessellation by Cappellari and Copin (2003). As the philosophy of the existent binning techniques is quite different from that of BATMAN, it will be very interesting to compare how uneven tessellations affect the estimation of different galaxy properties on resolved scales, such as the kinematics (velocity, velocity dispersion) of both stars and gas, mean stellar ages, chemical abundances, etc.

Moreover, as we have already discussed in the context of our test cases, following different methodologies (e.g. choices of the input data) may yield different results even for a given tessellation algorithm. Another example, from a totally realistic science case (the thesis work of MsC. O.S. Choudhury), consist in measuring the radial dependence of stellar population properties (metallicity [Fe/H], α-enhancement [α/Fe], and stellar age) of massive quiescent disc galaxies in the CALIFA survey. To this purpose he carried out an angular binning, with adaptive bin sizes, to acquire a minimum S/N to perform the analysis. As a result of his study he finds that the disk contains two differing regimes depending on surface density. Fainter outskirts of some of the galaxies of his sample depict an unexpected enhancement of α-elements. It is not the scope of this section to cover this result or its implications, but to explain how BATMAN could help in this analysis. One of the plausible explanations of this strange behaviour could be an ill-defined binning. It is important to decipher whether this annuli tessellation is appropriate and whether these α-enhanced regions are real (if they are large or small, preferentially located in the outer parts of these objects, etc.). Hence we wondered:

What kind of binning would BATMAN *propose for this specific problem?*

O.S. Choudhury uses PyParadise SPS code (Husemann, Choudhury & Walcher in prep.) to simultaneously derive the kinematics of the objects and extract the stellar continuum. He will then measure the different metal abundances required for his study. To this purpose his analysis pipeline focuses on the fitting of two stellar features, the Hβ(4861Å) and the Mgb (triplet, $\sim$5173Å) absorption lines. Hence, we cut $\sim$35 layers of a CALIFA datacube (corresponding to NGC0842, one of the objects with α-enhanced outskirts) covering the ranges where these features are located [4850-4876, 5161-5198]. We then provided BATMAN with different versions of such dataset: a *raw* dataset, i.e. the data as provided by the CALIFA collaboration, a *flux-normalized*, a *velocity-corrected* and a combination of the last two. In Figure 4.7 we can see the different output tessellations that BATMAN provides for every case. Case #1 corresponds to the binning of the *raw* datacube. We can see that the tessellation roughly traces annular bins. We can interpret the overall shape of the bins in terms of the intensity of the absorption lines and the continuum, which seems to be the stronger information enclosed in the input data (driving BATMAN performance). This result is reinforced with the results of test cases #2 an #3. If we correct the datacube from line-of-sight velocity, case#2, the binning pattern remains almost invariant with respect to case #1. On the contrary, if we normalize the spectra in the considered range, case #3, BATMAN recovers a tessellation that resembles the velocity map of the object (i.e. BATMAN is capable of recovering the velocity of the object only when the information of the intensity of the line is subtracted). When we combine both corrections (i.e. the datacube is *velocity-corrected* and *flux-normalized*), case #4, BATMAN barely recovers any region. We can interpret these results in terms of the information contained in the Hβ and Mgb absorption features and their errors as given in the dataset. Intensity seems to be the dominant information contained in

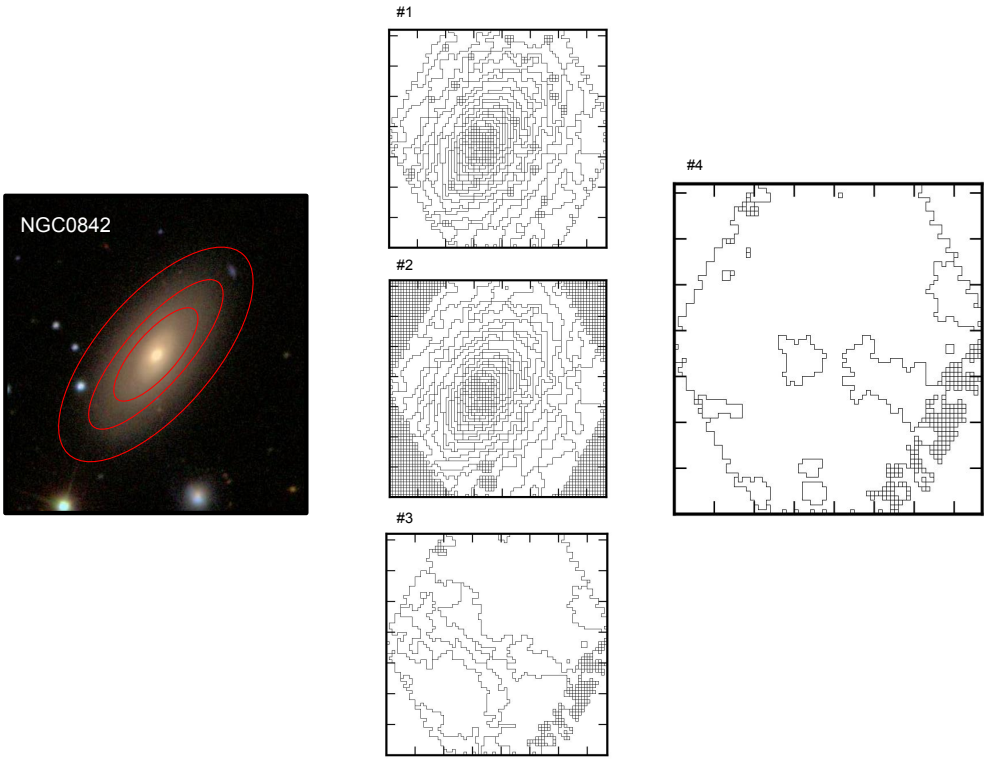

FIGURE 4.7: Illustration of the analysis procedure carried out with the galaxy NGC0842. Left figure depicts the SDSS iamge of the object with and illustration of the annular bins MsC O.S. Choudhury is considering in his thesis work. BATMAN binning #1 (top) is the result of applying the algorithm to the "raw" datacube, as it provided by the CALIFA collaboration. #2 (middle) shows the binning of the velocity-corrected datacube while #3 (bottom) corresponds to the flux-normalized one. Finally, #4 (right) represents the binning obtained when the algorithm is run on the velocity-corrected and flux-normalized datacube

the example datacube, together with a much weaker velocity signal. Once the dataset is corrected from these two features, nothing seems to remain. Therefore, *How can we interpret* BATMAN *results with respect to the strange α-enhancement in the outer parts of the galaxy and the convenience of the annuli binning?*. First, BATMAN algorithm does not detect any particular region located in the outskirts of this object, at least not directly related to the Hβ and Mgb absorption features. Hence, the α-enhancement observed in O.S. Choudhury's work is either driven by other features in the stellar spectra or is not related to any local process going on in the outer parts of this system. Consequently, if the analysis conducted by O.S. Choudhury is properly corrected from velocity and the spectra is normalized in a coherent way, annuli binning is compatible with the "image-characterization" conducted by BATMAN binning algorithm, as case #4 tessellation shows no features incompatible with it.

Once it is decided that there is indeed relevant information in a given data set, one comes to the question:

What do we gain by using BATMAN *(or any other) tessellation algorithm?*

Let us discuss our point of view with another example: the well-known BPT diagram (Baldwin, Phillips, and Terlevich, 1981), very often used in order to discriminate the *star-forming* or *LINER/AGN* nature of the observed nebular emission. It requires the measurement of four emission lines (Hα, Hβ, [OIII] and [NII]), some of which may be relatively weak. In Section 2.2.3 we argued that imposing a S/N threshold to the complete set of lines ($S/N > 2$ in that particular case) introduces a severe bias, similar to imposing EW(Hα)>10 Å, $(u - r) < 2.3$, or SSFR$> 3 \times 10^{-11}$ yr^{-1} for our *star-forming* subsample. In order to illustrate the advantages of binning IFS data, we considered the flux measurements of the four lines for a star-forming galaxy, NGC5947. The data, obtained from the CALIFA collaboration (Sánchez et al., 2012a), were obtained using SHIFU (see Section 4.4.2). We binned the four emission-line maps together as a 4-layer "multi-image". Left column in Figure 4.8 shows the unbinned data: Hα flux (top), BPT diagram (middle) and and colour-coded map distinguishing SF and *liner-like* regions (bottom). The right column shows the binned counterpart. BATMAN binning defines larger regions among the *liner-like* dominated areas of the object, leading to a reduction in the scatter in the BPT diagram and the slimming of the observed trends, resembling the well-known "seagull-shape". The SF regions of the system are clearly located along the spiral arms of the galaxy, while the *liner-like* ones are found in the inter-arm regions and the nucleus of the object. In this example, BATMAN is capable of reducing the scatter in the BPT diagram by means of producing a coherent binning. Such a reduction of the scatter suggests that the distribution of lines ratios in the BPT diagram (in particular, the sharp differences between arm and inter-arm regions) is due to physical reasons (e.g. the density and temperature of the gas responsible for the observed nebular emission) rather than systematic effects or random statistical fluctuations of the measured ratios arising from poor S/N.

In the context of the present thesis, the study of the "ageing" of galaxies presented in Chapter 3 is also based on the use of low-S/N resolved IFS data. Quite often, observers either impose a S/N threshold (or bin their IFS data to reach a minimum signal-to-noise) that is considered sufficient (according to subjective criteria) to trust the results. For the specific case of the colour-equivalent width diagram (Figure 3.1), imposing a S/N threshold would remove most of the data corresponding to the outskirts of galaxies, while binning may lead to more or less severe loss of information depending on the details of the prescription followed. As illustrated in this chapter, one of the possible uses of the BATMAN algorithm is to bin directly an IFS datacube, performing the tessellation based on the raw spectra, prior to carrying out any measurements. The exact approach we present here consists on running

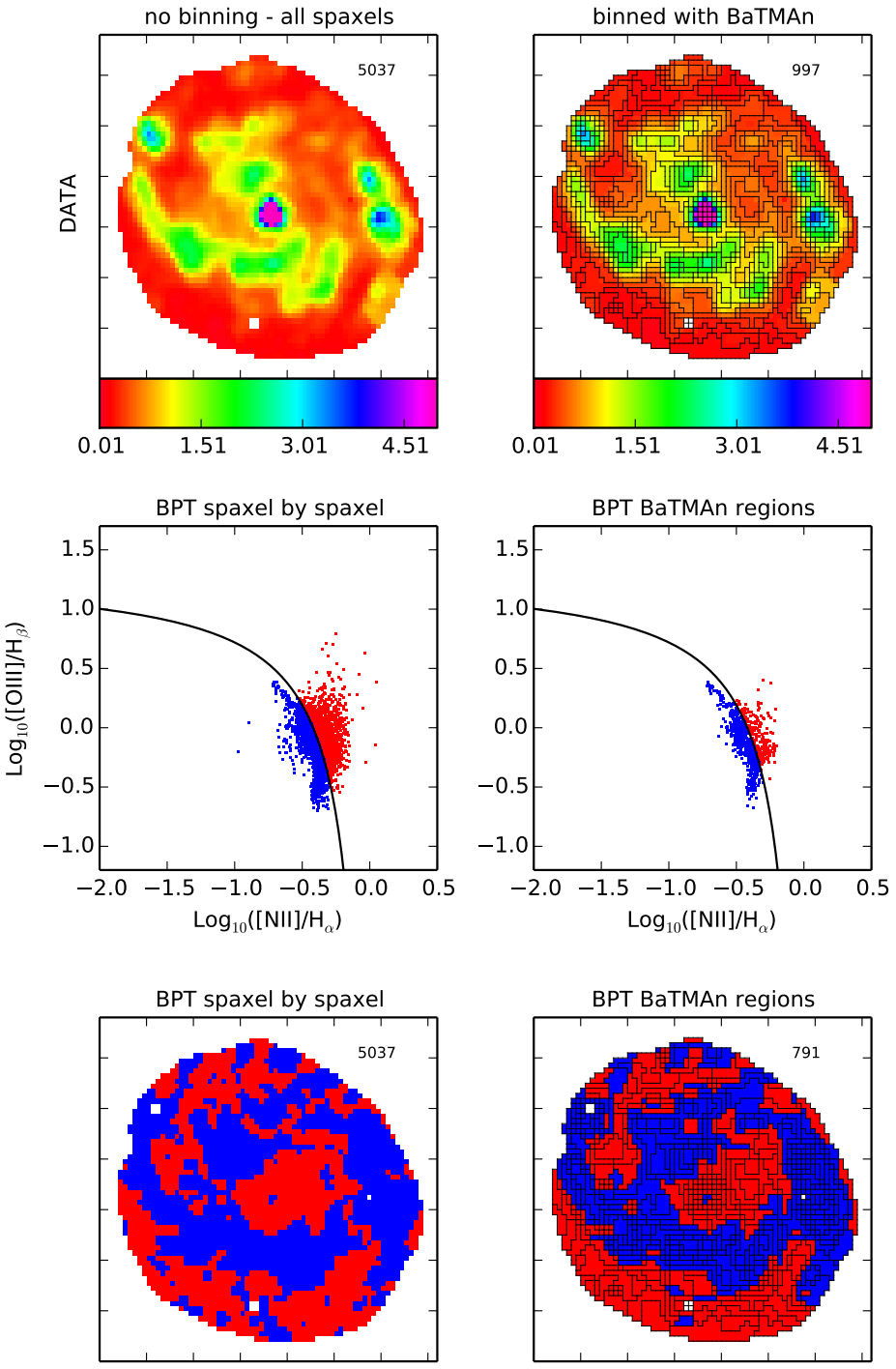

FIGURE 4.8: Unbinned (left) and binned (right) Hα flux map (top), BPT diagram (middle) and colour-coded map (bottom, following the SF/AGN separation of BPT diagram) of the galaxy NGC5947. Data corresponds to the CALIFA collaboration and flux measurements have been derived using SHIFU pipeline (see Section 4.4.2). Flux units correspond to 10^{-16} erg/s/cm^2, typically used in the CALIFA collaboration.

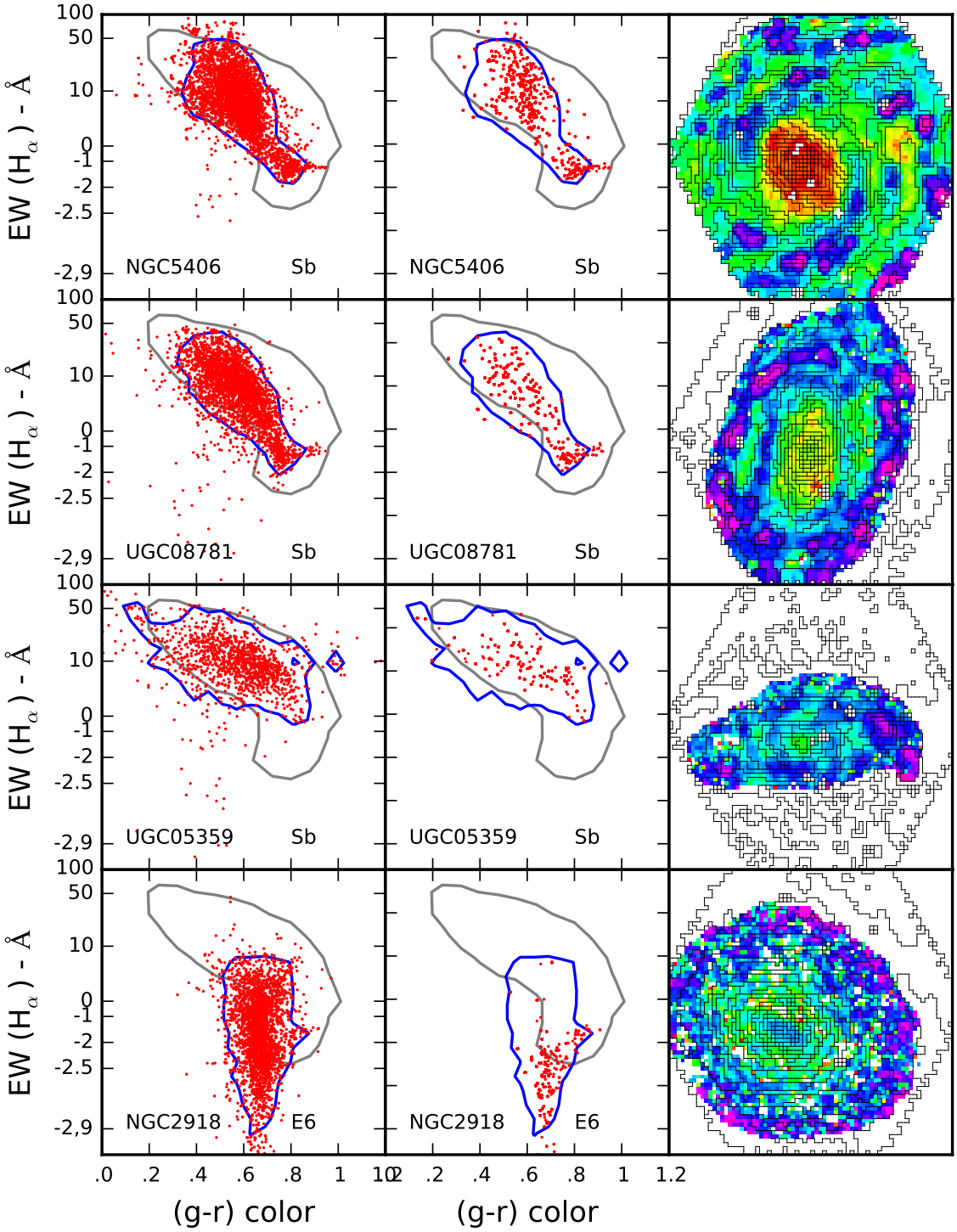

FIGURE 4.9: Galactic colour-equivalent width diagram depicted in Chapter 3 of four of the objects of the CALIFA sample. The unbinned, *spaxel-by-spaxel* SHIFU-measured (one value per spaxel) is plotted in the left column while the post-processed BATMAN-binned SHIFU-measured (one value per region) is depicted in the middle column. The gray contour corresponds to the 90% of the sample considered in Paper I (SDSS). The blue contour is the equivalent contour for the given galaxy spaxel-by-spaxel. An Hα map together with the tessellation generated by BATMAN is plotted in the right column to illustrate the performance of the algorithm.

BATMAN in "multi-λ" mode on a 40 Å-interval around the Hα line ($\lambda_{\mathrm{H}\alpha,\mathrm{obs}} \pm 20$ Å), implying a $\sim$20-layer multi-image. Although we aim to reduce the scatter both in the (g-r) colour and the EW(Hα), the former will not be (that much) affected by scatter. For this reason we focus on the Hα line to bin our dataset and enhance that information. Once the BATMAN tessellation is done, we run SHIFU on the binned dataset and plot the outcome in Figure 4.9.

The results show that the tessellations produced by BATMAN (right column) are consistent with the morphology of the objects and even recover some of the star-forming regions present in NGC5406 and UGC08781 (top-two panels). Even in the cases where the number of points has been reduced significantly, the trends observed in the spaxel-by-spaxel analysis (left column) remain unaltered (middle column), and it is now clearer, thanks to the reduced scatter, that the differences between the observed colour-equivalent width diagrams are indeed real, and therefore there is *not* a unique ageing sequence: although the objects/regions evolve, on average, from the upper left to the lower right, the precise path through the colour-equivalent width diagram does depend on the details of the star formation (and arguably gas accretion) history. Furthermore, we now clearly distinguish a secondary trend in the case of NGC2918 (bottom panel) that remained hidden in the unbinned cloud of low signal-to-noise data. From the four galaxies considered, only UGC05359 can be unambiguously classified as star-forming. For the other three systems, the outer regions are located along (very different) "ageing sequences", whereas the spaxels in the central part are arranged similarly to the "quenched sequence" defined in Chapter 2. The connection with galaxy morphology (bulge/disk decomposition, velocity dispersion) is the subject of ongoing work.

4.7 Conclusions

This chapter describes the Bayesian Technique for Multi-image Analysis (BATMAN), a new segmentation algorithm designed to characterize and coherently tessellate simultaneously many layers of a given multi-image, which we define as a dataset containing two regularly-sampled spatial dimensions and an arbitrary number n_λ of 'spectral' layers, such as e.g. Integral-Field Spectroscopic (IFS) data.

BATMAN's tessellation attempts to identify spatially-connected regions that are statistically consistent with the underlying signal being constant, given the information (measurements and corresponding errors) provided in the input dataset. If the difference between any two regions is found to be significant, they are kept separate in order to avoid unnecessary loss of information. It is important to note that these considerations are independent on the signal-to-noise ratio: if two regions carry the same information (have compatible signal within the errors), they should always be merged together; if they do not, it may be completely unphysical to average over them, and BATMAN will keep them separate.

We also present in the previous sections of this chapter a set of test cases that comprises both synthetic and real data analysed in different ways. BATMAN is not designed with a specific goal or to solve a given problem. The possible applications of the code are infinite (some were shown already, some we will briefly sketch in Section 4.6, and some we cannot even imagine). However, the posed test cases (even when finite) allow us to test the performance of the algorithm and provide some guidance for its further scientific (or not) use. According to the results of these tests, we conclude that:

1. The output tessellation depends on the precise choice of the input data set, and therefore it is of paramount importance to devote some time to investigate the information that should be considered relevant as a preliminary step of any scientific analysis.

2. BATMAN adapts to the spatial structures present in the data for a wide variety of morphologies, regardless of the statistical properties of the noise. By construction, gradients pose a significant challenge to the algorithm. When they are present, the output tessellation tends to trace the isocontour lines.

3. The exact number and size of the regions are mainly set by the local signal-to-noise ratio. The higher the S/N of the data, the easiest it is to distinguish whether two spaxels/regions are different. When S/N is low, many spaxels may be consistent with having a similar signal, and only a small number of large-size, independent regions can be identified.

4. The precise value adopted for the combined prior parameter K, the only free parameter of the algorithm, also affects the number and size of the regions in the output tessellation by setting the end of the iterative procedure. Lower values of K result in more iterations and therefore a smaller number of (larger) regions. This may have a substantial impact on the number of (potentially spurious) structures identified on the smallest scales, particularly when $n_\lambda = 1$ ('monochromatic' mode).

5. In the proposed formalism, the expected values $\mu_{r\lambda}$ of the posterior probability distribution of the signal within each region are given by the inverse variance-weighted average (4.11). Our synthetic tests show that these values provide a good representation of the true signal.

6. The formal errors $\sigma_{r\lambda}$, given by expression (4.12), are indicative of the true uncertainties, but they may underestimate them by as much as a factor of the order of two (e.g. in the presence of gradients and/or spurious regions).

7. Our analysis of real astronomical data shows that the segmentation of IFS datacubes is a complex task, involving many issues that are specific to the scientific problem under study. Our tests based on NGC 2906, focusing on the measurement of several Balmer lines, suggest that BATMAN may be most helpful in the low S/N regime. The algorithm is capable of recovering the underlying structure of the object even in the most difficult case (Hδ), especially when it is applied directly on the CALIFA data (and not so much when the SHIFU measurements are taken as input). The reduction of the noise with respect to the spaxel-by-spaxel (no binning) approach is clearly visible in the galaxy outskirts.

8. The application of BATMAN algorithm to our scientific problem, the study of the *ageing* process, results in a complete success. The algorithm effectively reduces the scatter in the colour-equivalent diagram verifying the existence of the different trends observed in the unbinned data. At the same time, the significant reduction of the noise leads to the discovery of previously hidden features in the "ageing diagram".

Let us stress once again that, in contrast to many other segmentation algorithms, BATMAN aims to preserve all the spatial information contained in the original data, as long as it is considered statistically significant. Such philosophy represents a new (and, in the opinion of the authors, much needed) approach to the analysis of astronomical images in the advent of the vast amount and spatial resolution of IFS data to come.

Chapter 5

The SELGIFS data challenge. Generating Synthetic IFS observations

This chapter is a based on the article:
"The SELGIFS data challenge: generating synthetic observations of CALIFA galaxies from hydrodynamical simulations"
by G. Guidi, J. Casado, Y. Ascasibar & C. Scannapieco
∼ draft version ∼

5.1 Introduction

We have already emphasized in this thesis the tremendous impact of Integral Field Spectroscopy (IFS) in the field of astronomy and astrophysics. Several observational programmes have produced, or will soon provide, systematic IFS surveys targeted at different galaxy populations, both in the local Universe, such as e.g. SAURON (Bacon et al., 2001), DiskMass (Bershady et al., 2010), Atlas3D (Cappellari et al., 2011), CALIFA (Sánchez et al., 2012a), SAMI (Croom et al., 2012), or MaNGA (Bundy et al., 2015), as well as at high redshift, such as e.g. SINS (Förster Schreiber et al., 2009), KMOS^{3D} (Wisnioski et al., 2015), or KROSS (Bower and Bureau, 2014). Although all these datasets differ widely in terms of both the number of galaxies observed and the number of spaxels sampling each object, the total number of spectra is, in most cases, so large that a significant part of the analysis must necessarily rely on fully automated procedures (see also Chapter 4). In the near future, instruments such as MUSE (Bacon et al., 2004), WEAVE (Dalton et al., 2014), or HARMONI (Thatte et al., 2014) will routinely produce even larger datasets just for a single galaxy, and their likely use in survey mode will increase the number of spectra to be analysed by several orders of magnitude.

One of the obvious advantages of IFS is that it allows to obtain much more information about the galaxies than single-fibre or long-slit spectroscopy. Having spatially-resolved spectra over a significant extent of a galaxy offers an unprecedented level of detail on the local physical properties of its gas, dust, and stars, as well as valuable constraints on other important variables, such as its dark matter content. However, it comes at the price of a higher level of complexity in the analysis of the data. For instance, the precise way in which spatial information is treated may have a crucial impact on the feasibility of any scientific case as a function of the signal-to-noise ratio (S/N) of the observations. Typically, different binning schemes have been used to tackle this issue, showing that they can be at the same time the solution to the problem and the origin of a new one. In the previous chapter (4) we showed that the optimal binning strategy is completely dependent on the specific problem under consideration, and a thorough study is necessary on a case-by-case basis. Moreover, the use of mock datasets (test datasets whose "properties/solutions" are known) in the development of BATMAN algorithm emphasizes the need for such thorough calibration.

It is the goal of extending the "RGB: circle, triangle, ellipse" calibration problem of Chapter 4 to every IFS analysis tool that leads to the present *SELGIFS data challenge* project. In this new chapter we describe (and present) the generation of reliable synthetic IFS observations, created with the aim of calibrating existent (and forecoming) analysis tools. Our goal is to provide a series of synthetic benchmark problems, based on numerical simulations, that are representative of the analyses typically carried out on observations of real galaxies. Current hydrodynamical simulations are able to follow the intertwined evolution of gas, dark matter, and stars over cosmic time, and then connect the observable properties of the galaxies with their merger and accretion history. Although they suffer from finite spatial and mass resolution, and a significant part of the relevant physics is implemented at the sub-resolution level through simple numerical schemes (whose details have a significant influence on the results, see e.g. Scannapieco et al., 2012), several simulation projects have recently been able to create fairly realistic galaxies (e.g. Governato et al., 2010; Aumer et al., 2013; Vogelsberger et al., 2014; Wang et al., 2015; Governato et al., 2007; Scannapieco et al., 2008; Nelson et al., 2015; Schaye et al., 2015).

In order to meaningfully compare such simulated data with observations or real galaxies, let alone to provide a physical interpretation of the results (see e.g. Scannapieco et al., 2010; Bellovary et al., 2014; Michałowski et al., 2014; Hayward et al., 2014; Smith and Hayward, 2015; Hayward and Smith, 2015; Guidi, Scannapieco, and Walcher, 2015; Guidi et al., 2016), it is critical that the output of the simulations is post-processed, first generating a 'synthetic observation' that mimics as closely as possible all the known selection effects and biases inherent to one particular instrument/survey, and then processing these data with the same algorithms and techniques that are applied to the actual observations.

Rather than constraining the recipes for star formation, feedback, and metal enrichment in hydrodynamical simulation codes, we are now interested in constructing realistic mock observations that can be used to test the different tools and prescriptions that may be applied to IFS data. The main advantage of this kind of experiments with respect to a purely observational approach is that the *correct* solution (i.e. the physical properties of the galaxies) to be recovered is accurately known, which makes possible to detect, quantify, and perhaps even correct systematic errors. Some efforts in this direction have recently been undertaken by Kendrew et al. (2016), who have used the HSIM pipeline (Zieleniewski et al., 2015) to create synthetic observations of simulated high-redshift galaxies that reproduce the conditions of the HARMONI instrument (Thatte et al., 2014) and test its capabilities in the context of IFS of stellar absorption lines.

In the work that will be presented in this chapter we use hydrodynamical simulations of galaxies in a cosmological setting to generate a set of synthetic observations that mimic the Calar Alto Legacy Integral-Field Area (CALIFA) survey (Sánchez et al., 2012a) in terms of the field of view, spatial and spectral resolution, noise statistics, and data format. We have post-processed the output of different cosmological simulations carried out with the galaxy formation codes by Scannapieco et al. (2005), Scannapieco et al. (2006), and Aumer et al. (2013) with the radiative transfer code SUNRISE (Jonsson, 2006; Jonsson, Groves, and Cox, 2010). Our final products, that will be publicly available through a web interface[1] once the work is published, consist of several items. On one hand we provide resolved maps of the physical properties (masses, ages, metallicities) of our simulated galaxies (calculated directly from the snapshots), maps of the model emission line intensities and absorption line indices after radiative transfer. On the other hand we provide the synthetic datacubes in CALIFA format (ready to use as if they were real observations). It is our long-term goal to use the proposed 'Data Challenge' to carefully evaluate the merits and drawbacks of

[1] http://astro.ft.uam.es/SELGIFS/

different strategies that may be followed in order to infer the physical properties from real data.

5.2 Hydrodynamical simulations

To produce our mock data sample we use three hydrodynamical simulations of galaxies in a ΛCDM Universe, generated from a dark-matter simulation with the zoom-in technique (Tormen, Bouchet, and White, 1997). The initial conditions for the hydrodynamical simulations are taken from the Aquarius dark-matter only simulation (Springel et al., 2008), identifying at redshift zero halos that are possible candidates for the formation of galaxies with properties similar to the Milky Way (i.e. with virial mass between 0.7 and 1.7×10^{12} $M_\odot$, and a quiet merger history in the recent past, excluding halos with neighbours more massive than half of their mass within a spherical region of 1.4 Mpc radius at $z = 0$,see Scannapieco et al. (2009)). The cosmological parameters assumed are the following: $\Omega_\mathrm{m} = 0.25$, $\Omega_\Lambda = 0.75$, $\Omega_\mathrm{b} = 0.04$, $\sigma_8 = 0.9$, and $H_0 = 100\,h$ km s^{-1} Mpc^{-1} with $h = 0.73$. The simulations have, at redshift $z = 0$, mass resolution of $1 - 2 \times 10^6$ $M_\odot$ for dark matter particles and of $2 - 5 \times 10^5$ $M_\odot$ for stellar/gas particles, and gravitational softening of $300 - 700$ pc.

Two halos, that we name C-CS$^+$ and E-CS$^+$ (first letter identifies the Aquarius halos according to the Springel et al. convention) have been simulated with a new version of Scannapieco et al. (2005) and Scannapieco et al. (2006) model (CS hereafter), which implements chemical enrichment and Supernovae (SNe) feedback in the Tree-PM SPH code Gadget-3 (Springel, 2005). The updated version used for this work (CS$^+$ model, Poulhazan et al., in prep.) concern the use of new metal yields (from Portinari, Chiosi, and Bressan 1998) including chemical enrichment from AGB stars by Portinari et al. (1998); Marigo (2001), a new IMF (Chabrier 2003), while the assumed cooling function is the one by Sutherland and Dopita (1993) as in the original Scannapieco et al. model.

The third halo (D-MA) is simulated with the Aumer et al., 2013 independent update (MA hereafter) to the CS model. MA model is different from CS in the chemical yields (which also include AGB stars contribution) with the additional modelling of metal diffusion in the ISM, in the use of a Kroupa IMF, and in the cooling function, which is taken from Wiersma, Schaye, and Smith, 2009. More important, the energy feedback from SNe is, unlike in the CS$^+$ model where feedback is purely thermal, divided into a thermal and a kinetic part, and the code also includes the feedback on the ISM of the radiation pressure due to massive young stars. The MA model gives in general stronger feedback compared to CS/CS$^+$, and hence younger, more metal rich and disk-dominated galaxies (for details on this model we refer the reader to Aumer et al. 2013).

Properties of the simulated galaxies

The measurement of some of the integrated properties of these simulated objects is described as follows and listed in Table 5.1. However, these properties do not correspond to the particles associated to the above mentioned halos, as defined by the SUBFIND algorithm (Springel et al., 2001), but to a sub-sample corresponding to those enclosed in the "virtually-observed" CALIFA field-of-view (see Section 5.4).

- **Total stellar mass:** mass in star particles inside the region sampled by the FoV in units of $\log[M_*/M_\odot]$.
- **$r-$band absolute magnitude:** absolute magnitude in the $r-$band obtained by summing the spectra of all spaxels and convolving the total spectrum with the $r-$band filter (Gunn et al., 1998; Gunn et al., 2006).

Name	Projection	Total mass	Abs mag	Stell age (log [yr])		Stell met (log [$Z/Z_\odot$])		v_{disp}	Gas met	Redshift	Lum dist
		$\log(M_*/M_\odot)$	($r-$band)	$\log\langle age\rangle_M$	$\log\langle age\rangle_L$	$\log\langle Z\rangle_M$	$\log\langle Z\rangle_L$	[km/s]	[12+log (O/H)]		[Mpc]
C-CS$^+$_0	face-on	10.55	-20.94	10.01	9.90	-0.34	-0.32	86.0	8.75	0.013	58.1
C-CS$^+$_1	45°	10.57	-20.96	10.01	9.90	-0.34	-0.32	121.3	8.73	0.013	58.1
C-CS$^+$_2	edge-on	10.58	-20.82	10.01	9.91	-0.35	-0.33	146.3	8.70	0.013	58.1
E-CS$^+$_0	face-on	10.10	-19.76	10.01	9.93	-0.37	-0.42	59.3	8.44	0.018	80.8
E-CS$^+$_1	45°	10.12	-19.86	10.01	9.91	-0.38	-0.44	78.7	8.32	0.018	80.8
E-CS$^+$_2	edge-on	10.15	-19.91	10.00	9.91	-0.40	-0.46	94.4	8.33	0.018	80.8
D-MA_0	face-on	10.70	-21.70	9.83	9.65	-0.17	-0.02	48.1	9.11	0.024	108.2
D-MA_1	45°	10.71	-21.69	9.83	9.65	-0.17	-0.02	102.8	9.11	0.024	108.2
D-MA_2	edge-on	10.73	-20.82	9.82	9.65	-0.17	-0.02	138.2	9.11	0.024	108.2

TABLE 5.1: Global properties of the simulated galaxies used to generate the CALIFA mock datacubes, calculated in the same field of view and projection of the corresponding synthetic observations.

- **Mean stellar age:** global mean stellar age weighted by mass ($\log\langle age\rangle_M$ as defined in Section 5.5.1) and by luminosity at $\lambda = 5635$ Åcalculated with STARBURST99 ($\log\langle age\rangle_L$). The units are $\log$ [yr].
- **Mean stellar metallicity:** global mean stellar metallicity weighted by mass ($\log\langle Z\rangle_M$) and by luminosity at $\lambda = 5635$ Å ($\log\langle Z\rangle_L$). Both measurements are in logarithmic solar units with $Z_\odot = 0.02$.
- **Velocity dispersion:** we compute the velocity dispersion along the line of sight by considering the stellar particles in the simulation that enter the FoV in the different projections. We weight the velocity of each particle by its luminosity at $\lambda = 5635$Å. The units are km/s.
- **Mean gas metallicity:** we derive the mean oxygen abundance of the gas 12 + log(O/H) as the mean of the (O/H) ratio of each gas particle.
- **Redshift:** redshift at which we "shift" the spectra in accordance with the physical size of the FoV enclosing ~ 2 half-light radii R_{50} (see Section 5.4). We use the cosmological calculator by Wright (2006) assuming the Planck Collaboration et al. (2015) cosmological parameters.
- **Luminosity distance:** luminosity distance corresponding to the given redshift as provided by Wright (2006) calculator.

Together with the global properties described above we also calculate the spatially-resolved ones, i.e. corresponding to the subsample of particles enclosed in the "virtually defined" spaxels (see Section 5.4.1). We reffer to these maps of directly measured properties as *high-level* product datacubes and represent the 'solutions' to be recovered by the observational algorithms (some examples can be seen in Figure 5.3). Note here that we include in this maps the effect of the spatial Point Spread Function (PSF, see Section 5.4.3), in order to make them directly comparable to the synthetic IFS observations. We enter now the detailed description of their calculation.

- **Stellar mass/Stellar mass density:** the stellar mass and stellar mass density maps have been derived considering the mass in star particles corresponding to every spaxel. The units are $\log\,[M_*/M_\odot]$ and $\log\,[M_*/(M_\odot\,\mathrm{pc}^2)]$ respectively.
- **Mass-weighted mean stellar age:** we compute the mass-weighted mean stellar ages as the logarithm of the mean of the ages in every spaxel. The units are $\log$ [yr].

$$\log\langle age\rangle_M \;=\; \log\left[\frac{\sum_n M_n\cdot age_n}{\sum_n M_n}\right]$$

- **Mass-weighted mean stellar metallicity:** we derive the mean mass-weighted stellar metallicities, where Z_n is the metalllicty of a stellar particle[2] in solar units (with $Z_\odot = 0.02$). The units are $\log[Z/Z_\odot]$.

$$\log\langle Z\rangle_M \;=\; \log\left[\frac{\sum_n M_n\cdot Z_n}{\sum_n M_n}\right]$$

- **Star formation rate:** the maps of the spatially-resolved SFRs are generated considering the amount of stellar mass formed in the last 10 Myr (a similar timescale to that

[2]The metallicity of every stellar particle is measured as...

of most observational indicators, see Kennicutt (1998)). SFR is measured in units of $[M_\odot/\mathrm{yr}]$.

- **Luminosity-weighted mean stellar age:** we compute the luminosity-weighted mean stellar age by weighting the star particle ages with their flux L_n at $\lambda = 5635$Å (calculated with STARBURST99[3]). The units are $\log[\mathrm{yr}]$.

$$\log\langle age\rangle_L = \log\left[\frac{\sum_n L_n \cdot age_n}{\sum_n L_n}\right]$$

- **Luminosity-weighted mean stellar metallicity:** to derive the mean luminosity-weighted stellar metallicity, we weight the metallicty of a stellar particle Z_n (in solar units assuming $Z_\odot = 0.02$) with the luminosity L_n calculated at 5635Å (using STARBURST99 SPS model). Measured in units of $\log[Z/Z_\odot]$.

$$\log\langle Z\rangle_L = \log\left[\frac{\sum_n L_n \cdot Z_n}{\sum_n L_n}\right]$$

- **Mean velocity/Velocity dispersion (stars):** the line-of-sight mean velocity v_{mean} and velocity dispersion v_{disp} maps (both in units of km/s) have been computed from their theoretical prescriptions and weighted by the luminosity of the particles at 5635Å (obtained with STARBURST99).

$$v_{\mathrm{mean}} = \frac{\sum_n L_n \cdot v_n}{\sum_n L_n}$$
$$v_{\mathrm{disp}} = \sqrt{\frac{\sum_n L_n \cdot (v_n - v_{\mathrm{mean}})^2}{\sum_n L_n}}$$

5.3 Simulated spectra

We now introduce the process of adding light to our simulated particles. We post-process the simulation snapshots at redshift zero with the Monte Carlo Radiative Transfer code SUNRISE (Jonsson, 2006; Jonsson, Groves, and Cox, 2010), considering as input for the radiative transfer post-processing only the particles belonging to the main halo in the hydrodynamical simulations, as determined by the SUBFIND algorithm (Springel et al., 2001). SUNRISE is a 3-D polychromatic Monte Carlo radiative transfer code, which is able to self-consistently simulate the emission and propagation of light in a dusty Inter Stellar Medium (ISM) from hydrodynamical snapshots, to obtain the full UV-to-submillimetre Spectral Energy Distribution (SED). The resulting SED includes the contribution of stellar and nebular emission, dust absorption and re-emission in the infrared, and hence shows stellar absorption features, emission lines, as well as the effects of kinematics on broadening the absorption and emission lines. This process consists of several steps:

1. SUNRISE assigns a specific spectrum to every star particle depending on its age and metallicity normalized by the mass of the particle.

[3]To calculate luminosity-weighted quantities we use the flux at $\lambda = 5635$Å following the choice done in several studies of the CALIFA galaxies, e.g. González Delgado et al. (2014), Sánchez et al. (2016c), and Ruiz-Lara et al. (2016).

- For star particles older that 10 Myr, spectra from the STARBURST99 Stellar Population Synthesis (SPS) model (SB99, Leitherer et al. 1999) are assigned. To create the input stellar model we have selected the Padova 1994 stellar tracks (Fagotto et al., 1994a; Fagotto et al., 1994b) assuming a Kroupa IMF (Kroupa, 2002) with $\alpha = 1.3$ for $m_{\rm star} = 0.1 - 0.5$ M$_\odot$ and $\alpha = 2.3$ for $m_{\rm star} = 0.5 - 100$ M$_\odot$. The low-resolution spectra (which have sampling ~ 20) have been computed choosing the Pauldrach/Hillier stellar atmospheres, while for the high-resolution region of the STARBURST99 spectra ($3000 - 7000$ with sampling of 0.3) we have used the fully theoretical atmospheres by Martins et al. (2005). The final input stellar model is the combination of the low-resolution spectra for wavelengths $\lambda < 3000$, $\lambda > 7000$, and the high-resolution spectra in the range $3000 \leq \lambda \leq 7000$; the use of a stellar model with different spectral resolutions is motivated by the fact that SUNRISE needs high-resolution spectra to include the effects of the kinematic broadening on the spectral lines, which however is possible only between $3000 \leq \lambda \leq 7000$ with STARBURST99.
- Star particles younger than 10 Myr are assumed to be the source of significant amount of ionizing photons, which are efficiently absorbed by the surrounding gas producing recombination lines and forming an HII region; to these young star particles a modified spectrum is assigned, that takes into account the effects of photo-dissociation and recombination of the gas. The spectra coming from the HII regions are pre-computed with the photo-ionization code MAPPINGS III (Groves, Dopita, and Sutherland, 2004; Groves et al., 2008), and depend several properties of the star particle and the gas surrouning it.

2. After SUNRISE assigns stellar or nebular spectra to all star particles, in the radiative transfer stage randomly-generated photon packets are propagated through the dusty ISM (assuming a constant dust-to-metals ratio of 0.4 according to Dwek 1998) with a Monte Carlo approach. Since in the multi-phase model of the ISM implemented in our hydrodynamical code (Scannapieco et al., 2006) each gas particle has a single temperature, density and entropy (while other ISM models may have cold/hot phases in a given gas particle, e.g. Springel and Hernquist 2003) the amount of dust is directly linked to the total amount of metals in each gas particle (for a discussion of the effects of the ISM sub-resolution structure on radiative transfer calculations see Hayward et al. 2011; Snyder et al. 2013; Lanz et al. 2014). Dust extinction is described by a Milky Way-like curve with $R_V = 3.1$ (Cardelli, Clayton, and Mathis, 1989; Draine, 2003), while for dust scattering the phase function by Henyey and Greenstein (1941) is adopted. The $\sim 10^7$ Monte Carlo rays generated by the SUNRISE algorithm are traced on an adaptive grid made by $\sim 30\,000 - 150\,000$ cells covering a region of (120 kpc)^3 with minimum cell size of ~ 250 pc, calculated assuming in SUNRISE a value of tolerance tol$_{met} = 0.1$ and metals opacity $\kappa = 3 \times 10^{-5}$ kpc^2 M$_\odot^{-1}$ (see Jonsson 2006 for details).

3. Model cameras are placed around the simulated galaxies to sample different viewing angles, obtaining the SED in each pixel for each camera. In our calculations we place cameras with three different orientations (defined according to the alignment of the total angular momentum of the stars with the z direction) for each galaxy, respectively face-on, 45° and edge-on. The flux in the cameras can be convolved with bandpass filters to get broadband magnitudes and images as in Fig. 5.1, which shows the (u, r, z)-band color-composite images of the simulated galaxies in the three orientations; the region of the simulations observed by the CALIFA hexagonal field of view is in red in this figure.

C-CS$^+$

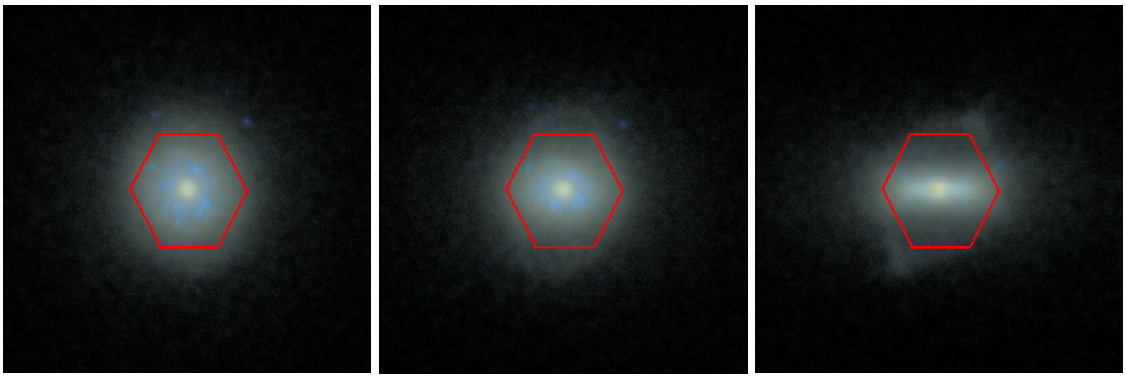

E-CS$^+$

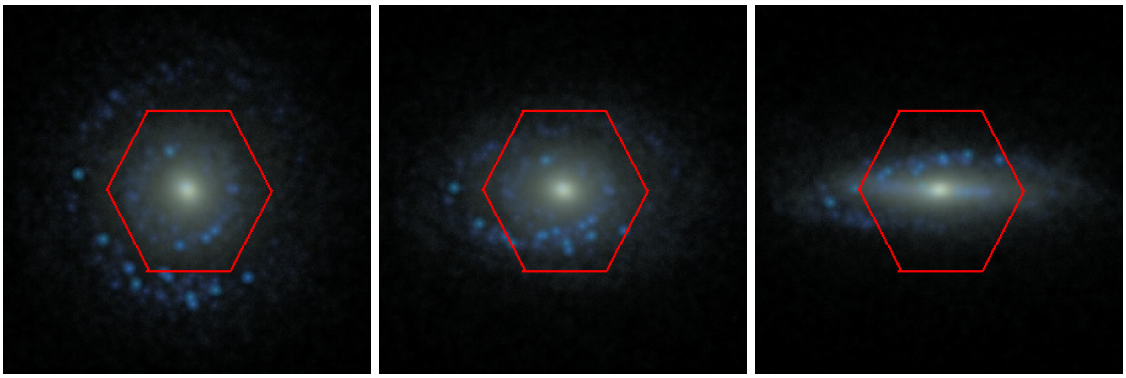

D-MA

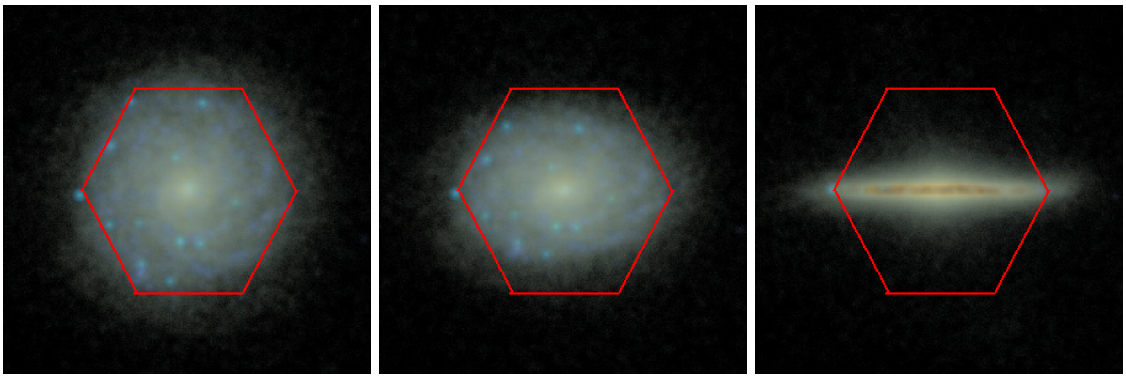

FIGURE 5.1: Composite synthetic broadband images created in the (u, r, z)-bands using the Lupton et al. (2004) composition algorithm for our three simulated galaxies (from top to bottom, C-CS$^+$, E-CS$^+$, and D-MA) in a field of view of 60×60 kpc with 300×300 pixels. The orientations are, from left to right, face-on, $45°$ and edge-on, labelled in the synthetic datacubes as _0, _1 and _2 respectively. The red hexagon is the region of the simulations sampled by the CALIFA field of view, with physical sizes of $\sim 19, 27, 35$ kpc respectively for the C-CS$^+$, E-CS$^+$ and D-MA galaxies.

Measurements on the simulated spectra
As part of the *high-level* product datacubes we also provide resolved maps of some spectral features as measured from the computed *noiseless* (prior to the addition of noise, see Section 5.4.3) stellar-only and gas-only datacubes. The exact procedure is described as follows, and an example of the maps is shown in Figure 5.4), where the emission lines corresponding to the BPT diagram (Baldwin, Phillips, and Terlevich, 1981) (H_α, H_β, [OIII]5007, [NII]6584)) are depicted. Note again that we always include de effect of the spatial PSF in our product datacubes.

- **Lick indices:** we derive the strength of the Lick stellar absorption features from the stellar-only (switching-off the nebular emission), noiseless datacube generated in the CALIFA V500 format (see Section 5.4.2). The measurements are conducted prior to the inclusion of the spectral PSF. A list of these absorption features depicted in Table 5.2.

- **Emission line intensities of the nebular component:** fluxes for the emission lines listed in Table 5.3 are measured from the noiseless IFS synthetic datacubes (CALIFA V500 format) after the subtraction of the stellar component from the noiseless stellar-only datacubes used to derive the Lick indices. We measure the flux of each emission line as the total residual flux integrated in the wavelength range given in Table 5.3 for every line. Note again that we do not consider the effect of the spectral PSF. It is also important to emphasize here that the nebular emission in the datacubes is limited to the stellar particles younger than 10 Myr (HII regions), as we do not count on any other sources of ionizing photons. The results are provided in CALIFA flux units: 10^{-16}erg/s.

In order to reduce the random noise introduced by the SUNRISE Monte Carlo algorithm the simulation process described above is run ten times (both for the high and low-resolution part of the spectra) changing only the random seeds. Once the spaxel size is fixed later on in the process (see coming Section, 5.4) the resulting spectra is averaged over the ten different random realizations

5.4 Virtual observations

In this section we describe the procedure followed to convert the output of the SUNRISE algorithm into state-of-the-art IFS observations. Although the procedure we describe in the following sections is valid for any given IFS observation we aim to reproduce, we choose the CALIFA survey as the dataset to mimic for the present work. We will present now some of the technical properties of the CALIFA - PMAS/PPAK observations and the characterization and further implementation of its observational noise

5.4.1 Field-of-view (FoV)

CALIFA sample selection criteria (Walcher et al., 2014) and observing strategy (three points dither pattern, Sánchez et al. 2012b) were carefully conceived to reach a filling factor of 100% across the FoV and guarantee to cover the entire optical extension of the galaxies up to ~ 2.5 effective radii R_e. The CALIFA datacubes present a typical spaxel physical size of ~ 1 kpc, with a $\sim 77'' \times 73''$ 2D distribution of spectra with $1'' \times 1''$ spatial sampling and 3″ Full Width at Half Maximum (FWHM) spatial resolution (Sánchez et al., 2012a). To reproduce these properties in our synthetic datacubes, we first derive for each object the half-light radius R_{50} in the r-band from low-resolution radiative transfer simulations with

Name	Index Bandpass (Å)	Blue continuum bandpass (Å)	Red continuum bandpass (Å)	Units	Reference
CN_1	4142.125 - 4177.125	4080.125 - 4117.625	4244.125 - 4284.125	mag	Worthey et al. (1994)
CN_2	4142.125 - 4177.125	4083.875 - 4096.375	4244.125 - 4284.125	mag	Worthey et al. (1994)
Ca4227	4222.250 - 4234.750	4211.000 - 4219.750	4241.000 - 4251.000	Å	Worthey et al. (1994)
G4300	4281.375 - 4316.375	4266.375 - 4282.625	4318.875 - 4335.125	Å	Worthey et al. (1994)
Fe4383	4369.125 - 4420.375	4359.125 - 4370.375	4442.875 - 4455.375	Å	Worthey et al. (1994)
Ca4455	4452.125 - 4474.625	4445.875 - 4454.625	4477.125 - 4492.125	Å	Worthey et al. (1994)
Fe4531	4514.250 - 4559.250	4504.250 - 4514.250	4560.500 - 4579.250	Å	Worthey et al. (1994)
Fe4668	4634.000 - 4720.250	4611.500 - 4630.250	4742.750 - 4756.500	Å	Worthey et al. (1994)
$H\beta$	4847.875 - 4876.625	4827.875 - 4847.875	4876.625 - 4891.625	Å	Worthey et al. (1994)
Fe5015	4977.750 - 5054.000	4946.500 - 4977.750	5054.000 - 5065.250	Å	Worthey et al. (1994)
Mg_1	5069.125 - 5134.125	4895.125 - 4957.625	5301.125 - 5366.125	mag	Worthey et al. (1994)
Mg_2	5154.125 - 5196.625	4895.125 - 4957.625	5301.125 - 5366.125	mag	Worthey et al. (1994)
Mgb	5160.125 - 5192.625	5142.625 - 5161.375	5191.375 - 5206.375	Å	Worthey et al. (1994)
Fe5270	5245.650 - 5285.650	5233.150 - 5248.150	5285.650 - 5318.150	Å	Worthey et al. (1994)
Fe5335	5312.125 - 5352.125	5304.625 - 5315.875	5353.375 - 5363.375	Å	Worthey et al. (1994)
Fe5406	5387.500 - 5415.000	5376.250 - 5387.500	5415.000 - 5425.000	Å	Worthey et al. (1994)
Fe5709	5696.625 - 5720.375	5672.875 - 5696.625	5722.875 - 5736.625	Å	Worthey et al. (1994)
Fe5782	5776.625 - 5796.625	5765.375 - 5775.375	5797.875 - 5811.625	Å	Worthey et al. (1994)
Na D	5876.875 - 5909.375	5860.625 - 5875.625	5922.125 - 5948.125	Å	Worthey et al. (1994)
TiO_1	5936.625 - 5994.125	5816.625 - 5849.125	6038.625 - 6103.625	mag	Worthey et al. (1994)
TiO_2	6189.625 - 6272.125	6066.625 - 6141.625	6372.625 - 6415.125	mag	Worthey et al. (1994)
$H\delta_A$	4083.500 - 4122.250	4041.600 - 4079.750	4128.500 - 4161.000	Å	Worthey and Ottaviani (1997)
$H\gamma_A$	4319.750 - 4363.500	4283.500 - 4319.750	4367.250 - 4419.750	Å	Worthey and Ottaviani (1997)
$H\delta_F$	4091.000 - 4112.250	4057.250 - 4088.500	4114.750 - 4137.250	Å	Worthey and Ottaviani (1997)
$H\gamma_F$	4331.250 - 4352.250	4283.500 - 4319.750	4354.750 - 4384.750	Å	Worthey and Ottaviani (1997)
D4000_n		3850.000 - 3950.000	4000.000 - 4100.000		Balogh et al. (1999)

TABLE 5.2: List of the absorption line indices for which the strength in each spaxel is provided, together with the definition of the continuum and bandpass wavelength ranges.

Species	Line center (Å)	Lower/ upper bounds (Å)
[Ne III]3869	3869.060	$3859 - 3879$
Hδ	4101.734	$4092 - 4111$
Hγ	4340.464	$4330 - 4350$
[O III]4363	4363.210	$4350 - 4378$
Hβ	4861.325	$4851 - 4871$
[O III]4959	4958.911	$4949 - 4969$
[O III]5007	5006.843	$4997 - 5017$
HeI 5876	5875.670	$5866 - 5886$
[N II]6548	6548.040	$6533 - 6553$
Hα	6562.800	$6553 - 6573$
[N II]6584	6583.460	$6573 - 6593$
[S II]6717	6716.440	$6704 - 6724$
[S II]6731	6730.810	$6724 - 6744$

TABLE 5.3: List of the emission line intensities provided in the product datacubes. Line centers, lower and upper bounds are taken from the Sloan Digital Sky Survey-Garching DR7 analysis (available at the URL http://wwwmpa.mpa-garching.mpg.de/SDSS/DR7/).

a FoV of 60×60 kpc, and we calculate the physical size of the spaxels assuming that a FoV of $78'' \times 78''$ with spatial sampling $1'' \times 1''$ covers a region up to $2 \times R_{50}$ of each simulated galaxy. We also compute the redshift corresponding to the physical size of the spaxels for the CALIFA $1'' \times 1''$ aperture, assuming the Planck Collaboration et al. (2015) cosmological parameters.

5.4.2 Spectral properties

Before entering the description of the spectral properties reproduced in our synthetic datacubes we note here that SUNRISE is run ten times in every case in order to reduce the random noise. Is in this particular point of the calculation (after the definition of FoV and spaxel size) that we average the spectra in every spaxel, resulting in a signal-to-noise, (S/N, where the noise corresponds to the standard deviation over the ten realizations) of $\sim 300 - 400$ in the central regions and $\sim 8 - 10$ in the outskirts of the objects.

After the averaging is done we begin modifying the spectra. Two different overlapping spectral setups are available in the CALIFA collaboration and will hence be reproduced here: the V500 low-resolution mode covering the range $3749 - 7501$ with sampling $\mathrm{d}_{\lambda 500} = 2.0$ and FWHM spectral resolution $\delta_{\lambda 500} = 6.0$, and the blue mid-resolution setup V1200 that covers the range $3650 - 4840$ with spectral sampling $\mathrm{d}_{\lambda 1200} = 0.7$ and FWHM resolution $\delta_{\lambda 1200} = 2.3$ (Sánchez et al., 2012a; García-Benito et al., 2015a).

To reproduce these spectral properties in the mock datacubes we must first cover their respective *spectral ranges*. However, running SUNRISE including the effects of the stellar kinematics on the spectra is only possible between the wavelengths $3000 - 7000$. To cover the full spectral range of the CALIFA V500 configuration ($3749 - 7501$) we generate two different sets of radiative transfer simulations for each object, one at higher resolution including the kinematics (between $3000 - 7000$), and other at lower resolution (from $\lambda = 7000$ to 7600) without kinematics. We paste the SEDs together at $\lambda = 7000$. This way we are able to cover entirely the CALIFA V500 wavelength range (the V1200 range is fully covered by the high-resolution stellar model), although the redder part of the spectrum has a

spectral resolution lower than the CALIFA sampling. The regions of the spectra generated with the low-resolution stellar model will be flagged as bad pixels in the datacubes (see Section 5.5.2), and should not be used for SED fitting analysis [4].

Then we *redshift the spectra* to the corresponding distance and *resample* them according to the above mentioned spectral sampling. We further remove the wavelengths outside the V500 and V1200 spectral ranges, as well as some of the outer spaxels to obtain a charasteristic 77″ × 73″ hexagonal FoV configuration.

5.4.3 Different sources of noise

Different sources of error are considered and implemented in our datacubes. First, we account for both, spatial and spectral Point Spread Functions (PSF). To do so we convolve the two spatial dimensions of our synthetic 3-dimensional datacubes with a two dimensional Gaussian PSF to account for the 3″ spatial resolution Full Width Half Maximum (FWHM) of the CALIFA observations. We also include the effect of the PSF in the spectral dimension by convolving it with a one-dimensional Gaussian kernel. The known FWHM values for the PMAS/PPak spectrograph are $\delta_{\lambda 500} = 6.0$ and $\delta_{\lambda 1200} = 2.3$ for the V500 and V1200 setups respectively.

We also consider the charasteristic noise of the detector by adding random Gaussian error to the datacubes with zero mean and σ_n standard deviation, as modelled from a sample of CALIFA galaxies. Its precise derivation is described as follows:

Characterizing CALIFA noise

In order to characterize the noise associated to the PMAS/PPak instrument we have considered a sample of 20 objects from the CALIFA survey and performed a spatial and spectral analysis of the error in both the V500 and V1200 setups. The analysed sample covers a set of different visually-classified morphological types (Walcher et al., 2014) consistent of 9 spiral galaxies (3 face-on, 3 edge-on and 3 with intermediate inclination $\sim 45^o$), 7 ellipticals and 4 objects in the process of merging. The results of the analysis show that the dependance of the noise with the intensity of the signal, characteristic of charge-coupled devices, can be modelled with a simple parametric formula:

$$\sigma_n = \sigma_0 \sqrt{1 + \frac{I_n}{I_0}} \tag{5.1}$$

I_n and σ_n refer to the intensity and the noise provided in the CALIFA datacube normalized to the median value of the intensity in the given datacube, i.e. $\sigma_n = \sigma \setminus I_{50}$ and $I_n = I \setminus I_{50}$. We use normalized errors and fluxes in order to obtain a uniform object-independent unit-free characterization of the noise. σ_0 and I_0 are the parameters we aim to fit. The first term σ_0 in the equation is associated to the 'white noise' in the detector, while the second one $\propto \sqrt{I_n/I_0}$ accounts for the Poisson noise (or shot noise), known to be characteristic of photon counting detectors and typically scaling as $\sim \sqrt{I}$.

We fit our data to equation 5.1 and average our results over the 20 objects considered in the analysis. The values obtained (for both setups) are summarized in Table 5.4, together with the main properties of the simulated datacubes: spatial and spectral dimensions (N_α, N_δ, N_λ), spectral sampling (d_λ) and spectral resolution (δ_λ). Fig. 5.2 shows an example of the fitted noise-intensity relation for three of galaxies. White solid line corresponds to the best fitting of our modelled detector noise.

Our analysis also shows that the detector noise does no depend on wavelength, except for expected edge effects. This border effect is not modelled nor included. Artifacts appear

[4] Notice that when we redshift the synthetic spectra we reduce the range of bad pixels, starting from the wavelength $\sim 7090 - 7170$ depending on the redshift of the object.

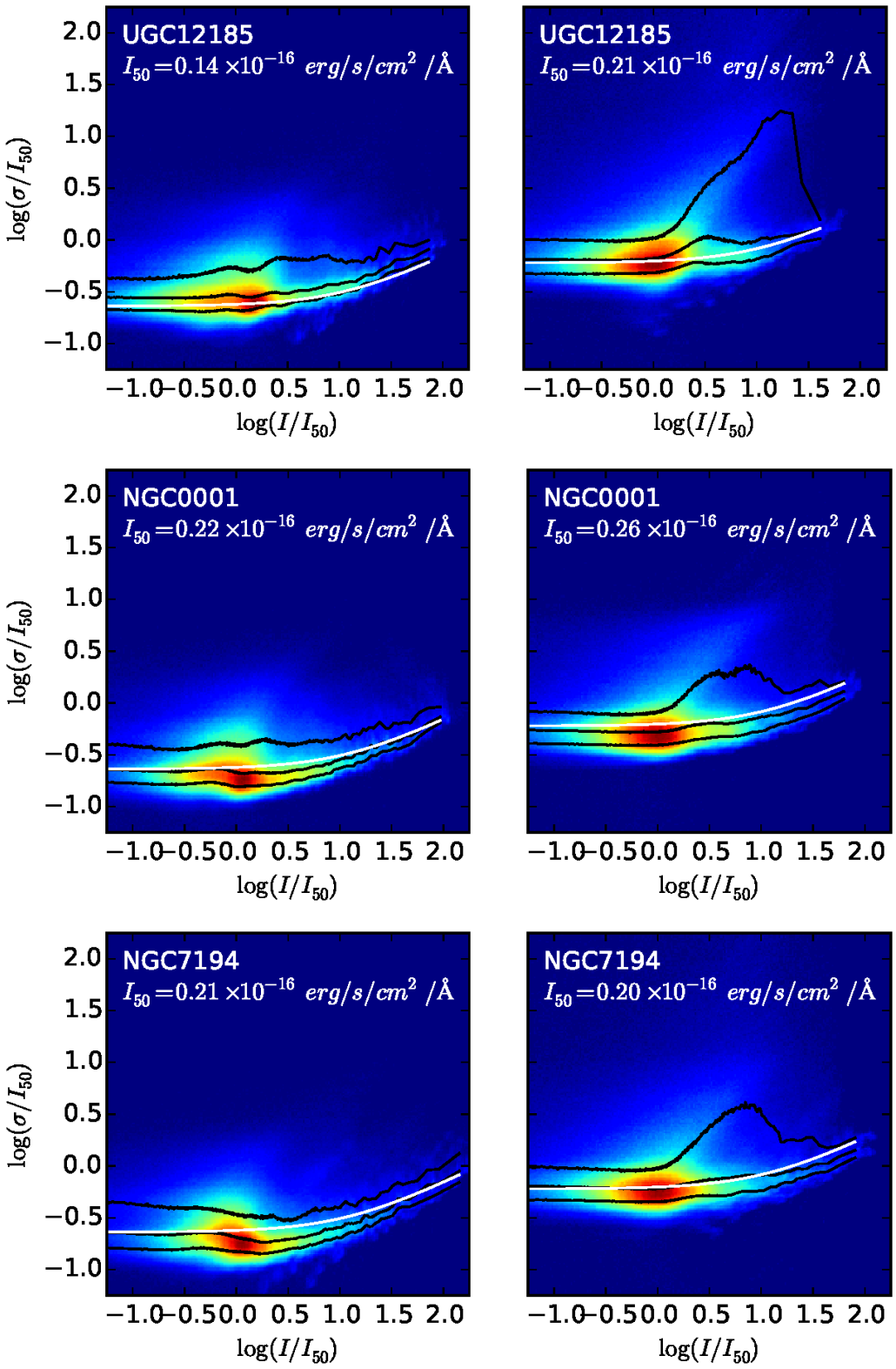

FIGURE 5.2: Color maps showing the distribution of the noise σ relative to the signal I, normalized to the median value of the signal I_{50} (in logarithmic scale) for three out of the twenty galaxies considered to characterize the properties of the noise. Left (right) panels displays the values corresponding to the V500 (V1200) setup. Black solid lines correspond to the median and $\pm 1\sigma$ value of the distributed noise at a given intensity. White solid lines show the best-fit curves, obtained averaging the values fitted for each galaxy over the full sample of 20 objects; the parameters of the white curve σ_0 and I_0 are given in Table 5.4. In these plots the linear colour scale corresponds to the number of pixels in the CALIFA datacubes ($\sim 10^7$ in total both for the V500 and V1200 configuration) at a given signal and noise.

Setup	N_α	N_δ	N_λ	d_λ	δ_λ	σ_0	I_0
V500	77	73	1877	2.0 Å	6.0 Å	0.23	12.10
V1200	77	73	1701	0.7 Å	2.3 Å	0.6	11.26

TABLE 5.4: Sizes of the simulated datacubes in the spatial and spectral dimensions ($N_\alpha, N_\delta, N_\lambda$), spectral sampling and spectral resolution ($d_\lambda, \delta_\lambda$), and the best-fitted noise parameters of equation 5.1 (σ_0, I_0).

when we study the spatial distribution of the noise, probably as a result of an error itn the pointing of the observations and the application of dithering scheme. This effect is impossible to measure and hence it will not be included. Another relevant effect if the well-known noise correlation caused by that dithering scheme (see Husemann et al., 2013; García-Benito et al., 2015a)). Since our goal is to set the basis in order to generate state-of-the-art synthetic IFS data and not to approach the specific problem of combining the PMAS/PPak observations and the CALIFA observational strategy, we will not consider this correlation of the noise.

5.5 The SELGIFS data challenge

The main goal of this work is to provide the scientific community with a reliable set of synthetic IFS observations and corresponding comparable maps of directly measured propeties that allow testing existing (and future) dedicated analysis tools and pose observational strategies to tackle specific scientific problems.

The data are distributed through the web page `http://astro.ft.uam.es/SELGIFS/` hosted by the Universidad Autónoma de Madrid. The description of the different files and their formatting is presented in the following sections:

5.5.1 High-level product datacubes

The direct measurements of resolved (spaxel-by-spaxel) galaxy properties described in Sections 5.2 and 5.3 are provided in separate files. Their names and format are listed below:

GALNAME.stellar.fits: contains the resolved maps obtained directly from the hydrodynamical simulations. The file consists of a single HDU unit holding an 8-layer matrix containing the 8 77 $\times$ 73 maps of the properties described in Section 5.2. The header includes the information about the physical property stored in every layer (DESC_*) and its units (UNITS_*). * reffers to the layer number.

GALNAME.Lick_indices.fits encloses the resolved maps for the 26 Lick indices measured from the noiseless stellar-only datacube (see Section 5.3 and Table 5.2). The file consists of a single HDU unit holding a 26-layer matrix containing the 26 77 $\times$ 73 maps of the different absorption features. The header includes the information about the lick index name (DESC_*) and its measured units (UNITS_*). * reffers to the layer number.

GALNAME.nebular.fits encloses the resolved maps for the 13 nebular lines measured from the noiseless gas-only datacube (see Section 5.3 and Table 5.3). The file consists of a single HDU unit holding a 13-layer matrix containing the 13 77 $\times$ 73 maps of the nebular lines. The header includes the information about the line names (DESC_*), line wavelength in rest frame (LAMBDA_*) and its units (UNITS_*). * reffers to the layer number.

HDU	Extension name	Format	Content
0	PRIMARY	32-bit float	flux density in units 10^{-16} erg/s/cm^2/
1	ERROR	32-bit float	1σ error on the flux density
2	ERRWEIGHT	32-bit float	error weighting factor
3	BADPIX	8-bit integer	bad pixel flags (1=bad, 0=good)
4	FIBCOVER	8-bit integer	number of fibers used to fill each spaxel

TABLE 5.5: Structure of the CALIFA FITS files in DR2 (from García-Benito et al. 2015b).

5.5.2 Synthetic observations

The simulated IFS datacubes described in Section 5.4 are stored in two different files identified following the CALIFA DR2 naming convention: GALNAME.V500.rscube.fits.gz and GALNAME.V1200.rscube.fits.gz for the V500 and V1200 setups respectively. The data structure of the simulated data closely follows the one adopted in CALIFA, namely datacubes in the standard FITS file format. Every fits file contains the data for a single galaxy stored in five FITS HDU (Header Data Units, see Table 5.5), every one of them providing different information according to the data format of the pipeline V1.5 used in DR2 (García-Benito et al., 2015a). The first two axes in the datacubes (N_α, N_δ) correspond to the spatial dimensions (along the right ascension and declination) with a 1" $\times$ 1" sampling. The third dimension (N_λ) represents the wavelength axis, consistent with the discussed wavelength ranges and spectral samplings depicted in Table 5.4. Here we summarize the content of each HDU:

0) Primary (PRIMARY)
The primary HDU contains the measured flux densities in CALIFA units of 10^{-16} erg s^{-1} cm^{-2}Å^{-1}.

1) Error (ERROR)
This extension provides the values of the 1σ noise level in each pixel, calculated according to Eq. 5.1. In the case of bad pixels, we store a value of 10^{10} following the CALIFA data structure.

2) Error weight (ERRWEIGHT)
In the CALIFA datacubes, this HDU gives the error scaling factor for each pixel, in the case that all valid pixels of the cube are co-added; in our case we set all the values to 0.

3) Bad pixel (BADPIX)
This extension stores a flag advising on potential problems in a pixel; in the CALIFA dataset this may occur for instance due to cosmic rays contamination, bad CCD columns, or the effect of vignetting. In our datacubes we flag as bad pixel (i.e. equal to 1) the regions in the spectra that are generated with the lower-resolution stellar model (see Section 5.3).

4) Fiber coverage (FIBCOVER)
This HDU, available only from DR2, accounts for the number of fibers used to recover the flux, and is set to 0 in our mock datacubes.

FITS header informations

The FITS header of the simulated datacubes stores only the most relevant keywords available in the DR2 header. Most of the DR2 keywords containing informations about the pointing, the reduction pipeline, galaxy extinction, sky brightness, etc. have been removed. In addition to the mandatory FITS keywords, we store in the primary HDU the information about declination and right ascension of the object (according to the Greisen and Calabretta 2002 standard). We give arbitrary values to these two parameters to avoid problems with visualization tools. The flux unit has been stored under the keyword PIPE UNITS as in the CALIFA datacubes, and also under the keyword BUNIT following the most recent FITS file keywords definition by Pence et al. (2010).

5.5.3 Ageing, quenching and the SELGIFS data challenge

This work is of paramount importance for our given scientific problem. The synthetic datacubes we have generated, even taking into account that the simulated galaxies may not be fully realistic and the degeneracies associated to the SUNRISE radiative transfer technique, have the power to provide crucial information about the *ageing* process. As we know the physical properties (age, metallicity, mass, gas content, star formation history, etc) associated to every defined region of the simulated dataset, we can connect them to its location in the color-equivalent width diagram and verify our interpretations. Besides, this dataset has the power to optimize our analysis by indicating whether there are other SSFR indicators, such as the Hδ absorption line, the D4000 index or other colours, that are better for our analysis, i.e. clearer indicators of the *ageing* process and suitable candidates for alternative"ageing diagrams". Finally, this work can also be used to prepare future observations, as it can provide information about the physical scales involved in the process (larger or smaller spatial resolution, brighter or fainter features that require different exposure times, etc.)

5.6 Conclusions

In this last chapter of the thesis we have presented the *"Selgifs Data Challenge"*, a project led by G. Guidi in which we use hydrodynamical simulations of galaxies formed in a cosmological context to generate synthetic Integral Field Spectroscopy observations mimicking the properties of the CALIFA survey (Sánchez et al., 2012a).

In particular, we have post-processed simulation snapshots with the radiative transfer code SUNRISE in order to obtain their spatially-resolved spectral energy distributions. These spectra contain the light emitted by the stars and the nebulae (young stars) in the simulations, and consider the broadening of the absorption and emission lines due to kinematics, as well as the extinction by the dust in the ISM. The input parameters in SUNRISE have been tuned to reproduce the properties of the CALIFA instrument in terms of field of view size, number of spaxels and spectral range. After we obtain the results of the radiative transfer, we adjust the simulated spectra to the redshift matching the physical size covered by the spaxels and the angular resolution of the PMAS instrument and we cut and resample its wavelength range and sampling to mimic both CALIFA observational setups. We also reproduce the instrumental spatial and spectral PSF of the CALIFA sample by convolving our 3-dimensional datasets with 2D/1D Gaussian PSFs in the spatial/spectral dimension. Finally, we include the detector noise in our synthetic datacubes by adding gaussian random noise as modelled from a sample of 20 galaxies extracted from the CALIFA sample (considering both setups, V500 and V1200)

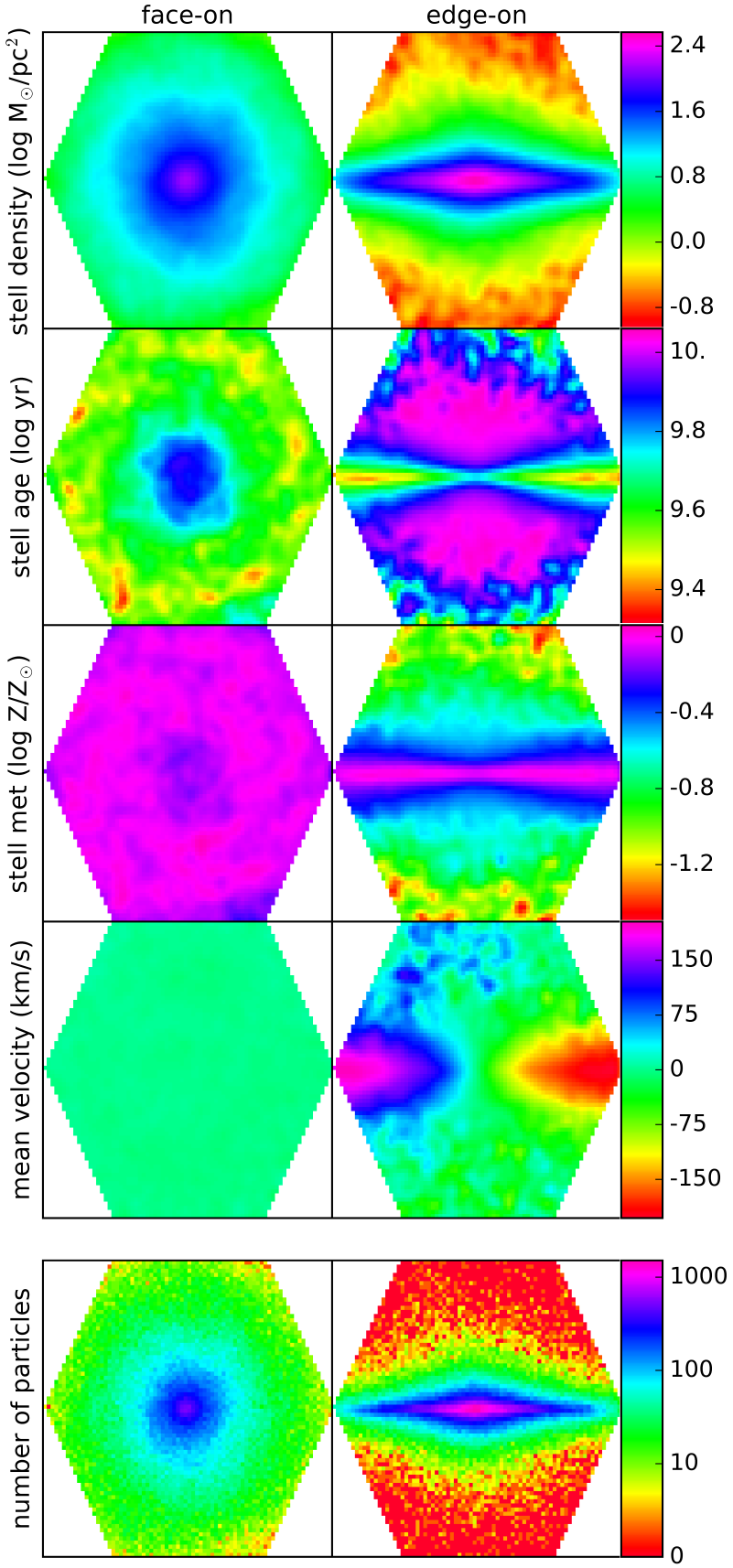

FIGURE 5.3: Spatially-resolved stellar properties of two simulated galaxies, D-MA_0 (face-on) on the left and D-MA_2 (edge-on) on the right. These maps show, from top to bottom, the stellar mass density, the mean luminosity-weighted ages and metallicities, the mean velocity along the line of sight, and the number of stellar particles in each spaxel (in logarithmic colour scale).

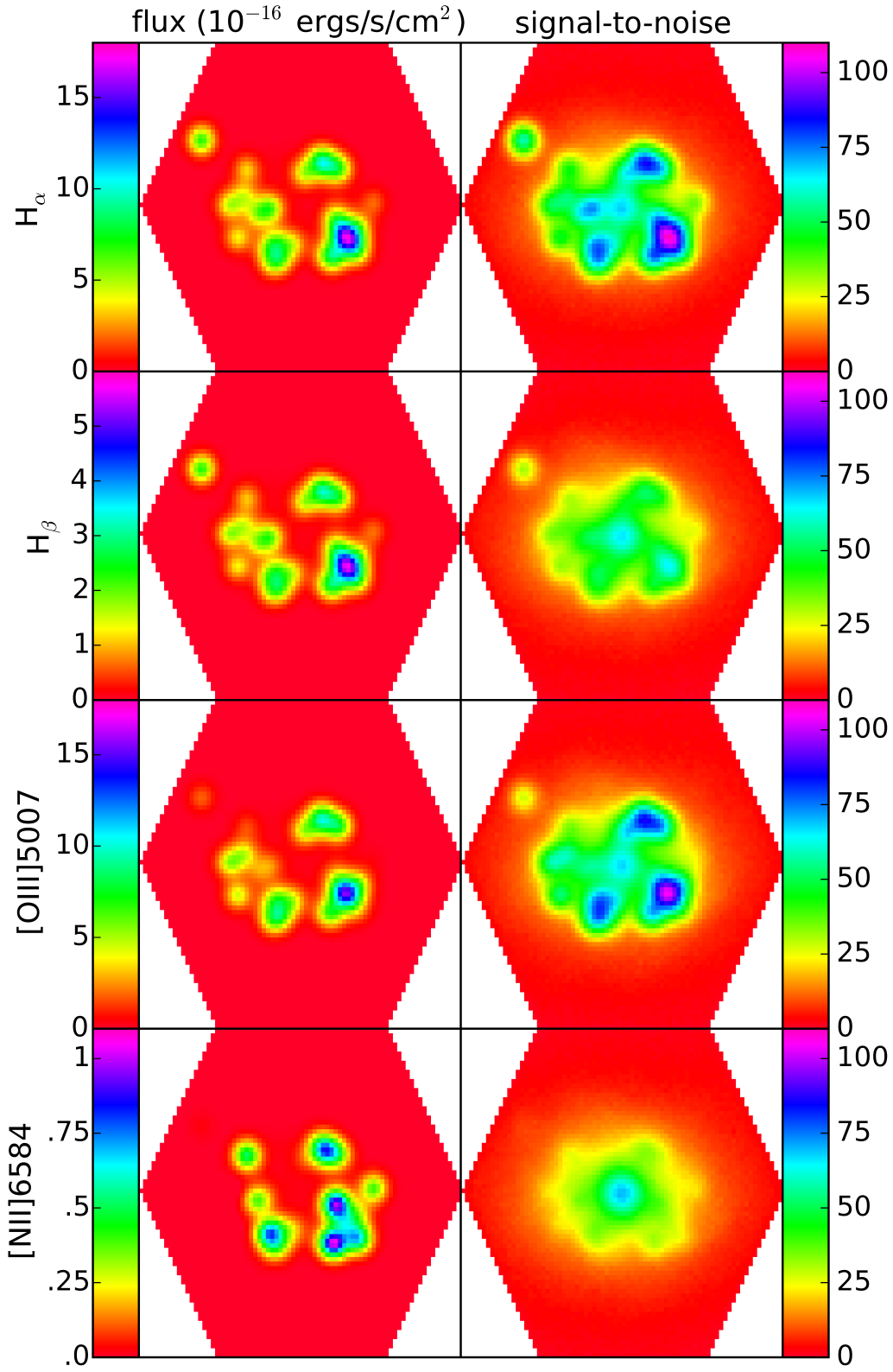

FIGURE 5.4: Maps of the intensity the BPT nebular emission lines for the galaxy C-CS$^+$_1, together with the corresponding maps of the signal-to-noise, calculated as the mean of the signal-to-noise on the wavelength region of the corresponding line.

Our final sample consists of 18 datacubes (3 objects with 3 different orientations and formated in the two observational setups). We generate and provide, together with the synthetic IFS observations, a corresponding set of *high-level* product datacubes, i.e. resolved maps of several properties computed directly from the simulations and/or simulated noiseless datacubes. We aim to provide observers with a powerful benchmark to test the accuracy of their analysis tools and set the basis for a reliable comparison between simulations and IFS observational data.

Although this work is specifically designed to reproduce the properties of the CALIFA observations, the method illustrated in this paper can be easily extended to mimic other integral field spectrographs such as MUSE (Bacon et al., 2004), WEAVE (Dalton et al., 2014), MANGA (Bundy et al., 2015) or SAMI(Allen et al., 2015). The present project can also be extended to use other hydrodynamical simulations, which will be very important in order to enlarge the given the dataset and consider a more complete sample in terms of galaxy total mass, gass content, merger history, etc.

With respect to the scientific scope of the thesis, this work will be critical in order to confirm the proposed *ageing* hypothesis and guide our further efforts in this respect. The provided data may be used for almost any scientific project involving IFS data, as it will help to optimize their analysis and to interpret the observed trends. Moreover, it can also be used for other purposes, such as preparing future observations, and we hope that, in general, it contributes to encourages collaboration among observers and simulators.

Chapter 6

Summary and outlook

The field of galaxy formation and evolution has experienced a rapid growth in the recent years. From the observational side, the large samples obtained by magnitude-limited surveys (such as e.g. SDSS) have enabled statistically-robust analyses that have shed light on the properties of galaxies in the local universe and the processes they undergo, leading to new hypotheses and evolutionary scenarios. Simultaneously, the advent of integral-field spectroscopy has provided a vast amount of high-quality, spatially-resolved data (CALIFA, MUSE, MaNGA, etc.) that have opened the door to a complete new field of study, not only in terms of galaxy evolution but even in terms of the data analysis itself (this thesis is a good example of it). The theoretical side has also experienced great progress. Multiple simulation projects (Aquarius, Eagle) are now capable of generating realistic galaxies in large cosmological volumes (thanks in part to advances in computational resources, both hardware and software, as well as to an improved understanding of the physics), providing the necessary framework for a meaningful comparison between theory and observations.

In this dissertation we approach galaxy evolution by analysing global and local properties of galaxies with the ultimate goal of disentangling the physical mechanisms that drive star formation. To tackle this scientific problem we use a sample of galaxies extracted from SDSS and a reduced set of integral-field spectroscopy (IFS) observations from the CALIFA survey. As a main result of this study we highlight the concept of *ageing* (secular evolution driven by gas consumption) and suggest its universality among galaxies. The inclusion of IFS observations in our analysis led us to explore new approaches in the analysis of these kind of data. This work illustrates both the power and the complexity of such analysis, as well as the need for dedicated tools and their careful calibration.

The present thesis can be divided in two parts: a first one focused in the analysis of observational data (Chapters 2 and 3) and a second one devoted to the design of analysis and calibration tools for IFS observations. The following sections summarize the main results of both strands of work and pose a set of future projects.

6.1 The gentle evolution of galaxies

6.1.1 Ageing in the SDSS

The work presented in Chapter 2 is a statistical study of galaxy evolution that focuses on the self-regulation of star formation in the local universe, and it served as inceptive step for the entire work covered in this thesis dissertation. We selected a sample of ~ 82000 galaxies from the SDSS DR7 spectroscopic catalogue, applying a selection criteria that restricts our sample in apparent magnitude, redshift, and position in the sky to ensure a robust environmental characterization. This sample is further classified into four different types depending on their location in the BPT diagram: *star-forming*, *passive*, *agn* and *intermediate* (this last subsample encloses systems with low S/N in the spectral lines involved in the above mentioned diagram).

- The analysis of the *star-forming* subsample suggests that the evolution of these systems is dominated by internal processes, i.e. 'nature', as we do not find, on average, any statistically-significant signature of external factors ('nurture') driving their SSFR.
- A second result, and a very important one for the evolution of this thesis project, reveals that the restriction in signal-to-noise used to define our *star-forming* subsample creates an artificial bimodality when comparing *star-forming* and *passive* galaxies. The inclusion of the *intermediate* population leads to the discovery of the *ageing* sequence and emphasizes the need of considering (carefully) low signal-to-noise data (this result led to the work presented in Chapter 4).
- A complete analysis of multiple galaxy properties (mass, metallicity, morphology, interactions, environment and SSFR) for this statistically robust sample leads us to the following conclusions:

    1. In low-density environments, most present-day galaxies are distributed along a relatively narrow 'ageing sequence' in the EW(Hα)-($u-r$) plane. At the 'chemically young' extreme (blue colours and high equivalent widths), galaxies have high SSFR, display low metallicities, and present late-type or uncertain morphologies. Conversely, at the 'chemically old' extreme, galaxies tend to display elliptical morphologies because the SSFR is insufficient to rebuild a significant disk.
    2. A secondary 'quenched sequence' shows up in dense environments, consistent with a very rapid truncation of the star formation activity. Most of the objects in this possible 'quenched' phase display early-type or uncertain morphologies.

The results of this initial work are consistent with a scenario where 'nature' is more important than 'nurture' in regulating star formation in galaxies. We then propose *ageing* as an *unavoidable* evolutionary process, still compatible with galaxies being 'quenched' in dense environments and/or suffering 'rejuvenation' episodes associated to (nature- or nurture-induced) extreme bursts of star formation. The ability to return to the 'ageing sequence' after such events is linked to the external gas supply. Galaxies would become 'red and dead' either when they exhaust their gas reservoir and have negligible specific star formation (end of the 'ageing sequence') or when they suffer a quenching event in a dense environment and they are no longer capable of accreting gas ('quenched sequence'). Mergers and galaxy-galaxy interactions may temporarily affect the instantaneous SSFR, but they merely seem to add statistical fluctuations to the main relation.

6.1.2 Ageing in CALIFA galaxies

In Chapter 3 we present a continuation of the work conducted in Chapter 2, extending the study of the colour-equivalent width diagram and the process of *ageing* to galaxies observed within the CALIFA collaboration, using the broad coverage of CALIFA observations ($\sim 2R_e$) to verify the process of *ageing* on resolved scales and study it to a greater extent within these objects.

We consider 24 galaxies from the set of 41 objects studied in Chapter 2 that are included in the CALIFA main sample. As these galaxies are restricted to the redshift range $z \sim 0.02 - 0.03$, the field of view of the PPAK/PMAS instrument (hexagon of $65'' \times 74''$) ensures a physical coverage of the order of $\sim 28 - 40$ kpc. These objects are characterized in terms of mass, morphology, and environment similarly to the analysis conducted with SDSS galaxies. To this aim we also make use of ancillary data available within the CALIFA collaboration in addition to some of the observational proxies derived in the previous

work. STARLIGHT (stellar population synthesis algorithm) and SHIFU (line fitting software) are used to analyse and derive galaxy properties from our IFS datacubes, such as EW(Hα), galaxy colours, etc. The BATMAN binning algorithm is also used to verify the observed trends and reduce the scatter in the *ageing* diagram. A complete study of the loci of the different regions (spaxels) of every galaxy in the colour-equivalent width diagram is conducted in terms of local (surface brightness) and global (morphology, environment, and total stellar mass) properties. The results obtained show that:

- The morphological (Galaxy Zoo project), environmental ($R_5/\bar{r}$ criteria) and mass (M_r) characterizations employed in Chapter 2 are consistent with the different proxies used within the CALIFA collaboration.
- Aperture effects in SDSS data are not only large but terribly misleading when considering the position/location of an object in the colour-equivalent width diagram.
- *Ageing* is not limited to the brightest regions of galaxies, typically targeted by the SDSS fibre, but takes place across the galaxy (at least, to the entire extent covered by the field of view of the PMAS instrument). Although affected by scatter, most of the individual spaxels are located within the 90% density contour obtained for the 10^5 SDSS galaxies analysed in Chapter 2.
- The resolved colour-equivalent width diagram of any given galaxy depends on its environment, morphology and total mass (global properties), reinforcing the results based on SDSS spectra. In particular:
  1. Regions (spaxels) of isolated late-type objects populate the "primitive" part of the ageing sequence.
  2. Early-types systems, regardless of the environment they reside in, populate the "evolved" part of the sequence.
  3. Some of the "intermediate" objects depict a steeper trend in the diagram, that could be related to a faster evolutionary phase.
- For every object, though, the regions broadly spread in the colour-equivalent width diagram, showing a dependence with the local surface brightness. Central parts of galaxies, displaying higher surface brightnesses, tend to be located in the "evolved" part of the sequence, while the outer counterparts show higher EW(Hα) and bluer colours consistent with star formation (even mild SF in the case of early-type systems). This result suggests that the physical mechanism(s) responsible for the evolution of galaxies (and hence, the *ageing* process) behaves in an inside-out fashion.

To sumarize, the process of *ageing* first proposed in the analysis of the SDSS galaxy sample is verified in this secondary work. This gentle evolutionary process takes place across the entire galaxy and depends on both, local and global properties. This work emphasizes the fact that Integral Field Spectroscopy has the power to unravel new physics taking place on resolved scales. Conversely, it also poses the need of new tools that carefuly analyse this new type of data to obtain the maximum benefit.

6.2 New tools for new data

6.2.1 BaTMAn and the low signal-to noise IFS data

In Chapter 4 we present BATMAN (Bayesian Technique for Multi-image Analysis), a new binning tool designed to characterize and coherently tessellate simultaneously many layers

of a given multi-image (i.e. a generalized version of an IFS datacube). The idea of developing BATMAN algorithm arises from the need to carefully analyse the low signal-to-noise areas that appear in extended resolved observations of galaxies (e.g. outskirts of galaxies in the CALIFA sample presented in Chapter 3).

This work comprises two separate parts, the mathematical formulation of the binning technique and its testing using synthetic and real data. BATMAN's tessellation algorithm follows a different philosophy with respect to other existing binning tools, as it attempts to identify spatially-connected regions that are statistically consistent with carrying the same information (measurements and corresponding errors). BATMAN is conceived to bin our data "only" if possible, with the ultimate goal of avoiding unnecessary loss of information. The posed test cases considered are specifically devised to test the performance of the segmentation tool and provide some guidance for its further use. This analysis allows us to conclude that:

- In all our test cases, the output tessellations successfully adapt to the spatial structures present in the input data for a wide variety of morphologies, regardless of the statistical properties of the noise. Nevertheless, the optimal segmentation does depend on the precise choice of the input data set. It is thus of paramount importance to investigate the information that should be considered relevant as a preliminary step of any scientific analysis.

- Our synthetic tests show that the mean values for the intensity within each region, estimated from the posterior probability distribution, provide a good representation of the true signal, whereas the formal errors, although indicative of the true uncertainties, may underestimate them by a factor of the order of two. The tests conducted with real astronomical data reveal that BATMAN may be most helpful in the low S/N regime (e.g. reduction of the noise with respect to the original data is clearly visible in the galaxy outskirts).

- When BATMAN is applied to the CALIFA datacubes prior to measuring colours and equivalent widths, the number of regions and the associated scatter are significantly reduced (specially in the outer parts). All the trends observed in the spaxel-by-spaxel analysis persist, confirming the robustness of the results and the successful performance of binning algorithm. In addition, it is now clearer that there may be different paths through the colour-equivalent width diagram and that many galaxies contain extended regions along both the "ageing" and "quenching" sequences.

To summarize, one of the main objectives of this work is to approach IFS binning in a new way, with the ultimate goal of preserving all the statistically-significant information contained in the original data. This philosophy represents a novel and much needed approach to the analysis of astronomical images, which we believe will be of crucial importance in the advent of the vast amount and spatial resolution of IFS data to come.

6.2.2 Synthetic IFS observations

In Chapter 5 we present the *"SELGIFS Data Challenge"*, a project led by G. Guidi that proposes a pioneering approach to connect integral-field observations and state-of-the-art hydrodynamical simulations. This project aims to set the basis for a coherent comparison between the two types of data and provide the scientific community with reliable synthetic IFS datacubes that allow testing analysis tools. The success of this work is of paramount importance. On the one hand, it will facilitate the use of simulations to interpret observations and to study the effects of different physical processes that galaxies undergo on their

observable properties. On the other hand, a reliable comparison between the two datasets is crucial to test the different recipes implemented in the hydrodynamical codes (specially in the sub-resolution regime).

In this work we use three hydrodynamical simulations of galaxies re-simulated using the zoom-in technique on three Milky way-like halos selected from the Aquarius dark-matter only simulation. These simulated objects have been post-processed with the radiative transfer code SUNRISE in order to obtain the spectral energy distributions associated to the stellar particles. Three different orientations are considered for every given object. This "virtual observations" attempt to mimic the properties of IFS observations from the CALIFA survey and account for stellar emission and absorption features, nebular emission, dust extinction, and line broadening due to kinematics.

We provide a final sample of 18 datacubes: 3 objects in 3 different orientations and formatted in the two observational setups available in the CALIFA survey (V500 and V1200). To generate these datacubes we have considered the following observational properties, specific of the PMAS/PPak instrument (but the procedure is extensive to any given IFS survey):

- *Physical size within the field-of-view*. Objects are virtually "placed" at a certain redshift so that the characteristic PMAS/PPak FoV ($\sim 78'' \times 78''$) covers a region of approximately $2R_{50}$ for every simulated galaxy. The spectra generated with SUNRISE are redshifted to match this value.

- *Spatial and spectral resolution*. The effects of the spatial and spectral point spread functions are included by convolving our datacubes first in the spatial dimensions with a 2D Gaussian kernel of 3" FWHM and later in the spectral direction with a 1D Gaussian with FWHM values $\delta_{\lambda 500} = 6.0$Å and $\delta_{\lambda 1200} = 2.3$Å for the V500 and V1200 setups, respectively.

- *Detector noise*. We finally include random Gaussian error in our data to account for the detector noise, using a simple model of the error variance based on the analysis a sample of 20 CALIFA galaxies (considering both setups).

A key aspect of this work is that we also generate and provide what we refer to as *high-level* product datacubes, i.e. 2-dimensional maps of some galactic properties computed directly from the simulations and/or measured directly from noiseless versions of the synthetic datacubes. These product datacubes provide observers with a "solution" to test the accuracy of their analysis pipelines and open the way for a meaningful comparison with the theoretical results provided by numerical simulations. The advent of new IFS data (MUSE, WEAVE, MANGa, SAMI, etc.) and large hydrodynamical simulations (EAGLE) makes the present time ideal to work on this synergy. We believe this type of detailed comparison is necessary, and we hope that the robustness and versatility of the methodology proposed in this work to generate mock IFS observations facilitates collaboration at the always exciting interface between theory and observation.

6.3 Outlook

The scientific work conducted in this thesis dissertation leaves a generous number of unsolved questions, and it can (should) be extended in several aspects. A crucial piece still missing in the puzzle of *ageing* in galaxies is:

- *Reproduce and interpret the process of ageing from theory*
  It is of paramount importance to verify the process of ageing from the theoretical

point of view. To this purpose we propose to use both simple analytical models as well as state-of-the-art cosmological hydrodynamical simulations (in connection with the work conducted in Chapter 5) to investigate what physical conditions (if any) may be able reproduce the colour-equivalent width diagram observed on resolved scales and the connection with global galactic properties (Chapter 3).

However, the are many other interesting projects (some of them ongoing). From the observational point of view, we would like to:

- *Extend the IFS sample*
  We aim to extend the study of the *ageing* process by considering the entire CALIFA dataset, 900 galaxies (main and extension samples). We would like to also consider data from the AMUSING survey (MUSE) and other available IFS samples such as MaNGa, CARS, etc., depending on availability. In all cases, a complete and consistent environmental and morpho/kinematical characterization of the selected sample will be required.

- *Study the timescales involved in the process of ageing*
  In order to study in greater detail the timescales involved in the "ageing" process we will consider other SSFR proxies, such as the Hδ absorption line, the D4000 index, or other galaxy colours. This, together with the estimation of other resolved galaxy properties, such as the mass, metallicity, age, kinematics, gas content, etc. can shed light on the physical processes playing a major role in driving galaxy evolution.

From the theoretical point of view:

- *Implement diffuse emission in the synthetic observations*
  The nebular emission included in the *SELGIFS data challenge* (synthetic IFS datacubes) is only associated to the youngest stellar particles in the simulation (ages < 10 Myr). It is then restricted to very compact regions in the virtual observations. It will be of great interest to include the radiation emitted by the Diffuse Ionized Gas (DIG) in order to obtain more realistic synthetic spectral energy distributions (SEDs) and be able to trace the gas component in our synthetic IFS observations to the entire extent of the objects.

- *Extend the SELGIFS data challenge*
  Our goal in this case is to continue the work conducted with the Aquarius simulation by creating a much more ambitious survey of synthetic observations. We aim to use other galaxies in the Aquarius suite and hopefully include some galaxies from the Eagle simulation project. This project will consist in two separate phases:

  1. Extend the existing galaxy sample. The preliminary catalogue of observations consists of only 3 galaxies that have evolved peacefully in almost absolute isolation. We propose to consider a "complete" sample of simulated objects based on the aspects we believe are relevant for the study of galaxy evolution. That is, we need a larger sample that encompasses objects with different masses, living in different environments, that have undergone different merging histories and that depict different gas contents (which we expect is of paramount importance). This is an ongoing project for which we have already applied, together with Dr. Noam Libeskind in the Leibniz Institute for Astrophysics Potsdam (AIP), to get access to the EAGLE simulation data (that has already provided promising scientific results related to the proposed problem).

2. Time evolution in the existing catalogue. Once we have gathered a complete set of galaxies, it will be also very useful to consider different redshift cuts in the simulation. If we can combine this project with the theoretical recovery of the *ageing* in galaxies, this approach will allow us to study the evolution of the "ageing" process in the simulated objects.

The use of galaxy simulations will allow us to study how "local" and "global" properties of galaxies affect different star formation histories (SFH) and the secular evolution of galaxies, as well as whether/how it can be recovered from the observed colour-equivalent width diagram (and/or any other proxies of the recent/past star formation activity). Although this kind of research is certainly not new, we hope that the combination of the simulations, the analytical models, the generation of synthetic IFS datacubes, and the comparison with state-of-the-art IFS observations will provide a renewed focus on the topic.

Finally, from a technical and philosophical point of view, in Chapter 4 we raise the question of *how IFS data should be approached in order to extract the maximum knowledge without biasing our results and/or losing information*. BATMAN algorithm is a powerful tool to help us address that problem at the earliest stage, and we aim to squeeze it to discover:

- *The multiple uses of* BATMAN
  In Section 4.6 we present some preliminary results showing some of the plausible uses of BATMAN. A detailed and comprehensive study on how the BATMAN algorithm can be used to improve the measurement of weak lines, study the kinematics from integrated spectra, disentangle multiple populations, etc. will be of paramount importance to understand both the performance of the binning tool and, more importantly, what are the limits of the science that can be done with a given IFS dataset. By combining the extension of the SELGIFS data challenge with a thoughtful use of the BATMAN algorithm, we will attempt to shed some light on the minimum observational requirements to reliably measure the most relevant physical processes. Those measurements, rigorously compared to the results of numerical simulations, will eventually constrain the main mechanisms that are responsible for galaxy formation and evolution.

Chapter 7

Closing Remarks

From a philosophical point of view, this thesis work presents two main ideas that pose a change in the established paradigm of galaxy evolution and the way in which astronomical data are handled.

On the one hand, we argue that the process of "ageing" is the main mode of galaxy evolution. According to our results, star formation in galaxies is regulated by the secular consumption of the cold gas reservoir (nature) and does not require of any "external" mechanism (nurture: e.g. mergers, harassment, ram-pressure stripping). Contrary to the widely accepted view, we reject the idea that a discrete quenching event drives any transition from a star-forming to a passive state. Actually, we do deny the existence of such a bimodality in the galaxy population. Instead, we claim that the "ageing" process leads to a smooth, continuous distribution of galaxy colours and masses and that the observed bimodal distribution is to a great extent the result of a selection effect. Moreover, we conjecture that the ability of the galaxy to accrete gas would control the "ageing" process and may be responsible for the morphology of the system. Thus, galaxy morphology might be a "consequence" of the physical processes taking place in the galaxy (and not its cause), which is a new approach that we hope will be considered in future work in the field.

On the other hand, we also present in this work a new strategy to handle integral-field spectroscopy data. We aim to illustrate in this manuscript the need of revisiting the design and calibration of astronomical analysis tools in the advent of the new data to come. Integral-field spectroscopy has the power to unravel physical processes that so far have been hidden in the spatial "sub-resolution" regime. However, we will not be able to extract all this valuable information if we do not analyse the data in a coherent and statistically-robust manner. In this sense, we would like to argue that simulations provide an excellent benchmark to test existing and forthcoming analysis pipelines and verify not only their results but also the estimated uncertainties, whose importance can hardly be overstressed.

Chapter 8

Traducción: Resumen y conclusiones

8.1 Resumen

La presente tesis aborda el tema de la formación y evolución de galaxias con el objetivo de clarificar cuál es el mecanismo (o los mecanismos) responsable de regular la formación estelar en el universo local.

En primer lugar volvemos a plantear el debate clásico "nature or nurture", naturaleza o crianza, en el contexto de la evolución galáctica. Para ello analizamos una muestra de $\sim$82000 galaxias extraídas del catálogo Sloan Digital Sky Survey. En nuestro análisis relacionamos dos indicadores de la tasa de formación estelar específica (specific star formation rate, SSFR), el ancho equivalente (EW en sus siglas en inglés) de la línea Hα y el color (u-r), con otras propiedades físicas de las galaxias: masa, metalicidad, entorno, morfología y la presencia de vecinos cercanos. Este estudio da lugar al descubrimiento de la llamada "secuencia de envejecimiento" ("ageing sequence") en el plano color-EW. Dicha secuencia favorece un escenario evolutivo en el que la conversión gradual del gas en estrellas (proceso natural/intrinseco) es la principal responsable de regular la formación estelar en las galaxias. Asimismo, será responsable también de transformar las galaxias de su estado "primitivo", en que son pobres en metales y forman estrellas intensamente, a un estado más "evolucionado", en que son más ricas en metales y forman estrellas de manera más suave, "evolucion pasiva".

De cara a estudiar cómo dependen los resultados anteriores de las propiedades locales y globales de las galaxias, investigamos en detalle el diagrama color-EW, esta vez a escala resuelta, para una muestra de $\sim$40 objetos de la colaboración CALIFA (incluidos también en el estudio anterior). Los datos de espectroscopía de campo integral (IFS en sus siglas en inglés) revelan que el proceso de "envejecimiento" ("ageing") tiene lugar de dentro hacia afuera (las partes centrales de las galaxias muestran signos de estar más evolucionadas) y que está presente en toda la galaxia. La posición (y por tanto el estado evolutivo actual) de cada una de las regiones analizadas en las galaxias parece estar determinado por procesos a escala local. No obstante, las propiedades globales las mismas (y en especial su morfología) parecen jugar también un papel relevante.

El empleo de datos con baja señal ruido (signal-to-noise, S/N) ha sido crucial en la obtención de los resultados anteriores. Por ello, de cara a extraer de manera óptima toda la información de este tipo de datos, hemos desarrollado el algoritmo de segmentación multidimensional BaTMAn ("Bayesian Technique for Multi-image Analysis"), con la intención última de binear de manera coherente observaciones de espectroscopía de campo integral. Al aplicar el algoritmo a nuestros datos hemos reducido de manera significatica la dispersión en el diagrama color-EW y demostrado convincententemente que existen diferentes tendencias en el mismo, dependientes de los detalles de la historia de formación estelar a escala local.

Desde nuestro punto de vista, la aparición de nuevas (y numerosas) observaciones que

usan la técnica de espectroscopía de campo integral requiere del desarrollo de nuevas herramientas y metodologías. Estas requerirán, a su vez, de un riguroso calibrado (tanto de las medidas como de sus errores asociados) y por tanto, de un conjunto de casos de prueba cuya solución sea conocida. A tal efecto, la parte final de esta tesis describe la producción de observaciones sintéticas (IFS) a partir de simulaciones hidrodinámicas de galaxias y que reproducen las propiedades de las de la muestra de CALIFA. Este proyecto (en curso) nos permitirá explorar la estrategia óptima para estudiar el "envejecimiento" en las galaxias con datos de IFS (existentes y futuros) y proporcionará a la comunidad científica una herramienta para verificar el correcto funcionamiento de las herramientas de análisis.

8.2 Conclusiones finales

Desde un punto de vista filosófico, la presente tesis doctoral presenta dos ideas que suponen un cambio en algunos planteamientos establecidos en la comunidad científica, tanto en relación con las hipótesis sobre la evolución de las galaxias como en la manera en que analizan típicamente los datos astronómicos.

Por una parte, en el presente trabajo sostenemos que el llamado proceso de "envejecimiento" ("ageing") que tiene lugar en las galaxias representa su principal modo evolutivo. Tal y como muestran nuestros resultados, la formación estelar en las galaxias está regulada por el consumo gradual del gas frío disponible en la galaxia y no requiere de ningun mecanismo externos ("nurture/crianza": mergers, harrasment o ram-pressure stripping). En contra de la opinión general, nosotros rechazamos la hipótesis de que un evento discreto sea el responsable de "enfriar" ("quench") la formación estelar en las galaxias y transformarlas en objetos "pasivos". De igual modo, negamos la existencia de una bimodalidad en la población de galaxias. Nuestro trabajo propone que el proceso de "envejecimiento ("ageing") da lugar a una distribución continua y suave de colores y masas en la pobación de galaxias y que la citada bimodalidad no es sino el producto de un efecto de selección. Más aún, nosotros proponemos que la capacidad de la galaxias para atraer dicho gas y convertirlo en estrellas controla dicho proceso de "envejecimiento" y puede llegar a ser responsable de la morfología que presenta el sistema. En tal caso, la morfología de las galaxias sería la consecuencia de los procesos físicos que ocurren en ellas y no su causa. Esperamos que esta nueva hipótesis sea considerada en futuros trabajos.

Por otra parte en esta tesis planteamos una nueva estrategia para abordar el análisis de los datos de espectroscopía de campo integral. Nuestro objetivo es poner en evidencia la necesidad de diseñar y calibrar las herramientas de anaálisis que se usan con este tipo de datos de cara a la ingente cantidad de los mismos que se van a producir en los próximos años. Esta técnica de observación ofrece la posibilidad de estudiar procesos físicos que hasta ahora estaban "ocultos" debido a la falta de resolución espacial. No obstante, no seremos capaces de extraer su máximo potencial si no analizamos dichos datos de manera coherente y siguiendo procedimientos estadísticamente rigurosos. En el presente trabajo mostramos que las simulaciones, en este caso de galaxias, son una excelente herramienta para evaluar el rendimiento de los diferentes algorítmos de analisis.

Bibliography

Abazajian, K. N. et al. (2009). "The Seventh Data Release of the Sloan Digital Sky Survey". In: *ApJS* 182, 543, pp. 543–558. DOI: 10.1088/0067-0049/182/2/543. arXiv: 0812.0649.

Allen, J. T. et al. (2015). "The SAMI Galaxy Survey: Early Data Release". In: *MNRAS* 446, pp. 1567–1583. DOI: 10.1093/mnras/stu2057. arXiv: 1407.6068.

Allington-Smith, J. (2007). "3D Instrumentation". In: *Science Perspectives for 3D Spectroscopy: Proceedings of the ESO Workshop held in Garching, Germany, 10-14 October 2005*. Ed. by Markus Kissler-Patig, Jeremy R. Walsh, and Martin M. Roth. Berlin, Heidelberg: Springer Berlin Heidelberg, pp. 3–13. ISBN: 978-3-540-73491-8. DOI: 10.1007/978-3-540-73491-8_1. URL: http://dx.doi.org/10.1007/978-3-540-73491-8_1.

Alloin, D. et al. (1979). "Nitrogen and oxygen abundances in galaxies". In: *A&A* 78, pp. 200–216.

Amorín, R. et al. (2009). "The host in blue compact galaxies.. Structural properties and scaling relations". In: *A&A* 501, pp. 75–88. DOI: 10.1051/0004-6361/200809591. arXiv: 0903.2861 [astro-ph.CO].

Ascasibar, Y. and J. Sánchez Almeida (2011). "Do galaxies form a spectroscopic sequence?" In: *MNRAS* 415, pp. 2417–2425. DOI: 10.1111/j.1365-2966.2011.18869.x. arXiv: 1104.1388 [astro-ph.CO].

Ascasibar, Y. et al. (2015). "Understanding chemical evolution in resolved galaxies – I The local star fraction-metallicity relation". In: *ArXiv e-prints* 1406.6397. arXiv: 1406.6397.

Ascasibar, Y. et al. (2016). "On the nature of diffuse ionized gas in galaxies – I The contribution of dust scattering to diffuse line emission". In: *ArXiv e-prints*. arXiv: 1602.08474.

Aumer, M. et al. (2013). "Towards a more realistic population of bright spiral galaxies in cosmological simulations". In: *MNRAS* 434, pp. 3142–3164. DOI: 10.1093/mnras/stt1230. arXiv: 1304.1559 [astro-ph.GA].

Bacon, R. et al. (2001). "The SAURON project - I. The panoramic integral-field spectrograph". In: *MNRAS* 326, pp. 23–35. DOI: 10.1046/j.1365-8711.2001.04612.x. eprint: astro-ph/0103451.

Bacon, R. et al. (2004). "The second-generation VLT instrument MUSE: science drivers and instrument design". In: *Ground-based Instrumentation for Astronomy*. Ed. by A. F. M. Moorwood and M. Iye. Vol. 5492. Society of Photo-Optical Instrumentation Engineers (SPIE) Conference Series, pp. 1145–1149. DOI: 10.1117/12.549009.

Bacon, R. et al. (2010). "The MUSE second-generation VLT instrument". In: *Ground-based and Airborne Instrumentation for Astronomy III*. Vol. 7735. SPIE Proceedings, p. 773508. DOI: 10.1117/12.856027.

Balcells, M. and P. J. Quinn (1990). "Merger origin for counterrotating cores in elliptical galaxies." In: *Dynamics and Interactions of Galaxies*. Ed. by R. Wielen, pp. 210–211.

Baldry, I. K. et al. (2004). "Quantifying the Bimodal Color-Magnitude Distribution of Galaxies". In: *ApJ* 600, pp. 681–694. DOI: 10.1086/380092. eprint: astro-ph/0309710.

Baldry, I. K. et al. (2006). "Galaxy bimodality versus stellar mass and environment". In: *MNRAS* 373, pp. 469–483. DOI: 10.1111/j.1365-2966.2006.11081.x. eprint: astro-ph/0607648.

Baldwin, J. A., M. M. Phillips, and R. Terlevich (1981). "Classification parameters for the emission-line spectra of extragalactic objects". In: *PASP* 93, pp. 5–19. DOI: 10.1086/130766.

Ball, N. M., J. Loveday, and R. J. Brunner (2008). "Galaxy colour, morphology and environment in the Sloan Digital Sky Survey". In: *MNRAS* 383, pp. 907–922. DOI: 10.1111/j.1365-2966.2007.12627.x. eprint: astro-ph/0610171.

Balogh, M. et al. (2004a). "Galaxy ecology: groups and low-density environments in the SDSS and 2dFGRS". In: *MNRAS* 348, pp. 1355–1372. DOI: 10.1111/j.1365-2966.2004.07453.x. eprint: astro-ph/0311379.

Balogh, M. L. et al. (1999). "Differential Galaxy Evolution in Cluster and Field Galaxies at z˜0.3". In: *ApJ* 527, pp. 54–79. DOI: 10.1086/308056. eprint: astro-ph/9906470.

Balogh, M. L. et al. (2004b). "The Bimodal Galaxy Color Distribution: Dependence on Luminosity and Environment". In: *ApJ* 615, pp. L101–L104. DOI: 10.1086/426079. eprint: astro-ph/0406266.

Bamford, S. P. et al. (2009). "Galaxy Zoo: the dependence of morphology and colour on environment". In: *MNRAS* 393, pp. 1324–1352. DOI: 10.1111/j.1365-2966.2008.14252.x. arXiv: 0805.2612.

Bedregal, A. G., A. Aragón-Salamanca, and M. R. Merrifield (2006). "The Tully-Fisher relation for S0 galaxies". In: *MNRAS* 373, pp. 1125–1140. DOI: 10.1111/j.1365-2966.2006.11031.x. eprint: astro-ph/0609076.

Behroozi, P. S. et al. (2015). "Using Galaxy Pairs to Probe Star Formation During Major Halo Mergers". In: *ArXiv e-prints*. arXiv: 1502.01342.

Bell, E. F. et al. (2004). "Nearly 5000 Distant Early-Type Galaxies in COMBO-17: A Red Sequence and Its Evolution since z˜1". In: *ApJ* 608, pp. 752–767. DOI: 10.1086/420778. eprint: astro-ph/0303394.

Bellovary, J. M. et al. (2014). "Effects of inclination on measuring velocity dispersion and implications for black holes". In: *MNRAS* 445, pp. 2667–2676. DOI: 10.1093/mnras/stu1958. arXiv: 1405.0286.

Bershady, M. A. et al. (2010). "The DiskMass Survey. I. Overview". In: *ApJ* 716, pp. 198–233. DOI: 10.1088/0004-637X/716/1/198. arXiv: 1004.4816.

Bertin, E. and S. Arnouts (1996). "SExtractor: Software for source extraction." In: 117, pp. 393–404. DOI: 10.1051/aas:1996164.

Blanton, M. R. and J. Moustakas (2009). "Physical Properties and Environments of Nearby Galaxies". In: *ARA&A* 47, pp. 159–210. DOI: 10.1146/annurev-astro-082708-101734. arXiv: 0908.3017.

Blanton, M. R. et al. (2005). "Relationship between Environment and the Broadband Optical Properties of Galaxies in the Sloan Digital Sky Survey". In: *ApJ* 629, pp. 143–157. DOI: 10.1086/422897. eprint: astro-ph/0310453.

Boselli, A. and G. Gavazzi (2006). "Environmental Effects on Late-Type Galaxies in Nearby Clusters". In: *PASP* 118, pp. 517–559. DOI: 10.1086/500691. eprint: astro-ph/0601108.

Bower, R. and M. Bureau (2014). "The KMOS Redshift One Spectroscopic Survey (KROSS)". In: *The Messenger* 157, pp. 38–40.

Bregman, J. N., P. Temi, and J. D. Bregman (2006). "The Ages of Elliptical Galaxies from Infrared Spectral Energy Distributions". In: *ApJ* 647, pp. 265–275. DOI: 10.1086/505190. eprint: astro-ph/0604399.

Bressan, A. et al. (2006). "The SPITZER IRS view of stellar populations in Virgo early type galaxies". In: *ArXiv Astrophysics e-prints*. eprint: astro-ph/0604068.

Brinchmann, J. et al. (2004). "The physical properties of star-forming galaxies in the low-redshift Universe". In: *MNRAS* 351, pp. 1151–1179. DOI: 10.1111/j.1365-2966.2004.07881.x. eprint: astro-ph/0311060.

Bundy, K. et al. (2015). "Overview of the SDSS-IV MaNGA Survey: Mapping nearby Galaxies at Apache Point Observatory". In: *ApJ* 798, 7, p. 7. DOI: 10.1088/0004-637X/798/1/7. arXiv: 1412.1482.

Burstein, D. et al. (2005). "The K-Band Luminosities of Galaxies: Do S0s Come from Spiral Galaxies?" In: *ApJ* 621, pp. 246–255. DOI: 10.1086/427408.

Calzetti, D. (2008). "Star Formation Rate Determinations". In: *Pathways Through an Eclectic Universe*. Ed. by J. H. Knapen, T. J. Mahoney, and A. Vazdekis. Vol. 390. Astronomical Society of the Pacific Conference Series, p. 121. arXiv: 0707.0467.

Cano-Díaz, M. et al. (2016). "Spatially Resolved Star Formation Main Sequence of Galaxies in the CALIFA Survey". In: *ApJ* 821, L26, p. L26. DOI: 10.3847/2041-8205/821/2/L26. arXiv: 1602.02770.

Cappellari, M. and Y. Copin (2003). "Adaptive spatial binning of integral-field spectroscopic data using Voronoi tessellations". In: *MNRAS* 342, pp. 345–354. DOI: 10.1046/j.1365-8711.2003.06541.x. eprint: astro-ph/0302262.

Cappellari, M. et al. (2007). "The SAURON project - X. The orbital anisotropy of elliptical and lenticular galaxies: revisiting the (V/σ, ϵ) diagram with integral-field stellar kinematics". In: *MNRAS* 379, pp. 418–444. DOI: 10.1111/j.1365-2966.2007.11963.x. eprint: astro-ph/0703533.

Cappellari, M. et al. (2011). "The ATLAS^{3D} project - I. A volume-limited sample of 260 nearby early-type galaxies: science goals and selection criteria". In: *MNRAS* 413, pp. 813–836. DOI: 10.1111/j.1365-2966.2010.18174.x. arXiv: 1012.1551.

Cappellari, M. et al. (2013). "The ATLAS^{3D} project - XX. Mass-size and mass-σ distributions of early-type galaxies: bulge fraction drives kinematics, mass-to-light ratio, molecular gas fraction and stellar initial mass function". In: *MNRAS* 432, pp. 1862–1893. DOI: 10.1093/mnras/stt644. arXiv: 1208.3523 [astro-ph.CO].

Cardelli, J. A., G. C. Clayton, and J. S. Mathis (1989). "The relationship between infrared, optical, and ultraviolet extinction". In: *ApJ* 345, pp. 245–256. DOI: 10.1086/167900.

Casado, J. et al. (2015). "Nature or nurture? Clues from the distribution of specific star formation rates in SDSS galaxies". In: *MNRAS* 451, pp. 888–903. DOI: 10.1093/mnras/stv949. arXiv: 1504.07010.

Chabrier, G. (2003). "Galactic Stellar and Substellar Initial Mass Function". In: *PASP* 115, pp. 763–795. DOI: 10.1086/376392. eprint: astro-ph/0304382.

Cid Fernandes, R. et al. (2005). "Semi-empirical analysis of Sloan Digital Sky Survey galaxies - I. Spectral synthesis method". In: *MNRAS* 358, pp. 363–378. DOI: 10.1111/j.1365-2966.2005.08752.x. eprint: astro-ph/0412481.

Cid Fernandes, R. et al. (2007). "Uncovering the chemical enrichment and mass-assembly histories of star-forming galaxies". In: *MNRAS* 375, pp. L16–L20. DOI: 10.1111/j.1745-3933.2006.00265.x. eprint: astro-ph/0610815.

Colbert, J. W., J. S. Mulchaey, and A. I. Zabludoff (2001). "The Optical and Near-Infrared Morphologies of Isolated Early-Type Galaxies". In: *AJ* 121, pp. 808–819. DOI: 10.1086/318758. eprint: astro-ph/0010534.

Cooper, M. C. et al. (2005). "Measuring Galaxy Environments with Deep Redshift Surveys". In: *ApJ* 634, pp. 833–848. DOI: 10.1086/432868. eprint: astro-ph/0506518.

Croom, S. M. et al. (2012). "The Sydney-AAO Multi-object Integral field spectrograph". In: *MNRAS* 421, pp. 872–893. DOI: 10.1111/j.1365-2966.2011.20365.x. arXiv: 1112.3367.

Dalton, G. et al. (2014). "Project overview and update on WEAVE: the next generation wide-field spectroscopy facility for the William Herschel Telescope". In: *Society of Photo-Optical Instrumentation Engineers (SPIE) Conference Series*. Vol. 9147. Society of Photo-Optical Instrumentation Engineers (SPIE) Conference Series, p. 0. DOI: 10.1117/12.2055132. arXiv: 1412.0843 [astro-ph.IM].

Darg, D. W. et al. (2010). "Galaxy Zoo: the properties of merging galaxies in the nearby Universe - local environments, colours, masses, star formation rates and AGN activity". In: *MNRAS* 401, pp. 1552–1563. DOI: 10.1111/j.1365-2966.2009.15786.x. arXiv: 0903.5057 [astro-ph.GA].

de Vaucouleurs, G. (1948). "Recherches sur les Nebuleuses Extragalactiques". In: *Annales d'Astrophysique* 11, p. 247.

Diehl, S. and T. S. Statler (2006). "Adaptive binning of X-ray data with weighted Voronoi tessellations". In: *MNRAS* 368, pp. 497–510. DOI: 10.1111/j.1365-2966.2006.10125.x. eprint: astro-ph/0512074.

Doe, S. et al. (2007). "Developing Sherpa with Python". In: *Astronomical Data Analysis Software and Systems XVI*. Ed. by R. A. Shaw, F. Hill, and D. J. Bell. Vol. 376. Astronomical Society of the Pacific Conference Series, p. 543.

Draine, B. T. (2003). "Scattering by Interstellar Dust Grains. I. Optical and Ultraviolet". In: *ApJ* 598, pp. 1017–1025. DOI: 10.1086/379118. eprint: astro-ph/0304060.

Dressler, A. (1980). "Galaxy morphology in rich clusters - Implications for the formation and evolution of galaxies". In: *ApJ* 236, pp. 351–365. DOI: 10.1086/157753.

Dressler, A. and J. E. Gunn (1983). "Spectroscopy of galaxies in distant clusters. II - The population of the 3C 295 cluster". In: *ApJ* 270, pp. 7–19. DOI: 10.1086/161093.

Dressler, A. et al. (1997). "Evolution since z = 0.5 of the Morphology-Density Relation for Clusters of Galaxies". In: *ApJ* 490, pp. 577–591. eprint: astro-ph/9707232.

Dwek, E. (1998). "The Evolution of the Elemental Abundances in the Gas and Dust Phases of the Galaxy". In: *ApJ* 501, p. 643. DOI: 10.1086/305829. eprint: astro-ph/9707024.

Ebeling, H., L. N. Stephenson, and A. C. Edge (2014). "Jellyfish: Evidence of Extreme Ram-pressure Stripping in Massive Galaxy Clusters". In: *ApJ* 781, L40, p. L40. DOI: 10.1088/2041-8205/781/2/L40. arXiv: 1312.6135.

Edmunds, M. G. (1990). "General Constraints on the Effect of Gas Flows in the Chemical Evolution of Galaxies". In: *MNRAS* 246, p. 678.

Ellison, S. L. et al. (2008). "Galaxy Pairs in the Sloan Digital Sky Survey. I. Star Formation, Active Galactic Nucleus Fraction, and the Mass-Metallicity Relation". In: *AJ* 135, pp. 1877–1899. DOI: 10.1088/0004-6256/135/5/1877. arXiv: 0803.0161.

Emsellem, E. et al. (2007). "The SAURON project - IX. A kinematic classification for early-type galaxies". In: *MNRAS* 379, pp. 401–417. DOI: 10.1111/j.1365-2966.2007.11752.x. eprint: astro-ph/0703531.

Faber, S. M. et al. (2007). "Galaxy Luminosity Functions to z˜1 from DEEP2 and COMBO-17: Implications for Red Galaxy Formation". In: *ApJ* 665, pp. 265–294. DOI: 10.1086/519294. eprint: astro-ph/0506044.

Fagotto, F. et al. (1994a). "Evolutionary sequences of stellar models with new radiative opacities. III. Z=0.0004 and Z=0.05". In: 104, pp. 365–376.

— (1994b). "Evolutionary sequences of stellar models with new radiative opacities. IV. Z=0.004 and Z=0.008". In: 105, pp. 29–38.

Förster Schreiber, N. M. et al. (2009). "The SINS Survey: SINFONI Integral Field Spectroscopy of z ˜ 2 Star-forming Galaxies". In: *ApJ* 706, pp. 1364–1428. DOI: 10.1088/0004-637X/706/2/1364. arXiv: 0903.1872 [astro-ph.CO].

Freeman, K. C. (1970). "On the Disks of Spiral and S0 Galaxies". In: *ApJ* 160, p. 811. DOI: 10.1086/150474.

Freeman, P., S. Doe, and A. Siemiginowska (2001). "Sherpa: a mission-independent data analysis application". In: *Astronomical Data Analysis*. Ed. by J.-L. Starck and F. D. Murtagh. Vol. 4477. SPIE Proceedings, pp. 76–87. DOI: 10.1117/12.447161. eprint: astro-ph/0108426.

Fujita, Y. (1998). "Quantitative Estimates of Environmental Effects on the Star Formation Rate of Disk Galaxies in Clusters of Galaxies". In: *ApJ* 509, pp. 587–594. DOI: 10.1086/306518. eprint: astro-ph/9807120.

Gallazzi, A. et al. (2006). "Ages and metallicities of early-type galaxies in the Sloan Digital Sky Survey: new insight into the physical origin of the colour-magnitude and the Mg_2-σ_V relations". In: *MNRAS* 370, pp. 1106–1124. DOI: 10.1111/j.1365-2966.2006.10548.x. eprint: astro-ph/0605300.

García-Benito, R. et al. (2015a). "CALIFA, the Calar Alto Legacy Integral Field Area survey. III. Second public data release". In: *A&A* 576, A135, A135. DOI: 10.1051/0004-6361/201425080. arXiv: 1409.8302.

García-Benito, R. et al. (2015b). "CALIFA, the Calar Alto Legacy Integral Field Area survey. III. Second public data release". In: *A&A* 576, A135, A135. DOI: 10.1051/0004-6361/201425080. arXiv: 1409.8302.

Gilmore, G. et al. (2007). "The Observed Properties of Dark Matter on Small Spatial Scales". In: *ApJ* 663, pp. 948–959. DOI: 10.1086/518025. eprint: astro-ph/0703308.

Gomes, J. M. et al. (2016a). "Spiral-like star-forming patterns in CALIFA early-type galaxies". In: *A&A* 585, A92, A92. DOI: 10.1051/0004-6361/201525974. arXiv: 1511.00744.

Gomes, J. M. et al. (2016b). "Warm ionized gas in CALIFA early-type galaxies. 2D emission-line patterns and kinematics for 32 galaxies". In: *A&A* 588, A68, A68. DOI: 10.1051/0004-6361/201525976. arXiv: 1511.02191.

Gómez, P. L. et al. (2003). "Galaxy Star Formation as a Function of Environment in the Early Data Release of the Sloan Digital Sky Survey". In: *ApJ* 584, pp. 210–227. DOI: 10.1086/345593. eprint: astro-ph/0210193.

Gonçalves, T. S. et al. (2012). "Quenching Star Formation at Intermediate Redshifts: Downsizing of the Mass Flux Density in the Green Valley". In: *ApJ* 759, 67, p. 67. DOI: 10.1088/0004-637X/759/1/67. arXiv: 1209.4084 [astro-ph.CO].

González Delgado, R. M. et al. (2005). "Evolutionary stellar population synthesis at high spectral resolution: optical wavelengths". In: *MNRAS* 357, pp. 945–960. DOI: 10.1111/j.1365-2966.2005.08692.x. eprint: astro-ph/0501204.

González Delgado, R. M. et al. (2014). "The star formation history of CALIFA galaxies: Radial structures". In: *A&A* 562, A47, A47. DOI: 10.1051/0004-6361/201322011. arXiv: 1310.5517.

Governato, F. et al. (2007). "Forming disc galaxies in ΛCDM simulations". In: *MNRAS* 374, pp. 1479–1494. DOI: 10.1111/j.1365-2966.2006.11266.x. eprint: astro-ph/0602351.

Governato, F. et al. (2010). "Bulgeless dwarf galaxies and dark matter cores from supernova-driven outflows". In: *Nature* 463, pp. 203–206. DOI: 10.1038/nature08640. arXiv: 0911.2237.

Graham, A. W. et al. (2005). "Total Galaxy Magnitudes and Effective Radii from Petrosian Magnitudes and Radii". In: *AJ* 130, pp. 1535–1544. DOI: 10.1086/444475. eprint: astro-ph/0504287.

Greisen, E. W. and M. R. Calabretta (2002). "Representations of world coordinates in FITS". In: *A&A* 395, pp. 1061–1075. DOI: 10.1051/0004-6361:20021326. eprint: astro-ph/0207407.

Groves, B. et al. (2008). "Modeling the Pan-Spectral Energy Distribution of Starburst Galaxies. IV. The Controlling Parameters of the Starburst SED". In: *ApJS* 176, pp. 438–456. DOI: 10.1086/528711. arXiv: 0712.1824.

Groves, B. A., M. A. Dopita, and R. S. Sutherland (2004). "Dusty, Radiation Pressure-Dominated Photoionization. I. Model Description, Structure, and Grids". In: *ApJS* 153, pp. 9–73. DOI: 10.1086/421113. eprint: astro-ph/0404175.

Guidi, G., C. Scannapieco, and C. J. Walcher (2015). "Biases and systematics in the observational derivation of galaxy properties: comparing different techniques on synthetic observations of simulated galaxies". In: *MNRAS* 454, pp. 2381–2400. DOI: 10.1093/mnras/stv2050. arXiv: 1507.00347.

Guidi, G. et al. (2016). "Physical properties of galaxies: toward a consistent comparison between hydrodynamical simulations and SDSS". In: *ArXiv e-prints*. arXiv: 1602.06297.

Gunn, J. E. and J. R. Gott III (1972). "On the Infall of Matter Into Clusters of Galaxies and Some Effects on Their Evolution". In: *ApJ* 176, p. 1. DOI: 10.1086/151605.

Gunn, J. E. et al. (1998). "The Sloan Digital Sky Survey Photometric Camera". In: *AJ* 116, pp. 3040–3081. DOI: 10.1086/300645. eprint: astro-ph/9809085.

Gunn, J. E. et al. (2006). "The 2.5 m Telescope of the Sloan Digital Sky Survey". In: *AJ* 131, pp. 2332–2359. DOI: 10.1086/500975. eprint: astro-ph/0602326.

Haffner, L. M. et al. (2009). "The warm ionized medium in spiral galaxies". In: *Reviews of Modern Physics* 81, pp. 969–997. DOI: 10.1103/RevModPhys.81.969. arXiv: 0901.0941.

Hameed, S. and N. Devereux (2005). "Hα Imaging of Early-Type Sa-Sab Spiral Galaxies. II. Global Properties". In: *AJ* 129, pp. 2597–2616. DOI: 10.1086/430211. eprint: astro-ph/0506067.

Hancock, P. J. et al. (2012). "Compact continuum source finding for next generation radio surveys". In: *MNRAS* 422, pp. 1812–1824. DOI: 10.1111/j.1365-2966.2012.20768.x. arXiv: 1202.4500 [astro-ph.IM].

Hashimoto, Y. and A. Oemler Jr. (1999). "The Concentration-Density Relation of Galaxies in the Las Campanas Redshift Survey". In: *ApJ* 510, pp. 609–613. DOI: 10.1086/306600. eprint: astro-ph/9807275.

Hayward, C. C. and D. J. B. Smith (2015). "Should we believe the results of ultraviolet-millimetre galaxy spectral energy distribution modelling?" In: *MNRAS* 446, pp. 1512–1535. DOI: 10.1093/mnras/stu2195. arXiv: 1409.6332.

Hayward, C. C. et al. (2011). "What Does a Submillimeter Galaxy Selection Actually Select? The Dependence of Submillimeter Flux Density on Star Formation Rate and Dust Mass". In: *ApJ* 743, 159, p. 159. DOI: 10.1088/0004-637X/743/2/159. arXiv: 1101.0002 [astro-ph.CO].

Hayward, C. C. et al. (2014). "The total infrared luminosity may significantly overestimate the star formation rate of quenching and recently quenched galaxies". In: *MNRAS* 445, pp. 1598–1604. DOI: 10.1093/mnras/stu1843. arXiv: 1402.0006.

Heckman, T. M. et al. (1998). "The Ultraviolet Spectroscopic Properties of Local Starbursts: Implications at High Redshift". In: *ApJ* 503, pp. 646–661. DOI: 10.1086/306035. eprint: astro-ph/9803185.

Henyey, L. G. and J. L. Greenstein (1941). "Diffuse radiation in the Galaxy". In: *ApJ* 93, pp. 70–83. DOI: 10.1086/144246.

Hoyle, F. et al. (2005). "The Luminosity Function of Void Galaxies in the Sloan Digital Sky Survey". In: *ApJ* 620, pp. 618–628. DOI: 10.1086/427176. eprint: astro-ph/0309728.

Hubble, E. P. (1936). *Realm of the Nebulae*.

Hughes, T. M. et al. (2013). "The role of cold gas and environment on the stellar mass-metallicity relation of nearby galaxies". In: *A&A* 550, A115, A115. DOI: 10.1051/0004-6361/201218822. arXiv: 1207.4191 [astro-ph.CO].

Husemann, B. et al. (2013). "CALIFA, the Calar Alto Legacy Integral Field Area survey. II. First public data release". In: *A&A* 549, A87, A87. DOI: 10.1051/0004-6361/201220582. arXiv: 1210.8150 [astro-ph.CO].

Ideue, Y. et al. (2012). "The Role of Galaxy Interaction in Environmental Dependence of the Star Formation Activity at z ˜= 1.2". In: *ApJ* 747, 42, p. 42. DOI: 10.1088/0004-637X/747/1/42. arXiv: 1112.2260 [astro-ph.CO].

Iglesias-Páramo, J., J. M. Vílchez, and L. et al. Galbany (2013). "Aperture corrections for disk galaxy properties derived from the CALIFA survey. Balmer emission lines in spiral galaxies". In: *A&A* 553, L7, p. L7. DOI: 10.1051/0004-6361/201321460. arXiv: 1304.1644 [astro-ph.CO].

Ilbert, O. et al. (2014). "Evolution of the specific Star Formation Rate Function at z1.4 - Dissecting the mass-SFR plane in COSMOS and GOODS". In: *ArXiv e-prints*. arXiv: 1410.4875.

Janowiecki, S. and J. J. Salzer (2014). "The Unique Structural Parameters of the Underlying Host Galaxies in Blue Compact Dwarfs". In: *ApJ* 793, 109, p. 109. DOI: 10.1088/0004-637X/793/2/109. arXiv: 1408.3138.

Jonsson, P. (2006). "SUNRISE: polychromatic dust radiative transfer in arbitrary geometries". In: *MNRAS* 372, pp. 2–20. DOI: 10.1111/j.1365-2966.2006.10884.x. eprint: astro-ph/0604118.

Jonsson, P., B. A. Groves, and T. J. Cox (2010). "High-resolution panchromatic spectral models of galaxies including photoionization and dust". In: *MNRAS* 403, pp. 17–44. DOI: 10.1111/j.1365-2966.2009.16087.x.

Kaiser, N. (1987). "Clustering in real space and in redshift space". In: *MNRAS* 227, pp. 1–21.

Kauffmann, G. et al. (2004). "The environmental dependence of the relations between stellar mass, structure, star formation and nuclear activity in galaxies". In: *MNRAS* 353, pp. 713–731. DOI: 10.1111/j.1365-2966.2004.08117.x. eprint: astro-ph/0402030.

Kaviraj, S. et al. (2007). "UV-Optical Colors As Probes of Early-Type Galaxy Evolution". In: *ApJS* 173, pp. 619–642. DOI: 10.1086/516633. eprint: astro-ph/0601029.

Kendrew, S. et al. (2016). "Simulated stellar kinematics studies of high-redshift galaxies with the HARMONI Integral Field Spectrograph". In: *MNRAS* 458, pp. 2405–2422. DOI: 10.1093/mnras/stw438. arXiv: 1602.06983.

Kennicutt Jr., R. C. (1998). "Star Formation in Galaxies Along the Hubble Sequence". In: *ARA&A* 36, pp. 189–232. DOI: 10.1146/annurev.astro.36.1.189. eprint: astro-ph/9807187.

Kewley, L. J. et al. (2006). "The host galaxies and classification of active galactic nuclei". In: *MNRAS* 372, pp. 961–976. DOI: 10.1111/j.1365-2966.2006.10859.x. eprint: astro-ph/0605681.

Koopmann, R. A. and J. D. P. Kenney (1998). "The Trouble with Hubble Types in the Virgo Cluster". In: *ApJ* 497, pp. L75–L79. DOI: 10.1086/311283. eprint: astro-ph/9802210.

Koribalski, B. S. (2012). "Overview on Spectral Line Source Finding and Visualisation". In: 29, pp. 359–370. DOI: 10.1071/AS12030. arXiv: 1206.6916.

Kormendy, J. and R. Bender (1996). "A Proposed Revision of the Hubble Sequence for Elliptical Galaxies". In: *ApJ* 464, p. L119. DOI: 10.1086/310095.

— (2012). "A Revised Parallel-sequence Morphological Classification of Galaxies: Structure and Formation of S0 and Spheroidal Galaxies". In: *ApJS* 198, 2, p. 2. DOI: 10.1088/0067-0049/198/1/2. arXiv: 1110.4384.

Kormendy, J. and R. C. Kennicutt Jr. (2004). "Secular Evolution and the Formation of Pseudobulges in Disk Galaxies". In: *ARA&A* 42, pp. 603–683. DOI: 10.1146/annurev.astro.42.053102.134024. eprint: astro-ph/0407343.

Krajnović, D. et al. (2006). "Kinemetry: a generalization of photometry to the higher moments of the line-of-sight velocity distribution". In: *MNRAS* 366, pp. 787–802. DOI: 10.1111/j.1365-2966.2005.09902.x. eprint: astro-ph/0512200.

Krajnović, D. et al. (2011). "The ATLAS^{3D} project - II. Morphologies, kinemetric features and alignment between photometric and kinematic axes of early-type galaxies". In: *MNRAS* 414, pp. 2923–2949. DOI: 10.1111/j.1365-2966.2011.18560.x. arXiv: 1102.3801.

Kroupa, P. (2002). "The Initial Mass Function of Stars: Evidence for Uniformity in Variable Systems". In: *Science* 295, pp. 82–91. DOI: 10.1126/science.1067524. eprint: astro-ph/0201098.

Lamastra, A. et al. (2013). "The interaction-driven starburst contribution to the cosmic star formation rate density". In: *A&A* 552, A44, A44. DOI: 10.1051/0004-6361/201220754. arXiv: 1302.1363 [astro-ph.CO].

Lanz, L. et al. (2013). "Global Star Formation Rates and Dust Emission over the Galaxy Interaction Sequence". In: *ApJ* 768, 90, p. 90. DOI: 10.1088/0004-637X/768/1/90. arXiv: 1302.5011 [astro-ph.CO].

Lanz, L. et al. (2014). "Simulated Galaxy Interactions as Probes of Merger Spectral Energy Distributions". In: *ApJ* 785, 39, p. 39. DOI: 10.1088/0004-637X/785/1/39. arXiv: 1402.5151.

Leitherer, C. et al. (1999). "Starburst99: Synthesis Models for Galaxies with Active Star Formation". In: *ApJS* 123, pp. 3–40. DOI: 10.1086/313233. eprint: astro-ph/9902334.

Lequeux, J. et al. (1979). "Chemical composition and evolution of irregular and blue compact galaxies". In: *A&A* 80, pp. 155–166.

Li, C. et al. (2008). "Interaction-induced star formation in a complete sample of 10^5 nearby star-forming galaxies". In: *MNRAS* 385, pp. 1903–1914. DOI: 10.1111/j.1365-2966.2008.13000.x. arXiv: 0711.3792.

Lintott, C. J. et al. (2008). "Galaxy Zoo: morphologies derived from visual inspection of galaxies from the Sloan Digital Sky Survey". In: *MNRAS* 389, pp. 1179–1189. DOI: 10.1111/j.1365-2966.2008.13689.x. arXiv: 0804.4483.

Lupton, R. et al. (2004). "Preparing Red-Green-Blue Images from CCD Data". In: *PASP* 116, pp. 133–137. DOI: 10.1086/382245. eprint: astro-ph/0312483.

Makovoz, D. and F. R. Marleau (2005). "Point-Source Extraction with MOPEX". In: *PASP* 117, pp. 1113–1128. DOI: 10.1086/432977. eprint: astro-ph/0507007.

Marigo, P. (2001). "Chemical yields from low- and intermediate-mass stars: Model predictions and basic observational constraints". In: *A&A* 370, pp. 194–217. DOI: 10.1051/0004-6361:20000247. eprint: astro-ph/0012181.

Marinova, I. et al. (2008). "Characterizing Barred Galaxies in the Abell 901/902 Supercluster from STAGES". In: *New Horizons in Astronomy*. Ed. by A. Frebel et al. Vol. 393. Astronomical Society of the Pacific Conference Series, p. 231. arXiv: 0802.3910.

Martig, M. and F. Bournaud (2008). "Triggering of merger-induced starbursts by the tidal field of galaxy groups and clusters". In: *MNRAS* 385, pp. L38–L42. DOI: 10.1111/j.1745-3933.2008.00429.x. arXiv: 0712.0289.

Martin, D. C. et al. (2007). "The UV-Optical Galaxy Color-Magnitude Diagram. III. Constraints on Evolution from the Blue to the Red Sequence". In: *ApJS* 173, pp. 342–356. DOI: 10.1086/516639. eprint: astro-ph/0703281.

Martins, L. P. et al. (2005). "A high-resolution stellar library for evolutionary population synthesis". In: *MNRAS* 358, pp. 49–65. DOI: 10.1111/j.1365-2966.2005.08703.x. eprint: astro-ph/0501225.

Mendez, A. J. et al. (2011). "AEGIS: The Morphologies of Green Galaxies at 0.4 z 1.2". In: *ApJ* 736, 110, p. 110. DOI: 10.1088/0004-637X/736/2/110. arXiv: 1101.3353 [astro-ph.CO].

Men'shchikov, A. et al. (2012). "A multi-scale, multi-wavelength source extraction method: getsources". In: *A&A* 542, A81, A81. DOI: 10.1051/0004-6361/201218797. arXiv: 1204.4508 [astro-ph.IM].

Michałowski, M. J. et al. (2014). "Determining the stellar masses of submillimetre galaxies: the critical importance of star formation histories". In: *A&A* 571, A75, A75. DOI: 10.1051/0004-6361/201424174. arXiv: 1405.2335.

Molinari, S. et al. (2011). "Source extraction and photometry for the far-infrared and submillimeter continuum in the presence of complex backgrounds". In: *A&A* 530, A133, A133. DOI: 10.1051/0004-6361/201014752. arXiv: 1011.3946.

Moore, B., N. Katz, and G. Lake (1996). "On the Destruction and Overmerging of Dark Halos in Dissipationless N-Body Simulations". In: *ApJ* 457, p. 455. DOI: 10.1086/176745. eprint: astro-ph/9503088.

Morganti, R. et al. (2006). "Neutral hydrogen in nearby elliptical and lenticular galaxies: the continuing formation of early-type galaxies". In: *MNRAS* 371, pp. 157–169. DOI: 10.1111/j.1365-2966.2006.10681.x. eprint: astro-ph/0606261.

Moustakas, J., R. C. Kennicutt Jr., and C. A. Tremonti (2006). "Optical Star Formation Rate Indicators". In: *ApJ* 642, pp. 775–796. DOI: 10.1086/500964. eprint: astro-ph/0511730.

Muldrew, S. I. et al. (2012). "Measures of galaxy environment - I. What is 'environment'?" In: *MNRAS* 419, pp. 2670–2682. DOI: 10.1111/j.1365-2966.2011.19922.x. arXiv: 1109.6328 [astro-ph.CO].

Nelson, D. et al. (2015). "The Illustris Simulation: Public Data Release". In: *arXiv:1504.00362*. arXiv: 1504.00362.

Noeske, K. G. et al. (2007). "Star Formation in AEGIS Field Galaxies since z=1.1: Staged Galaxy Formation and a Model of Mass-dependent Gas Exhaustion". In: *ApJ* 660, pp. L47–L50. DOI: 10.1086/517927. eprint: astro-ph/0703056.

Panter, B. (2009). "Matching data and models in the Virtual Observatory." In: 80, p. 429.

Papaderos, P. et al. In:

Papaderos, P. et al. (1996). "Optical structure and star formation in blue compact dwarf galaxies. II. Relations between photometric components and evolutionary implications." In: *A&A* 314, pp. 59–72.

Park, C. et al. (2007). "Environmental Dependence of Properties of Galaxies in the Sloan Digital Sky Survey". In: *ApJ* 658, pp. 898–916. DOI: 10.1086/511059. eprint: astro-ph/0611610.

Pence, W. D. et al. (2010). "Definition of the Flexible Image Transport System (FITS), version 3.0". In: *A&A* 524, A42, A42. DOI: 10.1051/0004-6361/201015362.

Peng, Y.-j. et al. (2010). "Mass and Environment as Drivers of Galaxy Evolution in SDSS and zCOSMOS and the Origin of the Schechter Function". In: *ApJ* 721, pp. 193–221. DOI: 10.1088/0004-637X/721/1/193. arXiv: 1003.4747 [astro-ph.CO].

Pérez-Montero, E. and T. Contini (2009). "The impact of the nitrogen-to-oxygen ratio on ionized nebula diagnostics based on [NII] emission lines". In: *MNRAS* 398, pp. 949–960. DOI: 10.1111/j.1365-2966.2009.15145.x. arXiv: 0905.4621 [astro-ph.CO].

Planck Collaboration et al. (2015). "Planck 2015 results. XIII. Cosmological parameters". In: *ArXiv e-prints*. arXiv: 1502.01589.

Portinari, L., C. Chiosi, and A. Bressan (1998). "Galactic chemical enrichment with new metallicity dependent stellar yields". In: *A&A* 334, pp. 505–539. eprint: astro-ph/9711337.

Rodríguez-Muñoz, L. et al. (2015). "Recent Stellar Mass Assembly of Low-mass Star-forming Galaxies at Redshifts 0.3 z 0.9". In: *ApJ* 799, 36, p. 36. DOI: 10.1088/0004-637X/799/1/36. arXiv: 1411.0200.

Rosa-González, D. et al. (2007). "Thermal Emission from H II Galaxies: Discovering the Youngest Systems". In: *ApJ* 654, pp. 226–239. DOI: 10.1086/509105. eprint: astro-ph/0609181.

Rosales-Ortega, F. F. (2009). "Multi-dimensional analysis of the chemical and physical properties of spiral galaxies". PhD thesis. PhD Thesis, University of Cambridge, 2010.

Rubin, V. C., W. K. J. Ford, and N. . Thonnard (1980). "Rotational properties of 21 SC galaxies with a large range of luminosities and radii, from NGC 4605 /R = 4kpc/ to UGC 2885 /R = 122 kpc/". In: *ApJ* 238, pp. 471–487. DOI: 10.1086/158003.

Ruiz-Lara, T. et al. (2016). "No direct coupling between bending of galaxy disc stellar age and light profiles". In: *MNRAS* 456, pp. L35–L39. DOI: 10.1093/mnrasl/slv174. arXiv: 1511.03499.

Salim, S. et al. (2007). "UV Star Formation Rates in the Local Universe". In: *ApJS* 173, pp. 267–292. DOI: 10.1086/519218. arXiv: 0704.3611.

Sánchez, S. F. et al. (2012a). "CALIFA, the Calar Alto Legacy Integral Field Area survey. I. Survey presentation". In: *A&A* 538, A8, A8. DOI: 10.1051/0004-6361/201117353. arXiv: 1111.0962.

Sánchez, S. F. et al. (2012b). "CALIFA, the Calar Alto Legacy Integral Field Area survey. I. Survey presentation". In: *A&A* 538, A8, A8. DOI: 10.1051/0004-6361/201117353. arXiv: 1111.0962.

Sánchez, S. F. et al. (2012c). "Integral field spectroscopy of a sample of nearby galaxies. II. Properties of the H ii regions". In: *A&A* 546, A2, A2. DOI: 10.1051/0004-6361/201219578. arXiv: 1208.1117.

Sánchez, S. F. et al. (2013). "Mass-metallicity relation explored with CALIFA. I. Is there a dependence on the star-formation rate?" In: *A&A* 554, A58, A58. DOI: 10.1051/0004-6361/201220669. arXiv: 1304.2158.

Sánchez, S. F. et al. (2014). "A characteristic oxygen abundance gradient in galaxy disks unveiled with CALIFA". In: *A&A* 563, A49, A49. DOI: 10.1051/0004-6361/201322343. arXiv: 1311.7052 [astro-ph.CO].

Sánchez, S. F. et al. (2016a). "CALIFA, the Calar Alto Legacy Integral Field Area survey: IV. Third Public data release". In: *ArXiv e-prints*. arXiv: 1604.02289.

Sánchez, S. F. et al. (2016b). "Pipe3D, a pipeline to analyse integral field spectroscopy data: II. Analysis sequence and CALIFA dataproducts". In: *ArXiv e-prints*. arXiv: 1602.01830 [astro-ph.IM].

Sánchez, S. F. et al. (2016c). "Pipe3D, a pipeline to analyze Integral Field Spectroscopy Data: II. Analysis sequence and CALIFA dataproducts". In: *RMxAA* 52, pp. 171–220. arXiv: 1602.01830 [astro-ph.IM].

Sandage, A. (2005). "The Classification of Galaxies: Early History and Ongoing Developments". In: *ARA&A* 43, pp. 581–624. DOI: 10.1146/annurev.astro.43.112904.104839.

Sandage, A. and N. Visvanathan (1978). "Color-absolute magnitude relation for E and S0 galaxies. III - Fully corrected photometry for 405 galaxies: Comparison of color distributions for E and S0 field and cluster galaxies". In: *ApJ* 225, pp. 742–750. DOI: 10.1086/156537.

Sanders, D. B. and I. F. Mirabel (1996). "Luminous Infrared Galaxies". In: *ARA&A* 34, p. 749. DOI: 10.1146/annurev.astro.34.1.749.

Sanders, J. S. and A. C. Fabian (2001). "Adaptive binning of X-ray galaxy cluster images". In: *MNRAS* 325, pp. 178–186. DOI: 10.1046/j.1365-8711.2001.04410.x. eprint: astro-ph/0011500.

Sargent, W. L. W. and L. Searle (1970). "Isolated Extragalactic H II Regions". In: *ApJ* 162, p. L155. DOI: 10.1086/180644.

Savage, R. S. and S. Oliver (2007). "Bayesian Methods of Astronomical Source Extraction". In: *ApJ* 661, pp. 1339–1346. DOI: 10.1086/515393. eprint: astro-ph/0512597.

Scannapieco, C. et al. (2005). "Feedback and metal enrichment in cosmological smoothed particle hydrodynamics simulations - I. A model for chemical enrichment". In: *MNRAS*

364, pp. 552–564. DOI: 10.1111/j.1365-2966.2005.09574.x. eprint: astro-ph/0505440.

— (2006). "Feedback and metal enrichment in cosmological SPH simulations - II. A multiphase model with supernova energy feedback". In: *MNRAS* 371, pp. 1125–1139. DOI: 10.1111/j.1365-2966.2006.10785.x. eprint: arXiv:astro-ph/0604524.

— (2008). "Effects of supernova feedback on the formation of galaxy discs". In: *MNRAS* 389, pp. 1137–1149. DOI: 10.1111/j.1365-2966.2008.13678.x. arXiv: 0804.3795.

Scannapieco, C. et al. (2009). "The formation and survival of discs in a ΛCDM universe". In: *MNRAS* 396, 696 (S09). DOI: 10.1111/j.1365-2966.2009.14764.x. arXiv: 0812.0976.

Scannapieco, C. et al. (2010). "An observer's view of simulated galaxies: disc-to-total ratios, bars and (pseudo-)bulges". In: *MNRAS* 407, pp. L41–L45. DOI: 10.1111/j.1745-3933.2010.00900.x. arXiv: 1001.4890 [astro-ph.GA].

Scannapieco, C. et al. (2012). "The Aquila comparison project: the effects of feedback and numerical methods on simulations of galaxy formation". In: *MNRAS* 423, pp. 1726–1749. DOI: 10.1111/j.1365-2966.2012.20993.x. arXiv: 1112.0315 [astro-ph.GA].

Schawinski, K. et al. (2007). "Observational evidence for AGN feedback in early-type galaxies". In: *MNRAS* 382, pp. 1415–1431. DOI: 10.1111/j.1365-2966.2007.12487.x. arXiv: 0709.3015.

Schawinski, K. et al. (2010). "Galaxy Zoo: The Fundamentally Different Co-Evolution of Supermassive Black Holes and Their Early- and Late-Type Host Galaxies". In: *ApJ* 711, pp. 284–302. DOI: 10.1088/0004-637X/711/1/284. arXiv: 1001.3141 [astro-ph.CO].

Schawinski, K. et al. (2014). "The green valley is a red herring: Galaxy Zoo reveals two evolutionary pathways towards quenching of star formation in early- and late-type galaxies". In: *MNRAS* 440, pp. 889–907. DOI: 10.1093/mnras/stu327. arXiv: 1402.4814 [astro-ph.GA].

Schaye, J. et al. (2015). "The EAGLE project: simulating the evolution and assembly of galaxies and their environments". In: *MNRAS* 446, pp. 521–554. DOI: 10.1093/mnras/stu2058. arXiv: 1407.7040.

Schiminovich, D. et al. (2007). "The UV-Optical Color Magnitude Diagram. II. Physical Properties and Morphological Evolution On and Off of a Star-forming Sequence". In: *ApJS* 173, pp. 315–341. DOI: 10.1086/524659. arXiv: 0711.4823.

Searle, L. and W. L. W. Sargent (1972). "Inferences from the Composition of Two Dwarf Blue Galaxies". In: *ApJ* 173, p. 25. DOI: 10.1086/151398.

Sersic, J. L. (1968). *Atlas de galaxias australes*.

Shen, S. et al. (2003). "The size distribution of galaxies in the Sloan Digital Sky Survey". In: *MNRAS* 343, pp. 978–994. DOI: 10.1046/j.1365-8711.2003.06740.x. eprint: astro-ph/0301527.

Skillman, E. D. (1996). "Neutral Hydrogen in Dwarf Galaxies". In: *The Minnesota Lectures on Extragalactic Neutral Hydrogen*. Ed. by E. D. Skillman. Vol. 106. Astronomical Society of the Pacific Conference Series, p. 208.

Smith, D. J. B. and C. C. Hayward (2015). "Deriving star formation histories from photometry using energy balance spectral energy distribution modelling". In: *MNRAS* 453, pp. 1597–1607. DOI: 10.1093/mnras/stv1727. arXiv: 1507.07554.

Snyder, G. F. et al. (2013). "Modeling Mid-infrared Diagnostics of Obscured Quasars and Starbursts". In: *ApJ* 768, 168, p. 168. DOI: 10.1088/0004-637X/768/2/168. arXiv: 1210.6347 [astro-ph.CO].

Speagle, J. S. et al. (2014). "A Highly Consistent Framework for the Evolution of the Star-Forming "Main Sequence" from z ~ 0-6". In: *ApJS* 214, 15, p. 15. DOI: 10.1088/0067-0049/214/2/15. arXiv: 1405.2041.

Springel, V. (2005). "The cosmological simulation code GADGET-2". In: *MNRAS* 364, pp. 1105–1134. DOI: 10.1111/j.1365-2966.2005.09655.x. eprint: arXiv:astro-ph/0505010.

Springel, V. and L. Hernquist (2003). "Cosmological smoothed particle hydrodynamics simulations: a hybrid multiphase model for star formation". In: *MNRAS* 339, pp. 289–311. DOI: 10.1046/j.1365-8711.2003.06206.x. eprint: arXiv:astro-ph/0206393.

Springel, V. et al. (2001). "Populating a cluster of galaxies - I. Results at [formmu2]z=0". In: *MNRAS* 328, pp. 726–750. DOI: 10.1046/j.1365-8711.2001.04912.x. eprint: astro-ph/0012055.

Springel, V. et al. (2008). "The Aquarius Project: the subhaloes of galactic haloes". In: *MNRAS* 391, pp. 1685–1711. DOI: 10.1111/j.1365-2966.2008.14066.x. arXiv: 0809.0898.

Stetson, P. B. (1987). "DAOPHOT - A computer program for crowded-field stellar photometry". In: *PASP* 99, pp. 191–222. DOI: 10.1086/131977.

Strateva, I. et al. (2001). "Color Separation of Galaxy Types in the Sloan Digital Sky Survey Imaging Data". In: *AJ* 122, pp. 1861–1874. DOI: 10.1086/323301. eprint: astro-ph/0107201.

Surace, J. A. et al. (1998). "HST/WFPC2 Observations of Warm Ultraluminous Infrared Galaxies". In: *ApJ* 492, pp. 116–136. DOI: 10.1086/305028.

Sutherland, R. S. and M. A. Dopita (1993). "Cooling functions for low-density astrophysical plasmas". In: *ApJS* 88, pp. 253–327. DOI: 10.1086/191823.

Tajiri, Y. Y. and H. Kamaya (2002). "Dynamical condition of neutral hydrogen envelopes of dwarf galaxies and their possible morphological evolution". In: *A&A* 389, pp. 367–373. DOI: 10.1051/0004-6361:20020594. eprint: astro-ph/0204301.

Tanaka, M. et al. (2004). "The Environmental Dependence of Galaxy Properties in the Local Universe: Dependences on Luminosity, Local Density, and System Richness". In: *AJ* 128, pp. 2677–2695. DOI: 10.1086/425529. eprint: astro-ph/0411132.

Tapia, M. T., M. Balcells, and M. C. Eliche-Moral (2010). "Galaxy Disk Heating as a Result of Minor Mergers". In: *American Institute of Physics Conference Series*. Ed. by V. P. Debattista and C. C. Popescu. Vol. 1240. American Institute of Physics Conference Series, pp. 423–424. DOI: 10.1063/1.3458555.

Tasca, L. A. M. et al. (2014). "The evolving SFR-M_star relation and sSFR since z˜5 from the VUDS spectroscopic survey". In: *ArXiv e-prints*. arXiv: 1411.5687.

Telles, E., J. Melnick, and R. Terlevich (1997). "The morphology of H II galaxies". In: *MNRAS* 288, pp. 78–107. eprint: astro-ph/9701062.

Telles, E. and R. Terlevich (1995). "The environment of HII galaxies". In: *MNRAS* 275, pp. 1–8. eprint: astro-ph/9501084.

Terlevich, R. et al. (2004). "How old are HII galaxies?" In: *MNRAS* 348, pp. 1191–1196. DOI: 10.1111/j.1365-2966.2004.07432.x. eprint: astro-ph/0311542.

Thatte, N. A. et al. (2014). "HARMONI: the first light integral field spectrograph for the E-ELT". In: *Ground-based and Airborne Instrumentation for Astronomy V*. Vol. 9147. SPIE Proceedings, p. 914725. DOI: 10.1117/12.2055436.

Thomas, D. et al. (2005). "The Epochs of Early-Type Galaxy Formation as a Function of Environment". In: *ApJ* 621, pp. 673–694. DOI: 10.1086/426932. eprint: astro-ph/0410209.

Tormen, G., F. R. Bouchet, and S. D. M. White (1997). "The structure and dynamical evolution of dark matter haloes". In: *MNRAS* 286, pp. 865–884. eprint: astro-ph/9603132.

Trager, S. C. et al. (2000). "The Stellar Population Histories of Early-Type Galaxies. II. Controlling Parameters of the Stellar Populations". In: *AJ* 120, pp. 165–188. DOI: 10.1086/301442. eprint: astro-ph/0004095.

Tully, R. B. (1987). "Nearby groups of galaxies. II - an all-sky survey within 3000 kilometers per second". In: *ApJ* 321, pp. 280–304. DOI: 10.1086/165629.

Tully, R. B., J. R. Mould, and M. Aaronson (1982). "A color-magnitude relation for spiral galaxies". In: *ApJ* 257, pp. 527–537. DOI: 10.1086/160009.

van Zee, L. (2001). "The Evolutionary Status of Isolated Dwarf Irregular Galaxies. II. Star Formation Histories and Gas Depletion". In: *AJ* 121, pp. 2003–2019. DOI: 10.1086/319947. eprint: astro-ph/0101135.

Vazdekis, A. et al. (2010). "Evolutionary stellar population synthesis with MILES - I. The base models and a new line index system". In: *MNRAS* 404, pp. 1639–1671. DOI: 10.1111/j.1365-2966.2010.16407.x. arXiv: 1004.4439 [astro-ph.CO].

Vilchez, J. M. (1995). "On the Spectroscopic Properties of Star-Forming Dwarf Galaxies in Different Environments". In: *AJ* 110, p. 1090. DOI: 10.1086/117589.

Vogelsberger, M. et al. (2014). "Introducing the Illustris Project: simulating the coevolution of dark and visible matter in the Universe". In: *MNRAS* 444, pp. 1518–1547. DOI: 10.1093/mnras/stu1536. arXiv: 1405.2921.

Walcher, C. J. et al. (2008). "The VVDS-SWIRE-GALEX-CFHTLS surveys: physical properties of galaxies at z below 1.2 from photometric data". In: *A&A* 491, pp. 713–730. DOI: 10.1051/0004-6361:200810704. arXiv: 0807.4636.

Walcher, C. J. et al. (2014). "CALIFA: a diameter-selected sample for an integral field spectroscopy galaxy survey". In: *A&A* 569, A1, A1. DOI: 10.1051/0004-6361/201424198. arXiv: 1407.2939.

Wang, L. et al. (2015). "NIHAO project - I. Reproducing the inefficiency of galaxy formation across cosmic time with a large sample of cosmological hydrodynamical simulations". In: *MNRAS* 454, pp. 83–94. DOI: 10.1093/mnras/stv1937. arXiv: 1503.04818.

Whitaker, K. E. et al. (2014). "Constraining the Low-mass Slope of the Star Formation Sequence at 0.5 z 2.5". In: *ApJ* 795, 104, p. 104. DOI: 10.1088/0004-637X/795/2/104. arXiv: 1407.1843.

Wiersma, R. P. C., J. Schaye, and B. D. Smith (2009). "The effect of photoionization on the cooling rates of enriched, astrophysical plasmas". In: *MNRAS* 393, pp. 99–107. DOI: 10.1111/j.1365-2966.2008.14191.x. arXiv: 0807.3748.

Wijesinghe, D. B. et al. (2012). "Galaxy And Mass Assembly (GAMA): galaxy environments and star formation rate variations". In: *MNRAS* 423, pp. 3679–3691. DOI: 10.1111/j.1365-2966.2012.21164.x. arXiv: 1205.3368 [astro-ph.GA].

Wisnioski, E. et al. (2015). "The KMOS^{3D} Survey: Design, First Results, and the Evolution of Galaxy Kinematics from 0.7 = z = 2.7". In: *ApJ* 799, 209, p. 209. DOI: 10.1088/0004-637X/799/2/209. arXiv: 1409.6791.

Worthey, G. and D. L. Ottaviani (1997). "Hγ and Hδ Absorption Features in Stars and Stellar Populations". In: *ApJS* 111, pp. 377–386. DOI: 10.1086/313021.

Worthey, G. et al. (1994). "Old stellar populations. 5: Absorption feature indices for the complete LICK/IDS sample of stars". In: *ApJS* 94, pp. 687–722. DOI: 10.1086/192087.

Wright, E. L. (2006). "A Cosmology Calculator for the World Wide Web". In: *PASP* 118, pp. 1711–1715. DOI: 10.1086/510102. eprint: astro-ph/0609593.

Wyder, T. K. et al. (2007). "The UV-Optical Galaxy Color-Magnitude Diagram. I. Basic Properties". In: *ApJS* 173, pp. 293–314. DOI: 10.1086/521402. arXiv: 0706.3938.

Yang, X. et al. (2007). "Galaxy Groups in the SDSS DR4. I. The Catalog and Basic Properties". In: *ApJ* 671, pp. 153–170. DOI: 10.1086/522027. arXiv: 0707.4640.

Yi, S. K. et al. (2005). "Galaxy Evolution Explorer Ultraviolet Color-Magnitude Relations and Evidence of Recent Star Formation in Early-Type Galaxies". In: *ApJ* 619, pp. L111–L114. DOI: 10.1086/422811. eprint: astro-ph/0411327.

Zieleniewski, S. et al. (2015). "HSIM: a simulation pipeline for the HARMONI integral field spectrograph on the European ELT". In: *MNRAS* 453, pp. 3754–3765. DOI: 10.1093/mnras/stv1860. arXiv: 1508.04441 [astro-ph.IM].